DEVELOPING A BIOSENSOR WITH APPLYING KALMAN FILTER AND NEURAL NETWORK TO ANALYZE DATA FOR FUSARIUM DETECTION

A Thesis Submitted to the College of
Graduate and Postdoctoral Studies
In Partial Fulfilment of the Requirements
For the Degree of Doctor of Philosophy
In the Department of Electrical and Computer Engineering
University of Saskatchewan

By
Son Ng. Pham

Saskatoon, Saskatchewan, Canada

Permission to Use

In presenting this thesis in partial fulfilment of the requirements for a Postgraduate degree from the University of Saskatchewan, it is agreed that the Libraries of this University may make it freely available for inspection. Permission of copying this thesis in any manner, in whole or in part, for scholarly purposes may be granted by the professor who supervised my thesis work or, in their absence, by the Head of the Department of Electrical and Computer Engineering or the Dean of the College of Graduate and Postdoctoral Studies in which my thesis work was done. It is understood that any copying or publication or use of this thesis or parts thereof for financial gain shall not be allowed without the written permission of the author. An appropriate recognition shall be given to me and to the University of Saskatchewan in any scholarly use which may be made of any material in my thesis.

Requests for permission to copy or to make other use of material in this thesis in whole or part should be addressed to:

Head of the Department of Electrical and Computer Engineering
57 Campus Drive
University of Saskatchewan
Saskatoon, Saskatchewan, Canada
S7N 5A9

OR

Dean
College of Graduate and Postdoctoral Studies
University of Saskatchewan
116 Thorvaldson Building, 110 Science Place
Saskatoon, Saskatchewan S7N 5C9 Canada

Abstract

Early detection of *Fusarium* is arduous and highly desired as the detection assists in protecting crops from the harmful potential of plant pathogens which affect the quality and quantity of agriculture products. The thesis work concentrates on searching an approach for *Fusarium* spore detection and developing portable, reliable and affordable *Fusarium* detection device. The system can also promptly and continuously sample and sense the presence of the fungus spores in the air. From the investigation of the *Fusarium oxysporum* Chlamydospores by ATR-FTIR spectroscopy, a distinct infrared spectrum of the Chlamydospore was collected. There are two typical infrared wavelengths can be used for *Fusarium* detection: 1054cm^{-1} (9.48µm) and 1642cm^{-1} (6.08µm). Infrared (IR) light is a form of electromagnetic wave which its wavelength ranges from around 0.75µm to 1000µm and it is invisible to human eyes. To be familiar with the light concepts and quantities, it is necessary to start working with the visible light which is also a form of electromagnetic wave with the wavelength range from about 0.3µm to 0.75µm. A visible spectrometer, which automatically corrects data error caused by unstable light, was built. By using the Kalman filter algorithm, Matlab simulations and training program, the appropriate coefficients to apply to the Kalman corrector were found. The experiments proved that the corrector in the visible spectrometer can reduce the data error in the spectra at the order of 10 times.

From the knowledge of working with the visible spectrometer and visible light, the task of searching the detecting approach and building the device in the IR spectrum was reconsidered. The *Fusarium* detection device was successfully built. Among other components to build the device, there are two essential thermopiles and one infrared light source. The infrared light source emits an IR spectrum from 2µm to 22µm. The two thermopiles working on the IR wavelengths of λ_1=6.09±0.06µm and λ_2=9.49±0.44µm are used for *Fusarium* spore detection analysis. The Beer-Lambert assists in quantifying the number of spores in the sample. The group distinction coefficient supports in distinguishing the *Fusarium* spore from other particulates in the experiments (pollen, turmeric, and starch). Pollen was chosen as it is often present in crop fields, and the other two samples were chosen as they help to verify the work of the system. The group distinction coefficients of *Fusarium* (1.14±0.15), pollen (0.13±0.11), turmeric (0.79±0.07) and starch (0.94±0.07) are distinct from each other.

The size of *Fusarium* spore is from about 10μm to 70μm. To mitigate the influence of the other particulates, such as pollens or dust which their sizes are not in the above range, a bandpass particle filter consists of a cyclone separator and a high voltage trap were designed and built. The particles with the sizes not in the interested range are eliminated by the filter. From simulations by the COMSOL Multiphysics and experiments, the particle filter proves that it works well with the assigned particle size range. The filter is useful as it helps to sample a certain size range which contains the interested bio objects.

As other electronic devices, the *Fusarium* detection device encountered several common types of noises (thermal noise, burst noise, and background noise). These noises along with the thermopile signals are amplified by the amplifiers. These amplifiers have high gain coefficients to amplify weak signals in nV to μV in magnitude. These noises depend on the operating conditions such as power supplies or environment temperature. If the operating conditions can be monitored, the information of the conditions can be used to correct the error data. To perform the correction task, the neural network was selected. To make a NN working, it requires sufficient data to train. In this research, the training data were collected in one week to record as much as possible working conditions. In addition to the thermopile data, the training data also included the environment temperature and the 5V and 9V voltage-regulator data. Then, the trained NN was applied to fix error data. The contribution of this NN method is the use of operating conditions to fix error data.

Although the errors in the data can be corrected well by the trained NN, several other problems still exist. In the samples of *Fusarium*, starch, pollen, and turmeric, the group-distinction coefficients of *Fusarium* and starch are very similar. To distinguish better the samples with similar group distinction coefficients, the existing *Fusarium* detection device was upgraded with a broadband thermopile. The extra thermopile was used along with λ_1 and λ_2 thermopiles to analyze the reflecting IR light of the samples. To pre-process the thermal noise and burst noise, an adaptive and cognitive Kalman algorithm was proposed. Burst noise is expressed in the form of outliers in the thermopile data. To detect these outliers, a mechanism of using first-order and second-order discrete differentiation of the data and correcting the burst noise and thermal noise was introduced. To study the effectiveness of this pre-processing, the pre-processed data and raw data were applied in the NN training. The main stopping parameters in the training are the number of epochs, absolute mean error, and entropy. The pre-processed data and the trained NN were used for distinguishing samples. The three-thermopile *Fusarium* detection device led to a use of a validation area to

distinguish the samples with similar group-distinction coefficients. The results prove that the use of three thermopiles works very well.

The research provides a comprehensive approach of designing system, particulate sampling, particulate filtering, signal processing, and sample distinguishing. The results from the experiments prove that the proposed approach can detect not only *Fusarium* but also many other different bio-objects. For further work from this research, the *Fusarium* detection apparatus should be tested in the crop fields infected by *Fusarium* spores. The outcomes of the research can be applied in other areas such as food safety and human living or hospital environment to detect not only *Fusarium* spores but the other pathogens, spores, and molds.

Acknowledgments

I would like to express my deepest gratitude to my supervisor, Professor Anh Dinh. Throughout my work for the research program at the University of Saskatchewan, I have received invaluable guidance, caring support, and helpful encouragement from Professor Anh Dinh. Without this instruction and support, I could hardly finish my research program. I thank to the funding provided by the Ministry of Agriculture, Government of Saskatchewan, Canada under Project Number 20140220. I also thank the Vietnam International Education Development (VIED) under the Ministry of Education and Training of Vietnam (MOET) for the financial support.

I would also like to thank to my committee members for their valuable comments. Especially, I am thankful to Professor Sven Achenbach and Mr. Garth Wells for their truthful suggestions on my work. I would also like to extend my gratefulness to the support from the support engineers of the Department of Electrical and Computer Engineering, especially Mr. Peyman Pourhaj. I thank my friends, especially Kien Doan and Thuan Chu, who shared their valuable experience in academic life at this university.

I would like to express my great gratitude to my family who are my Dad, Mom, wife, and children. They are always beside me and help me to concentrate on my work.

Finally, I would like to thank all the people who helped me to finish my thesis work. A few words mentioned here could not sufficiently and adequately demonstrates my appreciation to all whom I have met and worked with.

Table of Contents

List of Tables

List of Figures

List of Abbreviations

0D	Zero dimension
1D	One dimension
2D	Two dimensions
3D	Three dimensions
AAS	Active air sampler
ACKF	Adaptive-cognitive Kalman filter
ADC	Analog digital converter
AE	Absolute error
BASF	Badische Anilin-und Soda-Fabrik
BG	Background
BR	Broadband
CCD	Charge-coupled device
CFD	Computational fluid dynamics
CFI	Chlorophyll fluorescent imaging
CP	Correlation parameter
DC	Direct current
DNA	Deoxyribonucleic acid
ERR	Error
FDK	*Fusarium* damaged kernels
FEM	Finite element method
FHB	*Fusarium* head blight
FTIR	Fourier transform infrared
FP	Front peak
HV	High voltage
IC	Integrated circuits
IR	Infrared
MEMs	Micro-electromechanical
MFP	Mean front peak
MMN	Min max normalization

MP	Max peak
MWP	Mean whole peak
NDIR	Nondispersive infrared
NN	Neural network
OCS	Operating condition set
PAS	Passive air sampler
PD	Peak data
PDA	Potato dextrose agar
PM	Particulate matter
PMMA	Polymethyl methacrylate
qPCR	Polymerase-chain-reaction
RE	Relative error
RF	Radio frequency
SBG	Standard background
SMP	Standard max peak
SPECs	Spectrometers
UV	Ultra violet
VA	Validation area
VIS	Visible

1. Introduction

1.1. Motivation

Fusarium affects the immunization system of both human and animal, and as a result, undesired consequence can happen [C1.1– C1.3]. However, plants are the most influenced by the fungus, because, to the plants, this fungus brings fungal diseases such as crown rot, root rot, *Fusarium* dry rot, *Fusarium* wilt, and in particular, the *Fusarium* head blight (FHB) [C1.4– C1.10]. Canada is one of the top three wheat product exporters in the world, but according to BASF Canada Inc., to maintain this position, Canadian agriculture must confront with FHB and this is one of the biggest yearly challenges [C1.11] and the main factor resulting in *Fusarium* damaged kernels (FDK) [C1.11, C1.12]. Yearly, FHB has resulted in "$50 million to $300 million in losses" for Western Canada since the 1990s [C1.11]. In 2016, Alberta suffered a bad loss of $12.8 million due to FHB and FDK [C1.12]. Therefore, an early detection of the *Fusarium* spore presence in the field in order to have the appropriate treatment is the significant to prevent or mitigate the losses.

Many *Fusarium* detection approaches have been introduced. In [C1.13], G. Schiro et al. used spore traps to sample the air, then applying polymerase-chain-reaction (qPCR) machine and DNASTAR software to analyse the collected samples to detect and quantify the pathogen, such as *Fusarium*. Similarly, in [C1.14], J. S. West et. al pointed out that a qPCR machine can translate the amount of pathogen DNA into a number of *Fusarium* spores or spore density. In [C1.14], thermal images recorded by thermal camera was used to map diseases of the canopy of wheat or cereal plants in the field. In this method, the black and white images are acquired by converting the near infrared images. The infection places have the white color.

In [C1.15], Bauriegel et al. reported the experiments on spraying the pathogen into the wheat plants. The pathogen source of 250,000 *Fusarium* culmorum spores/ml was sprayed at condition of 20±2ºC, 70% humidity and 12hour lighted period by SON-T Plus 400W sodium-vapor lamps on three consecutive days. Every week, the wheat spikelets were studied three times using chlorophyll fluorescent imaging (CFI) to evaluate the ratio fluorescent. From the difference in CFI of healthy and infected spikelets, the infection level can be determined.

In [C1.1], *Fusarium* samples were identified by mass spectrometry. The samples were extracted from the patients in the L'hôpital Saint-Antoine, Paris, France. In another research [C1.16], the authors nurtured *Fusarium* samples in nutrient environments, and used mass spectrometry to measure mass-to-charge ratio to record the mass spectrum. The mass spectrum of the samples helps to recognize and categorize *Fusarium* spores as each substance has a distinct spectrum. In other *Fusarium* studies [C1.17, C1.18], infrared spectrum of absorption or emission of the investigated objects were recorded by near infrared and Fourier transform infrared (FTIR) spectroscopies. Analogous with mass spectrum, each infrared spectrum presents for each substance. A database of many substance spectra will help to identify whether the spectrum of the studied sample is of *Fusarium* or not.

Vinayaka et al. in [C1.19] introduced another method of applying impedance values. In this method, an impedance-based mould sensor which is gold electrodes built on a glass base can help to measure impedances of the samples. On the electrode surface, a small chamber containing agar gel is put on it. When the gel catches *Fusarium* spores, the spores develop and induce a gel pH change. This leads to the change in impedance. Methyl red indicator dye is used to monitor the pH change. The work proves that in 24 hours, which is the essential time for the spore development, the spore can be detected.

The effectiveness of these methods was shown through the studies mentioned above, however, several obstacles which may deter them from putting into practice. First, most of the machines are large, so it is cumbersome to have quick tests on the fields. Second, the training for operators is strict, as the operators must manoeuvre the machines properly and precisely. Third, the prices of these devices are high, because they are specialized for particular applications. Last but not least, the maintenance fees of these machines are mostly very high.

1.2. Research objectives

Solving the mentioned obstacles is the target of this thesis work. The focus is in the designing of a low cost, portable, accurate, and reliable device to detect and quantify *Fusarium* in the air. To achieve the target, several outstanding research objectives are set and detailed as follows.

- Developing an error correction module by applying Kalman algorithm to be used in portable device in which small battery is the main power source. The output voltage from the battery decreases with time to a certain value that can affect stability of the light source in a spectrometer to analyze gas or other samples. In this step, the focus is to build an effective error corrector for the 24-bit visible spectrometer. Along with the use of the Kalman algorithm, the spectrometer is equipped with light source, light sensors, and optical devices such as focus lens, collimated lens, and window filter. The Beer-Lambert law is also required in the developing of the device. This step contributes to the new approach by applying Beer-Lambert law and Kalman algorithm in developing of portable visible spectrometer and other spectrum analysis devices in higher wavelength spectrum, in particular the short-wave and mid-wave infrared spectrometers.

- Developing an approach to detect and analyze *Fusarium* which can be used to build a portable and low-cost device. As mentioned above, the previous detection methods require expensive systems which are not suitable for field detection. Using spectra analysis to detect *Fusarium* spores requires the system which operates in the spectrum in which the spores react to certain wavelengths distinctively. The wavelengths must be found before the system can be designed and data analysis can be conducted. Selection of an appropriate electromagnetic wave range and the detector type is important in the building of the detection device. Beer-Lambert law is to be used to construct a group distinction coefficient in order to distinguish the samples as each substance has a specific coefficient. Spore detection is based on the group distinction coefficient while the quantity of the spores in the sample is estimated by using the absorption relationship of the spore to selected electromagnetic wave range. This step contributes significantly in the developing of a new bio-sensor system which is portable, low cost, low maintenance without the requirement for operators.
- Developing an air sampler to select particular particulate sizes to reduce interference and improve detection accuracy. As *Fusarium* spore sizes are from 10µm to 70µm, it is meaningful and important to select only the particulates in that range floating in the air while removing other unwanted samples. This bandpass particle filter assists in mitigating the "noise" caused by unwanted particulates such as pollens, dust, and other spores. This task requires the participation in many areas including material, physics, mechanical devices, and electricity. Before building a prototype and test, simulation of the complete system must be performed, COMSOL is an appropriate tool in this case. Cyclone and high voltage trap are the main components in such particulate filter. This step contributes in the use of a

combination of mechanical and electrical devices to filter out the unwanted particulates in an air sampler.

- Developing a method to reduce noise to improve decision in the *Fusarium* detection device. As in any electronic system, this device inherits intrinsic and extrinsic noises. Thermal, shot, flicker, and burst noises may cause significant errors in the data which represent the presence of particular substance, for example the *Fusarium* in the sample. Several approaches can be investigated, in which, the improvement of the Kalman algorithm and the use of neural network to remove the noise are appropriate. The focus should be on training of the neural network. The training data must be collected under variety of noise and operating condition before applying into the data to make detection decision. This step contributes in the use of neural network and Kalman algorithm in mitigation noises in spectral analysis systems.
- Developing a method for better distinguishing of two samples with similar group-distinction coefficients. In reality, this similarity results in difficulty and error in detection decision for the substances having similar physical structure and chemical compounds. Further modification and upgrading the device is required in particular hardware. The addition of hardware assists in collecting more information for data analysis. A knowledge of the substance absorption detected by a broadband thermopile combines with the narrow band thermopiles will further separate the group-distinction coefficients. This step contributes in the methodology to improve reliability and detection accuracy.

1.3. Organization of the thesis

The rest of the thesis is arranged as follows. As this thesis is of manuscript type, most chapters are independent therefore Chapter 2 is used to provide the background of the methods used for the design of the devices, as well as the formation of the experiments in the project. Chapter 3 is extracted from a journal paper published in 2017. This chapter describes the method and results of the design, development, construction and testing of a visible spectrometer. In this chapter, the Kalman algorithm which is applied for a linear output. The other algorithms such as greedy or divide and conquer algorithm are also used to achieve the best performance. Chapter 4 comes from a journal paper published in 2018. The chapter introduces the developing of a nondispersive thermopile device and its testing results. The Beer-Lambert law, the group distinction coefficient, and the IR components used in the *Fusarium* detection device are described in detail. In this chapter, the quantification and the detection methods of the *Fusarium* spores are also presented.

A journal paper published in 2019 is used in Chapter 5 to discuss the work and the principle of a bandpass particle filter which is a combination of the HV trap and a quad-inlet cyclone separator. The simulation results of the trap and the separator are described along with the important analysis on the simulation results. Chapter 6 is based on a submitted journal paper which concentrates on the applying of an artificial neural network to process noise for the developed *Fusarium* detection device. In this chapter, the monitoring information of the operating condition and the background noise is utilized as the training data for the neural network. The trained neural network, then, is applied to correct new data under new operating conditions and background information. Chapter 7 is another published journal paper describes the techniques to improve reliability and fidelity of the *Fusarium* detection device. The improvement comes from the upgrading the device with a broadband thermopile to analyze the IR reflection from the sample in the air trap. In addition, an adaptive and cognitive Kalman algorithm and a neural network are applied to process thermal noise, burst noise, and background noise. To evaluate the work of the applied methods, entropy is used to provide an estimation method on the working efficiency of the Kalman algorithm and the neural network. The final chapter summarizes the project and suggests further investigations to continue the research and bring the results to apply in real applications.

References

[C1.1] C. Marinach-Patrice et al., “Use of mass spectrometry to identify clinical Fusarium isolates,” Clinical Microbiology and Infection, vol. 15, no. 7, pp. 634–642, Jul. 2009.

[C1.2] M. Nucci and E. Anaissie, “Fusarium Infections in Immunocompromised Patients,” Clinical Microbiology Reviews, vol. 20, no. 4, pp. 695–704, Oct. 2007.

[C1.3] G. Antonissen et al., “The Impact of Fusarium Mycotoxins on Human and Animal Host Susceptibility to Infectious Diseases,” Toxins, vol. 6, no. 2, pp. 430–452, Jan. 2014.

[C1.4] Y. Lin et al., “A Putative Transcription Factor MYT2 Regulates Perithecium Size in the Ascomycete Gibberella zeae,” PLoS ONE, vol. 7, no. 5, p. e37859, May 2012.

[C1.5] N. A. Foroud, S. Chatterton, L. M. Reid, T. K. Turkington, S. A. Tittlemier, and T. Gräfenhan, “Fusarium Diseases of Canadian Grain Crops: Impact and Disease Management Strategies,” Future Challenges in Crop Protection Against Fungal

Pathogens, A. Goyal and C. Manoharachary, Eds. New York, NY: Springer New York, 2014, pp. 267–316.

[C1.6] E. D. de Toledo-Souza, P. M. da Silveira, A. C. Café-Filho, and M. Lobo Junior, “Fusarium wilt incidence and common bean yield according to the preceding crop and the soil tillage system,” Pesq. agropec. bras., vol. 47, no. 8, pp. 1031–1037, Aug. 2012.

[C1.7] A. Adesemoye et al., “Current knowledge on Fusarium dry rot of citrus,” Citrograph, no. December, pp. 29–33, 2011.

[C1.8] A. Peraldi, G. Beccari, A. Steed, and P. Nicholson, “Brachypodium distachyon: a new pathosystem to study Fusarium head blight and other Fusarium diseases of wheat,” BMC Plant Biol, vol. 11, no. 1, p. 100, 2011.

[C1.9] R. D. Martyn, “Fusarium Wilt of Watermelon: 120 Years of Research,” in Horticultural Reviews: Volume 42, J. Janick, Ed. Hoboken, New Jersey: John Wiley & Sons, Inc., pp. 349–442, 2014.

[C1.10] F. Leslie, B. A. Summerell and S. Bullock, The Fusarium Laboratory Manual. Iowa Blacwell, 2006, https://doi.org/10.1371/journal.pone.0037859.

[C1.11] BASF Canada Inc., “Fusarium Management Guide.” BASF Canada Inc. Available: https://agro.basf.ca. [Accessed: 01-Oct.-2019].

[C1.12] Zoia Komirenko, “Economic Cost of Fusarium.” Alberta Agriculture and Forestry, Government of Alberta, Jul-2018. Available: https://www.alberta.ca/open-government-program.aspx. [Accessed: 01-Oct.-2019].

[C1.13] G. Schiro, G. Verch, V. Grimm, and M. Müller, “Alternaria and Fusarium Fungi: Differences in Distribution and Spore Deposition in a Topographically Heterogeneous Wheat Field,” JoF, vol. 4, no. 2, p. 63, May 2018.

[C1.14] J. S. West, G. G. M. Canning, S. A. Perryman, and K. King, “Novel Technologies for the detection of Fusarium head blight disease and airborne inoculum,” Trop. plant pathol., vol. 42, no. 3, pp. 203–209, Jun. 2017.

[C1.15] E. Bauriegel, A. Giebel, and W. B. Herppich, “Rapid Fusarium head blight detection on winter wheat ears using chlorophyll fluorescence imaging,” J. Appl. Bot. Food Qual., vol. 83, no. 2, pp. 196–203, 2010.

[C1.16] M. Marchetti-Deschmann, W. Winkler, H. Dong, H. Lohninger, C. P. Kubicek, and G. Allmaier, “Using spores for Fusarium spp. Classification by MALDI-based intact cell/spore mass spectrometry," Food Technol. Biotechnol., vol. 50, no. 3, pp. 334–342, 2012.

[C1.17] A. Salman, L. Tsror, A. Pomerantz, R. Moreh, S. Mordechai, and M. Huleihel, "FTIR spectroscopy for detection and identification of fungal phytopathogenes," Spectroscopy, vol. 24, no. 3–4, pp. 261–267, 2010.

[C1.18] E. Tamburini, E. Mamolini, M. De Bastiani, and M. G. Marchetti, "Quantitative determination of Fusarium proliferatum concentration in intact garlic cloves using near-infrared spectroscopy," Sensors (Switzerland), vol. 16, no. 7, 2016.

[C1.19] P. Papireddy Vinayaka et al., "An Impedance-Based Mold Sensor with on-Chip Optical Reference," Sensors, vol. 16, no. 10, p. 1603, Sep. 2016.

[C1.20] Horiba Scientific, A Guidebook to Particle Size Analysis, www.horiba.com/fileadmin/uploads/Scientific/Documents/PSA/PSA_Guidebook.pdf. [Accessed: 17 May, 2019].

[C1.21] Anne Renstrom, "Exposure to airborne allergens: a review of sampling methods," Journal Environment Monitor, vol. 4, no. 4, pp. 619–622, Jun. 2002.

[C1.22] K. Toma et al., "Repetitive Immunoassay with a Surface Acoustic Wave Device and a Highly Stable Protein Monolayer for On-Site Monitoring of Airborne Dust Mite Allergens," Analytical Chemistry, vol. 87, no. 20, pp. 10470–10474, Oct. 2015.

[C1.23] G. Vasilescu, "Physical Noise Sources," in Electronic Noise and Interfering Signals - Principles and Applications, Printed in Germany: Springer, pp. 45–67, 2004.

[C1.24] Texas Instruments, "Noise Analysis in Operational Amplifier Circuits," Texas Instrument, 2007. [Online]. Available: http://www.ti.com/. [Accessed: 01-Aug-2019].

[C1.25] E. B. Moullin and H. D. M. Ellis, "The spontaneous background noise in amplifiers due to thermal agitation and shot effects," Institution of Electrical Engineers - Proceedings of the Wireless Section of the Institution, vol. 9, no. 26, pp. 81–106, 1934.

2. Background

In this chapter, the background relating to the research will be introduced and discussed. It includes the function, structure and type of spectrometers, the group-distinction coefficient, air samplers, simulations, and the unstable operation processing by applying Kalman filter and neural network used in this research. More details of the devices, algorithms or simulations can be seen in the sub-sections.

2.1. Optical spectrometer

An optical spectrometer is a device for analysing electromagnetic wavelengths of a large light range spectrum. It is commonly used to analyse sample materials. The phase of samples can be solid, liquid, or gas. The molecules of samples can absorb or reflect the incident light from a certain incident light source. Relating to ultraviolet (UV) or visible (VIS) radiation absorption, the outer electrons are excited and transit from ground states to excited states. The ground state can be π bonding, σ bonding, or non-bonding molecular orbital. The excited state can be π^* or σ^* anti-bonding molecular orbital. Generally, an electron transiting between two certain orbitals requires an appropriate excitation photon energy which also relates to a certain wavelength. The photon energy equals the energy gap between the two orbitals. Besides this absorption, infrared absorption is actually more widely used in practice as in the infrared (IR) spectrum, there are many more molecule types which can interact with IR. As IR radiation energy is smaller than ultraviolet and visible energy, IR energy is hardly to provoke an electron transition between the molecular orbitals. It mainly pertains to the vibration and rotation of molecules when they absorb IR photons. The explanation can be based on the interaction of the dipole moment of molecules and the electric or magnetic field of the incident electromagnetic wave. The interaction can cause stretching (symmetric and asymmetric) and bending (rocking, scissoring, wagging, and twisting). In addition to these vibrations, vibrational coupling can happen between a bending vibration and a stretching vibration, two bending vibrations, or two stretching vibrations, …. After interacting with a sample, the interacted light output is analysed. This analysis can reveal the features of the investigated sample [C2.1– C2.3].

The light source used to provide electromagnetic wavelength is important, as its spectrum must be large enough for analysis. There are two classes of light sources widely used in spectrometers: continuous sources such as argon, xenon, hydrogen or tungsten lamps, and line sources such as hallow cathode lamps or lasers [C2.4]. Both types of dispersive and nondispersive devices can modify the incident light from a light source to the interested wavelengths. These sources can work in UV, VIS or infrared ranges. To continuous IR sources, based on method and technology, they could be classified into four common types: bulb, wound, filament and micro-electromechanical (MEMs) sources [C2.5]. Based on whether a dispersive or nondispersive device is used in a spectrometer, the spectrometer can be classified as a dispersive or nondispersive spectrometer.

A dispersive spectrometer will have a dispersive element which can be a monochromator grating or a prism to separate the incident light beam. The work of spectrometers can be explained by diffraction, diffusion, and refraction theories [C2.6]. This type of spectrometer can be used to investigate gas, liquid or solid materials. The light beam can be shined through the sample before being dispersed by a prism or a monochromator.

A nondispersive spectrometer will have a nondispersive element which can have a filter to remove undesired wavelengths and allow the necessary wavelengths to go through. The filter can utilize the absorption feature of materials such as glass to filter infrared light or gases such as carbon dioxide, argon or xenon. An optical filter which is a sandwich of thin layers also based on the interference between the incident and reflected lights to select desired wavelengths [C2.7, C2.8]. For instant, in P. Wang et al. [C2.9], germanium and niobium-pentoxide bandpass filters of 160nm and 300nm bandwidths were fabricated by a “microwave plasma-assisted sputter reactor”; the thicknesses of germanium and niobium-pentoxide layers were controlled and monitored by Inficon IC/5, a thin film deposition controller [C2.10]. Nondispersive devices are often applied in gas detection.

Detectors for UV-Vis spectrometers to analyse light intensity of the wavelengths can be photomultiplier tubes, charge-coupled devices and photodiodes [C2.11, C2.12]. In the infrared (IR) range, the IR detectors can be categorized as: “thermal detector which is wavelength-independent type and quantum (or photon which is wavelength-dependent type” [C2.5]. The heat caused by incident IR light heats up thermal detectors and the detector output resistance or voltage will change correspondingly. A quantum detector converts certain photon energy into current, voltage or the photon energy influences the conductivity of the detector [C2.5]. In the thermal detector category, there could be four subcategories: thermopile/thermocouple, bolometer, pneumatic cell, and pyroelectric detectors. In the quantum detector category, based on the work principles, there are two subcategories: intrinsic and extrinsic detectors [C2.5]. As infrared range is large, it can be divided into three smaller ranges: near IR range of 0.75µm to 3µm, middle IR range of 3µm to 6µm, and far IR range of 6µm to 15µm. To deal with each IR range, there will be certain typical IR detectors.

2.2. Group distinction coefficient

In spectrometer application, the Beer-Lambert law is an important principle, because it provides a method of quantifying a substance by estimating the absorbance of the substance. The absorbance is calculated by applying the latter equation:

$$A = -\log T = -\log\left(\frac{P_\lambda}{P_{0,\lambda}}\right) \tag{2.1}$$

where *A* is the absorbance coefficient (n.u.), and *T* is transmittance coefficient (n.u.); $P_{0,\lambda}$ is the IR power of the light source at the wavelength λ (W/Sr); P_λ is the power of the light λ going through a sample (W/Sr) [C2.9, C2.12, C2.13]. To determine the quantity of the sample, the following equation can be employed:

$$A = \varepsilon.c.l \tag{2.2}$$

where ε is extinction or attenuation coefficient (L/mol.cm); *c* is the concentration of the absorbing substance (mol/L); *l* is the length of solution which the light passes through (cm). Therefore, if *A* can be estimated from equation (2.1), the concentration can be calculated by equation (2.2).

In spectrum analysis, each substance has a distinct spectrum and this feature helps to identify substances. However, investigating spectra of the substances requires a spectrometer or spectroscopy which is expensive and cumbersome. Let's call P_{0,λ_1}, P_{λ_1}, P_{0,λ_1}, and P_{λ_2} are the monochromatic power measurements (W/Sr) of the light source λ_1, the light λ_1 passing through the sample, the light source λ_2, and the light λ_2 passing through the sample respectively. As we want to use these quantities in detection. Generally speaking, the ratio between $\frac{P_{\lambda_1}}{P_{0,\lambda_1}}$ and $\frac{P_{\lambda_2}}{P_{0,\lambda_2}}$ is nonlinear. If the intensity of the light source changes, the ratio will be changed too. As a result, it cannot be used to detect an object. A method to linearize the correlation of these quantities should be found first. From Beer-Lambert law, we found that the group-distinction coefficient of the two carefully-selected wavelengths from the spectrum of the sample can help to identify a particular sample from the other samples [C2.13]. The group-distinction coefficient is defined as the following equation:

$$\eta = \frac{\varepsilon_{\lambda_1}}{\varepsilon_{\lambda_2}} = \frac{\log\left(\frac{P_{\lambda_1}}{P_{0,\lambda_1}}\right)}{\log\left(\frac{P_{\lambda_2}}{P_{0,\lambda_2}}\right)} \tag{2.3}$$

in which ε_{λ_1} and ε_{λ_2} are the attenuation coefficients corresponding λ_1 and λ_2 respectively. Equation (2.3) is the key to solve the problem of *Fusarium* (*F.*) identification and reduction of expense and dimensions of the *Fusarium* detection device which was designed in this research.

From equation (2.3), to be able to detect and analyse *Fusarium*, λ_1 and λ_2 should be defined. *Fusarium* was sampled from rotten garlic and then nurtured using Potato Dextrose Agar (PDA). After around 4 to 6 weeks, the nurtured samples form spores and hyphae. These samples were analyzed by a Fourier Transform Infrared (FTIR) spectroscopy. Based on the FTIR spectrum of the *Fusarium* samples, λ_1 and λ_2 were distinctly determined.

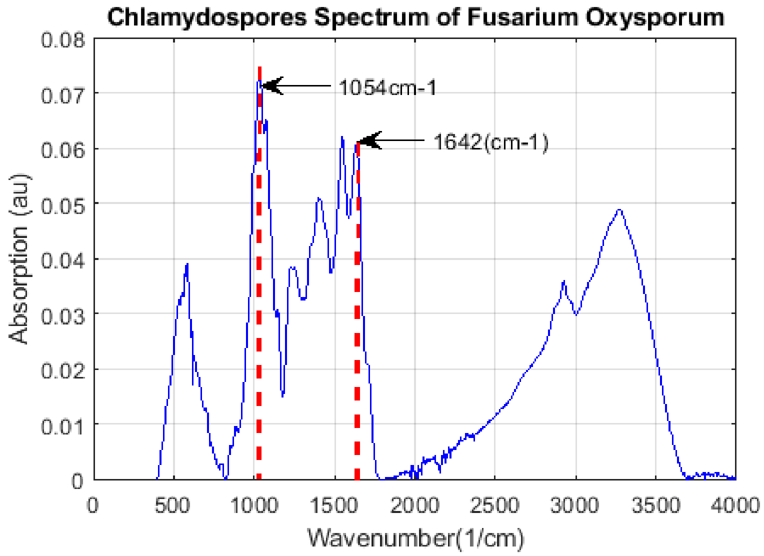

Figure 2. 1. FTIR spectrum of *Fusarium* and the two distinct wavelengths λ_1 and λ_2.

2.3. Air sampler

Fusarium species can be dispersed into the environment by the air phase, water phase, or the combination of the above phases (*Fusarium* in bubles in water, or in tiny water drops taken away by wind) [C2.13]. As air phase accounts for many serious *Fusarium* contamination cases, the

Fusarium detection method was built by using the air-phase. In this method, the first step is that the air must be sampled.

There are several methods to sample the air, in which these methods can be sorted into two main classes: active air sampler (AAS) and passive air sampler (PAS). Each class has its own advantages and disadvantages. Generally, PASs often have either sticky or high viscosity medium to catch particulates in the air when it flows through the medium. Although a PAS is non-expensive, its temporal resolution is low. It is because PASs depend on wind [C2.14– C2.16]. On the other side, AASs are, generally, more expensive than PASs, but their temporal resolutions are high and stable because of using electric devices, such as vacuum pump, air pump or rotary motor to maintain the sampling rate [C2.15, C2.17]. Practically, AASs are used more widely than PASs.

As *Fusarium* spores can have the sizes from around 10µm to 70µm, retaining only the particles in that size range is necessary to avoid the interference of the unwanted particles which are not in that range. The combination of a quad-inlet cyclone separator and a high voltage (HV) trap can conduct the task and become a particle bandpass filter as shown in Figure 2.2.

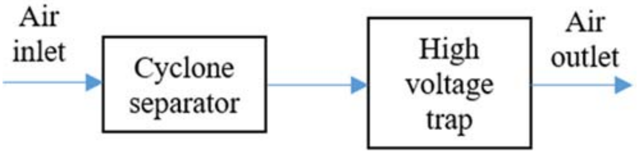

Figure 2. 2. Bandpass particle filter

In the figure, the air goes through the cyclone first and then through the high voltage (HV) trap. The operation of the cyclone can be explained by the gravity, drag, buoyancy, and centrifugal forces [C2.18]. The velocity equation of particles in the cyclone is:

$$v_p = \frac{d_p^2 . \rho_p . v_t}{18\mu_g . R} \tag{2.4}$$

in which, d_p is particle diameter (m); ρ_p is particle mass density (kg/m^3); v_t: particle velocity (m/s); μ_g is the air viscosity (Ns/m^2); R is the orbital radius. It can be seen that $v_p \sim d_p^2$, where v_p points toward the wall the cyclone. Therefore, the large particles are caught by the cyclone and the small particles escape to the output. The cyclone works as a low pass particle filter. As the remaining particles enter the HV trap, they are polarized and interact with the electric field created by the HV. The force excerted on the particle is the dielectrophoretic force:

$$F_{DEP} = \pi \frac{d_p^3}{4} \frac{\varepsilon_m(\varepsilon_p - \varepsilon_m)}{\varepsilon_p + 2\varepsilon_m} \nabla |E|^2 \tag{2.5}$$

where, ε_m is the medium permittivity; ε_p is the particle permittivity [C2.19]. Equation (2.5) shows that $F_{DEP} \sim d_p^3$. Consequently, the large particles tend to be caught by the HV trap and the small particles can flee away. The HV trap is a high pass-particle filter. Finally, the combination of these two components will form a bandpass filter of the particle size.

2.4. Simulation

In physical and engineering problems in practice, there are the differential, partly differential, or integration equations. To many reality problems, the traditional method of using calculus theories is difficult to reach the solutions. By using approximation, the problems can be more favorably solved. The development of the approximation-calculation methods has led in forming many well-known simulation softwares such as NASTRAN, ANSYS, CASTEM, or COMSOL Multiphysics. Basically, a simulation program mimics a certain physics phenomenon, a process or a system in reality by applying approximate conditions of that phenomenon or system. Thus, a simulation can be considered as a physical model and the model good or bad is reflected by if the simulation outcomes are close to the real results. A simulation also helps to reduce the time spending for conducting real experiments which can be expensive and time consuming. In addition, it supports in understanding more clearly about the simulated phenomenon or system.

Some well-known approximation methods were introduced such as Euler, Newton, Runge-Kutta, Milne, Hamming, finite difference time domain (FDTD), or finite element methods (FEM). Depending on the type of problem, an approximation method can be chosen to solve. In these methods, FEM is probably the most popular as it can be applied in many types of technical problems. The calculation procedure of FEM is as the following [C2.20]:

Step 1: Domain discretization in which the problem domain is divided into subdomains or finite elements. The elements can be straight lines, triangles, quadrilaterals, hexahedrons, and tetrahedrons.

Step 2: Forming element equations or approximation equations for finite elements. The original equations will be approximated by the element equations. The element equations can be polynomial or trigonometrical functions. The polynomial functions are often chosen as the differentiation or integration calculation is easier. Additionally, the precision in calculation can be increased by increasing the order of the approximation polinomial funtions [C2.20].

Step 3: Equation assembling to obtain global equations.

Step 4: Solving the global equations to find the unknowns.

In this research, to design a bandpass particle filter as well as a HV trap for *Fusarium* detection system, before building and integrating them into the system, it is essential to know whether they can work as expected by simulation. To conduct the task, COMSOL Multiphysics was used. This software is a cross-platform one and applies FEM to solve engineering and physical problems [C2.21, C2.22]. The software comprises many modules, namely Fluid and Heat, Mechanical, Electrical, Chemical, Structural and Acoustics, and Multiphysics modules. In each module, there are many submodules, for examples, Electrical: *AC/DC, RF, Wave Optics, Ray Optics, ...,* or Fluid and Heat: *CFD, Mixer, Microfluidics, Subsurface Flow, ...* From the software manual book [C2.23], there is a Model Builder which is important to support for 0D or 1D Axisymmetric, 1D, 2D and 3D simulations.

Another advantage of using COMSOL Multiphysics is that the designed-geometrical structure can be exported and saved for later use. The *geometry* in COMSOL can be converted into stereo lithography (STL) file which is a standard file for 3D printing. Therefore, it can help to save time to redesign the structure in another software for further steps after simulation. Alternatively, instead of creating the STL file from *geometry*, this file can be formed by going to the *Mesh* node of the *Component* branch in the *Model Builder*. One useful note, in simulation, the layer thickness of the geometry is often set zero. A 3D printer cannot print out a stable and hard structure in this case. Thus, before exporting the geometry, one should adjust the layer thickness not equal to zero.

2.5. Unstable operation processing

To a portable device, a battery is an essential part to power the device. As the device can be used at certain location for a long time, the output of the battery can be unstable at certain time and can impact the fidelity of the device [C2.5, C2.12]. In addition, thermal noise, shot noise, avalanche noise, burst noise, and background noise also impact on the function of the device [C2.13, C2.24, C2.25]. In the device, thermal, burst, and background noises influenced the thermal signals. There are many approaches to process these noises such as analog filter or digital filter. Kalman algorithm can be used to reduce thermal and burst noises by adjusting the process noise for instant, while the background noise and the influence of the battery are processed by employing neural network [C2.26].

2.5.1. Kalman algorithm

Kalman algorithm was suggested in 1960 by Rudolf E. Kalman and can be applied in many areas such as navigation, tracking objects, or finance [C2.27– C2.29]. In general, a Kalman algorithm has two stages: prediction stage and observation stage. At prediction stage, the current discrete-time state is estimated from the previous observation state. Then, the error covariance is calculated by using the previous process noise covariance and state covariance. In the observation stage, the Kalman gain and the state is calculated by applying the just mentioned state and the error covariance in the prediction stage. Finally, the state covariance is evaluated by employing the error covariance and Kalman gain. As Kalman is an optimal algorithm, its outputs are improved continuously based on a recursive method of evaluating the prediction and covariance. In addition, a system can be either linear or nonlinear, if the state of the system is investigated. Therefore, there are Kalman algorithms which can be applied to different types of the systems.

In the research of *Fusarium* detection [C2.30], the Kalman algorithm was applied to correct the thermal or Johnson and burst noises. The process noise in the algorithm was adjusted depend on the types of noise (thermal noise, burst noise, and the magnitude). As the burst noise causes outliers, an outlier-detection mechanism was designed. Besides, a recursive mechanism was simply built in the algorithm to recall itself N times. N was a positive-integer number. The process noise and N depended on the magnitude of the burst noise. Based on the background noise correction by applying neural network (NN), the efficiency of the noise correction was evaluated. The evaluation criteria were the training times, entropies, and absolute errors of the non-preprocessed and preprocessed data. The diagram of correction-efficiency evalutation is illustrated in Figure 2.3.

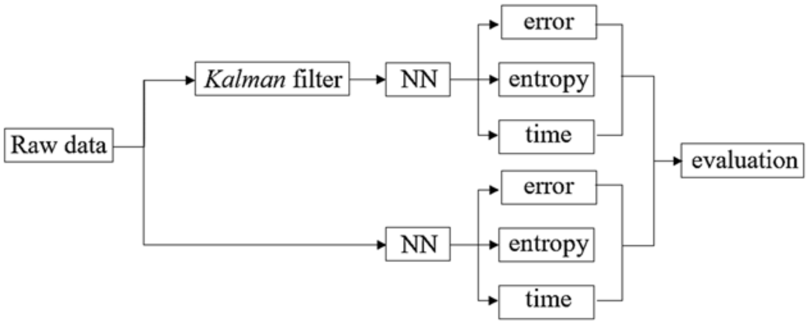

Figure 2. 3. Efficiency evaluation of with and without preprocessing.

2.5.2. Neural network

Neural network (NN) is a branch of machine learning technology [C2.30]. There are many NN applications such as image processing, remote sensing, or signal processing [C2.31– C2.33]. Basically, a NN system includes many artificial neuron which simulates a biology neuron [C2.34, C2.35]. An artificial neuron may have one or multiple input and output. These inputs will be summed up after being multiplied with weight coeffcients and adding a bias coefficient. The sum then is activated by an acitvation function. The activation function can be sigmoid, ReLU, softplus, or linear function [C2.34-C2.36]. A NN has an input layer, an output layer, and many hidden layers. The number of the neurons or nodes in each hidden layer and the number of the hidden layers are somewhat arbitrarily selected. In reality, these numbers can be selected by experiment and cognition. The weights and biases can be found by NN training and by certain algorithm. There are many algorithms to search the weights and biases such as backpropagation algorithm (BPA), stochastic gradient descent (SGD), Newton algorithm, or Levenberg-Marquardt algorithm (LMA) [C2.30].

To train the NN, a temperature sensor and two voltage monitor modules were installed into the *Fusarium* detection device. Applying the Kalman algorithm to preprocess raw data and employing NN can reduce undesired noise and error, thereby the *Fusarium* identification and quantification will be more precise. To have a good correction, it is recommended to collect as many thermopile data as possible in different operating condition.

In training NN, there are stopping criteria to control the training procedure. The criteria can be based on absolute error, mean square error, epoch number, etc. In our training NN, we used epoch number, mean square error, and entropy. In signal processing, entropy is a quantity to measure the uncertainty or the randomness. Since the training NN tends to reduce the background noise, the entropy of the differentiation of the processed data will be improved in comparison with the entropy of the differentiation of the raw data [C2.30].

References

[C2.1] A. Salman, L. Tsror, A. Pomerantz, R. Moreh, S. Mordechai, and M. Huleihel, “FTIR spectroscopy for detection and identification of fungal phytopathogenes,” Spectroscopy, vol. 24, no. 3–4, pp. 261–267, 2010.

[C2.2] Kris Walker, “Spectrometer Technology and Applications,” AZoM.com, 31-Oct-2013. [Online]. Available: https://www.azom.com/article.aspx?ArticleID=10245. [Accessed: 05-Jun-2019].

[C2.3] Thermo Fisher Scientific Co., *FT-IR vs. Dispersive Infrared - Theory of Infrared Spectroscopy Instrumentation*, Thermo Fisher Scientific Co.. Available: http://www.thermo.com.cn/. [Accessed: 05-Jun-2019].

[C2.4] “Theoretical background: Light Sources-Different types of light sources - Avantes.” [Online]. Available: https://www.avantes.com/support/theoretical-background/light-sources/960-introduction-light-sources/462-different-types-of-light-sources. [Accessed: 05-Jun-2019].

[C2.5] S. Pham and A. Dinh, “Analysis on Nondispersive Infrared Device Characteristics Using Thermopile,” The IEEE 32nd Canadian Conference on Electrical and Computer Engineering (CCECE), Edmonton, Canada, p. 4, May 2019.

[C2.6] “Spectrometer,” Chemistry LibreTexts, 02-Oct-2013. [Online]. Available: https://chem.libretexts.org/Bookshelves/Analytical_Chemistry/Supplemental_Modules_(Analytical_Chemistry)/Instrumental_Analysis/Spectrometer. [Accessed: 05-Jun-2019].

[C2.7] M. Swickrath, M. Anderson, S. McMillin, and C. Broerman, “Application of Commercial Non-Dispersive Infrared Spectroscopy Sensors for Sub-ambient Carbon Dioxide Detection,” in 42nd International Conference on Environmental Systems, San Diego, California, July 15-19, 2012.

[C2.8] Louise Helen Crawley, “Application of Non-Dispersive Infrared (NDIR) Spectroscopy to the Measurement of Atmospheric Trace Gases,” Master of Science, University of Canterbury, Christchurch, New Zealand, New Zealand, 2008.

[C2.9] P. Wang et al., “Optimised Performance of Non-Dispersive Infrared Gas Sensors Using Multilayer Thin Film Bandpass Filters,” Coatings, vol. 8, no. 12, p. 472, Dec. 2018.

[C2.10] IC/5 Thin Film Deposition Controller Manual, Inficon, http://www.manualsdir.com/manuals/562551/inficon-ic_5-thin-film-deposition-controller.html. [Accessed: 01-Aug-2019].

[C2.11] C. Knappe, F. A. Nada, M. Richter, and M. Aldén, “Comparison of photo detectors and operating conditions for decay time determination in phosphor thermometry,” Review of Scientific Instruments, vol. 83, no. 9, p. 094901, Sep. 2012.

[C2.12] S. Pham and A. Dinh, “Using the Kalman Algorithm to Correct Data Errors of a 24-Bit Visible Spectrometer,” Sensors, vol. 17, no. 12, p. 2939, Dec. 2017.

[C2.13] Son Pham, Anh Dinh, and Khan Wahid, “A Nondispersive Thermopile Device with an Innovative Method to Detect Fusarium Spores,” IEEE Sensors Journal, vol. 19, issue 19, pp. 8657-8667, Jun. 2019.

[C2.14] B. Feng, B. Chen, W. Zhuo, and W. Zhang, “A new passive sampler for collecting atmospheric tritiated water vapor,” Atmospheric Environment, vol. 154, pp. 308–317, Apr. 2017.

[C2.15] S. J. Hayward, T. Gouin, and F. Wania, “Comparison of Four Active and Passive Sampling Techniques for Pesticides in Air,” Environmental Science & Technology, vol. 44, no. 9, pp. 3410–3416, May 2010.

[C2.16] Jacek Namiesnik and Tadeusz Gorecki, “Passive Sampling,” Trends in Analytical Chemistry, vol. 21, no. 4, pp. 276–291, 2002.

[C2.17] M. Dvořák, P. Janoš, L. Botella, G. Rotková, and R. Zas, “Spore Dispersal Patterns of Fusarium circinatum on an Infested Monterey Pine Forest in North-Western Spain,” Forests, vol. 8, no. 11, p. 432, Nov. 2017.

[C2.18] Daniel A. Vallero, *Fundamentals of air pollution* 4th Edition, Amsterdam; Boston: Elsevier, 2007.

[C2.19] J. S. C. Herbert A. Pohl, “Dielectrophoretic Force,” *J. Theor. Biol.*, vol. 37, no. 1, pp. 1–13, Oct. 1972.

[C2.20] Z. Chen, *Finite element methods and their applications*. Berlin; New York: Springer, 2005.

[C2.21] V. Gerlich, K. Sulovská, and M. Zálešák, “COMSOL Multiphysics validation as simulation software for heat transfer calculation in buildings: Building simulation software validation,” Measurement, vol. 46, no. 6, pp. 2003–2012, Jul. 2013.

[C2.22] S. Rebiai, H. Bahouh, and S. Sahli, “2-D simulation of dual frequency capacitively coupled helium plasma, using COMSOL multiphysics,” IEEE Transactions on Dielectrics and Electrical Insulation, vol. 20, no. 5, pp. 1616–1624, Oct. 2013.

[C2.23] “Introduction to COMSOL Multiphysics,” COMSOL Multiphysics, p. 198 http://static.comsol.com/doc/IntroductionToCOMSOLMultiphysics.pdf. [Accessed: 05-Jun-2019]

[C2.24] G. Vasilescu, “Physical Noise Sources,” in Electronic Noise and Interfering Signals - Principles and Applications, Printed in Germany: Springer, pp. 45–67, 2004.

[C2.25] Texas Instruments, “Noise Analysis in Operational Amplifier Circuits,” Texas Instrument, 2007. [Online]. Available: http://www.ti.com/. [Accessed: 01-Aug-2019].

[C2.26] S. Pham and A. Dinh, “Adaptive-Cognitive Kalman Filter and Neural Network for an Upgraded Nondispersive Thermopile Device to Detect and Analyze Fusarium Spores,” *Sensors*, vol. 19, no. 22, p. 4900, Jan. 2019.

[C2.27] A. Motwani, S. K. Sharma, R. Sutton, and P. Culverhouse, “Interval Kalman Filtering in Navigation System Design for an Uninhabited Surface Vehicle,” The Journal of Navigation, vol. 66, no. 5, pp. 639–652, Sep. 2013.

[C2.28] I. A. Iswanto and B. Li, “Visual Object Tracking Based on Mean-shift and Particle-Kalman Filter,” Procedia Computer Science, vol. 116, pp. 587–595, Jan. 2017.

[C2.29] D. Lautier, “The Kalman Filter In Finance: An Application to Term Structure Models of Commodity Prices and A Comparison Between the Simple and The Extended Filters,” Dauphine University BIRD, working paper, p. 25, 2012, https://basepub.dauphine.fr/handle/123456789/9193. [Accessed: 01-Aug-2019]

[C2.30] K. P. Murphy, Machine learning: a probabilistic perspective. Cambridge, MA: MIT Press, 2012.

[C2.32] Y. Zhang, Machine Learning. INTECH Open Access Publisher, 2010.

[C2.33] J. Deshmukh and U. Bhosle, “Image Mining Using Association Rule for Medical Image Dataset,” Procedia Computer Science, vol. 85, pp. 117–124, Jan. 2016.

[C2.34] Y. Wang, G. Wu, G. (Sheng) Chen, and T. Chai, “Datamining based noise diagnosis and fuzzy filter design for image processing,” Computers & Electrical Engineering, vol. 40, no. 7, pp. 2038–2049, Oct. 2014.

[C2.35] C. C. Wall, K. Karnauskas, M. B. Joseph, J. McGlinchy, and B. R. Johnson, “Navigating noise when comparing satellite and acoustic remote sensing data,” The Journal of the Acoustical Society of America, vol. 144, no. 3, pp. 1744–1745, Sep. 2018.

[C2.36] K. Suzuki, Ed., Artificial Neural Networks - Architectures and Applications. InTech, 2013.

[C2.37] K. Suzuki, Ed., Artificial Neural Networks - Methodological Advances and Biomedical Applications. InTech, 2011.

3. Designing Kalman Corrector for a 24-Bit Visible Spectrometer

Published as:

Son Pham and Anh Dinh, "Using Kalman Algorithm to Correct Data Error of A 24-Bit Visible Spectrometer," *MDPI Sensors*, 2017, 17(12), 2939; 20 pages, doi:10.3390/s17122939.

As discussed in the previous parts, it is essential to work with the visible light of 0.3μm to 0.75μm wavelength range and to be familiar with optical devices, quantities as well as the Beer-Lambert law. From that purpose, a portable 24-bit visible spectrometer was designed, built, and tested. Through experiments, a difficult problem of controlling the light intensity of the light source happened. The light intensity was not stable and affected the sample analysis procedure. To overcome the problem, a Kalman corrector was designed. In this corrector, a non-linear function and the Kalman algorithm were co-operatively applied. The non-linear function was selected from several functions which were proposed by a hypothesis of the possible forms of correlation function of the corrected data Y, data with error y, and the error dx: $Y= y + dy = y + f(dx)$.

In this manuscript, the device and the algorithms are firstly introduced. The method of finding the correction function and the correction coefficients is presented later. The results are shown to prove the efficiency of the corrector module.

The main contribution to this chapter comes from the first author, while the second author supervises the experiment process and the content of the paper.

Using Kalman Algorithm to Correct Data Error of A 24-Bit Visible Spectrometer

Son Pham; Anh Dinh

Abstract

To reduce cost, increase resolution, and reduce errors due to changing in light intensity of the VIS SPEC, a new technique is proposed which applies the Kalman algorithm along with the simple hardware setup and implementation. In real time, the SPEC automatically corrects spectral data error resulting from an unstable light source by adding photodiode sensor to monitor the change in light source intensity. Kalman algorithm is applied on the data to correct the errors. The light intensity instability is one of the sources of error is considered in this work. The change in light intensity is due to the remaining longevity, working time and physical mechanism of the halogen lamp, and/or battery and regulator stability. Coefficients and parameters for the processing are determined from MATLAB simulations based on two real types of datasets, which are mono-changing and multi-changing datasets, collected from the prototype SPEC. From the saved datasets, and based on Kalman algorithm, and other computer algorithms such as divide-and-conquer algorithm and greedy technique, the simulation program implements the search of process noise covariance, correction function and its correction coefficients. Then, these components, which will be implemented into the processor of the SPEC, Kalman algorithm and the light-source-monitoring sensor are essential to build the Kalman corrector. Through experimental results, the corrector can reduce the total error in the spectra in the order of 10 times; at certain typical local spectral data, it can reduce the error up to 60 times. The experimental results prove that accuracy of the SPEC increases considerably by using Kalman corrector in the case of changing in light source intensity. The proposed Kalman technique can be applied to other applications to correct the errors due to the slow change in certain system components.

Index Terms: spectrometer, spectrum, Kalman, filter, noise reduction, corrector.

3.1. Introduction

The VIS SPEC applies Beer-Lambert law to find the substance concentration [C3.1]. Sensitivity and accuracy of a SPEC depend on several factors, one of these is, firstly, the analog-to-digital converter (ADC) which is responsible for digitalizing measured analog signal from the sensors and providing resolution to the spectrometer [C3.2]. Secondly, another important factor affects the accuracy is the system stability such as light intensity, voltage regulator, ambient and operating temperature. The stability of the system can be improved by smoothing techniques and data correction methodology [C3.3, C3.4].

Most of SPECs on the market use 16-bit ADC and charge-coupled device and CMOS sensors which account for the high prices [C3.4, C3.5]. Therefore, to increase the SPEC's sensitivity and to reduce the cost, ADS1252 [C3.6], and BPW-34 [C3.7] are chosen as they are non-expensive.

Many approaches and techniques have been used to increase quality of the SPEC [C3.3]. The change in the light intensity emitted from the 12V-50W halogen lamp [C3.8, C3.9] and lead acid battery [C3.10], which is used to help the SPEC portable, drift are the causes of error in such devices. Though, the light intensity from the lamp in the device has been controlled by a voltage regulator to keep it stable, yet the emitted light intensity may be fluctuated by some reasons such as the usable-remaining longevity, working time, and physical mechanism of the halogen lamp [C3.8, C3.9] and the battery. In addition, ambient temperature changes can directly affect the light emission from the halogen lamp [C3.9] and to the battery capacity [C3.10] which, finally, possibly, influence the light intensity from the light source. All these factors can cause light intensity unstable at some ranges as the measurement time goes. If this instability happens during a spectral measurement, the intensity of the investigated spectrum will be unstable as well. Thus, the recorded digital data will contain error which corresponds to the light intensity changing.

Noting that the errors in the data, which have the causes previously mentioned, are different from the errors caused by photon shot noise, dark noise, and Johnson or thermal noise [C3.11, C3.12] in which the contribution of shot and Johnson noises dominate the dark noise. For an exposing period, which is smaller than five minutes, the dark noise and dark current are minor and negligible [C3.13]. The Johnson noise can be tackled by applying trans-impedance amplifiers [C3.3, C3.12], whereas the shot noise can be treated by low-pass filter circuits [C3.3] or digital filters such as moving-average filter [C3.14]. Since these noises in a SPEC were previously discussed in the other paper [C3.3] and in other materials [C3.11, C3.12], in this work, the noises or also-called errors of data possibly caused by the light intensity instability and quantization are investigated.

Through experimental observation, two main types of light intensity change which were seen during experiments are the mono-trend style which can be the result of the gradual weakness of the battery, or the physical-working mechanism of the halogen, and the multi-trend style which can be caused by the waving-output voltage for the lamp and is not as quick as a shot noise. Although the output voltage has been regulated by a voltage regulator, small or uncommon-large amplitudes of oscillation can be seen, that may result from unideal conditions such as unsteady temperature, unstable load, or poor-quality capacitors [C3.15]. As the halogen lamp is 12V-50W and the operating voltage is around 12V, the average current goes through the lamp is around 4A. Moreover, the lamp must be warmed up at least 15 minutes to 30 minutes before using [C3.16, C3.17]. In addition, after a 15-minute warm-up, the output voltage of the battery, which is full charge before use, starts dropping [C3.12]. In the next period of 33 minutes, the voltage drop will be approximate to 1V, i.e., about 30mV/min.

Consequently, the instability can affect the quality of the spectral measurement without awareness. As a result, it is essential to monitor the light source intensity to compensate for the change in intensity in order to reduce error in a SPEC. In this design of the SPEC, a second photodiode is inserted in the light path to monitor its potential light intensity change. On the other hand, observing the light intensity change, spectral data and its error caused by the light change, one can recognize the correlation between them. Thus, by studying such correlation, the spectral error can be corrected or minimized. This study is implemented by using MATLAB simulations, in which the program uses the Kalman algorithm and the proposed correction functions to find necessary parameters such as process noise covariance. The parameters and coefficients are to be used in hardware implementation of the SPEC.

3.2. Methodology

In this work, the VIS SPEC structure is shown in the diagram of Figure 3.1. The system is separated into device 1 and device 2 for convenience in implementation, experiment, and observation.

In device 1, the battery supplies energy for the halogen lamp through an adjustable voltage regulator having 3 power 2N1544 transistors [C3.18] to provide load current and the regulator

LM317 [C3.19] to control the output voltage. The maximum current through these three transistors is around 15A and the output voltage can be adjusted from around 6V to 12V. In device 1, lens 1 and lens 2 with the focuses of about 61.5 ± 0.5mm and 36.0 ± 0.5mm respectively collimate the light from the halogen lamp. Figure 3.2 shows more details of device 2.

In device 2, the collimated light from the device 1 goes through the slits units which are designed by metal blades. These slits are used to decrease the cross section of the light into thin-slit light to reduce the diffractive effect [C3.20]. In between the first two slits, there is a sample holder whereby a 1mm-wide-quartz cuvette is inserted. When the light goes through the sample, the sample absorbs the energy of certain wavelengths of the incident light and the remained light provides useful information about the sample. However, to get this information, this transmitted light must be continuously processed by another process where the light shines onto a monochromator, which is a reflective grating, and the light is separated into mono lights. The period of the grating is 747 ± 11nm. The grating can be deviated from the incident light by the stepper motor [C3.20] having 4096 steps/round. Moreover, the modified-5V 28BYJ-48 stepper motor [C3.21] having 82,944/round can drive the grating to deviate from the incident light. Thus, each rotating step equals to 75.752 x 10^{-6} radian or 0.0043 degrees. Based on the grating, the wavelength of the light can be calculated by using the relating formula among incident light, mono diffracted light and the grating period:

$$m\lambda = d(sin\theta_i + sin\theta_m) \tag{3.1}$$

where m is diffraction order, d is grating period, θ_i is incident angle, and θ_m is diffraction angle.

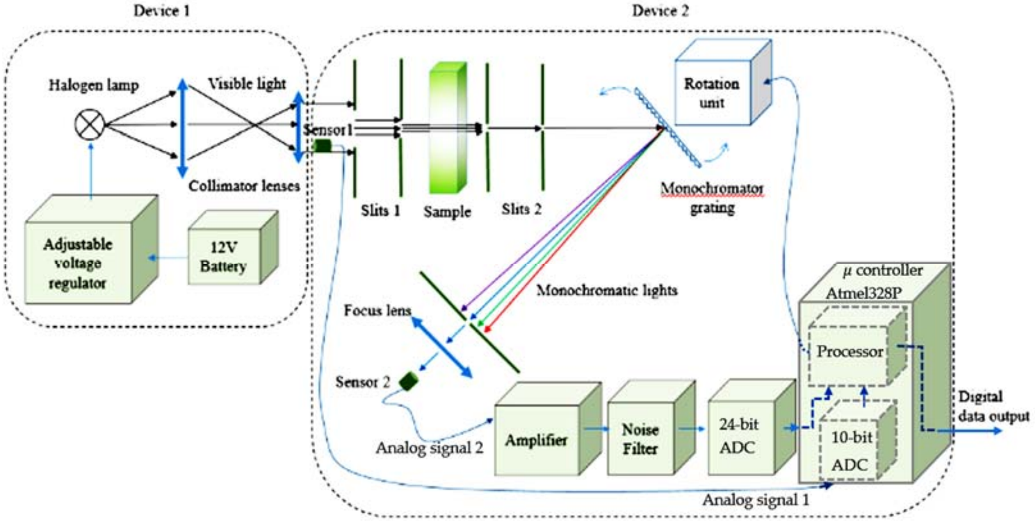

Figure 3.1. Block diagram of the VIS SPEC. Device 1 provides visible light and device 2 analyzes sample spectrum and sends digital data to a computer.

The mono lights are then directed to sensor 2 which is a photodiode, BPW-34, the diode is used to measure the intensity of the mono lights. Signal from sensor 2 is then properly amplified and filtered by the amplifier and the two low pass filters before collected, processed and filtered again to eliminate noise by the 24-bit ADC and the Atmel328P microcontroller [C3.22]. From Figure 3.1, the signals from sensor 1 and sensor 2 after amplified and filtered by the electronic circuits are sent to ADCs and the digital signals then enter the microcontroller.

Now the details of the error correction mechanism are presented. Basically, the light-source monitoring sensor 1 collects the light-source intensity data, x, and the spectral sensor 2 records spectral data, y, to send to the microcontroller for further processing. In case, the light-source intensity is stable, there are no errors for both x and y. Therefore, $x = x_{real}$, and $y = y_{real}$, where x_{real} and y_{real} are the real value of x and y respectively. If the light intensity is unstable, then $x \neq x_{real}$, and $y \neq y_{real}$. The difference of these values can be defined as error values, and:

$$dx = x - x_{real};\ dy = y - y_{real} \tag{3.2}$$

From experiment, when the light intensity is decreased, the spectral intensity is also decreased; and, inversely, when the light intensity is increased, the spectral intensity is also increased. Therefore, y is proportional with x.

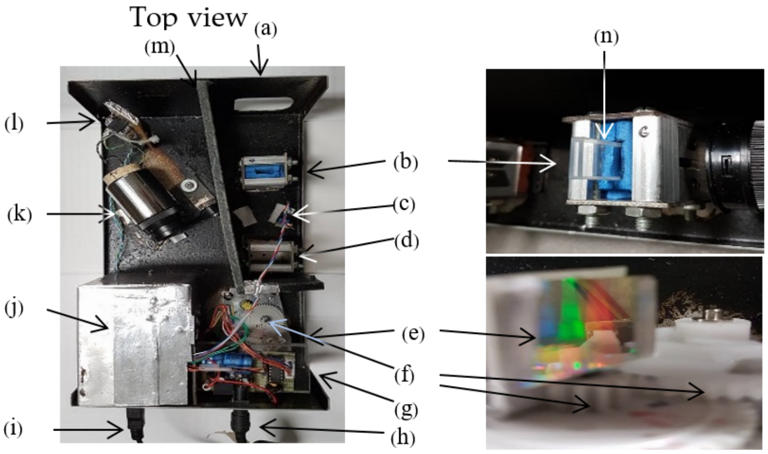

Figure 3.2**.** Device 2 components: (a) light entrance, (b), (d) slits on the two sides of each unit, (c) sensor 1, (e) grating and its close view, (f) gears are used to increase the scanning steps, one gear is attached to the grating, (g) 5V regulator circuit supply energy for other electronics units inside the device 2, and the driver circuit using ULN2003 IC controls the stepper motor, (h) power supply input, (i) digital data output, (j) metal box protects inner circuits, (k) sensor housing, (l) amplifier circuits are combined two low-pass filters which filter out noise greater than 50Hz, (m) wall protects the sensor 2 area from the light entrance area, (n) sample cuvette.

Consequently, from equation (3.2), it can be seen that *dy* is proportional with *dx*, so *dy* ~ *dx*. Thus, *dy* = *f*(*dx*), and:

$$Y = y + dy = y + f(dx) \tag{3.3}$$

where *Y* is the corrected data, and *f*(*dx*) is considered as correction function. *f* can be proportional with dx, $|dx|^2 * {dx}/{|dx|}$, dx^3, …, or $|dx|^{1/2} * {dx}/{|dx|}$, $dx^{1/3}$, ... Because the form of *f* is not known yet, let assume:

$$f(dx) = C_o * dx + C_1 * |dx|^2 * {dx}/{|dx|} + C_2 * dx^3 + \cdots + C_1' * |dx|^{1/2} * {dx}/{|dx|} + C_2' * dx^{1/3} + \cdots \tag{3.4}$$

where, C_o, C_1, C_2,…, C_1', C_2', …are proportional constant values which must be estimated by simulation on MATLAB software to have optimal coefficients. ${dx}/{|dx|}$ has only two values, -1 or +1, and indicates *dx* is negative or positive. To support for a successful simulation, some algorithms and technique are manipulated.

3.2.1. Greedy technique

The way to find out these constants' values are simple. It is based on the greedy technique [C3.23] in which equation (3.4) is used in the simulation. At first, all C_o, C_1, C_2,…, C_1', C_2', … are set to zero. Then, ΔC_o, ΔC_1, ΔC_2,…, $\Delta C_1'$, $\Delta C_2'$, … are the increment values of C_o, C_1, C_2,…, C_1', C_2', … respectively, and set to certain small values. With the greedy technique, the simulation program will start to find a certain proportional constant. Let's start with C_o. The program will add ΔC_o into C_o, then substitute C_o into equation (3.4) to calculate *dy* = *f*(*dx*). After that, put *dy* into equation (3.3) to have the corrected data, *Y*, and then compare *Y* with y_{real} to see whether *Y* is good or not. Theoretically, *Y* is good when *Y* equals to y_{real}. However, it is impossible, when there are many other factors such as circuit noise can influence to the estimation process. Thus, to know when the proportional estimation process should stop, some criteria such as absolute error (AR), relative error (RE), error (ERR), least square (LS), or correlation parameter (CP) [C3.14] have been applied, where the definitions of AE, RE, ERR, or LS are:

$$\text{AE} = \sum_{i=1}^{N} |Y(i) - y_{real}(i)|; \text{ RE} = \sum_{i=0}^{N} |Y(i) - y\_real\ (i)| \ / \ y\_real\ ;$$
$$\text{ERR} = \sum_{i=1}^{N} (Y(i) - y_{real}(i)); \text{ LS} = \sum_{i=1}^{N} (Y(i) - y_{real}(i))^2 \tag{3.5}$$

where i is the index of data vector *Y* and y_{real}, and *N* is the number of data points, as *Y* and y_{real} are discrete data. Let's take AE for instance, after estimate the AE, *a prior* AE is compared with *a posterior A*E. If *a posterior* AE < *a prior* AE, then the estimation of C_o still need to be processed again by adding it with ΔC_o. Inversely, the program will stop to search for C_o and move to another proportion constant. This process keeps going until all C_o, C_1, C_2,…, C_1', C_2', … are found to fulfill *f*.

The advantage of the greedy technique is feasible to apply, but the disadvantage is that the solution, *f*, and its correction coefficients results from the simulation program, is probably not the best one. For example, with a certain suggested *f*, if the order of searching the correction coefficients for *f* is C_o, C_1, C_2,…, C_1', C_2', … respectively, then the result is supposedly f_1. Again, changing the order of searching into C_2, C_1, C_o, …, C_2', C_1', …, one can get $f_2 \neq f_1$. Thus, if *n* orders of searching are conducted, there can be *n* different forms of *f*. To determine which *f* is the better one, the above criteria are looked at. Consequently, among these forms there should be the best one.

In practice, when the form of the correction function is long and complicated, then it is not efficient to code in a microcontroller. Moreover, it also increases running time in the measurement which may lead to further error. For example, the running time for a measurement of more than five minutes raises dark noise [C3.11] and/or potential light-intensity error during that time. Therefore, in practice, several cognitive short forms of *f* are proposed for the simulation program.

3.2.2. Divide and conquer algorithm

From experiment, the correction function found from the Greedy technique cannot effectively and adequately corrects the range of the interested spectrum. To circumvent the difficulty, the investigated range is divided into smaller subdomain. At each of these subdomains, there will be a correction function and corresponding parameters to conquer it. This technique is called divide-and-conquer algorithm [C3.24]. Therefore, data error of each subdomain will be mitigated by the function. Supposedly, there are *n* sub ranges, and so, there are *n* correction functions. In the operation program, the main data domain *R* is cut into twelve subdomains, R_i.

$$\begin{cases} R_{1,} R_2, \dots, R_{11}, R_{12} \leq R \\ R_1 \cup R_2 \cup \dots \cup R_{11} \cup R_{12} = R \end{cases} \tag{3.6}$$

Theoretically, the smaller the sub ranges are divided, the better the corrected data are. However, when the number of the sub ranges increases, the time which is used to process data will be longer. There must be a balance among measuring time, the number of sub ranges, and the measured data. In this work, through experiments, twelve sub ranges are formed to perform the data correction task. As mentioned above, to achieve the best results, MATLAB simulation will be used to search for them. In the MATLAB code, some sub recursive functions are built and recalled continuously in the simulation. In general, the problem is just shrinking into smaller domains to get better simulation results which serve for the later steps.

3.2.3. Kalman algorithm

There is one more obstacle still able to intervene the searching of best C_o, C_1, C_2,…, C_1', C_2', …. In practice, after running the searching simulation with the raw data *x*, to get *f*, and applying it to correct the spectral data, the results are not satisfied as expect. Since, when the raw light-source-monitoring data, *x*, which could have noises [C3.11, C3.12, C3.13], quantization error [C3.14], and unstable light-intensity error, are sent to *f*, not only is the unstable light-intensity error transformed by *f* but also by the mixture of noises and quantization error. These noises and quantization error will make the operating criteria (AE, RE, ERR, LS, or CP) work ineffectively and inadequately. Consequently, *x* must be treated by certain approaches before use.

Moreover, the chosen approach should be applicable and feasible for the microcontroller code and satisfies real-time application without any processing lag and procrastination. For feasibility, two outstanding there are algorithms moving average [C3.14] and Kalman algorithm [C3.23, C3.25, C3.26]. For real-time applications, Kalman algorithm has been proved by some simple experiments that dominates the moving average algorithm. After being treated by the Kalman algorithm, ideally, *dx* ($dx = x - x_{real}$) containing only unstable light-intensity error, which is useful information, will be ready to serve for the correction process.

Details of the Kalman algorithm can be found in [C3.23, C3.25, C3.26], it is necessary to focus on some equations and quantities of the theory for later applying explanation. First, the system is supposed to be linear [C3.26, C3.27], so its state equation has the form of:

$$\boldsymbol{X_k = A_k X_{k-1} + B_k U_k + W_k} \tag{3.7}$$

where $\boldsymbol{X_k}$ and $\boldsymbol{X_{k-1}}$ are the state vector, and $\in \boldsymbol{R^n}, \boldsymbol{A_k}$, is the n×n state transition matrix, $\boldsymbol{B_k}$ is the optional n×l control input matrix, $\boldsymbol{U_k}$ is the control vector, and $\in \boldsymbol{R^l}$, and $\boldsymbol{W_k}$ is the process noise vector. The observation vector of the system is:

$$\boldsymbol{Z_k} = \boldsymbol{H_k X_k} + \boldsymbol{V_k} \tag{3.8}$$

in which $\boldsymbol{Z_k}$ is the observation or measurement vector, and $\in \boldsymbol{R^m}$, $\boldsymbol{H_k}$ is the m×n observation matrix, and $\boldsymbol{V_k}$ is the measurement noise vector. Then, the noise happening in the device is assumed to be white noise in the frequency domain, while in the time domain, its probability density has the Gaussian shape at each point on the time axis [C3.27]. The normal probability distributions of $\boldsymbol{W_k}$ and $\boldsymbol{V_k}$ are:

$$\begin{cases} p(\boldsymbol{W_k}) \sim N(0, \boldsymbol{Q_k}) \\ p(\boldsymbol{V_k}) \sim N(0, \boldsymbol{R_k}) \end{cases} \tag{3.9}$$

where $\boldsymbol{Q_k}$ and $\boldsymbol{R_k}$ are process-noise covariance and measurement-noise covariance, respectively. Their normal probability density functions have the form of:

$$f(x) = \frac{1}{\sqrt{2\pi\sigma_x}} exp\left[-\frac{x^2}{2\sigma_x^2}\right] \tag{3.10}$$

where x stands for one state of the state vector or one observation of the observation vector. σ_x is the standard deviation of x [C3.29]. Besides that, from stochastic theory, in a deviation range and a three-time deviation range from the mean, there will contain 68.27 percent, and 99.73 percent of the measured values, respectively [C3.27, C3.30]. Therefore, from the comment and the experiment error theory [C3.31], the error can be approximated to the three-time deviation. From [C3.29, C3.32], the standard deviation of the sample is:

$$\sigma = \sqrt{\frac{\sum_j^N (x_j - \bar{x})^2}{N}} \tag{3.11}$$

with:

$$\bar{x} = \frac{1}{N}\sum_j^N x_j \tag{3.12}$$

According to [C3.14], *"a priori and a posteriori estimate errors*" can be defined respectively as:

$$\boldsymbol{e_k^-} = \boldsymbol{X_k} - \boldsymbol{\hat{X}_k^-} \tag{3.13}$$

$$\boldsymbol{e_k^+} = \boldsymbol{X_k} - \boldsymbol{\hat{X}_k^+} \tag{3.14}$$

where $\boldsymbol{\hat{X}_k^-} \in R^n$ is *a priori* estimate at discrete time $\boldsymbol{k}$ providing information of the previous process, and $\boldsymbol{\hat{X}_k^+} \in \boldsymbol{R^n}$ is *a posteriori* estimate at discrete time $\boldsymbol{k}$ providing information of the measurement

$\boldsymbol{Z_k}$. From (3.13) and (3.14), the covariance of *a priori* error and the covariance of *a posteriori* error are respectively:

$$\boldsymbol{P_k^-}=\mathrm{E}[\boldsymbol{e_k^- e_k^{-T}}] \tag{3.15}$$

$$\boldsymbol{P_k^+}=\mathrm{E}[\boldsymbol{e_k^+ e_k^{+T}}] \tag{3.16}$$

A posteriori estimate has the form [C3.11, C3.12, C3.14] of:

$$\boldsymbol{\widehat{X}_k^+}=\boldsymbol{\widehat{X}_k^-} + \boldsymbol{K_k}(\boldsymbol{Z_k} - \boldsymbol{H_k\widehat{X}_k^-})=(\mathbf{1}\text{-}\boldsymbol{K_kH_k})\,\boldsymbol{\widehat{X}_k^-}+\boldsymbol{K_kZ_k} \tag{3.17}$$

where $(\boldsymbol{Z_k} - \boldsymbol{H_k\widehat{X}_k^-})$ is the residual or measurement innovation which shows the difference between the measurement and *a priori* estimate, and K_k, named Kalman gain or blending factor, is chosen by minimizing the covariance in (3.16). From [C3.26, C3.27, C3.32], $\boldsymbol{K_k}$ is:

$$\boldsymbol{K_k} = \boldsymbol{P_k^- H_k^T}(\boldsymbol{H_k P_k^- H_k^T} + \boldsymbol{R_k})^{-1} \tag{3.18}$$

From (3.18), when the measurement noise covariance is small, $\boldsymbol{Z_k}$ has high fidelity and Kalman gain will be large. At that time, from (3.17), the weight coefficient of $\boldsymbol{Z_k}$ is greater than the weight of $\boldsymbol{\widehat{X}_k^-}$, so $\boldsymbol{\widehat{X}_k^+}$ will "*believe*" more in $\boldsymbol{Z_k}$ than $\boldsymbol{\widehat{X}_k^-}$. Inversely, as $\boldsymbol{P_k^-}$ is small, Kalman gain will be small and $\boldsymbol{\widehat{X}_k^+}$ will "*believe*" more in $\boldsymbol{\widehat{X}_k^-}$ than $\boldsymbol{Z_k}$. Figure 3.3 shows the operation loop of Kalman algorithm.

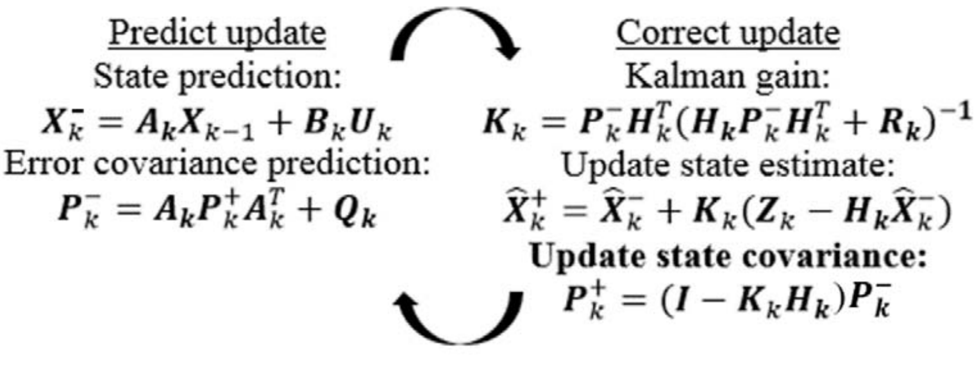

Figure 3.3. Kalman filter operation loop

In practice, $\boldsymbol{Q_k}$ and $\boldsymbol{R_k}$ can be estimated before applying the Kalman filter. In the study, $\boldsymbol{R_k}$ is calculated by several rough measured data, but $\boldsymbol{Q_k}$ is determined by MATLAB simulation to get the best results. These values, during operation, can be constant, so be presented without discrete-time subscript *k*. From [C3.23, C3.25, C3.26], one can see that $\boldsymbol{R_k}= \sigma^2$. In practice, $\boldsymbol{R_k}$ is easily determined by using equation (3.11) and equation (3.12).

3.2.4. Performance description

In this section, all the processes manipulated to process data with the order of correction function, process noise covariance, and correction coefficients findings, by MATLAB simulation are presented.

First, in equations (3.1), (3.2), and (3.4), the values of real data of sensor 1 and sensor 2 were mentioned and known. However, that is only a hypothesis to help establish the processing algorithm. In practice, the values measured in stable conditions are considered approximately equal to the real values and are reference values to serve for comparison and calculation in simulation. The flowchart in Figure 3.4 shows the core algorithm for simulation program, where $\boldsymbol{Y}_1$ and $\boldsymbol{Y}_2$ are spectral data measured in unsteady conditions and good conditions respectively, whereas $\boldsymbol{X}_1$ and $\boldsymbol{X}_2$ are light intensity data recorded in these two cases. Conventionally, $\boldsymbol{X}_1$ and $\boldsymbol{Y}_1$ are data with unstable-light-intensity data with error, and $\boldsymbol{X}_2$ and $\boldsymbol{Y}_2$ are reference data.

Second, noticing that $\boldsymbol{Y}_1$ and $\boldsymbol{Y}_2$ are 24-bit data, while $\boldsymbol{X}_1$ and $\boldsymbol{X}_2$ are 10-bit data. Then, $\boldsymbol{Q_1}$, e_{11}, and $\Delta\boldsymbol{Q}$, respectively are process noise covariance, measurement error, and the decrement of $\boldsymbol{Q_1}$ sequentially. Especially, e_{12} takes two roles, *a posterior* error and *a priori* error in the Kalman module. Many data, $\boldsymbol{X}_1$, $\boldsymbol{X}_2$, $\boldsymbol{Y}_1$, and $\boldsymbol{Y}_2$, were measured and saved in datasets before the simulations. $LS_{current}$ and LS_{save} are the least square parameters which are used to operate the loop. b_1, b_2, …, and b_5 which are the fixed values are set to satisfy the condition:

$$0<b_1<b_2<\ldots<b_5<\boldsymbol{Y}_{max} \qquad (3.19),$$

and they are considered as "boundary" values to help divide the grand spectral data domain into subdomains. In the simulation program, the maximum potential number of the subdomains which are non-empty is 12, if the minimum data value is smaller than b_1, the maximum data value is greater than b_5, and at any range of $(0, b_1)$, $[b_1, b_2)$, …, $[b_4, b_5)$, $[b_5, \boldsymbol{Y}_{max}]$ both positive and negative $\boldsymbol{dX}$ values exist. C_1, C_2, …, C_{12} are the correction parameters, whereas dC is the increment of these parameters.

3.2.4.1 Correction function finding

As discussed above, to make the correction function feasible and applicable, several short forms of equation (3.4) are proposed. They are sequentially replaced into the simulation program which is illustrated by the flowchart in Figure 3.4. Thus, the simulation program will help to find the correction coefficients for the suggested functions. After finishing each simulation, the program will return not merely $\boldsymbol{Q_1}$, C_1, C_2, …, C_{12}, but also AE, ERR, LS, or CP which can be used as the quality assessment criteria of the correction functions. Therefore, which correction function with the prominent assessment parameters is to be adopted. The simulation program starts by loading data $\boldsymbol{X}_1$, $\boldsymbol{X}_2$, $\boldsymbol{Y}_1$, and $\boldsymbol{Y}_2$ from the assigned datasets and initiating the values for $\boldsymbol{Q_1}$, e_{11}, e_{12}, $\Delta\boldsymbol{Q}$, $LS_{current}$, LS_{save}, b_1, b_2, …, b_5, and *dC*.

In the flowchart, $\boldsymbol{X}_1$ and $\boldsymbol{X}_2$ are processed by the ***Kalman*** algorithm to mitigate the quantization error and electronic noises, which may remain, albeit being filtered by hardware filters, to keep the light-source-intensity information as clean as possible. The searching simulation is not successful if the light-source data still have high quantization error and noises. Furthermore, to empower the corrector to work effectively and adequately, the data from sensor 1 and sensor 2 should be collected by applying unstable-light-intensity styles from gradual to fast changes and from mono-changing, to multi-changing styles with large enough fluctuation amplitudes to use in the simulation. However, at this stage, the correction coefficients of the correction function are the priority, so $\boldsymbol{Q_1}$ is cognitively set to a certain value that is good enough for the simulation and of course, larger than Q_{min}. $\Delta\boldsymbol{Q}$ is set to zero to not influence on $\boldsymbol{Q_1}$.

Let's look at the operation in the flowchart of Figure 3.4. At first, $LS_{current} = 0 < LS_{save} = 1$ and $\boldsymbol{Q_1} > Q_{min}$ satisfy the main condition in the flowchart. Then, $\boldsymbol{Q_1}$ is decreased by a $\Delta\boldsymbol{Q} = 0$, so it does not change. $\boldsymbol{X}_1$ and $\boldsymbol{X}_2$ are smoothed by the ***Kalman*** module that returns $\bar{\boldsymbol{X}}_1$ and $\bar{\boldsymbol{X}}_2$ respectively prior to calculate $\boldsymbol{dX} = \bar{\boldsymbol{X}}_1 - \bar{\boldsymbol{X}}_2$. Then, the **Division** function is called to divide $\boldsymbol{dX}$, $\boldsymbol{Y}_1$, and $\boldsymbol{Y}_2$ into smaller domains. At this point, the divide-and-conquer algorithm is applied to separate the grand data domain into smaller domains which are more easily to conquer and to find the solution. The way to divide the data is illustrated in the flowchart of Figure 3.5.

In this function, there are thirteen indexes, *i, j, k, l, m, n, o, r, s, t, u, v, w* to address data points in the vector $\boldsymbol{dX}$, $\boldsymbol{Y}_1$, and $\boldsymbol{Y}_2$. Initially, *i* is smaller than the number of data elements of $\boldsymbol{Y}_1$ that is checked by the first condition in Figure 3.5. *i* is increased one unit and the condition of whether $\boldsymbol{dX}(i)$ is positive is checked. With either "Yes" or "No" this first data element, $\boldsymbol{Y}_1$ is compared with b_1, b_2, b_3, b_4, and b_5 to see to which data subdomain it must belong to. The difference here is that if $\boldsymbol{dX}(i) > 0$, the first six subdomains, $\bar{Y}_{1,1}$, $\bar{Y}_{1,2}$, …, $\bar{Y}_{1,6}$ for $\boldsymbol{Y}_1$, $\bar{Y}_{2,1}$, $\bar{Y}_{2,2}$, …, $\bar{Y}_{2,6}$ for $\boldsymbol{Y}_2$, $\overline{\boldsymbol{dX}}_{1,1}$, $\overline{\boldsymbol{dX}}_{1,2}$, …, $\overline{\boldsymbol{dX}}_{1,6}$ of $\boldsymbol{dX}$, are used for the arrangement. In case $dX(i) < 0$, the second six subdomains, $\bar{Y}_{1,1}$, $\bar{Y}_{1,2}$, …, $\bar{Y}_{1,6}$ for $\boldsymbol{Y}_1$, $\bar{Y}_{2,1}$, $\bar{Y}_{2,2}$, …, $\bar{Y}_{2,6}$ for $\boldsymbol{Y}_2$, $\overline{\boldsymbol{dX}}_{1,1}$, $\overline{\boldsymbol{dX}}_{1,2}$, …, $\overline{\boldsymbol{dX}}_{1,6}$ of $\boldsymbol{dX}$, are used for the assembly. When $\boldsymbol{dX}(i) = 0$, the running point will jump back to the first condition. Then, the same procedure is repeated until i, loop index, is larger than the number of the data elements of $\boldsymbol{Y_1}$. Especially, when all vector $\boldsymbol{dX} = 0$, the division will return twelve empty subdomains. In this case, there is no need to fix spectral data. When all $\boldsymbol{dX} > 0$, from Figure 3.5, the left side condition boxes will be conducted. Consequently, the first six subdomains are none-empty, and the second six subdomains are empty. Inversely, when all $\boldsymbol{dX} < 0$, the second six subdomains are none-empty, and the first six subdomains are empty.

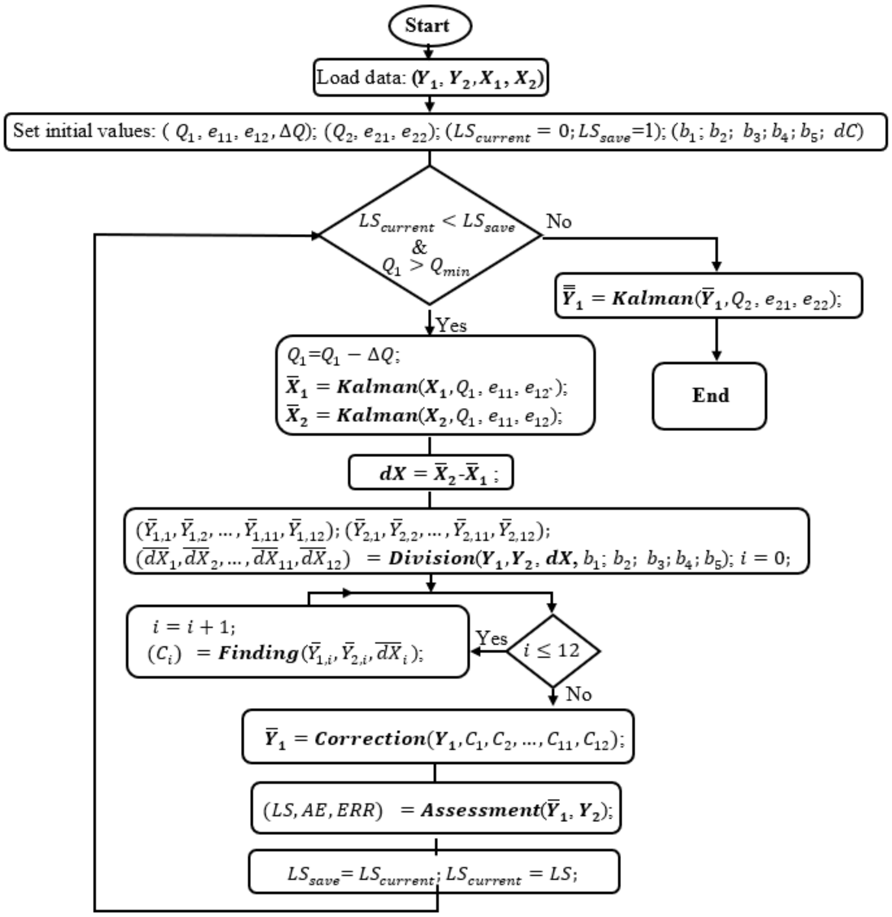

Figure 3.4. The simulation flowchart to find correction parameters or process noise covariance $\boldsymbol{Q_1}$.

Again, from Figure 3.4, after receiving the returned twelve data subdomains, the main simulation program will call the ***Finding*** function to find the correction coefficients. The simulation initiates index i from 1 to 12 to access data in the subdomains. The algorithm of this module is shown in Figure 3.6. The data subdomain of order i, $\overline{Y}_{1,i}, \overline{Y}_{2,i}, \overline{dX}_i$, are loaded. In this process, ls_{curent} and ls_{save} are also the least square values to serve for operating the loop. When

$ls_{curent} < ls_{save}$ and $\bar{Y}_{1,i}$ is different from null, C_i is increased by a dC. $ls_{curent} < ls_{save}$ condition means the currently corrected sub-data is better the previous corrected data, so this sub-data still can be better amended. Then, the suggested correction function is applied to fix $\bar{Y}_{1,i}$ and returns $\bar{\bar{Y}}_{1,i}$. Next, the subprogram will call ***Assessment*** function to calculate LS, AE, ERR based on equation (3.5), the corrected data, $\bar{\bar{Y}}_{1,i}$, and reference data, $\bar{Y}_{2,i}$, and updates ls_{save} with ls_{curent}, and ls_{curent} with LS. Then, the subprogram keeps going back to the operating condition until $ls_{curent} > ls_{save}$ which means the current corrected data cannot be further corrected. From the flowchart in Figure 3.4, the finding module is called twelve times to access all the subdomains without noting of whether they are null or not.

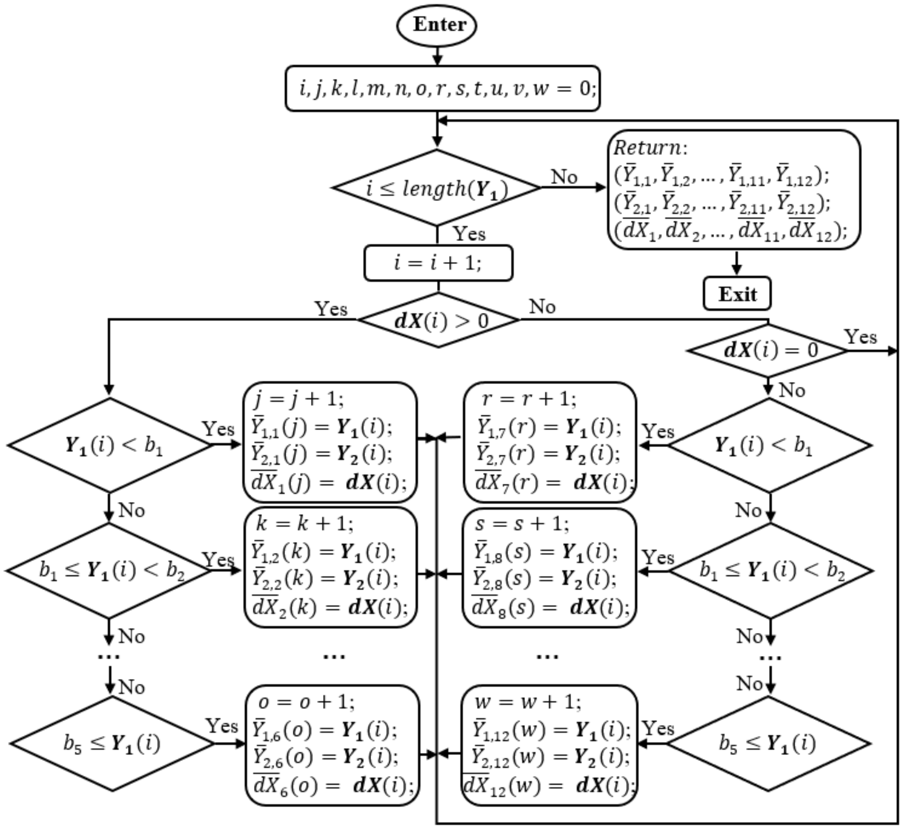

Figure 3.5. The diagram is presented for Division function.

After escaping from the finding module and having all correction coefficients, the main simulation program will apply these values to correct all the sub data, $\bar{Y}_{1,1}$, $\bar{Y}_{1,2}$, …, $\bar{Y}_{1,6}$, of the grand spectral data, $\boldsymbol{Y}_1$ by calling the ***Correction*** function which is built from the suggested correction function, *f*. The equation is in the form:

$$\bar{\bar{Y}}_{1,i}(\mathrm{j}) = \bar{Y}_{1,i}(\mathrm{j}) + C_i * f[(\overline{dX}_i(\mathrm{j}), \bar{Y}_{1,i}(\mathrm{j})] \tag{3.20}$$

Then, the ***Assessment*** will help to evaluate LS, ERR, AE, or CP by using $\boldsymbol{Y}_1$ and $\boldsymbol{Y}_2$. Thus, it is similar to the above description of how the least square criterion works that the program will not stop when $LS_{current} < LS_{save}$….

Finally, in the end, the simulation will return many coefficients, but the most interesting coefficients are LS, ERR, AR, and CP. Therefore, with each suggested short-form correction function, there are the most interesting coefficients. Assessing these coefficients, the best one is chosen to be used in the correction function.

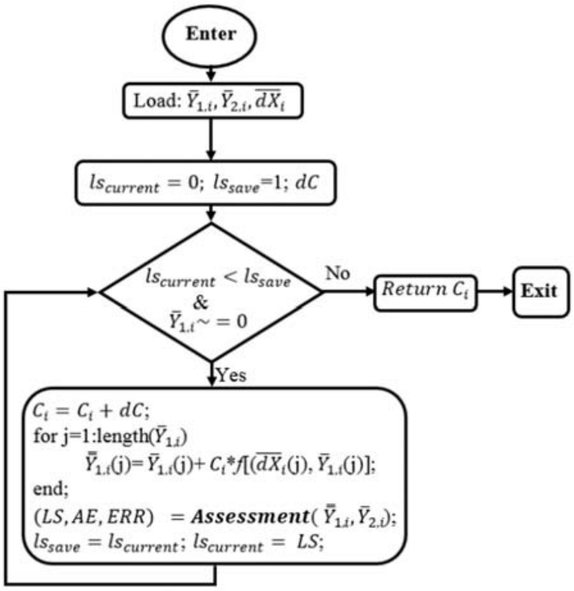

Figure 3.6. The *Finding* flowchart for correction parameters

3.2.4.2. Process noise covariance finding

After finding the appropriate correction function from the suggested functions, the simulation program is applied again to find the process noise covariance, $\boldsymbol{Q}_1$. Although, $\boldsymbol{Q}_1$ used above is good enough, it may not be the best to assure the light-source-intensity data as clean as possible. As mentioned above, many types of data will be used to serve the simulation. Currently, $\Delta\boldsymbol{Q}$ is cognitively set to a certain value which is small enough for the searching simulation. The procedure exactly repeats what is described in section *2.4.1*, except for the main operating condition must account for the condition $\boldsymbol{Q}_1 < Q_{min}$, and at every loop, $\boldsymbol{Q}_1$ is decreased by a $\Delta\boldsymbol{Q}$. When the condition $LS_{current} < LS_{save}$ and $\boldsymbol{Q}_1 < Q_{min}$ cannot be satisfied, the simulation program will cease to return $\boldsymbol{Q}_1$. This value of process noise covariance is to be expected that can keep the best light-source data from the noise.

3.2.4.3. Correction coefficients finding

After the above crucial steps, the main simulation program, which having the flowchart depicted in Figure 3.4, simply reinstalls the found correction function and $\boldsymbol{Q}_1$ back into itself to find C_1, C_2, …, C_{12}. Before that, $\Delta\boldsymbol{Q}$ is set to zero. At the end, it returns correction coefficients.

3.2.4.4. Application

After the simulation step, all necessary key components, correction function, correction coefficients, and process noise covariance are provided and ready to apply in the device and to build the Kalman corrector. Figure 3.7 illustrates the procedure of collecting and processing data. The light intensity signal from sensor 1 enters the 10-bit ADC and the spectral intensity signal from sensor 2 goes to the 24-bit ADC.

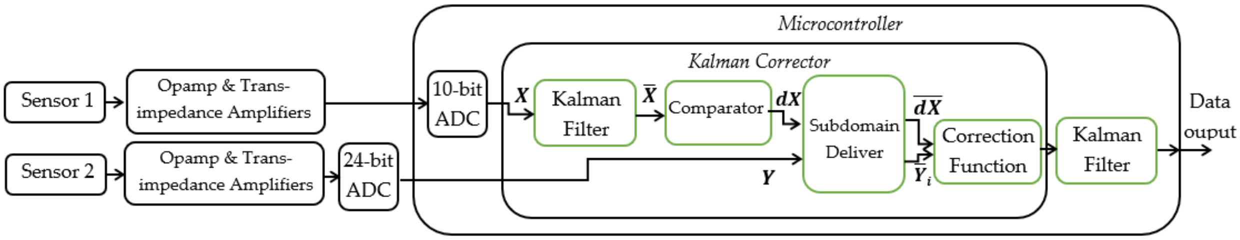

Figure 3.7. The main roles of Kalman algorithm and their correlation with other parts

These signals are digitalized to become digital data. $\boldsymbol{X}$ is filtered out noises and quantization error by $\boldsymbol{Q_1}$ to become $\bar{\boldsymbol{X}}$. Next, the compare block will calculate $\boldsymbol{dX}$ which $\boldsymbol{dX} = \boldsymbol{X_o} - \boldsymbol{X}$, where $\boldsymbol{X_o}$ is a loosely optional value. $\boldsymbol{X_o}$ can be equal to a certain standard value or a measured value which is measured ahead before any spectral measurement. Then, $\boldsymbol{dX}$ and $\boldsymbol{Y}$ values will be delivered by the subdomain deliver to assigned data subdomains which are characterized by b_1, b_2, …, b_5 and controlled by $\boldsymbol{dX}$. Here, the subdomain deliver works similar to the division. It will base on whether $\boldsymbol{dX}$ is positive or negative and to what range among (0, b_1), [b_1, b_2), …, [b_4, b_5), [b_5, $\boldsymbol{Y}_{max}$] $\boldsymbol{Y}$ belongs to. $\boldsymbol{Y}$ is then sent to the correction function which is governing the data subdomain corresponding with that range (section *2.4.1* and Figure 3.6). For example, if $\boldsymbol{dX} > 0$, and $0 < \boldsymbol{Y} < b_1$, then $\boldsymbol{Y}$ is sent to the corresponding subdomain, where is governed by a data correction function of $\boldsymbol{Y}_1$ founded by the previous simulation, to be thoroughly amended. This is performed in real time, so ***dX*** and ***Y*** are no longer data vector but rather discrete-time data measured at each discrete time.

3.3. Results

The light source in this study is visible, its spectrum is from 450nm to 750nm. For convenience in the following figures, on the vertical axis, the unit for the light intensity or spectra is an arbitrary unit (a.u). With the spectral intensity plot, the horizontal axis presents the step unit corresponding to the scanning steps of the stepper motor instead of wavelength unit or number wavelength unit which can be changed among them by using equation (3.1). The step value is changed to rotation angle and the angle is translated into wavelength. However, in the light-source intensity plots, the step value on the horizontal axis simply corresponds to the discrete time values in the sampling signal.

As described earlier, light intensity may increase or decrease randomly when the voltage regulator is not working well or changes due to other reasons such as physical conditions, ambient air temperature, lamp temperature, or warm up and working time. The changes can also be in mono trend by some conditions such as the drift of the battery. Before running the simulation program, many experimental data have been recorded to serve the simulations. The recorded data are collected under the un-change and slightly change working conditions to simulate the unstable factors as mentioned in the introduction which can lead to the slightly change in light intensity. Then data recorded in well working conditions (external stable power supply) serve as reference data for the assessment process.

3.3.1. Initial $\boldsymbol{Q}_1$ selection for simulation

In Figure 3.8, the red-dot line is the recorded raw 10-bit data of the light intensity source which was slightly adjusted to simulate unstable light source. Several values of $\boldsymbol{Q}_1$ are tested to study the features of $\boldsymbol{Q}_1$. One may see that the smaller the $\boldsymbol{Q}_1$ is, the smoother output data from the Kalman function will be. This leads to that $\boldsymbol{X}_1$, the blue line, is so smooth, when $\boldsymbol{Q}_1$ is so small, for example $\boldsymbol{Q}_1 = 10^{-8}$ (it is matching with this type of data and measurement error). Thus, not only the electronics noises and quantization error are removed but also some useful and crucial information from the light source. Obviously, this will ruin the process of the data correction and simulation.

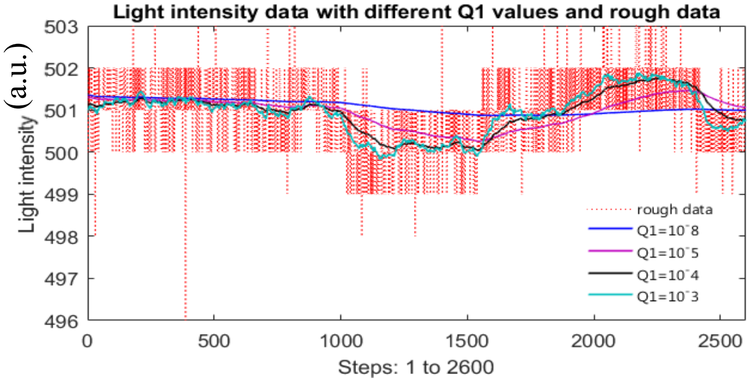

Figure 3.8. Raw intensity data and its filtered data with different $\boldsymbol{Q_1}$ values.

When $\boldsymbol{Q_1} = 10^{-3}$, the filtered data, $\overline{\boldsymbol{X}}_1$, plot is the cyan line. Currently, $\overline{\boldsymbol{X}}_1$ keeps much light-intensity information, but also some electronic noises and quantization error as well. If using this filtered data for simulation, the results, such as correction coefficients, or corrected spectral data, may not be the best.

Therefore, neither too large nor too small Q_1 can lead to good results which are demonstrated by plot groups of Figure 3.9. (a), and Figure 3.9. (b), respectively. In both cases, the corrected data are not close to or similar to the reference. Section *2.4.2* shows how to obtain an appropriate and adequate Q_1. To serve for the simulation of finding correction function which will be discussed in the next section, Q_1 is set to 10^{-3}.

3.3.2. Correction function choice

A multi-changing *data set 1* is loaded for test. The general initial values are: $b = 7*10^5$, $b_1 = b$, $b_2 = 2*b$, $b_3 = 3*b$, $b_4 = 3.6*b$, $b_5 = 4*b$, $\boldsymbol{Q_1} = 10^{-3}$, $e_{11} = e_{12} = 1$, and $e_{21} = e_{22} = 500$ (experimentally determined by equation (3.11) and equation (3.12)). With each correction function which is chosen, the increment, *dC*, of the correction parameters must be cognitively adjusted to a certain appropriate value that assures that the finding function will be called at least several times. This value should not be so small because the simulation process may last too long without better results. In the next section, four typical correction functions are investigated to select the most appropriate one in these. These proposed functions are based on experiment, evaluation, and observation of the results to adjust logically. Objectively, these correction functions are tested with the same *dataset 1*. Notice that, LS, AE, ERR, and CP are the controlling criteria that are also used as effective and qualitative parameters for the decision.

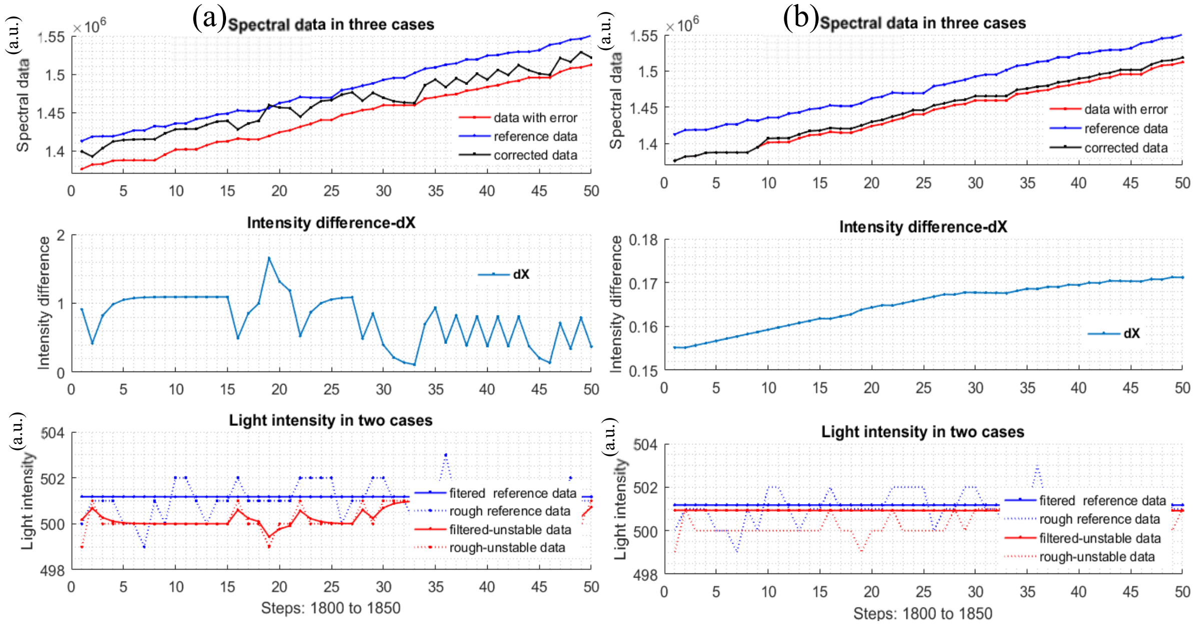

Figure 3.9. Results of measurement data and processed data (**a**) the three plots of data in the case of $Q1$=0.9, and (**b**) the three plots of data in case of $Q1 \approx 1.27*10^{-21}$.

In Table 3.1 below, in Table 3.1 below, f_A, f_B, f_C, and f_D are short correction function forms. The formulas of these functions are in Appendix A.

Table 3.1. LS, AE, ERR, and CP of f_A, f_B, f_C, and f_D are shown respectively.

	LS	AE	ERR	CP($\boldsymbol{Y_1}, \boldsymbol{Y_2}$)	CP($\overline{\boldsymbol{Y}}_{\boldsymbol{1}}, \boldsymbol{Y_2}$)	Feasibility
f_A	$2.159*10^{11}$	$1.483*10^{7}$	$2.773*10^{6}$	0.999608	0.999968	Medium
f_B	$1.846*10^{11}$	$1.3747*10^{7}$	$3.3367*10^{6}$	0.999608	0.9999769	Low
f_C	$1.9372*10^{11}$	$2.3045*10^{7}$	$3.3367*10^{6}$	0.999608	0.9999725	Low
f_D	$1.840*10^{11}$	$1.3719*10^{7}$	$2.8859*10^{6}$	0.999608	0.9999756	High

The LS, AE, and ERR are expected as small as possible, i.e., the corrected spectral data are similar to the reference spectral data. For CP, if the two signals of the data are very close to each other, CP will be approximate to one. In the table, an auxiliary index is the feasibility. Simply, it takes the values of relative evaluation which is based on the form of the correction function. If this index is high, the function is easily applied. In some cases, this index can strengthen a decision, albeit merely auxiliary one. In the table, the prominent values are highlighted. Observing Table 3.1, one possibly sees the most outstanding correction function is f_D, and the second one is f_B, finally, f_D is selected.

3.3.3. Process noise covariance search

After the correction function, $\overline{\overline{\boldsymbol{Y}}}_{\boldsymbol{1},\boldsymbol{i}}$(j) = $\overline{\boldsymbol{Y}}_{\boldsymbol{1},\boldsymbol{i}}$(j) + $\boldsymbol{C_i}$*$\overline{\boldsymbol{dX}}_{\boldsymbol{i}}$(j)* $\overline{\boldsymbol{Y}}_{\boldsymbol{1},\boldsymbol{i}}\boldsymbol{(j)}$, has been chosen, the process noise covariance, $\boldsymbol{Q_1}$, search is the next step. As previously discussed, to achieve an appropriate and adequate of $\boldsymbol{Q_1}$, many datasets which were measured under different light-intensity-changing styles are used. The multi-changing *dataset 2* to *dataset 19* (named by the authors) are chosen to be loaded into the simulation program. Table 3.2 provides the values of $\boldsymbol{Q_1}$ gathered after the simulations.

Table 3.2. $\boldsymbol{Q_1}$ values of multi-changing datasets

	dataset 2	*dataset 3*	*dataset 4*	*dataset 5*	*dataset 6*	*dataset 7*	*dataset 8*	*dataset 9*	*dataset 10*
$\boldsymbol{Q_1}$	0.0071	0.0321	0.0561	0.0147	0.0112	0.0076	0.0352	0.0119	0.0155

	dataset 11	*dataset 12*	*dataset 13*	*dataset 14*	*dataset 15*	*dataset 16*	*dataset 17*	*dataset 18*	*dataset 19*
$\boldsymbol{Q_1}$	0.0144	0.0349	0.0124	0.0203	0.0126	0.0249	0.0107	0.0165	0.0268

From the above $\boldsymbol{Q_1}$ search simulations corresponding with multi-changing data sets, a $\boldsymbol{Q_1}$ will be chosen. There will be some points of view in choosing $\boldsymbol{Q_1}$. For instance, one may suppose that the average $\boldsymbol{Q_1}$ partly satisfies all the cases of light intensity change or the greatest $\boldsymbol{Q_1}$ of the found values is the safe solution as the Kalman filter can catch up the possibly fastest and, obviously, slowest intensity change of the studied data sets. However, with the later philosophy, $\boldsymbol{Q_{1,max}}$ will be greater than the average one, $\overline{\boldsymbol{Q}}_{\boldsymbol{1}}$, and then the corrected data pertaining to $\boldsymbol{Q_{1,max}}$ is probably not as smooth as the corrected data of $\overline{\boldsymbol{Q}}_{\boldsymbol{1}}$. If $\boldsymbol{Q_{1,min}}$ is selected, there will probably be some quick-changing-light intensity not detected well by the Kalman. To implement in the device, the selected process noise covariance is $\overline{\boldsymbol{Q}}_{\boldsymbol{1}}$ = 0.0203. After selecting the best correction function and the appropriate $\boldsymbol{Q_1}$ for the Kalman module, the next process is to load the mono-changing data sets to find the correction parameters, C_i.

3.3.4. Correction parameters finding

In this section, the mono-changing datasets are viewed. In these datasets, there are two subtype data where one has spectral and light intensity data greater than the reference spectral and light intensity data, and the other one has spectral and light intensity data smaller than the reference spectral and light intensity data. Thus, with these types of the dataset, after division module is called, there should be six continuous empty data subdomains and six continuous non-empty data subdomains. The upper-subdomain data and lower-subdomain data are investigated separately to find the correction parameters. The full tables of the correction parameters are attached in Appendix B. Table 3.3 and Table 3.4 provide short results of the tables.

Table 3.3. C_i values of upper-subdomain data.

C_i of subdomains Data set	C_1	C_2	C_3	C_4	C_5	C_6	$\overline{dX}$
1	0.00386	0.00264	0.00245	0.00233	0.00208	0.00207	5.7078
…	…	…	…	…	…	…	…
30	0.00396	0.00254	0.00222	0.00229	0.00216	0.00211	28.5594

Table 3.4. Ci values of lower-subdomain data.

C_i of subdomains Data set	C_7	C_8	C_9	C_{10}	C_{11}	C_{12}	$\overline{dX}$
1	0.00355	0.00231	0.00219	0.00187	0.0019	0.00188	-20.2399
…	…	…	…	…	…	…	…
30	0.00347	0.00239	0.00215	0.0021	0.00197	0.00198	-29.5559
Average	**0.00351**	**0.00239**	**0.00210**	**0.00206**	**0.00201**	**0.00197**	

Notice that dX is adjusted from around the range of -40 to 30 units corresponding to the potential change of the light intensity. Each unit corresponds to approximately 4.9mV difference when the 10-bit ADC of the microcontroller is used. For a small change in light intensity, the relationship of dX and Ci is expected to be linear with that the best applied correction function, $\bar{\bar{Y}}_{1,i}$(j) = $\bar{Y}_{1,i}$(j) + C_i*$\overline{dX}_i$(j)* $\bar{Y}_{1,i}(j)$. When dX is adjusted to different positive and negative values which correspond to the simulations of different voltage increases and decreases, one can see from the plots of Figure 3.10 and Figure 3.11 that Ci and dX relationship is linear as expected and the slope angle is zero. In this case, one can take the mean values of Ci to make it as the correction coefficients of the corresponding subdomains.

3.3.5. Practice

Through experiments and simulations, the correction function below is used:

$$\bar{\bar{Y}}_{1,i}(j) = \bar{Y}_{1,i}(j) + C_i * \overline{dX}_i(j) * \bar{Y}_{1,i}(j),$$

and the noise process covariance, $\bar{Q}_1 = 0.0203$, and the correction coefficients, $C_1 = 0.003709$, $C_2 = 0.002577$, $C_3 = 0.002278$, $C_4 = 0.002368$, $C_5 = 0.002242$, $C_6 = 0.002215$, $C_7 = 0.003694$, $C_8 = 0.002449$, $C_9 = 0.002103$, $C_{10} = 0.002155$, $C_{11} = 0.002084$, $C_{12} = 0.002036$, have been found through the simulation described in the previous sections.

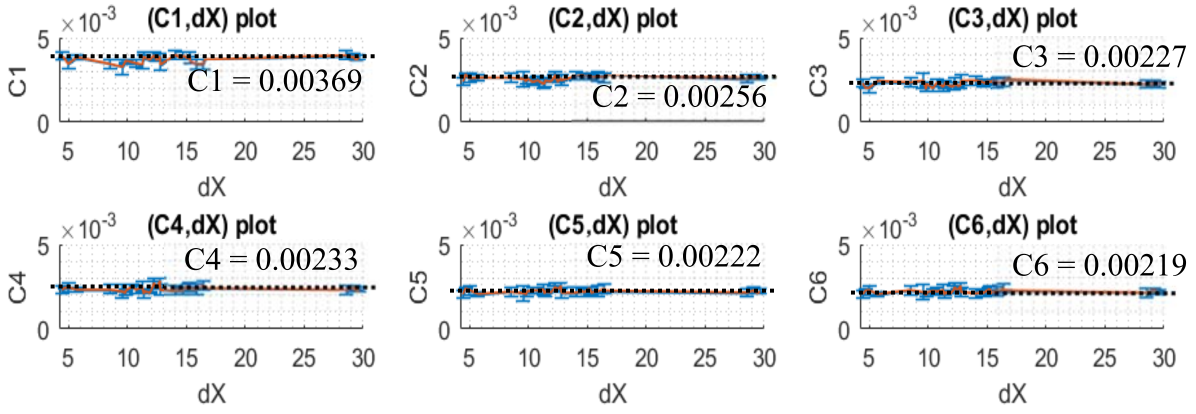

Figure 3. 10. The plots of correction coefficients and *dX* of upper-subdomain data

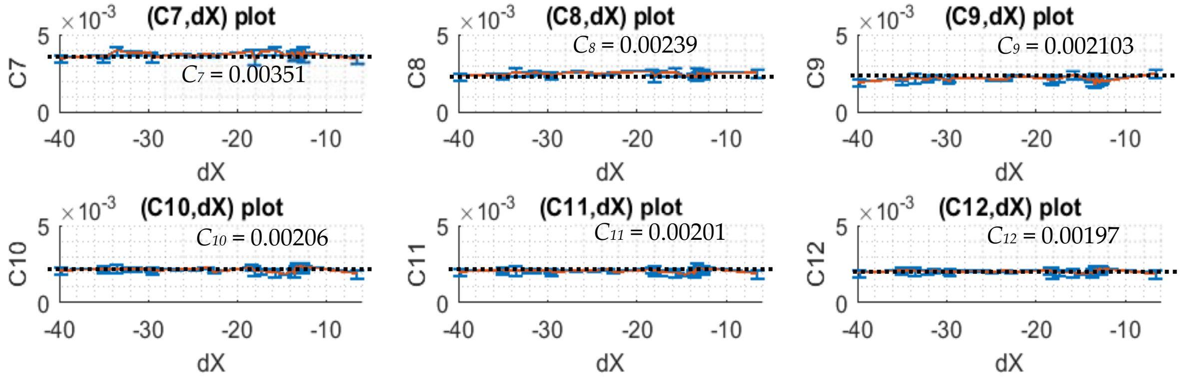

Figure 3.11. The plots of the correction coefficients and *dX* of lower-subdomain data

3.3.5.1. Dataset correction simulation

Now with the all the parameters and function found, one can check to see how the output data from the corrector is better than the uncorrected data. For the process assessment, two new quantities are added:

$$|dY_1| = |Y_2 - Y_1| \tag{3.21}$$

$$|dY_2| = |Y_2 - \overline{Y_1}| \tag{3.22}$$

Equations (3.21) and (3.22) are the absolute errors of the uncorrected data and corrected data, respectively. Figure 3.12 shows the plots of the new quantities, $|dY_1|$, $|dY_2|$ of the multi-changing data and mono-changing data of the two different styles datasets. The expectation here is that the absolute error plots is as close to the zero line as possible. From the plots, the corrected data is better than the uncorrected data. The intensity plots only illustrate how the light intensity was changed to simulate possible reality situations.

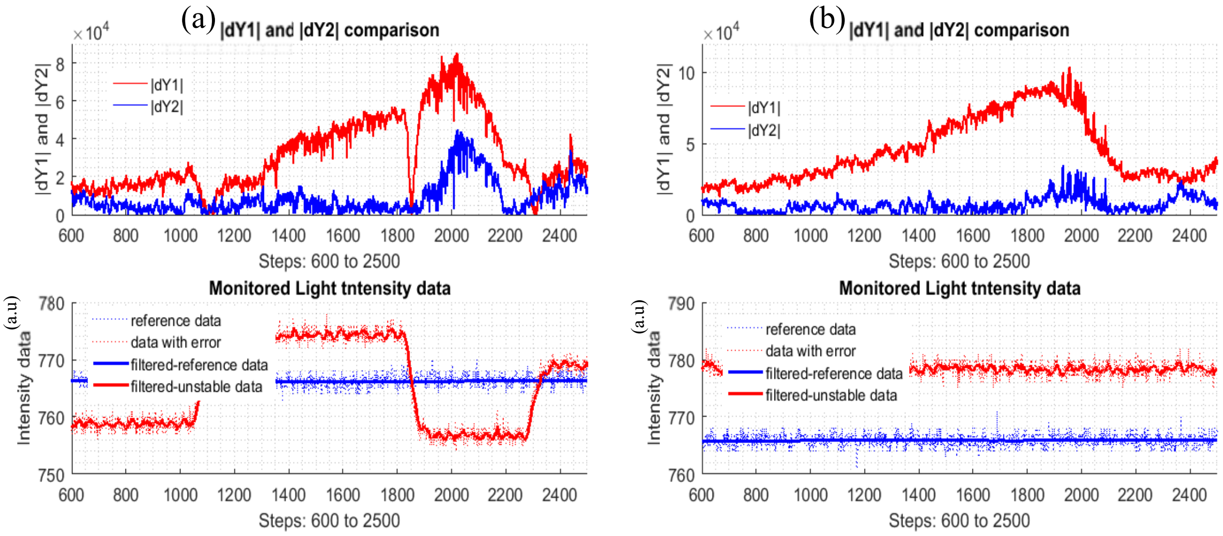

Figure 3.12. (a): $|dY_1|$ and $|dY_2|$ plots of multi-changing *dataset 24*; (b): $|dY_1|$ and $|dY_2|$ plots of lower-mono-changing dataset 1

3.3.5.2. Measurements on air, H_2O, and KMnO4 samples

After the simulation testing, the correction function and the parameters are applied into the device for further test. For the test, the reference data are still required. The light intensity of the light source is adjusted similarly when the data with error were recorded to serve for the above simulations. The difference here is the data with error will be corrected immediately by the corrector module which is coded into the Atmel328P processor. To check the effectiveness and ability of the corrector, several different types of samples are required (air, H_2O, and KMnO4 samples) under the light intensity changes in both mono-changing and multi-changing strategies. From experiment data, spectral data, light intensity data, and errors are plotted, Experimental results prove that the corrector module works well as can be seen in Figure 3.13. Note that there are four types of different samples and three types of plots in the figure to illustrate the work of the corrector. The errors of the data after the correction are also plotted.

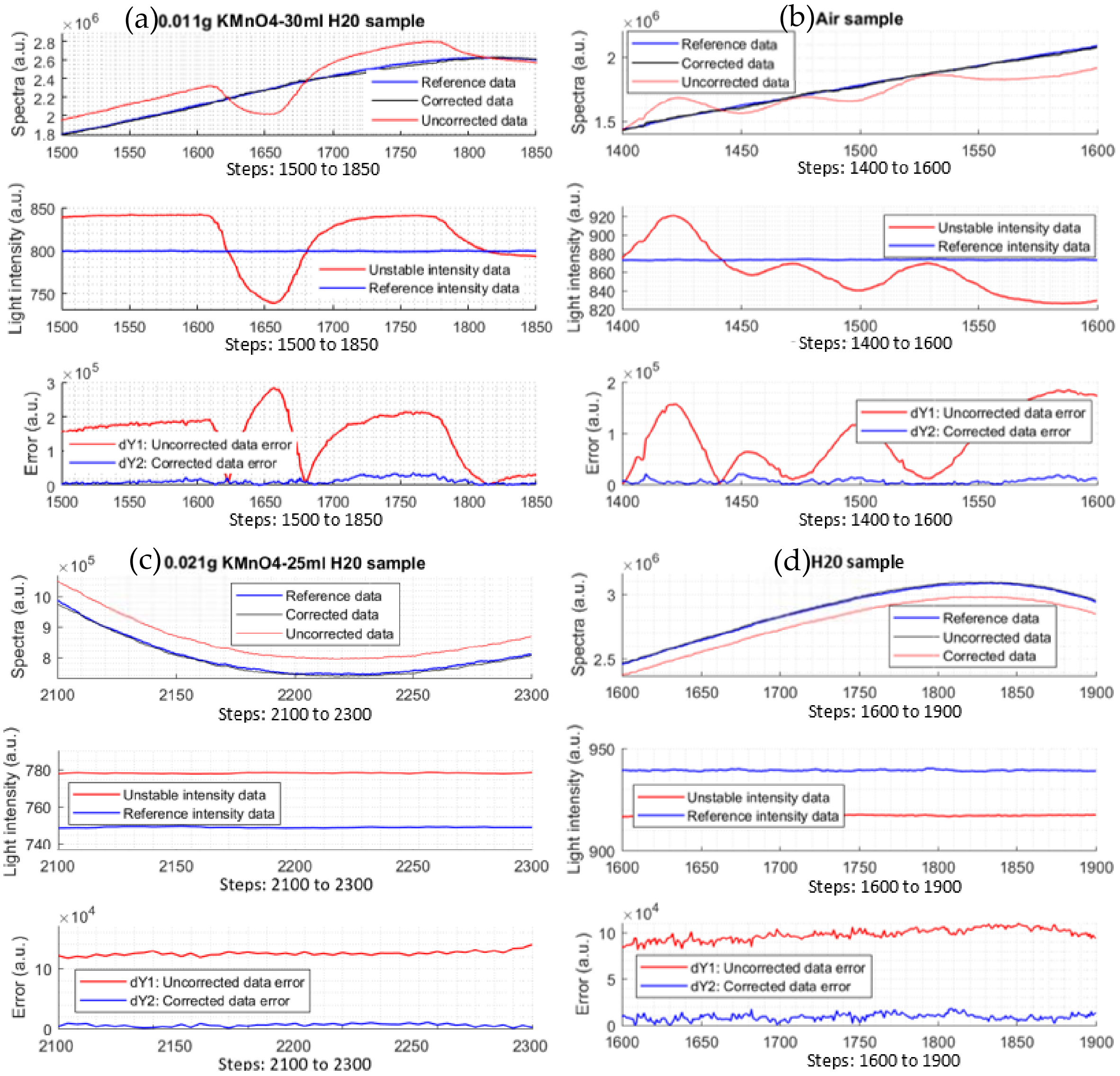

Figure 3.13. Experimental data of different samples. (d): 0.011g KMnO4 and 30ml distilled H_2O; (b): air; (c): 0.021g KMnO4 and 25ml distilled H_2O; (d): distilled H_2O.

By defining the simple formula, $r = \frac{|\boldsymbol{dY_1}|}{|\boldsymbol{dY_2}|}$, indicates how many times the corrector reduces the light-intensity error. According to calculation from the measured data, $r \approx 10$ times. At some local data points, it could reach to 60 to 70 times. This coefficient is a used as a merit to evaluate the effectiveness of the Kalman corrector. However, it just shows much meaningful when there is much light-intensity error happening, albeit a good coefficient.

3.4. Discussion and Conclusion

In general, the Kalman algorithm is modified as a corrector to compensate for the data error caused by the unstable light source in a VIS SPEC. The single-beam-24-bit visible spectrometer, which is empowered by an auxiliary photodiode sensor, an appropriate correction function, and Kalman algorithm, can automatically correct the error caused by the light-source-intensity instability which happens randomly or by drifting of the sources. In average, when there is error in the spectral data, it can be reduced approximately by 10 times. The results show a good performance both in simulations and experiments.

One drawback of the technique is the using of average of $\boldsymbol{Q_{1,min}}$ to $\boldsymbol{Q_{1,max}}$ from simulation. Section *3.3* provides a range of the applicable values of the noise process covariance. For being able to adapt to the diversity of light-intensity instability, the mean value of the range is selected. Consequently, the data with error may not be perfectly corrected due to either the lack of or not enough light-intensity error information and/or quantization errors still remaining in the light-intensity data.

To improve the ability of the corrector module, other methods can be applied along with this technique to achieve better results. For example, one can use moveable boundaries, instead of applying the currently fixed boundaries. With moveable boundaries, LS, AE, ERR, and correlation coefficient are still the operation criteria.

Appendix A

The short correction forms of the formulas used in section 3.2, Table 3.1:

$$f_A = \bar{Y}_{1,i}(\mathrm{j}) + C_i{*}\overline{dX}_i(\mathrm{j}){*}\bar{Y}_{1,i}^2(\mathrm{j}),$$

$$f_B = \bar{Y}_{1,i}(\mathrm{j}) + C_i{*}\overline{dX}_i(\mathrm{j}){*}\sqrt{\bar{Y}_{1,i}(j)},$$

$$f_C = \bar{Y}_{1,i}(\mathrm{j}) + C_i * \overline{dX}_i(\mathrm{j}) * \bar{Y}_{1,i}^{3/2}(j),$$

$$f_D = \bar{Y}_{1,i}(\mathrm{j}) + C_i * \overline{dX}_i(\mathrm{j}) * \bar{Y}_{1,i}(j).$$

Noticing that the form of f_A, f_B, f_C, and f_D is slightly different from equation (3.4). As in the experiments, authors found that the correction function work much more effectively if $\bar{Y}_{1,i}^{n}(j)$ is inserted, where n is 1, 2, 3, …, or 1/2, 1/3, 3/2. Thus, there is a relation between the correction function f with not only $\boldsymbol{dX}$ but also $\boldsymbol{Y}$.

Appendix B

The values of C_i of the upper-subdomain and lower-domain data are collected by simulation and used in section 3.4.

Table 3.3: C_i values of upper-subdomain data.

C_i of subdomains Data set	C_1	C_2	C_3	C_4	C_5	C_6	$\overline{\boldsymbol{dX}}$
1	0.00386	0.00264	0.00245	0.00233	0.00208	0.00207	5.7078
2	0.00345	0.00261	0.00202	0.00246	0.00231	0.00230	4.9686
3	0.00392	0.00240	0.00231	0.00231	0.00206	0.00206	4.4369
4	0.00377	0.00283	0.00204	0.00243	0.00240	0.00227	4.6495
5	0.00356	0.00238	0.00201	0.00248	0.00229	0.00226	10.3858
6	0.00359	0.00242	0.00196	0.00213	0.00206	0.00202	9.8095
7	0.00364	0.0026	0.00227	0.00230	0.00222	0.00216	9.8672
8	0.00328	0.00256	0.00247	0.00222	0.00212	0.00218	9.5766
9	0.00345	0.00264	0.00236	0.00233	0.00220	0.00230	8.5105
10	0.00391	0.00267	0.00238	0.00248	0.00229	0.00231	15.2758
11	0.00393	0.00272	0.00234	0.00225	0.00216	0.00213	14.6995
12	0.00380	0.00277	0.00238	0.00230	0.00224	0.00217	14.5844
13	0.00398	0.00272	0.00247	0.00224	0.00215	0.00210	14.0529
14	0.00391	0.00265	0.00215	0.00257	0.00238	0.00233	12.1743
15	0.00340	0.00249	0.00246	0.00232	0.00215	0.00219	12.7739
16	0.00341	0.00260	0.00236	0.00255	0.00236	0.00236	16.4325
17	0.00341	0.00265	0.00233	0.00234	0.00224	0.00219	15.8561
18	0.00357	0.00259	0.00242	0.00230	0.00215	0.00212	15.3245
19	0.00371	0.00274	0.00252	0.00240	0.00227	0.00224	16.5607
20	0.00342	0.00228	0.00210	0.00249	0.00234	0.00231	11.2676

21	0.00349	0.00248	0.00235	0.00232	0.00228	0.00222	10.7491
22	0.00384	0.00247	0.00234	0.00224	0.00221	0.00216	11.3957
23	0.00368	0.00238	0.00216	0.00243	0.00236	0.00232	12.4826
24	0.00391	0.00233	0.00223	0.00207	0.00208	0.00201	11.3750
25	0.00370	0.00242	0.00212	0.00214	0.00217	0.00211	11.9064
26	0.00386	0.00257	0.00218	0.00231	0.00221	0.00215	29.6674
27	0.00396	0.00254	0.00222	0.00229	0.00216	0.00211	28.5594
28	0.00385	0.00256	0.00221	0.00243	0.00228	0.00226	29.0910
29	0.00366	0.00255	0.00232	0.00222	0.00214	0.00212	29.4339
30	0.00388	0.00264	0.00229	0.00238	0.00224	0.00222	29.1488
Average	**0.00369**	**0.00256**	**0.00227**	**0.00233**	**0.00222**	**0.00219**	

Table 3.4: C_i values of lower-subdomain data.

C_j of subdomains Data set	C_7	C_8	C_9	C_{10}	C_{11}	C_{12}	$\overline{dX}$
1	0.00355	0.00231	0.00219	0.00187	0.0019	0.00188	-20.2399
2	0.00355	0.00226	0.00182	0.00225	0.00218	0.00209	-13.4950
3	0.00343	0.00253	0.00248	0.00189	0.00189	0.00187	-6.5176
4	0.00336	0.00232	0.00211	0.00209	0.00209	0.00196	-18.0569
5	0.00373	0.00242	0.00211	0.00206	0.002	0.00196	-13.2514
6	0.00381	0.00241	0.00203	0.00207	0.002	0.00197	-13.7458
7	0.00307	0.00226	0.00213	0.00194	0.00193	0.00188	-13.3111
8	0.00307	0.00236	0.00228	0.00203	0.00205	0.00202	-12.9464
9	0.00323	0.00199	0.00171	0.00186	0.00181	0.00172	-10.6810
10	0.00358	0.00251	0.00204	0.00234	0.00223	0.00213	-13.0744
11	0.00309	0.00239	0.00205	0.00197	0.00195	0.00201	-17.5519
12	0.00351	0.00229	0.00215	0.00183	0.00186	0.00183	-13.5530
13	0.00306	0.0021	0.00161	0.00195	0.00189	0.00185	-11.2250
14	0.00368	0.0023	0.00218	0.00185	0.00183	0.00187	-14.6510
15	0.00335	0.00238	0.00223	0.00187	0.00184	0.00188	-13.2710
16	0.00389	0.00253	0.00215	0.00205	0.00198	0.00196	-17.3292
17	0.00374	0.00249	0.00207	0.00227	0.00216	0.00209	-23.2423
18	0.00364	0.00248	0.00209	0.00219	0.0021	0.00201	-24.7748
19	0.00373	0.0026	0.00222	0.00214	0.00208	0.00205	-26.7884
20	0.00364	0.00255	0.00233	0.002	0.00199	0.00197	-22.6055

21	0.00347	0.00232	0.00204	0.00217	0.00212	0.00208	-35.0176
22	0.00341	0.00253	0.00227	0.00205	0.00202	0.00203	-22.3267
23	0.00382	0.00246	0.00207	0.00217	0.0021	0.00202	-32.2190
24	0.00373	0.00243	0.00202	0.00217	0.00209	0.00202	-41.6049
25	0.00347	0.00231	0.00191	0.00210	0.00201	0.00194	-39.7620
26	0.00379	0.00242	0.00198	0.00215	0.00206	0.00199	-29.6439
27	0.00309	0.00242	0.0022	0.00204	0.00197	0.00196	-22.4463
28	0.00361	0.00242	0.00214	0.00217	0.00213	0.00208	-35.0595
29	0.00383	0.00254	0.00227	0.00219	0.00208	0.00208	-31.3988
30	0.00347	0.00239	0.00215	0.0021	0.00197	0.00198	-29.5559
Average	**0.00351**	**0.00239**	**0.00210**	**0.00206**	**0.00201**	**0.00197**	

References

[C3.1] J. M. Parnis and K. B. Oldham, "Beyond the Beer-Lambert Law: The Dependence of Absorbance on Time in Photochemistry," *J. of Photochem. & Photobio., A: Chem.*, vol. 267, pp. 6-10, 2103. Available: https://doi.org/10.1016/j.jphotochem.2013.06.006.

[C3.2] N. Friedrich, "ADC Mysteries are finally explained," *Mic. & RF*. 47, Nov. 12, 2008. Available: https://www.mwrf.com.

[C3.3] S. Pham and A. Dinh, "Using Trans-impedance Amplifier and Smoothing Techniques to Improve Signal-to-Noise Ratio in a 24-bit Single Beam Visible Spectrometer," Proceedings of The IIER International Conference, Bangkok, Thailand, 105th, pp. 1-6, 2017. ISBN: 978-93-86291-88-2.

[C3.4] Mightex Co, "Miniature CCD spectrometers with high resolution and high stability," *Mightex Co.* [Online]. Available: http://www.mightexsystems.com. [Accessed: October 2017].

[C3.5] StellarNet Inc, "Analytical instrumentation – Surf the new wave in portable fiber optic spectrometry," *StellarNet Inc*. Available: https://www.stellarnet.us. [Accessed: October 2017].

[C3.6] Texas Instrument Inc., "Manual: 24-bit, 40khz analog-to-digital converter," *Texas Instrument Inc*. Available: http://www.ti.com. [Accessed: January 2017].

[C3.7] Osram Inc, “Silicon Pin Photodiode Version 1. 4. BPW 34 S,” *Osram Inc*. Available: http://www.osram-os.com. [Accessed: January 2017].

[C3.8] H. H. Jaffé and M. Orchin, “Theory and Applications of Ultraviolet Spectroscopy,” *New York: Wiley*, United States of America, ch. 6, pp. 111-115, 1962.

[C3.9] International Light Technologies Inc, “Tungsten halogen lamps,” *International Light Technologies Inc.* Available: https://www.intl-lighttech.com. [Accessed: November 25, 2017].

[C3.10] Power Sonic Co., “PS-1270 12 Volt 7.0 AH: Rechargeable Sealed Lead Acid Battery,” *Power Sonic Co.*. Available: http://www.powersonic.com. [Accessed: November, 2017].

[C3.11] S. Fullerton, K. Bennett, E. Toda, and T. Takahshi, “Orca-Flash4.0 Changing the game. Hama. Coper,” *Hamamatsu Photon Co.*. Available: https://www.hamamatsu.com. [Accessed: November 25, 2017].

[C3.12] Osi Optoelectronics Co, *Photodiode Characteristics and Applications*, Osi Optoelectronics Co, 2017. Available: http://www.osioptoelectronics.com. [Accesed on November 25, 2017].

[C3.13] Hamamatsu Photon Co., “What is dark noise?” *Hamamatsu Photon Co.*. Available: http://hamamatsu.com. [Accessed: November 2017].

[C3.14] S. W. Smith, “The Scientist and Engineer's Guide to Digital Signal Processing,” *California Technical*, United States of America, ch. 3, pp. 243-260, ch. 7, pp. 123-140, and ch. 15, pp. 277-284, 1999. ISBN: 0-9660176-7-6.

[C3.15] Texas Instrument Inc, *LP2980, LP2982, LP2985-Engineers note: Capacitors are key to voltage regulator design*, Texas Instrument Inc. Available: http://www.ti.com. [Accessed: November 2017].

[C3.16] T. Vo-Dinh, G. Gauglitz, *Handbook of Spectroscopy*, Wiley-VCH: Weinheim, Federal Republic of Germany, ch. 12, pp. 421-493, 2003. ISBN: 3-527-29782-0

[C3.17] C. Belton, *Lab Manual: UV-VIS*. Imperial College London, 2009. Available: http://www.webcitation.org/6v70Gyhg7. [Accessed: November 25, 2017].

[C3.18] 2N1544 Germanium PNP Transistor. Available: http://www.semicon-data.com/transistor/tc/2n/2N1544.html. [Accessed: October 15, 2017].

[C3.19] Texas Instrument Inc, *LM317 3-Terminal Adjustable Regulator*, Texas Instrument Inc. Available: http://www.ti.com. [Accessed: October 2017].

[C3.20] D. Halliday, R. Resnick, and J. Walker, *Fundamentals of Physics*. 9th ed. Wiley: New York, United States of America, Ch. 35, pp. 958-983, 1997. ISBN: 978-0-470-46908-8.

[C3.21] 28BYJ-48 Stepper Motor 5VDC. Available: http://www.webcitation.org/6ve05B41c. [Accessed on January 15, 2017].

[C3.22] Atmel 8-Bit Microcontroller with 4/8/16/32kbytes In-System Programmable Flash. Available: http://www.atmel.com/images/Atmel-8271-8-bit-AVR-Microcontroller-ATmega48A-48PA-88A-88PA-168A-168PA-328-328P_datasheet_Complete.pdf. [Accessed on January 2017].

[C3.23] A. Levitin, *Introduction to the Design & Analysis of Algorithms*, 3rd ed. Pearson: Boston, United States of America, ch. 5, pp. 169-174, and Ch. 9, pp. 315-322, 2012. ISBN: 978-0-13-231681-1.

[C3.24] R. Alur and A. Radhakrishna, *Scaling Enumerative Program Synthesis via Divide and Conquer*, Proceedings of Tools and Algorithms for the Construction and Analysis of Systems: 23rd International Conference, TACAS, ETAPS, Uppsala, Sweden, April 22-29, 2017. ISBN: 978-3-662-54580-5.

[C3.25] J. L. Melsa and D. L. Cohn, *Decision and Estimation Theory*, McGraw-Hill: New York, United States of America, ch. 11, pp. 244-251, 1978. ISBN: 0-07-041468-8.

[C3.26] M. S. Grewal, and A. P. Andrews, *Kalman Filtering: Theory and Practice Using MATLAB. 3rd ed. Hoboken*, N.J.: Wiley, ch. 3, pp. 100-167, 2008. ISBN: 0-521-40573-4.

[C3.27] P. S. Maybeck and M. S. George, *Stochastic Models, Estimation, and Control*, Vol. I, no. 5th ed: 282. Academic Press 10, pp.1-16. ISBN: 0-12-480701-1.

[C3.28] J. D. Vincent, *Fundamentals of Infrared Detector Operation and Testing*, Wiley Series in Pure and Applied Optics. Wiley: New York, United States of America, Ch. 6, pp. 275-30, 1990. ISBN: 0-471-50272-3.

[C3.29] S. M. Pandit and S. M. Wu, *Time Series and System Analysis, with Applications*, New York: Wiley, United States of America, Ch. 2, pp. 13-74, 1983. ISBN 0-471-86886-8

[C3.30] A. Harvey, *Forecasting, Structural Time Series Models and the Kalman Filter*, 1st Paperback ed. Cambridge; Cambridge University Press: New York, United States of America, Ch. 3, pp. 100-163, 1990. ISBN: 0-521-40573-4.

[C3.31] G. A. Carlson, *Experimental errors and uncertainty*, 2002. Available: http://www.webcitation.org/6u7N8FcKs. [Accessed: October 25, 2017].

[C3.32] G. Welch and G. Bishop, G, *An Introduction to the Kalman Filter*, UNC-Chapel Hill, United States of America, 2006. Available: http://www.webcitation.org/6u7M513uA. [Accessed: October 25, 2017].

4. A Nondispersive Thermopile Device with An Innovative Method to Detect Fusarium Spores

Published as:

Son Pham, Anh Dinh, and Khan Wahid, "A Nondispersive Thermopile Device with an Innovative Method to Detect Fusarium Spores," *IEEE Sensors Journal*, Vol. 19, No. 19, October 2019, pp. 8657-8667.

Inheritance from the previous work described in Chapter 3, an innovative device and method to detect *Fusarium* are presented in this chapter. A group distinction coefficient was derived from the Beer-Lambert law. The coefficient was applied to distinguish *Fusarium* spore from the other samples which were investigated in this work. The device was built using thermopiles working at two special wavelengths as the main sensors. These two special wavelengths were determined from the FTIR spectrum which were provided by investigating the *Fusarium* sample described in Chapter 2. The *Fusarium* sample was nurtured in the laboratory conditions and by a specific procedure. The detail of the device structure and components is described in the following manuscript. Additionally, a mechanism of sampling the air and analyzing the collected sample is also presented.

In this manuscript, the main contribution comes from the student (the first author). The two co-supervisors provide supervision.

A Nondispersive Thermopile Device with An Innovative Method to Detect Fusarium Spores

Son Pham, Anh Dinh, and Khan Wahid

Abstract

Early detecting for Fusarium spore in the air is highly desired as it helps to protect crops from the potential of dangerous fungal disease. This study focuses on developing a method and building a portable, reliable, and affordable device which can promptly and continuously detect the presence of Fusarium spores in the air. Based on Beer-Lambert law and the distinct infrared absorbance spectrum of substances, a specification logarithm ratio formula for two different wavelengths is developed. This is the main principle of the detection technique and design of the device. In the system, there are two sensitive infrared thermopiles which work on two specific infrared wavelengths, including $\lambda 1=6.09\pm0.06\mu m$ and $\lambda 2=9.49\pm0.44\mu m$. The thermopiles are used to measure infrared light intensity emitted by an infrared light source (2µm to 22µm) for Fusarium spore detection analysis. The detection is based on the group distinction coefficient. Beer-Lambert law also assists in the approximate estimation of the quantity of the spores. For testing detection ability of the system and method, besides *Fusarium* spore, other substances such as sunflower pollen, polyphenol, and starch were also used in the experiments. The experimental results indicate that the Fusarium group-distinction coefficient (1.14±0.15) is distinct from the other investigated substances (pollen: 0.13±0.11, turmeric: 0.79±0.07, and starch 0.94±0.07). The results prove that the system and the proposed method can be used to detect and quantify not only for Fusarium but also for other spores, molds, and specific pathogens.

Index Terms: Biosensor, Beer-Lambert law, group distinction coefficient, Fusarium spore, thermopile, detection method

4.1. Introduction

Fusarium can cause infection on human and animals by impairing the host immunization system and resulting in different undesired outcome [C4.1- C4.3]. The fungus impacts most on plants by leading to fungal diseases such as Fusarium head blight [C4.4- C4.6], *Fusarium* wilt [C4.7- C4.9], *Fusarium* dry rot [C4.9], crown rot, and root rot [C4.6, C4.10]. Therefore, an early detection of the spore appearance to have the treatment is the key to prevent Fusarium diseases from causing damages. The destruction caused by fungus disease has been seen around the world on many types of plants [C4.8- C4.12].

In the past, many methods and techniques to detect Fusarium have been proposed. In Bauriegel et al. [C4.11], after spraying 250,000 *Fusarium culmorum* spores/ml, the pathogen source, on three continuous days into wheat plants at condition of 20±2ºC, 70% humidity and 12h lighted period by SON-T Plus 400W sodium-vapor lamps, the plant spikelets were visually investigated three times per week to see the infection degree by using chlorophyll fluorescent imaging (CFI) to calculate the ratio fluorescent indicator [C4.11]. Based on the difference in chlorophyll fluorescent imaging of a healthy spikelet from the infected one, levels of disease will be classified. The authors have proven that the method is helpful in identifying *Fusarium culmorum* infection [C4.11]. Another method has been proposed in [C4.13], in which spore traps and quantitative polymerase-chain-reaction (qPCR) machine were used. The spore traps catch the particle samples in the air, then the samples are analyzed in a qPCR to identify quantity of pathogen DNA. The pathogen quantity is converted into the number of spores per air sampled cubic. Thermal camera to record images of the canopy of wheat or cereal plants in the field was also suggested. Then, the black and white images can be acquired by converting the near infrared images. The white areas show the infection places. The authors conclude that qPCR method is useful for onsite, as the device is portable, and the thermal imaging method is useful to detect early infection for many pathogens.

Mass spectrometry device was applied in [C4.1] to identify clinical Fusarium isolates, in which the samples were extracted from the patients in the L'hôpital Saint-Antoine, Paris, France. In Marchetti-Deschmann et al. [C4.14] the study used Fusarium samples nurtured on nutrient environment, and mass spectrometry was used to identify and classify Fusarium types as well. The authors used mass spectrometry to measure mass-to-charge ratio and provide mass spectrum to identify as well as classify Fusarium spores. In other Fusarium studies [C4.15- C4.16], Fourier transform infrared (FTIR) spectroscopy and near infrared spectroscopy were applied to measure infrared (IR) spectrum of absorption or emission of the investigated objects. Similar with mass spectrum, each substance also has its own infrared spectrum. The spectra of the object were compared with the database to come to the decision of whether the objects are Fusarium infected and of the degree of infection if it happens. In Vinayaka et al. [C4.17], another interesting approach was presented by using an impedance-based mold sensor which is gold electrodes built on a glass base. A reaction cavity which contains agar gel is located on the electrode surface. When the spores are transferred to the gel, it will grow up and cause the pH of the gel change. The pH change makes the impedance of the gel also change. To monitor the pH change, the methyl red indicator dye was used. According to the research, the method can detect the presence of spore or mold at least 24 hours, as it requires enough time for the spore to develop.

Although these described methods have been proven effectively, there are still some obstacles which may prevent them from applying in many practical applications. Most of the devices are large and requires tedious set-up, so it is difficult to have onsite tests for a quick result. The operators, who are assigned to operate the devices correctly and properly, must be well trained as the operations of these devices require strict procedures and are somewhat complicated. Consequently, these methods require not only the high cost to own the system but also the budget for operating and maintenance. To address and find the solutions to overcome the above obstacles, in this work, a method of using Beer-Lambert law and group distinction coefficient was proposed and a system was built to test the detection of Fusarium oxysporum and other objects. The rest of the paper is organized as follows. Section 2 provides the background of the method required for the design of the detection system. Section 3 describes the system in detail. Section 4 presents testing results and discussions about the challenges and achievements of the proposed method and designed system. Additionally, in this section, the setup target of the early detection of Fusarium and the method of using Beer-Lambert law and the group distinction coefficient to distinguish Fusarium from some other different substances are shown. Finally, Section 5 concludes the work.

4.2. Background

Fusarium species are fungal; the spores are dispersed through air and water and both media collaborate in spreading the spore [C4.18- C4.19]. The spreading also occurs in only one medium as the fungi try to exploit in order to convey themselves away. There are two dispersals: primary dispersal, by which the spore is carried away from the parent body, and secondary dispersal, by which any subsequent distribution happens after it comes to rest. In primary dispersal, the one-phase system has merely air or water while the two-phase system has both media involved in form of bubbles or the tiny drops containing the spores, conveying by the air [C4.18, C4.20- C4.23]. The single air phase takes the most responsibility for fungus dispersal. Consequently, in this work, the single air phase is chosen to investigate because of not only the most distribution of the spores, but also the feasibility in practical detection in the fields.

Fusarium graminearum spores on grain spikes or crop remainders can be dislocated by wind or ejection mechanisms. They can flee from the air laminar into the atmospheric turbulence featured by wind speed distribution and direction [C4.23- C4.25]. Once spores go to the turbulence, they can sneak through the canopy layer or flee into either the troposphere or stratosphere for long-distant journeys up to 400km [C4.19, C4.26]. The distance of the spores taken away by wind and by ejection mechanism depends on spore sizes, weights, and initial velocities [C4.23- C4.24]. After dispersal, the spores will be deposited by dry deposition (air currents and gravitation settling) or wet deposition (rain droplets) on the new hosts [C4.23].

Ascospore and macroconidia, in the air, can be caught for studying by using passive air sampling (PAS), in which free air flows into or onto a specific medium to collect sample [C4.27- C4.28]. PAS is inexpensive and does not need electricity; the disadvantages of this method is low temporal resolution due to low rates of air fluxes sampling and time consuming. Conversely, active sampling (AAS) trades cost of operation and maintenance for high temporal resolution and stable-adjustable air flow. AAS dominates PAS in practical applications [C4.28].

Since prompt detection of ascospore or macroconidia is one of the criteria, this work used AAS method as a part of the solution. Referred the AAS traps proposed in [C4.13], [C4.29- C4.31] and in the laboratory manual book of EMSL Analytical Inc. [C4.32], one of the common points is that all of them use surfaces having ability in catching bio-objects. The surfaces can be tape (AIR-O-CELL filter cassette), sticky rod, or wet agar (Andersen trap). In most cases, air samples collected by the AAS traps must be taken out or transferred to another medium for further processing such as microscope observation, FTIR spectroscopy or mass spectrometer. This step requires high skill and trained personnel, regardless time-consuming. In addition, the surfaces cannot be reused. One solution to solve those difficulties is to include the detectors inside the traps to analyze the samples. This work proposed an electrostatic interaction by using an electronic device to catch the spores. The catcher was included in the detection system. This solution keeps the features of catching spores and allows an add-on-reuse ability to the surface.

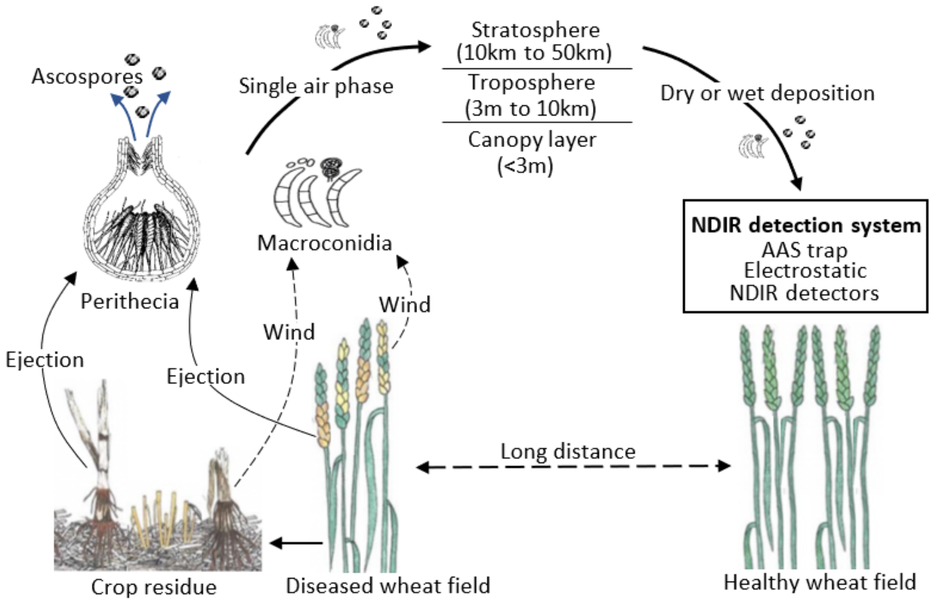

(a)

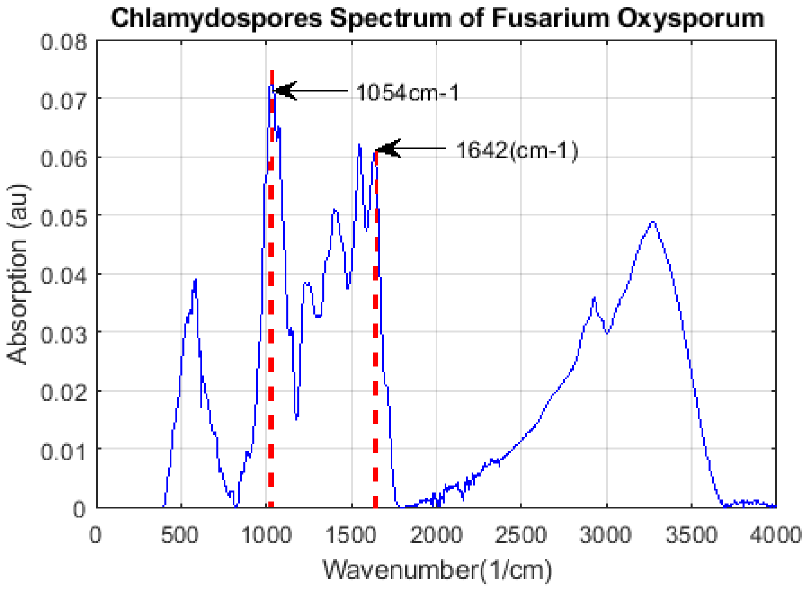

(b)

Figure 4.1. (a): Illustration of the spore ejection and spreading, (b): Absorption spectra of Fusarium oxysporum.

As mentioned, FTIR spectroscopy can provide IR spectra by analyzing the IR light interacting with substances or samples. The spectra assists in identifying the samples based on the differences in their spectra [C4.33- C4.34]. On a certain field such as wheat or corn fields, other biological objects (pollen or spore) often co-exist in the air. Some typical absorption or transmission peaks of the IR spectra of the objects are standing out and used for distinguishing the biological objects. These typical peaks correspond typical IR wavelengths, from which special IR detectors can work at these IR wavelengths. In general, an IR detector is a broadband device. A narrow bandpass (NBP) filter is used in front of the detector to retain the desired wavelengths. Detectors applying this technique are called nondispersive (NDIR) detectors and frequently used in gas sensing system. NDIR requires a steady or pulsed broadband IR source depending on the type of detectors [C4.35- C4.36]. In our proposed Fusarium detecting system, along with NDIR detectors, an appropriate broadband IR source must be carefully chosen.

Figure 4.1(a) illustrates the spores spreading methods in searching for the new hosts [C4.19, C4.23- C4.26]. Figure 4.1(b) provides the measured absorption spectra of the Fusarium oxysporum Chlamydospores (Chl.) which was investigated by the ATR-FTIR spectroscopy set up in the Chemical Department, Engineering College, University of Saskatchewan, Canada. The two typical wavenumbers 1054cm-1 (9.48μm), which is caused by Glycogen C-O stretching, and 1642cm-1 (6.08μm), which is caused by Amide C=O stretching, are targeted in the detection mechanism in this work. Based on the above description, the system was designed and the detection method was developed.

4.3. System Design and Detection Methodology

4.3.1. Design

The working flowchart and the functional description of the detection system are shown in Figure 4.2. The works and typical parameters of the design are presented in the followings.

- Vacuum pump: The pump is a micro-air pump (3V-6V DC, 620mA). The pump draws the external air into the trap at a flow of 2.5L/min using inlet/outlet tubes of 4.3mm in diameter.
- Trap: The trap is one of the most important parts of the system as it captures the samples for detection. Figure 4.3 provides an illustration of the trap structure and design. A polymethyl methacrylate (PMMA) box was divided into two smaller chambers by a blade. One chamber was used as a reference chamber, which was illustrated as hidden side of the sketch, to monitor IR light source, and the other one was used as air sampling trap which was the viewing side or the front side. On each chamber, two parallel silver-coated metal mirrors were attached onto

the bottom and the top surfaces. PMMA was used because of its low thermal conductivity to minimize the heat conduction from the IR source [C4.37]. Experiments prove that the PMMA plate can stop the mentioned wavelengths from the external environment.

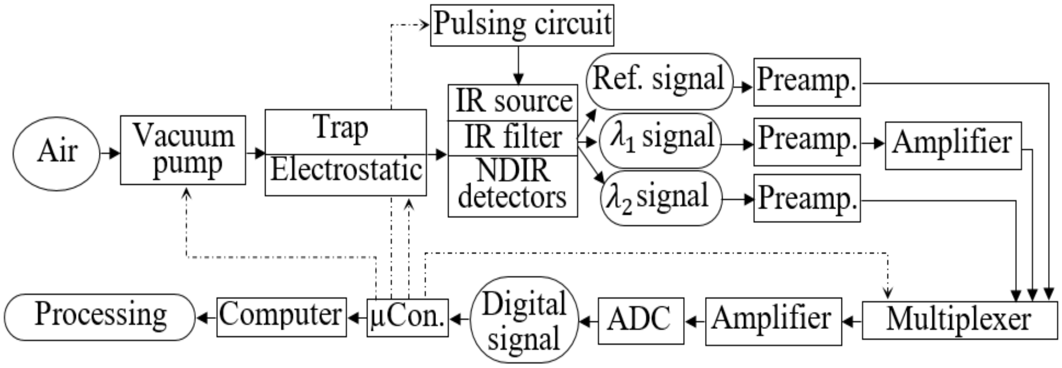

Figure 4.2. Diagram of the detection system. The dash lines are controlling buses provided by the microcontroller (µC) to control the corresponding devices.

From Figure 4.3(a), in the trap chamber or air sampling chamber, the light from an IR source will reflect on the silver-coated metal mirrors (dimensions: 20mm×5mm×1mm; reflectance spectrum: 400nm to 20µm). The light then goes through a Zinc Selenide (ZnSe) window (dimensions: 10mm×10mm×2mm; clear aperture: 90%; parallelism: <1; surface quality: 50-40) to reflect again on another orientation silver-coated mirror before being split by an uncoated beam splitter ZnSe plate. This plate has a dimension of 20mm×20mm×3mm; spectrum: 0.6µm to 16µm; at 45o, the transmission is 70%, and the reflection is 30% [C4.38]. This light will then pass through two IR filter windows, Northumbria Optical Coatings Ltd [C4.39], to excite the photo detectors. In the reference trap, the difference in the comparison with the sampling chamber is that the IR beam is not split by the beam splitter before going into the reference thermopile.

As the IR source was used for both chambers, Figure 4.3(b-i) shows the radiant surface of the IR source which was split by a blade at 3/4 ratio using for trap chamber and 1/4 ratio using for the reference chamber. The reason for these unbalancing ratios is that the photo bandwidth of the reference thermopile is much larger than the bandwidths of λ_1 and λ_2 thermopiles. Additionally, the IR beam assigned to the two thermopiles was split into two weaker beams for each thermopile. Therefore, it can receive more energy of the incident IR light. Figure 4.3(b-ii) also shows the top view structure of the thermopiles. The lengths of the light path going through the trap chamber to λ_1 and λ_2 thermopiles are D1 and D2, where D1=D2=58mm.

- Electrostatic: The mirrors were connected to a high voltage (HV) circuit (10KV output from 3.6V to 6V input) by a switch controlled by the microcontroller (µC). The mirrors, with electrostatic, can catch spores or light objects brought into the box by the vacuum pump. Another switch was used to drain all the electrostatic to ground after sampling. Then the system goes to the measurement step to avoid potential of electrostatic noise. When the electrostatic is removed, the samples still reside on the mirror due to Van der Waals and/or gravitational forces [C4.40]. Turning on a cleaning vacuum pump and turning off the HV circuit will help to clean the trap chamber from the previous measured samples.

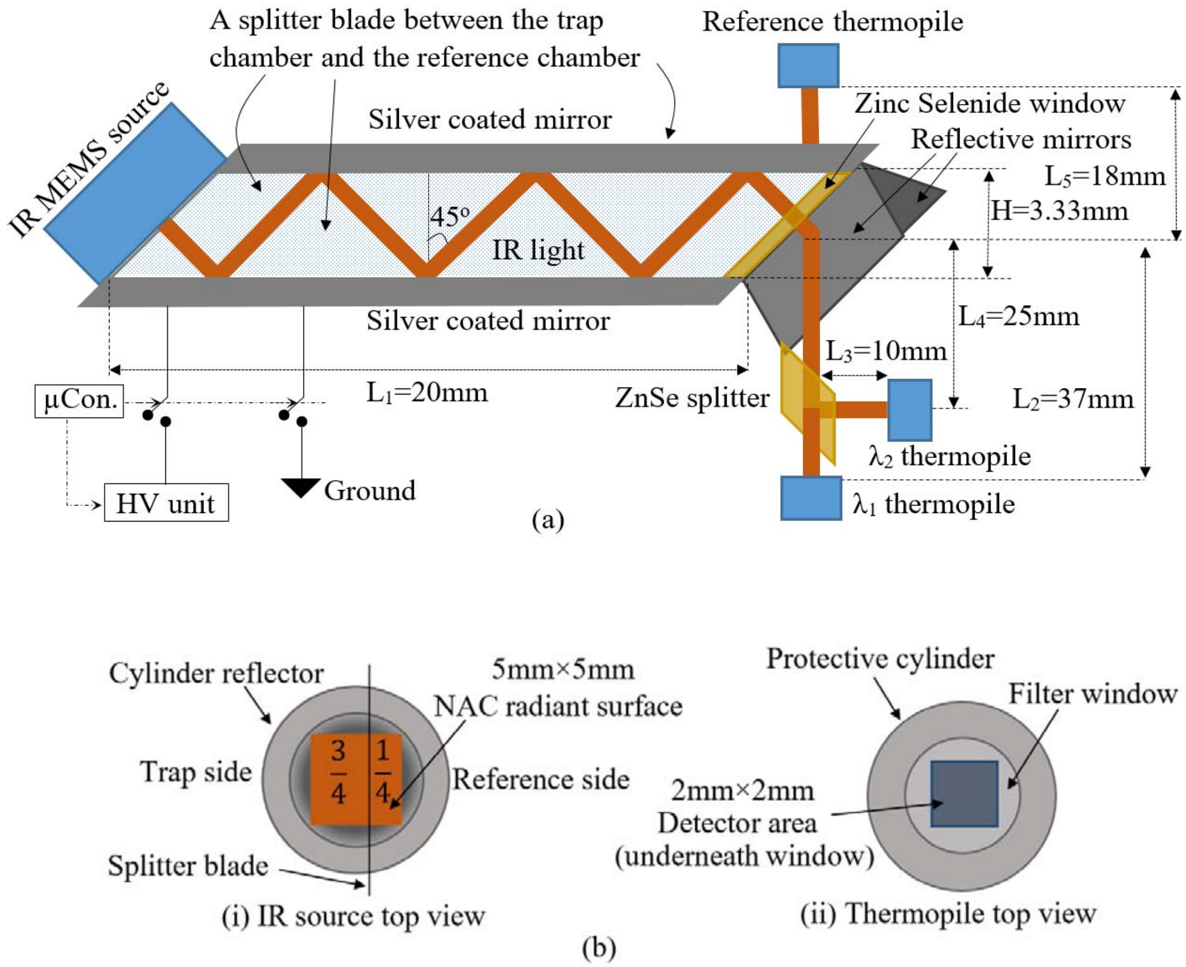

Figure 4.3. (a) Side view of the designed-trap-chamber sketch and IR light trajectory; (b-i) top view of the IR source; (b-ii) top view of the thermopile.

- Pulsing circuit: The circuit was mainly designed from a npn transistor and an IRFD9120 MOSFET [C4.41] which has an IS of 1A to tolerate the current of 141.4mA drawn by the IR light source. The FET is controlled by the µC. The pulsing circuit is also called IR pulse circuit, as it helps to control IR source. In this work, the period of the IR pulses was 5s with a duty cycle of τ=20%. Therefore, the modulation frequency was only 0.2Hz.
- IR source: The chosen IR source was the 2.2mm×2.2mm JSIR350-4-AL-C-D3.7-2-A5-I using MEMS technology [C4.42]. The active emitter layer had a multilayer nano amorphous carbon (NAC) membrane, and the base is silicon membrane [C4.43]. In the experiment, the setup voltage of the MEMS IR source was 5.65V with a current of 141.4mA. The input power was about 800mW, and the IR source temperature was 1,173K (900°C) [C4.42]. The emissivity spectrum of the light source is from 1µm to 20µm, and its lifespan is at least 50,000hr when the operating power is below 850mW. The time constant of the IR source is 17ms. In practice, a real object radiation is always less than a blackbody. The coefficient featuring that phenomenon is called extinction coefficient. According to [C4.43], the average extinction factor ($\bar{\varepsilon}$) is around 0.89 and from [C4.44] the total radiation energy per second of one unit area is:

$$\mathrm{Reff}\ (T) = \bar{\varepsilon}^*\int_0^\infty r(\lambda, T)\,d\lambda \qquad (4.1)$$

$$= \bar{\varepsilon}^*\int_0^\infty \frac{2hc^2}{\lambda^5}\cdot\frac{1}{e^{hc/\lambda k_B T}-1}\,d\lambda = \bar{\varepsilon}^*\sigma T^4$$

$$= 30\mathrm{kW/sr.m2} = 3\mathrm{W/sr.cm2}$$

- IR filter: IR filter windows select the incident IR light to the needed wavelength [C4.39] illustrated in Fig 1(b). One filter has the center wavelength (CWL) at λ1=6.088µm, the bandwidth (BW) of 49nm, and the transmission of 82.42% at CWL. The other filter CWL, BW, and transmission at CWL are λ2=9.487µm, 443nm, and 86.03% respectively. If the wavelength ranges from the CWLs are larger than twice BWs, the transmission is zero. From [C4.42] and [C4.43], the extinction factors at 6µm and 9.5µm wavelengths, are approximately 0.84 and 0.98.
- NDIR detectors: The 2mm×2mm 2M thin film-base single element thermopiles of Dexter Research Inc. were selected [C4.45]. Their spectral response is flat from 100nm to 100µm; the internal thermopile impedance, Rd, is about 10kΩ; the reaction time constant, tc, was 85ms, and the responsivity, R , was18.9V/W. Noise equivalent power (NEP) is a useful quantity

which is defined as the minimum measurable photo power of incident IR light to have signal-to-noise ratio (SNR) of unity in a 1Hz output bandwidth [C4.46- C4.47]. From Hamamatsu material [C4.48], as Johnson noise dominates shot noise (uncorrelated electrons) the NEP of the thermopiles is:

$$\text{NEP} = \sqrt{S_n}/\text{R} = 0.68\text{nW/Hz}1/2 \tag{4.2}$$

in which S_n=$4k_BTR_dB$; S_n is noise spectral density [C4.48]. In Hamamatsu material, the typical NEP of a thermopile with the active area of 1cm2 is 1.66nW/Hz1/2. Also, from the estimation, the actual incident powers that the reference, λ_1 and λ_2 detectors can receive are 0.183mW, 338.63nW and 194.767*10-8W respectively. In practice, NEP should be as small as possible, and much smaller than the incident light powers. Thus, this NEP proves the detectors are sensitive for this application. Similarly, the SNRs of the three cases are 87.6dB, 28dB and 43.25dB. The datasheet in [C4.45] provides the damage threshold value of P_{thres}=0.5W/cm2. From the above incident IR powers to the thermopiles, they are smaller than P_{thres}. Thus, the device safely operates without damaging. At a glance, from equation (4.1), the radiance from the source is Reff =3W/sr.cm2 which is greater than P_{thres}. Consequently, it is mandatory not to expose the detectors directly to the IR light source under any circumstances.

- Thermopile amplifications: As the output signals from λ_1, λ_2 and reference detectors were so weak, the signals must be pre-amplified, the op-amp used for this was the AD8629 from Analog Devices [C4.49]. Because λ_1 signal was too small ($V_{in_{\lambda_1}}$=6.4µV), the signal of the output of λ_1 pre-amplifier was connected to another amplifier which was also built from the AD8629. Then, the output from this amplifier and the other two signals of the preamplifiers were linked to three inputs of a multiplexer which was controlled by a micro controller Atmega328 on the Arduino board. The common output of the multiplexer were connected to an OPA320 amplifier [C4.50]. Thus, the OPA320 amplifier was shared by the three signals from the thermopiles. The gain of each signal channel is: $G_{\lambda_1,total}$=106.85dB, $G_{\lambda_2,total}$=86dB, and $G_{reference,total}$= 52dB.
- Multiplexer: The 74HC4051D [C4.51] was used to select one input from the input pins connected to the pre-amplifiers and connect it to the output pin as seen in Figure 4.2. The three selecting pins were controlled by the µC.
- ADC: The ADC was LTC2400 IC [C4.52] which was a 24-bit and was set to work at 4.096V with very low offset (0.5ppm) and noise (0.3ppm). The ADC digitizes the analog signal from

the OPA320 at the sampling rate of 153.6kHz. This digitizer can reach a 23-bit absolute dynamic range of ±223 from a resolution of 0.488µV.

- µC: The µC was an Atmega328 on an Arduino board. This µC controlled the relays, which conveyed electric power to the electrostatic circuit and the vacuum pump. The µC also controlled the pins of the pulsing circuit and the multiplexer on setting up the timing of the working unit as shown in Figure 4.2. The working sequence and the timing could be described as:

> Phase 1: Turning on the electrostatic (ES) and the pump for 1min to pump 2.5L of the air through the trap chamber for sampling purpose.
>
> Phase 2: Turning on the pulse circuit (Pulse) to supply power to the IR source in 8s to warm up. Set up: m=1, where m is used to monitor the measuring times; n=1, where n=1 is set for the reference thermopile; n=2: λ_1 thermopile; n=3: λ_2 thermopile.
>
> Phase 3: Turning off IR in 4s; simultaneously, connecting the nth thermopile signal to the multiplexer for recording data; keeping reading data from ADC and sending data to a computer.
>
> Phase 4: Turning on IR in 1s. n=n+1;
>
> Phase 5: If n≤3, then back to Phase 3
>
> Phase 6: If m≤ 5, then m=m+1 and reset n=1, back to Phase 3
>
> Phase 7: Resetting m=1 and n=1; resting in 10s before backing to phase 1 again for the next batch.

At a certain point in time, the trap chamber should be completely cleaned by connecting the metal mirror to the ground by a relay in 3 second to remove any electrostatic left. The cleaning pump is then turned on in 1 minute or longer to clean the sample in the trap. After that, the system should be standardized again to eliminate the effect of any sample residue. Experiment has shown that the pump can clean pretty well the HV trap. The timing and the measurement mechanism can be adjusted to observe and to find optimum performance.

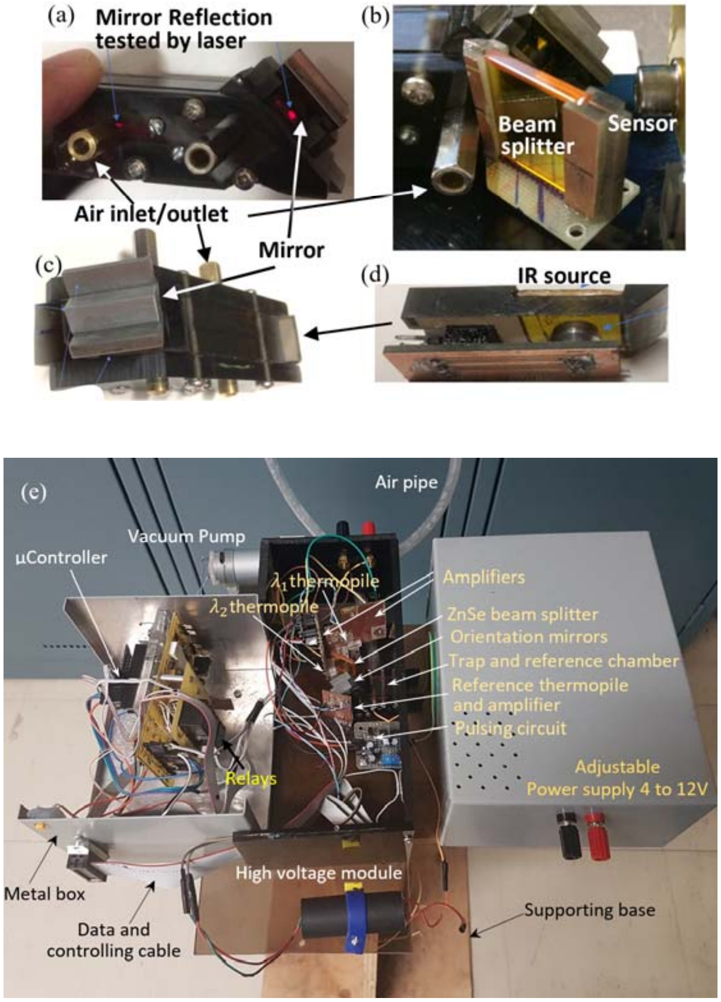

Figure 4.4. Structure of the modules and complete system. (a) Testing reflection and parallelism of the mirrors in trap and reference chambers; (b) Close view of ZnSe beam splitter and λ_2 thermopile; (c) Outer view of the detecting device; (d) IR source structure; (e) Inner structure of the entire analyzing system

4.3.2. Analyzing formula

Beer Lambert law [C4.53] is crucial in this work. There are several transformed forms of the law. In this project, the transmittance definition was used, and it was modified to meet the practical purpose without losing the meaning of the law:

$$T = \frac{P_\lambda}{P_{o,\lambda}} = 10^{-\varepsilon_\lambda . D . S} \tag{4.3}$$

where: $P_{o,\lambda}$: IR radiant power of the light source (W/sr)

P_λ: IR power of the light going through a sample (W/sr)

ε_λ: Extinction coefficient (1/obj.)

D: Sample density (obj./cm2)

S: Area of the sample (cm2)

obj.: Object is studied and caught on S area.

$P_{o,\lambda}$ and P_λ were measured by the thermopiles. From Figure 4.2 and the definition, if $P_{o,\lambda}$ is considered as the IR radiant power of the light source, then the reflection coefficient of the silver-coated mirrors and transmission coefficient of the ZnSe filters must equal to 1 to let the thermopiles transform the total $P_{o,\lambda}$ into a certain voltage. Obviously, in practice, the coefficients are always less than unity.

The substances have their own typical absorbance factors responding to different IR wavelengths, so it is convenient to build up a NDIR system to detect them. However, as mentioned, to detect Fusarium, it needs at least two wavelengths to determine the distinction factor from other different substances. Supposing that a certain substance is caught by the trap, at two certain IR wavelengths, λ_1 and λ_2, the tranmission T_{λ_1} and T_{λ_2} can be found:

$$T_{\lambda_1} = \frac{P_{\lambda_1}}{P_{o,\lambda_1}} = 10^{-\varepsilon_{\lambda_1}.D.S}$$

$$T_{\lambda_2} = \frac{P_{\lambda_2}}{P_{o,\lambda_2}} = 10^{-\varepsilon_{\lambda_2}.D.S}$$

After transformation, a factor can be defined as:

$$\eta = \frac{\varepsilon_{\lambda_1}}{\varepsilon_{\lambda_2}} = \frac{\log\left(\frac{P_{\lambda_1}}{P_{o,\lambda_1}}\right)}{\log\left(\frac{P_{\lambda_2}}{P_{o,\lambda_2}}\right)} \tag{4.4}$$

Because, ε_{λ_1} and ε_{λ_2} are constant, so η=constant. Theoretically, with a group of investigated substances and appropriately chosen λ_1 and λ_2, the ratio of $\eta = \frac{\varepsilon_{\lambda_1}}{\varepsilon_{\lambda_2}}$ of the substance can be differentiate from other substances. Thus η can be defined as a distinct factor of a group, or for conciseness, η is named as group-distinction factor.

On the other hand, from Beer-Lambert law, the density D of a sample can also be determined. First, D of the sample was determined by a microscope. Then, T_{λ_1} was calculated by using P_{λ_1} (or P_{λ_2}) and P_{o,λ_1} (or P_{o,λ_2}) which were measured by λ_1 thermopile (or λ_2 thermopile). Thus:

$$\varepsilon_{\lambda_1} = -\frac{\log\left(\frac{P_{\lambda_1}}{P_{o,\lambda_1}}\right)}{D*S} \tag{4.5}$$

Now, with an unknown density Dx of the sample, the density can be determined by the formula:

$$D_x = \frac{\log\left(\frac{P_{x,\lambda_1}}{P_{xo,\lambda_1}}\right)}{\varepsilon_{\lambda_1} * S} = D^* \frac{\log\left(\frac{P_{x,\lambda_1}}{P_{xo,\lambda_1}}\right)}{\log\left(\frac{P_{\lambda_1}}{P_{o,\lambda_1}}\right)}$$

4.3.3. Data processing

There are bias currents at the inputs of the amplifiers and the internal resistors in the thermopiles. The currents going through the internal resistors cause DC offset voltages at the inputs of the amplifiers. Moreover, due to the high gains and tolerant values of the resistors, the gains of the amplifiers are not stable. As a result, the DC outputs are unstable and influence the output signals of the amplifiers. Therefore, the DC voltages are considered as DC errors. On the other hand, noise caused by the amplifiers, the ADC, and crosstalk from the nearby wires also contribute to the challenge in data processing. Data processing techniques can be used to correct the data under the influenced by the DC error.

From the previous descriptions, when a certain sample stable data sets are analyzed, η should be a constant (i.e., does not variate from the mean value). Data processing technique is not presented here since this article just focuses on hardware design and detection mechanism. Thus, the results introduced here are used to prove the proposed hypothesis that η=constant and it is group-distinction coefficient.

4.3.4. Testing material

There are around seventy Fusarium species and it is not an easy task in distinguishing them [C4.5]. F. oxysporum is a cosmopolitan bio-object which was the main subject in this work. From [C4.5, C4.16, C4.54], the rotten garlic are mainly affected by F. proliferatum, F. culmorum, and F. oxysporum, among which F. proliferatum causes bulb rot, and the other two cause basal rot. Based on these features, rotten garlic bulbs were collected and their fungi were transmitted onto Potato dextrose Agar (PDA) Petri dishes which were prepared by a procedure described in The Fusarium Laboratory Manual [C4.5]. The dishes were placed in a handmade inoculation chamber for nurture and safety purposes. After 2-4 weeks, Fusarium samples were at their mature state. Using the microscope, the following fungi were distinguished: F. culmorum (Macroconidia: around 25µm wide and straight shape, from orange to brown colour; Microconidia: lack) and F. oxysporum

(Macroconidia: around 50 µm wide and straight shape, from white to pale violet colour; Microconidia: oval, elliptical or kidney shape, and plenty of false head on short monophialides) [C4.5].

At the mature state, the hyphae of F. oxysporum produces abundant Chlamydospores (Chl.) on PDA surface. The absorption spectrum of the Chl. is shown in Fig 1(b). In the experiments, the F. oxysporum Chl. was used as it is easy to manually transfer the spores into the device through a funnel. Figure 4.5 shows the microscopic photographs of the hyphae and the F. oxysporum Chl. after 4 weeks of nurturing. Figure 4.5(b) and 4.5(c) show Chlamydospores and their size between 15µm to 20µm.

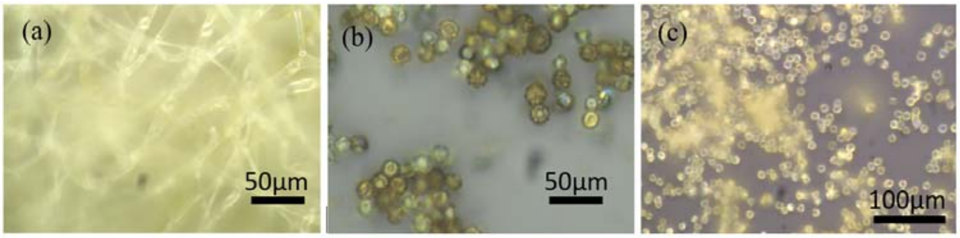

Figure 4.5. F. oxysporum's photos. (a): Hyphae; (b) and (c): Chl. photos at different scales.

As shown in Figure 4.1(b), the two typical wavelengths are λ_1=6.088µm (ν1=1,054cm-1), λ_2=9.487µm (ν1=1,642cm-1) for Fusarium detection purpose. As mentioned in the previous section, other substances should be involved in the test to verify if the bio-device can differentiate F. oxysporum from the other chosen substances. The selected substances include sunflower pollen, turmeric, and starch powders. Thus, there were totally five data categories for samples and no-sample. In the four data categories of samples, each one had more data sub-categories which were recorded at different sample densities.

4.4. Results and Discussions

The output data from the ADC are not only related to the incident power, P_{inc}, but also to the DC error and noise. After data processing to remove DC error, P_{inc} can be calculated from its digital output, N_{dig} , by:

$$P_{inc} = \frac{N_{dig} * resolution(\mu V)}{Respontivity(V/W) * Gain} \text{ (Watt)}$$

4.4.1 Device test

The testing procedure is introduced here. First, the data were collected in without-sample and with samples. Figure 4.6 shows five patches of data that were measured without sample. It can be seen that the DC errors or the backgrounds of λ_1 and λ_2 thermopiles were not steady. As a result, the outputs at the final amplifier of $\lambda_1$and λ_2 thermopiles varied due to DC errors. This introduced more challenges to process and retrieve useful information from the collected data. The noise and DC error of each type of signal can be calculated from the recorded data. As previously mentioned, the processing data approach is not presented in this paper.

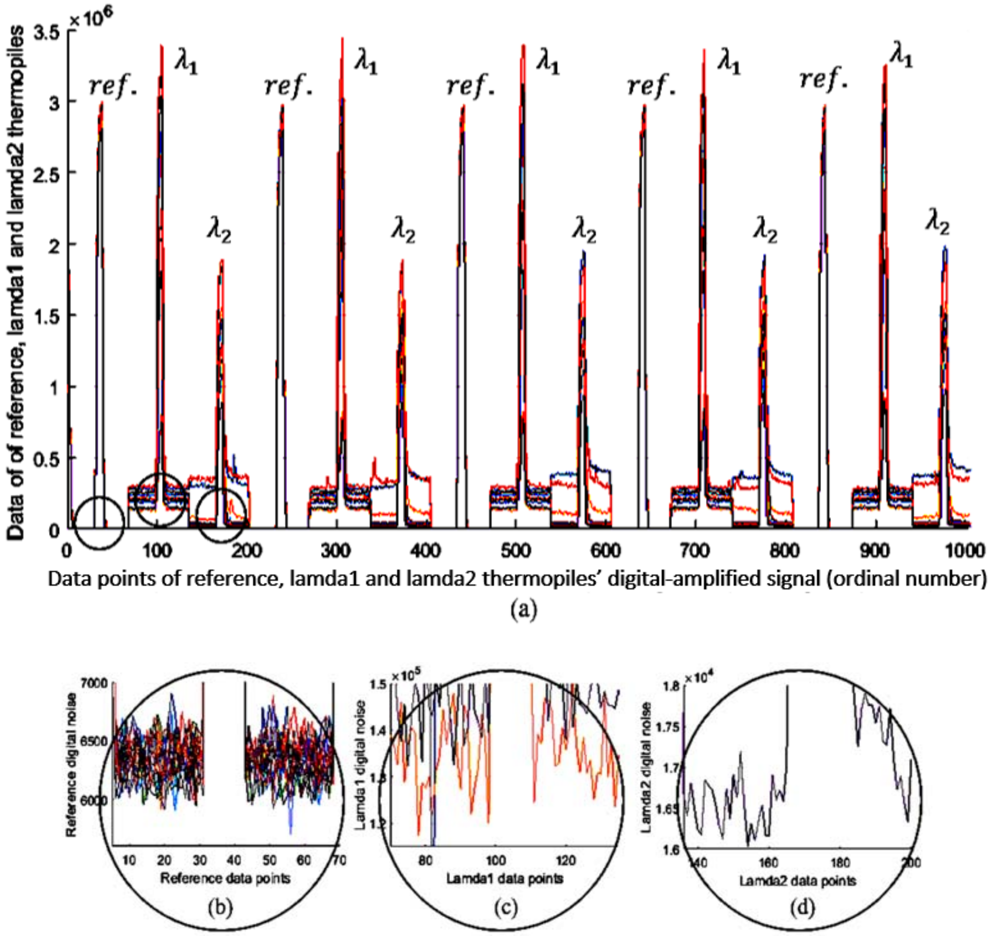

Figure 4.6. Collected data from the three thermopiles in case of no-sample. (a): measurement patches of five data groups. Each group includes data from each thermopile; (b): Noise and DC background of the reference thermopile; (c): Noise and DC background of λ_1 thermopile; (d): Noise and DC background of λ_2 thermopile.

4.4.2. Sample test

- Background data and peak data correlation

The total output at the final amplifiers varies with the change in DC error and background. By viewing the data in many cases to learn the movement laws of the amplifier outputs of λ_1 and λ_2 thermopile, it can help to reduce error in data. Four typical data of the four samples are introduced. Figure 4.7 shows the peak data and DC errors measured in the four cases of F. oxysporum, pollen, turmeric, and starch. The left plots of Figure 4.7(a), (b), (c) and (d) belong to the reference thermopile. In this case, it can be seen there was no correlation between peaks and DC errors. The middle and right plots of Figure 4.7(a), (b), (c) and (d) belong to λ_1 and λ_2 thermopiles. In these cases, there are clear correlations between the peaks and the DC errors.

Table 4.1 provides the correlation values between peaks and DC errors of the mentioned cases above. It supports for the upper statements. These values were calculated based on the practical data of Figure 4.7.

Table 4.1. Correlation factors of the samples

Samples	Reference correlation	$\boldsymbol{\lambda_1}$ correlation	$\boldsymbol{\lambda_2}$ correlation
Fusarium	-0.2014	0.9577	0.9673
Pollen	0.5945	0.9914	0.9935
Starch	-0.0201	0.9883	0.9581
Turmeric	-0.0028	0.9660	0.9764

In the reference correlation column of Table 4.1, except the pollen case, the other show that there was no correlation with negative values. That exception is caused by the outliers due to DC error. The outliers can be eliminated by data processing. The strong correlation in the cases of $\lambda_1$and λ_2 can help to correct data which were affected by the DC error.

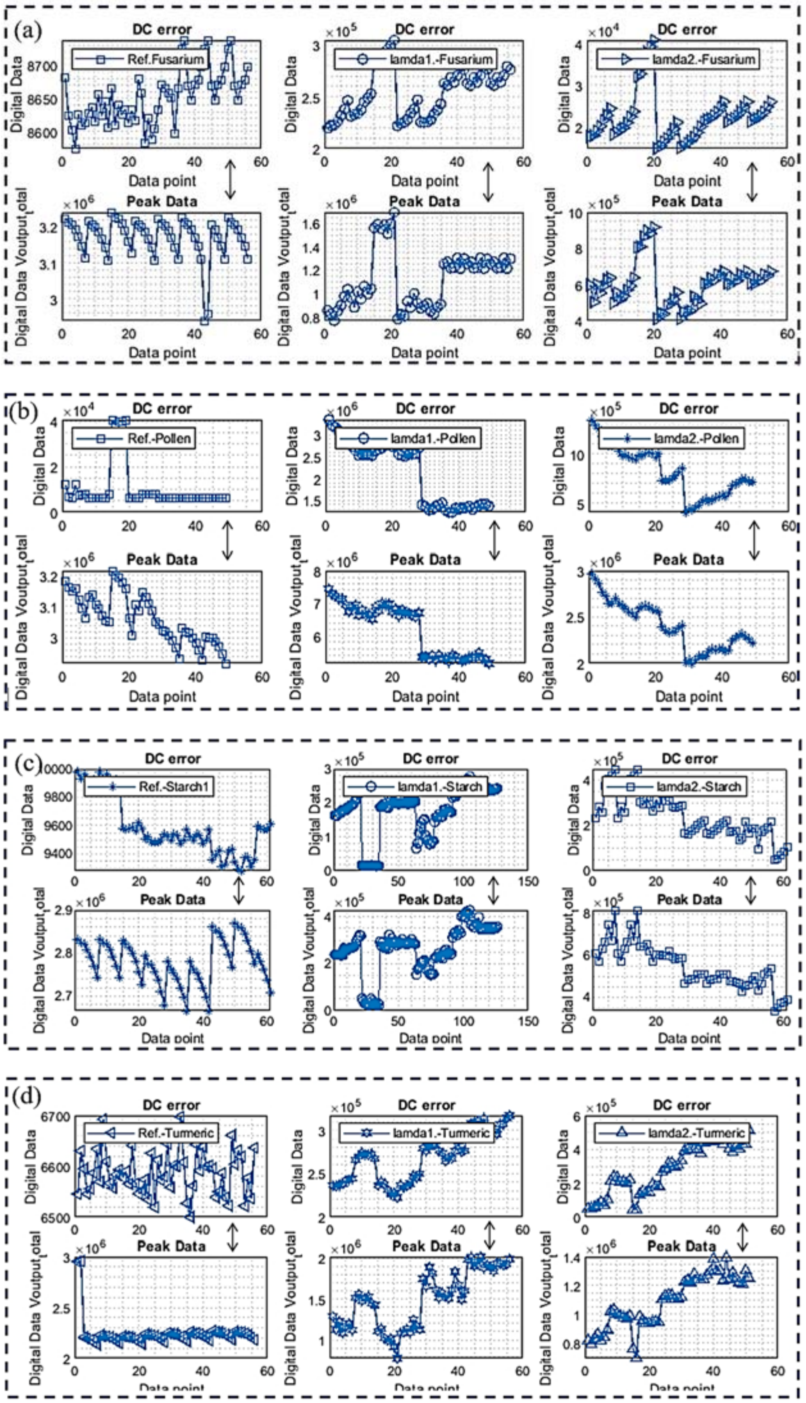

Figure 4.7. DC error and peak data correlation corresponding the four types of samples which are studied. (a): Fusarium (left: reference thermopile; middle: $\lambda_1$thermopile; right: $\lambda_2$thermopile); (b): Pollen (left: reference thermopile; middle: $\lambda_1$thermopile; right: $\lambda_2$thermopile); (c): Starch (left: reference thermopile; middle: $\lambda_1$thermopile; right: $\lambda_2$thermopile); (d): Turmeric (left: reference thermopile; middle: $\lambda_1$thermopile; right: $\lambda_2$thermopile);

As mentioned briefly in Data processing, there was a correlation among the change of average DC values and the peak data. Knowing the relationship between the DC error and the peak data can help to fix data with error. Figure 4.8 depicts the plots of the uncorrected and corrected data in the cases of F. oxysporum, pollen, starch and turmeric. It can be seen that the correction was effective. The corrected data now can be used in analysis. Table 4.2 shows η and its errors from the corrected data. The relative error of η of pollen sample case was large, because η and the absolute error were close to each other. The parameters in the table were extracted from the definition (4.4) of η:

$$\eta = \frac{\log\left(\frac{P_{\lambda_1}}{P_{o,\lambda_1}}\right)}{\log\left(\frac{P_{\lambda_2}}{P_{o,\lambda_2}}\right)} = \frac{x_1}{x_2}$$

so:

$$\varepsilon_\eta = \frac{\frac{\Delta P_{\lambda_1}}{P_{\lambda_1}} + \frac{\Delta P_{o,\lambda_1}}{P_{o,\lambda_1}}}{x_1} + \frac{\frac{\Delta P_{\lambda_2}}{P_{\lambda_2}} + \frac{\Delta P_{o,\lambda_2}}{P_{o,\lambda_2}}}{x_2}$$

Here, the total absolute error of the direct measurement of the quantity P_{λ_1} (or: P_{o,λ_1}, P_{λ_2}, P_{o,λ_2}) was calculated by:

$$\overline{\Delta P_{\lambda_1}} = \frac{1}{N}\sum_{i=1}^{N} \Delta P_{\lambda_{1i}}$$

where:

$$\Delta P_{\lambda_{1i}} = \left| P_{\lambda_{1i}} - \overline{P_{\lambda_1}} \right|$$

and:

$$\overline{P_{\lambda_1}} = \frac{1}{N}\sum_{i=1}^{N} P_{\lambda_{1i}}$$

$\Delta P_{\lambda_{1i}}$ is the absolute error at the ith measurement of P_{λ_1}, and $\overline{P_{\lambda_1}}$ is the mean value of N measurement times of P_{λ_1}.

Table 4.2. **η** values and its errors of the samples

Samples	**η**	±Δ**η**	$\boldsymbol{\varepsilon_\eta}$(%)
Fusarium	1.144	0.153	9.54
Pollen	0.136	0.116	85.0
Starch	0.939	0.0732	7.8
Turmeric	0.794	0.1387	17.5

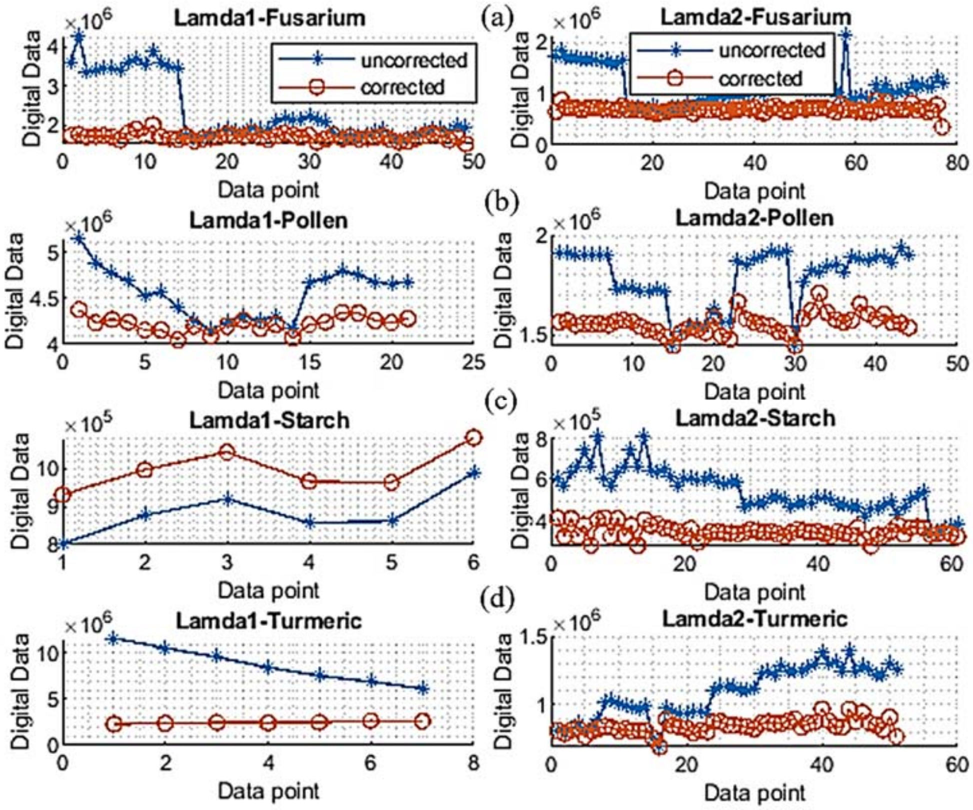

Figure 4.8. Illustration of uncorrected data and corrected data. (a): λ1 and λ2 data of Fusarium sample case; (b): λ1 and λ2 data of Pollen sample; (c): λ1 and λ2 data of Starch sample; (d): λ1 and λ2 data of Turmeric sample.

Figure 4.9 is the visualization of Table 4.2. From the table and the bar chart, it can be seen that the group-distinction coefficients are different from each other. It proves that the device can successfully distinguish F. oxysporum from the other substances.

Now, let's name N_i=$D_i.S$, where D_i is spore density of F. oxysporum at the i^{th} experiment, S is mirror areas (there are two mirrors, top and bottom), and Ni is the number of spores on the mirrors or in the trap chamber. The plots in Figure 4.10 were plotted from Table 4.3. The plots have proven that the data successfully satisfy Beer-Lambert law. When Ni changes, x_1 and x_2 must also change. The correlation of x_1 and x_2 is 0.9986. Thus, based on the Beer-Lambert law, the amount of *Fusarium oxysporum* can be determined by either λ_1 signal, λ_2 signal, or combination of the two thermopiles to increase precison.

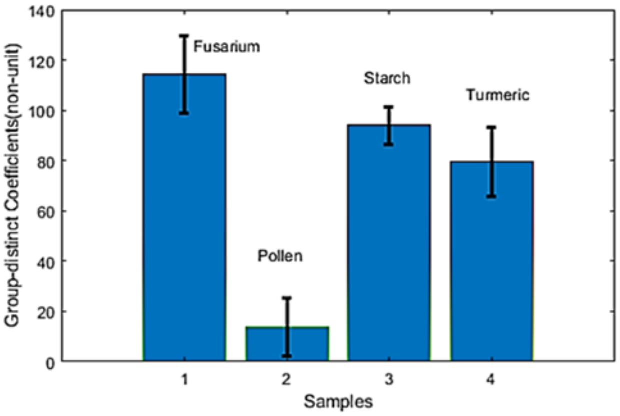

Figure 4.9. Bar chart of the distinct coefficients of the studied samples.

Table 4.3. $\boldsymbol{x_1}$, $\boldsymbol{x_2}$, their absolute errors and *Ni*

i	Ni	x_1	$\pm\Delta x_1$	x_2	$\pm\Delta x_2$
1	2.545*105	-0.5101	0.0325	-0.3501	0.0487
2	3.82*105	-0.7849	0.0610	-0.6482	0.0914
3	5.09*105	-0.9404	0.0272	-0.7636	0.0707
4	10.18*105	-2.0936	0.1411	-1.6924	0.1229

From the study on Fusarium long distance dispersal in corn fields in American [C4.19], the min and max values of the Fusarium spore densities in different months are D_{min}=6*104/L and D_{max}=271*104/L. The total time for a measurement patch is T=135s and the vacuum pump effectiveness is 2.5L/min. Based on Figure 4.10, one can set up that the system will give alert at N_{alert}=2.5*105 spores in the trap. In case of D_{min}, Table 4.4 shows that after around 270s the device can give alert. In case of D_{max}, Table 4.4 shows that after 135s the device will give alert.

Table 4.4. Alert time

	D_{min}=6*104/L		D_{max}=271*104/L		Time
i	N_i*	Alert	Ni**	Alert	
1	1.5*105<N_{alert}	No	67.7*105> N_{alert}	Yes	135s
2	3*105> N_{alert}	Yes	135.5*105>>N_{alert}	Yes	270s

N_i*=i*2.5L*D_{min}; N_i **=i*2.5L*D_{max}.

4.4.3. Discussions

Although, there is a very small interference between the distinct coefficients of Fusarium and starch sample, with a higher number of measuring patches, the device can accurately identify which object is present in the trap. Besides, in the experiments, starch and turmeric were added to test the ability of the device, they are barely existing in the fields. In the wheat field, either Fusarium spores and/or pollens can be present. In this case, distinguishing Fusarium spores and pollen is much easier as illustrated in Figure 4.9.

Results from the last two figures show that the system can also determine the number of F. oxysporum Chl. in the trap. If the extinction coefficient (ε_λ) is known ahead by experiments, then the estimation of $\log\left(\frac{P_\lambda}{P_{o,\lambda}}\right)$ will help to determine the spore number or spore density (Di=Ni/S). Thus, this feature possibly empowers the device to provide density information that is more meaningful.

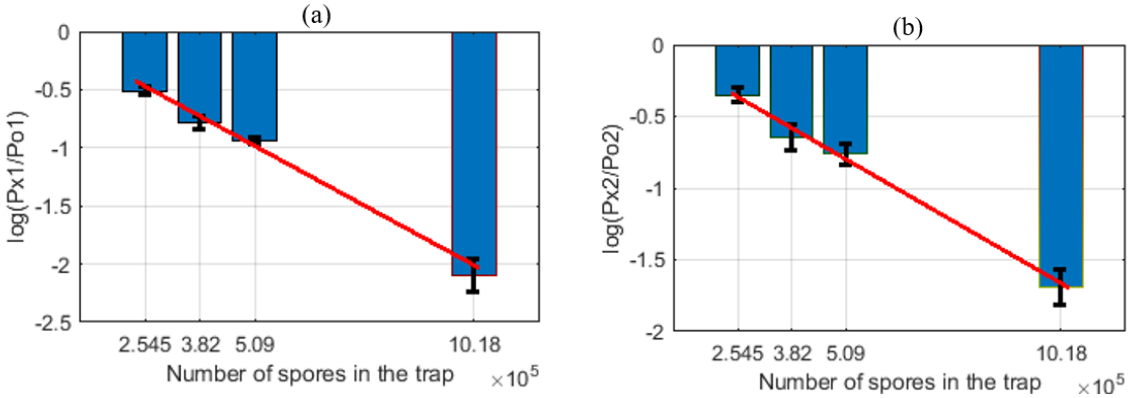

Figure 4.10. (a): Plot of the relation of number of F. oxyporum spores in the trap and x1; (b): Plot of the relation of number of F. oxyporum spores in the trap and x2.

DC errors play a role in the detection of the system. To assist the device working more reliable and providing better results, standard DC values can be determined from the typical bias currents given by the manufacturers of the preamplifiers and/or from the experimental observations.

The reflecting mirrors in the trap chamber and the reference chamber also contribute in the sensitivity of the device. First, the mechanism of the detection is based on the difference among the incident IR power which a thermopile can receive in case of no-sample ($P_{o,\lambda}$) and with sample (P_λ). With an unchanged sample density, the greater number of times that the IR light reflects on the mirrors, the more difference the IR powers are. This poses a limitation on the length of the mirrors. With a long mirror length, the IR light is extremely weak when it lands on the detectors.

At a certain time, the trap needs to be cleaned, and IR power of incident light to the thermopile should be standardized to eliminate the influence of potential residue samples. The time when the trap needs to be cleaned can be determined by monitoring the signal level in the chamber.

Processing the recorded data is complex because of the high gain, DC error, and noise. Therefore, the careful selection of amplifiers and other components are essential to mitigate DC error and noise.

Note that the two chosen wavelengths are based on not only the F. oxysporum Chl. absorption spectrum but also on the atmosphere spectrum to avoid undesired IR interference from the air.

This method can be applied for other bio-objects detection with appropriate light spectrum, light source, and detectors. The device was tested in the laboratory environment to measure the samples. In the field environment including high air temperature and humidity, the system should operate normally with the chosen components and parts when the modules were built. There are some unexpected spikes from the data which cannot be explained at this time; this may occur only on this first prototype. However, these can be easily eliminated by using simple data processing techniques.

4.5. Conclusions

To protect crops from threat of dangerous fungal pathogen, an early detecting approach for Fusarium spores in the air was proposed and tested. This study provides a new approach in detecting based on group-distinction coefficient, $\eta=\frac{\varepsilon_{\lambda_1}}{\varepsilon_{\lambda_2}}$. This factor is defined from Beer-Lambert law. One can see that η is the key for the successful work of the system and the detection mechanism has not been previously developed. The experimental results prove that the system can distinguish F. oxysporum from other samples. As far as the idea of using NDIR detectors, electrostatic and AAS to detect Fusarium is concerned, the system differs from other existing biosensor methods.

The NDIR device is portable, reliable, and affordable which can quickly and consecutively sense the presence of Fusarium spore in the atmosphere. The recent reviews on biosensor trends published in 2016 [C4.55] and in 2018 [C4.56] describe many types of sensors. A common feature of these biosensors is that they require bio-receptors (antibodies, enzymes, nucleic acids, organelles, etc.) which is used to catch the target objects. These biosensors also need transducers which transform sensing events into measurable signals. The new approach of this work removes the above tedious tasks and complexities. Stand-alone device with embedded system can be easily installed in the field to monitor the presence of Fusarium. The system can also be connected to IoT ready devices to transfer the data or the results to the cloud for certain agriculture applications.

References

[C4.1] C. Marinach-Patrice *et al.*, "Use of mass spectrometry to identify clinical Fusarium isolates," *Clin. Microbiol. Infect.*, vol. 15, no. 7, pp. 634–642, 2009.

[C4.2] M. Nucci and E. Anaissie, "Fusarium infections in immunocompromised patients," *Clin. Microbiol*. Rev., vol. 20, no. 4, pp. 695–704, 2007.

[C4.3] G. Antonissen et al., "The impact of Fusarium Mycotoxins on human and animal host susceptibility to infectious diseases," *Toxins (Basel).*, vol. 6, no. 2, pp. 430–452, 2014.

[C4.4] Y. Lin et al., "A putative transcription factor MYT2 regulates perithecium size in the Ascomycete Gibberella zeae," *PLoS One*, vol. 7, no. 5, 2012.

[C4.5] F. Leslie, B. A. Summerell and S. Bullock, *The Fusarium Laboratory Manual*. Iowa Blacwell, 2006, https://doi.org/10.1371/journal.pone.0037859.

[C4.6] A. Peraldi, G. Beccari, A. Steed, and P. Nicholson, "Brachypodium distachyon: A new pathosystem to study Fusarium head blight and other Fusarium diseases of wheat," *BMC Plant Biol.*, vol. 11, 2011, https://doi.org/10.1186/1471-2229-11-100.

[C4.7] R. D. Martyn, "Fusarium Wilt of Watermelon: 120 Years of Research," in *Horticultural Reviews: Volume 42*, no. July 2014, J. Janick, Ed. West Lafayette: John Wiley & Son, 2014, pp. 349–442. http://doi.wiley.com/10.1002/9781118916827.ch07

[C4.8] E. D. de Toledo-Souza, P. M. da Silveira, A. C. Café-Filho, and M. Lobo Junior, "Fusarium wilt incidence and common bean yield according to the preceding crop and the soil tillage system," *Pesqui. Agropecu. Bras.*, vol. 47, no. 8, pp. 1031–1037, 2012.

[C4.9] A. Adesemoye et al., "Current knowledge on Fusarium dry rot of citrus," *Citrograph*, no. December, pp. 29–33, 2011.

[C4.10] N. A. Foroud, S. Chatterton, L. M. Reid, T. K. Turkington, S. A. Tittlemier, and T. Gräfenhan," Fusarium Diseases of Canadian Grain Crops: Impact and Disease Management Strategies," in *Future Challenges in Crop Protection Against Fungal Pathogens*, New York, 2014, pp. 267-316.

[C4.11] E. Bauriegel, A. Giebel, and W. B. Herppich, "Rapid Fusarium head blight detection on winter wheat ears using chlorophyll fluorescence imaging," *J. Appl. Bot. Food Qual.*, vol. 83, no. 2, pp. 196–203, 2010.

[C4.12] M. Haidukowski et al., "Effect of prothioconazole-based fungicides on Fusarium head blight, grain yield and deoxynivalenol accumulation in wheat under field conditions," *Phytopathol*. Mediterr., vol. 51, no. 1, pp. 236–246, 2012.

[C4.13] J. S. West, G. G. M. Canning, S. A. Perryman, and K. King, "Novel Technologies for the detection of Fusarium head blight disease and airborne inoculum," *Trop. Plant Pathol.*, vol. 42, no. 3, pp. 203–209, 2017.

[C4.14] M. Marchetti-Deschmann, W. Winkler, H. Dong, H. Lohninger, C. P. Kubicek, and G. Allmaier, "Using spores for Fusarium spp. Classification by MALDI-based intact cell/spore mass spectrometry," *Food Technol. Biotechnol.*, vol. 50, no. 3, pp. 334–342, 2012.

[C4.15] A. Salman, L. Tsror, A. Pomerantz, R. Moreh, S. Mordechai, and M. Huleihel, "FTIR spectroscopy for detection and identification of fungal phytopathogenes," *Spectroscopy*, vol. 24, no. 3–4, pp. 261–267, 2010.

[C4.16] E. Tamburini, E. Mamolini, M. De Bastiani, and M. G. Marchetti, "Quantitative determination of Fusarium proliferatum concentration in intact garlic cloves using near-infrared spectroscopy," *Sensors (Switzerland)*, vol. 16, no. 7, doi: 10.3390/s16071099, 2016.

[C4.17] P. P. Vinayaka et al., "An Impedance-Based Mold Sensor with on-Chip Optical Reference," 2016.

[C4.18] C. G. DOBBS, "on the Primary Dispersal and Isolation of Fungal Spores," *New Phytol.*, vol. 41, no. 1, pp. 63–69, 1942.

[C4.19] J. J. Ooka and T. Kommedahl, "Winter and rain dispersal of Fusarium moniliforme in corn fields," *Phytopathology*, vol. 67. pp. 1023–1026, 1977.

[C4.20] J. Lacey and P. H. S. Gregory, “Philip herries gregory (1907–1986),” vol. 25, no. 3, pp. 159–160, 2009.

[C4.21] P. H. Gregory, “Spores In Air,” *Annu. Rev. Phytopathol.*, vol. 15, pp. 1–11, 1977.

[C4.22] P. H. Gregory, E. J. Guthrie, and M. E. Bunce, “Experiments on Splash Dispersal of Fungus Spores,” *Microbiol*, vol. 20, no. 1959, pp. 328–354, 1959.

[C4.23] M. D. Keller, G. Bergstrom, G. C. Bergstrom, and E. J. Shields, “The aerobiology of Fusarium graminearum,” no. November 2015, 2014.

[C4.24] F. Trail, I. Gaffoor, and S. Vogel, “Ejection mechanics and trajectory of the ascospores of Gibberella zeae (anamorph Fuarium graminearum),” vol. 42, pp. 528–533, 2005.

[C4.25] F. Cheli, S. Giappino, L. Rosa, G. Tomasini, and M. Villani, “Journal of Wind Engineering Experimental study on the aerodynamic forces on railway vehicles in presence of turbulence,” *Jnl. Wind Eng. Ind. Aerodyn.*, vol. 123, pp. 311–316, 2013.

[C4.26] I. Gouttevin, M. Lehning, D. Gustafsson, and S. Meteorological, “A two-layer canopy model with thermal inertia for an improved snowpack energy balance below needleleaf forest,” *Trends Anal. Chem.*, no. January, pp. 2379-2398, 2016.

[C4.27] T. Go´recki and J. Namies´nik, “Passive sampling,” vol. 21, no. 4, pp. 276–291, 2002.

[C4.28] S. J. Hayward, T. Gouin, and F. Wania, “Comparison of Four Active and Passive Sampling Techniques for Pesticides in Air,” *Environ. Sci. Technol.*, vol. 44, no. 9, pp. 3410–3416, 2010.

[C4.29] A. Bednarz and S. Pawłowska, “A fungal spore calendar for the atmosphere of Szczecin, Poland,” *Acta Agrobot.*, vol. 69, no. 3, pp. 1–9, 2016.

[C4.30] D. M. Gadoury, “A 7-Day Recording Volumetric Spore Trap,” *Phytopathology*, vol. 73, no. 11, p. 1526, 1983.

[C4.31] T. Sandle, “Selection of active air samplers,” European Journal of Parenteral and Pharmaceutical Sciences 15(4):119-124, 2010.

[C4.32] EMSL Analytica Inc., “Microbiology Sampling Guide,” 2014.

[C4.33] J. Guijarro, M. Engelhard, and F. Siebert, “Anion Uptake in Halorhodopsin from Natromonas pharaonis Studied by FTIR Spectroscopy: Consequences for the Anion Transport Mechanism †,” pp. 11578–11588, 2006.

[C4.34] Y. Chen, C. Zou, M. Mastalerz, S. Hu, and C. Gasaway, “Applications of Micro-Fourier Transform Infrared Spectroscopy (FTIR) in the Geological Sciences — A Review,” pp. 30223–30250, 2015.

[C4.35] Z. Yunusa, “Sensors & Transducers Gas Sensors: A Review,” Sensors and Transducers Journal, vol. 168, issue 4, pp. 61-75, 2014.

[C4.36] X. Liu *et al*., “A Survey on Gas Sensing Technology,” Sonsors, MDPI, 12(7), pp. 9635–9665, 2012.

[C4.37] N. Gupta and M. C. Chattopadhyaya, “Dynamics of adsorption of Ni (II), Co (II) and Cu (II) from aqueous solution onto newly synthesized poly [N- (4- [4- (aminophenyl) methylphenylmethacrylamide])],” Arabian Journal of Chemistry, 170(S2), doi: 10.1016/j.arabjc.2013.06.007, 2013.

[C4.38] Thorlab, “45° AOI Beamsplitter Compensation Plates, UV Fused Silica for UV to NIR,” *ThorLabs*. [Online]. Available: https://www.thorlabs.com.

[C4.39] Northumbria Optical, “Narrow Band Pass,” 2018.

[C4.40] P. Ghosh, “van der Waals Forces: Part I,” in NPTEL - *Chemical Engineering - Interfacial Engineering*, Guwahati.

[C4.41] Vishay Siliconix, “Power MOSFET, IRFD9120, SiHFD9120 datasheet, Oct. 2010.

[C4.42] Micro-Hybrid, “Infrared Radiation Source JSIR350-4-AL-C-D3.7-A5-I,” 2014. Available: www.eoc-inc.com/micro-hybrid/IRSource/JSIR350-4-AL-C-D3.7-A5-l.pdf%0A.

[C4.43] C. Koike, H. Hasegawa, and A. Manabe, “Extinction coefficients of amorphous carbon grains from 2100 Å to 340 μ m,” Astrophysics and Space Science, vol. 67, issue 2, pp. 495-502, 1980.

[C4.44] C. Johnson, *Mathematical Physics of BlackBody Radiation*, http://www.csc.kth.se/~cgjoh/blackbodyslayer.pdf, 2012.

[C4.45] Dexter Research Center, “2M Thin Film Based Thermopile Detector.” [Online]. Available: https://www.dexterresearch.com/?module=Page&sID=2m.

[C4.46] V. Mackowiak, J. Peupelmann, Y. Ma, and A. Gorges, “NEP – Noise Equivalent Power,” *Thorlabs*.

[C4.47] S. Leclercq, “Discussion about Noise Equivalent Power and its use for photon noise calculation,” http://www.iram.fr/~leclercq/Reports/About_NEP_photon_noise.pdf, 2007.

[C4.48] Hamamatsu, Thermal detectors. [Online]. Available: https://www.hamamatsu.com/resources/pdf/ssd/e07_handbook_Thermal_detectors.pdf

[C4.49] Analog Devices, “Zero-Drift, Single-Supply, Rail-to-Rail Input/Output Operational Amplifier AD8628/AD8629/AD8630,” AD8628/AD8629/AD8630 datasheet.

[C4.50] Texas Instruments, “OPAx320x Precision, 20-MHz, 0.9-pA, Low-Noise, RRIO, CMOS Operational Amplifier with Shutdown 1,” OPAx320 datasheet, 2016.

[C4.51] Toshiba, “74HC4051; 74HCT4051 8-channel analog multiplexer/demultiplexer,” 74HC4051/74HCT4051 datasheet, 2017 [Revised Sept. 2017].

[C4.52] Linear Technology, “24-Bit µPower No Latency ΔΣTM ADC in SO-8,” LTC2400 datasheet.

[C4.53] J. M. Parnis and K. B. Oldham, “Journal of Photochemistry and Photobiology A : Chemistry Beyond the Beer – Lambert law : The dependence of absorbance on time in photochemistry,” *Journal Photochem. Photobiol. A Chem.*, vol. 267, pp. 6–10, 2013.

[C4.54] M. Masratul Hawa, B. Salleh, and Z. Latiffah, “Characterization and pathogenicity of Fusarium proliferatum causing stem rot of Hylocereus polyrhizus in Malaysia,” A*nn. Appl. Biol.*, vol. 163, no. 2, pp. 269–280, 2013.

[C4.55] P. Mehrotra, “Biosensors and their applications – A review,” *J. Oral Biol. Craniofacial Res*., vol. 6, no. 2, pp. 153–159, 2016.

[C4.56] J. D. D. Habimana, J. Ji, and X. Sun, “Minireview: Trends in Optical-Based Biosensors for Point-Of-Care Bacterial Pathogen Detection for Food Safety and Clinical Diagnostics,” vol. 2719, no. May, 2018.

5. An Air Sampler with Particle Filter Using Innovative Quad-Inlet Cyclone Separator and High Voltage Trap

Published as:

Son Pham, Anh Dinh, “An Air Sampler with Particle Filter Using Innovative Quad-Inlet Cyclone Separator and High Voltage Trap,” *IEEE Sensors Journal*, Vol. 19, Issue: 22, November 2019, pp. 10176-10186.

Sampling the air flowing into the sensing system by applying electrostatic charge also catches undesired particles. These particles can interfere to the *Fusarium* analysis procedure. To reduce the unwanted interference, a quad-inlet cyclone separator was installed at the front of the high voltage trap. These two components form a bandpass particle filter to select only particles having the size of the *Fusarium* spores. In this chapter, the features and parameters of the *Fusarium*, turmeric, and starch were used in simulation. The relative dielectric coefficients of these samples were proposed and used in the simulations. The simulation provided appropriate dimensions of the cyclone separator and high voltage trap. The experiments and results proved the device work as expected. The combination of a cyclone separator and a high voltage trap to form a bandpass particle filter is novel and can be used in any air sampler.

In this manuscript, the main contribution comes from the student (the first author) while the main supervisor provides supervision.

Air Sampler with Particle Filter Using Innovative Quad-Inlet Cyclone Separator and High Voltage Trap

Son Pham, Anh Dinh

Abstract

The air sampler collects all the floating particles in the air. These particles are different in size and it is necessary to retain only the size range of the interested objects in the sampler. With the interest of sampling the Fusarium spores, which have particle diameter range of around 10µm to 70µm, and eliminating particles smaller than 10µm and particles larger than 70µm, in this study, a novel method of combining a quad-inlet cyclone separator and a high voltage trap is proposed. At small size, such cyclone separator is a new design having four inlets to facilitate the cyclone to intake the particles from any direction. The quad-inlet cyclone separator filters away the large size particles (low pass). By applying di-electrophoretic force in the high voltage portion, the trap can eliminate the small size particles (high pass). The combination of these two devices creates a system which works as a particle bandpass filter. To investigate the features as well as to study the appropriate parameters of the cyclone and the trap, the numerical simulations for the trap work have been performed by COMSOL Multiphysics. In the simulations, wheat, turmeric and Fusarium spore objects were investigated. From the simulation, the bandpass ranges of the wheat, turmeric and Fusarium samples are [19.5µm-75µm], [14.5µm-52.5µm] and [15.5µm-67µm], respectively. The experimental results have consolidated that the device can reduce the presence of small size particles, and especially filter well the particles which have size larger than 70µm. In addition, with homogeneous electric field in the HV trap, the sample distribution on the electrodes was fairly smooth which is useful in later quantifying *Fusarium* spores. By using a strong vacuum pump, the internal air sample could be cleaned easily for the next sampling. The designed particle trap can be widely applied in air sampling and analysis applications.

Index Terms— Air sampler, particle trap, cyclone, high voltage, simulation.

5.1. Introduction

Particle size is a significant factor for powders, aerosols, emulsions and suspensions as it influences the material properties such as dissolvability, flowability, penetrability, or viscosity [C5.1]. The size is also a property which assists in determining airborne allergens, pollutants, and pathogens which could be from molds, spores, pollens, flour, dust, smoke, virus or bacteria [C5.1-C5.7]. These airborne particulates are different in size ranges, in which the virus size is from around 0.005μm to 0.09μm [C5.6], or pollen size is from about 9μm to 120μm [C5.8]. If the sizes of investigated airborne objects are in a foreknown range, it is meaningful to build the sampler only samples the particles in the air in the range to mitigate noise interference from the other objects. An air sample is required to collect fungus spores in the field in order to reveal their existence. This is essential in the detection of *Fusarium* (*F.*) spore causing head blight disease in wheat. The size of the spore is in the range which is normally from 10μm to 70μm and a few of them can be around 100μm, such as *Fusarium Equiseti* macroconidia spore [C5.9, C5.10]. Therefore, the sampling device should be able to consecutively work in the range of 10μm to 70μm. In addition, the sampler should be portable and re-usable as the device must be installed in the field.

The air can be sampled by several methods where every method has its own advantages and disadvantages. Sampling devices can be divided into two categories, passive air sampler (PAS) and active air sampler (AAS). According to [C5.11- C5.13], the aerosol particles can be caught by allowing the air flow onto a particular medium which is high viscosity or sticky in a PAS. The advantages of the PASs are cheap and non-electricity, but the temporal resolution of these samplers is low because of their wind dependence and time consuming. On the contrary, an AAS must have at least a supporting electrical device such as vacuum pump [C5.12] or rotating motor [C5.14] which can maintain good resolutions of sampling tempo. One of the disadvantages of AASs is generally more expensive than the PAS. In practice, AASs overwhelm PASs.

To find the appropriate solution for the upper mentioned requirements, in this paper, active air sampling method has been chosen because of the advantages of the AASs. After investigating AASs, the cyclone air sampler has been selected to work as a pre-filter to eliminate the large particles (i.e., low-particle-size-pass filter). The advantage of this one in comparison with the other AASs is that there is no need for adhesive material. Then, based on the ability of electrostatic, a high voltage trap has been designed to work as the high-particle-size-pass filter. Both of the filters work together to collect desired particles in the size range from 10μm to 60μm.

The contents of the paper are setup into five sections. The second section is the background of the method used in the sampling. The third section is the experiment and simulation methods which provides in detail how the experiment and simulation were performed. The fourth section provides results and discussion about the achievement and the challenges in experiment and in simulation. In this section, the results will prove if device can work on the target bandpass. The final section concludes the work.

5.2. Background

In our *Fusarium* detection project, it requires sampling the air and analyzing the air sample [C5.15]. As mentioned above, *Fusarium* spore size range is [10µm - 70µm], the particles which are out of this range should be filtered away. In the air, the aerosol particulates are different in source, type, size and quantity which probably depend on the studied site and time. For instance, in Granada where is the non-industrialized city and located in the southeast of Spain, from March 2006 to February 2007, the authors of the research about aerosol particles in the city found that the quantity of particulate matters (PM) which are finer than 10µm (PM_{10}) and 1µm (PM_1) were not the same in the four seasons (spring, summer, autumn and winter) [C5.16]. Moreover, PM_1/ PM_{10} ratios of these particles generally were smaller than one during the year [C5.16].

Another research in 2006 about "*Trends in primary particulate matter emissions from Canadian agriculture*" pointed out that PM_{10} and $PM_{2.5}$ (particulate matter is finer than 2.5µm) contributed 82% and 76% to PM emission from Canadian agriculture respectively [C5.17]. In addition, in that research, the authors also identified other sources for PM emission. These include activities from wind, harvest, land preparation, animal feeding operations, fertilizer,…, from animal (poultry, pullet, broiler, turkeys, dairy cow …), crops (forage seed, buckwheat, canola, grain corn, silage corn, flaxseed, …) [C5.17]. Furthermore, the research has shown that pollen, spore and bacteria also contribute to PM of the atmosphere.

Therefore, in the application of *Fusarium* detection, it is essential to eliminate PM_{10}, $PM_{2.5}$, bacteria and most of pollen having the size either smaller than 10µm or larger than 60µm. The elimination assists in mitigation the noise interference caused by the above-mentioned PM, but still keep *Fusarium* spore in the system for detection and monitoring. As shown in Figure 5.1, the cyclone separator and high voltage trap are arranged in order and used to sample the air.

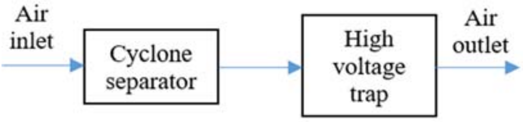

Figure 5.1. Air sampler

5.2.1. Cyclone separator

Two basic forms of cyclone separators are the axial inlet [C5.18] and the tangential inlet [C5.19] separators which are widely used in industry to filter out harmful particles. The cyclone separators also use to clean the air in the house. In these separators, gravity, buoyancy, drag, and centrifugal forces are exerted on the particles [C5.20]. For any type of cyclone, generally, it can be analyzed as the following:

The gravity force, F_G(N), of a particle with diameter d_p(µm), mass m_p(kg) and particle mass density ρ_p(kg/m^3), is:

$$F_G = m_p.g = \frac{\pi d_p^3.\rho_p.g}{6},$$

where, $g = 9.8\text{m/s}^2$ is gravity acceleration.

Buoyancy force (F_B) is caused by the displacement of the air, and F_B resists gravity force: $F_B = m_g.g = \frac{\pi d_p^3.\rho_g.g}{6}$, in which m_g(kg) is the mass of the displaced gas, and $\rho_g = 1.2\text{kg/m}^3$ is the mass density of the air. As ρ_g is practically much smaller than ρ_p, $F_B << F_G$. Thus, F_B can be neglected.

The drag force (F_D) is caused by the interaction of the particle with the gas. This interaction changes the momentum of the particle, so F_D equals to the momentum per unit time by the impartment of the gas:

$$F_D = \frac{A_p.\rho_g.V_p^2.C_D}{2} = \frac{\pi d_p^2.\rho_g.V_p^2.C_D}{8} \tag{5.1}$$

where, $A_p = \frac{\pi d_p^2}{4}$ (m^2) is cross sectional area of the particle; C_D is drag coefficient without unit; $V_p = \frac{\pi d_p^3}{6}$ (m^3) is particle volume. The flow pattern and velocity of the particle can affect the drag coefficient. The flow pattern is defined by dimensionless coefficient Re which is called Reynolds number introduced in chapter 16 in [C5.20] and:

$$\text{Re} = \frac{inertial\ forces}{viscous\ forces} = \frac{d_p.v_p.\rho_g}{\mu_g} \tag{5.2}$$

where, v_p(m/s) is the particle velocity; $\mu_g = 17.9\mu\text{Pa/s}$ is the gas viscosity at 20°C and 101.3kPa [C5.21]. When Re > 1000, the flow of fluids can be sorted into the turbulent or Newton region.

Otherwise, the flow is in the laminar or Stoke region. According to chapter 30 in [C5.20], if $d_p >$ 3μm and Re < 1, then $C_D = 24/\mathrm{Re}$; if 1 < Re < 1000, then $C_D = 18.5/\mathrm{Re}^{0.6}$; if Re > 1000, then $C_D =$ 0.44. In Stoke region, the drag force [C5.21] is:

$$F_D = 3\pi d_p . \mu_g . v_p \tag{5.3}$$

With any type of cyclone separator, the centrifugal force exerted on a particle is determined by the motion curvature (R is radius of the motion curvature), mass (m_p), and tangential velocity (v_t) of the particle in the cyclone:

$$F_C = m_p \frac{{v_t}^2}{R} \tag{5.4}$$

In practice, with a standing cyclone, F_D and F_C are mainly used to analyze the work of cyclone separators as the gravity force is perpendicular to the particle trajectory and the buoyance force is too small. From the feature of F_D and F_C, it can be seen that $\boldsymbol{F_D} \uparrow\downarrow \boldsymbol{F_C}$ [C5.20]. When F_D equals F_C, then $F = F_C - F_D = 0$. Thus, the particle velocity in cyclone is:

$$v_p = \frac{d_p^2 . \rho_p . v_t}{18 \mu_g . R} \tag{5.5}$$

Consequently, the particle velocity moving toward the cyclone wall is proportional to the square of the particle diameter. Therefore, the removal efficiency (DRE) of the cyclone trap is higher when the particle diameter is larger. The definition of DRE [C5.20] is:

$$\mathrm{DRE} = \frac{M_{in} - M_{out}}{M_{in}} \times 100\% \tag{5.6}$$

where, M_{in} and M_{out} are total mass of particle at certain diameter going in and out of the cyclone.

If fine PM which $d_p < 3$μm, then it is necessary to add "*Cunningham coefficient slip correction factor*" (C_C) [C5.20] into equation (5.5): $v_p = \frac{C_C . d_p^2 . \rho_p . v_t}{18 \mu_g . R}$.

In the process flow of the device, the air, after going through the cyclone separator, will enter the high voltage trap.

5.2.2. High voltage trap

Tai et al. [C5.22] suggested to use high voltage (HV) to trap aerosol particulates, or is sometime preferred to use, such as in to sample bacteria. Bowker et al. [C5.23] also used HV to research the electrostatic charge on pollen. In these two examples, the important force influencing on the particulates is the dielectrophoretic force (F_{DEP}). If $\boldsymbol{E}$ is the electric field created by the applied

HV, and there is a particle flowing into the electric field, the F_D exerted on the particle is:

$$F_{DEP} = \pi \frac{d_p^3}{4} \frac{\varepsilon_m(\varepsilon_p - \varepsilon_m)}{\varepsilon_p + 2\varepsilon_m} \nabla |E|^2 \tag{5.7}$$

where, ε_m is the relative dielectric or permittivity of the medium; ε_p is the relative dielectric of the particle [C5.24]. Equation (5.7) is built by an assumption that the particle is spherical with diameter d_p. From the equation, it can be seen that F_{DEP} is proportional to third order of d_p.

5.3. Materials, part design, simulation and experiment

5.3.1. Material

For the test, wheat powder, turmeric powder, and *Fusarium* (*F.*) *oxysporum Chlamydospore* (*Chl.*) were used. The turmeric powder was chosen as its mass density is similar to the *Fusarium* spore density. The wheat powder was chosen as its mass density (657kg/m^3) [C5.25] is pretty different from the mass density of turmeric (1341kg/m^3) [C5.26] and Fusarium spore (1,000kg/m^3) [C5.27]. Thus, it benefits in checking if the results of the simulation and practice are matched with each other. For *Fusarium* sample preparation, *Fusarium oxysporum* hyphae was taken from garlic infected by *Fusarium oxysporum,* and nurtured in Potato Dextrose Agar (PDA) at 25ºC in an incubator [C5.15] for safety [C5.9]. To investigate the particulate size contribution, an OLYMPUS U-MSSP Japan Microscope [C5.28] was used.

5.3.2. Part design and simulation

In the system, the cyclone separator is the prefilter and must be able to pass the particulates with d_p < 70µm to the second stage. Thus, its role is as a low-particle-pass filter (LPPF). The HV trap will be the second stage for the air flow. It will catch the particles with $d_p \geq$ 10µm and eliminate the particles with d_p < 10µm. Therefore, its role is as a high-particle-pass filter (HDPF). To realize a desired structure which can satisfy the above requirements, COMSOL Multiphysics 5.3 software was used to simulate the operation of a cyclone separator and a HV trap. Simulation helps to form the design structure for the parts. The procedure to have final designs for the discussed devices above is as the following steps:

- Step 1: form a temporary simulation structure in the simulation software and run the simulation.
- Step 2: analyze the simulation results to see if the devices can filter undesired particles. If not, then adjusting the diameters of the inlets, outlet and cyclone chamber of the cyclone separator, or the diameters of the inlet, outlet, or the dimensions of interaction chamber of the HV trap.
- Step 3: re-run simulation again, then repeat Step 2 until the results show desired features from the devices.

Before simulations, it is essential to estimate the Reynolds number to know what is the flow region which has to be applied in the simulation. From equation (5.2), the Reynolds number is estimated, and $\mathrm{Re} \approx 1.7 << 1000$, where, $d_p = 10\mu\mathrm{m}$; $v_p = 1\mathrm{m/s}$ is the velocity of the gas, which is an average wind speed in the Province of Saskatchewan, Canada [C5.29, C5.30]. Thus, in this case, the particle flows in the Stoke region. The *Single-Phase Laminar Flow* (SPLF) physics module was deployed in the simulations for both types of the devices. The air was compressible with $\mathrm{Ma} < 0.3$ which was the condition applied in the simulation; Ma is the Mach number and is the ratio of local flow velocity and the speed of sound in the medium [C5.31, C5.32]. Actually, as $\mathrm{Ma} < 0.3$, either incompressible or compressible conditions can be applied for this simulation [C5.32].

- *Cyclone separator*: We define $d_{\mathrm{High},\,50} = 70\mu\mathrm{m}$ as the cut-off particle diameter at which the number of 70μm particles at the outlet is half of the number of that particles at the inlet. From equation (5.3), (5.4) and (5.5), $d_{\mathrm{High},\,50}$ can be affected by the curvature trajectory radius, gas velocity, gas viscosity or mass of particle. The gas velocity, pressure at the inlet and pressure at the outlet are selected or calculated by referencing the parameters of the vacuum pump which is a 2.5L/min and 12V pump, or the practical parameters, such as the velocity of the cyclone inlets, $v = 1\mathrm{m/s}$. This velocity value was based on the wind speed in [C5.29, C5.30]. In this application, to achieve the desired $d_{\mathrm{High},\,50}$, the factors which were adjusted are the radius of the cyclone chamber, and the dimensions of the inlets and outlet. As mentioned before, the cyclone was designed to have four inlets located at four different directions which could receive the air sample from any direction. To study the particle trajectory, the *Particle Tracing for Fluid Flow* (PTFL) module was used. From the simulation, the final structure and the practical design are shown in Figure 5.2. Figure 5.2(a), (c) and (d) show the simulation structure, and Figure 5.2(b) is the experimental part built by the Prusa i3 MK3 3D printer. To have a printable version, the simulated cyclone structure was modified to add outer layers, because in the simulation, the thickness was zero.

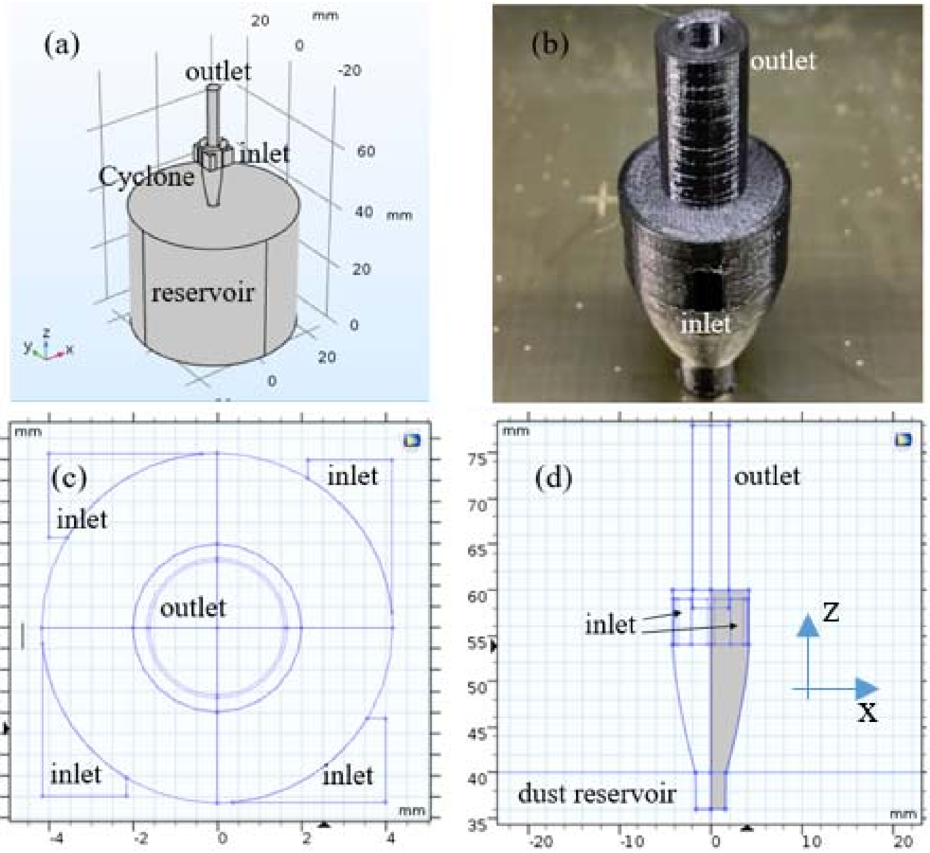

Figure 5.2. Quad-inlet cyclone simulation and its structures. (a): 3D simulation view of the cyclone separator and its reservoir; (b): the cyclone printed by a 3D printer; (c): projection of the quad-inlet cyclone on the x-y plane; (d): projection of the quad-inlet cyclone on the x-z plane.

- *High voltage trap*: $d_{Low, 50}$ = 10µm is defined as the low-cut-off diameter for the trap. Adjusting the high voltage applied onto the electrodes or the dimensions of the trap can influence on $d_{Low, 50}$. In the design, the height of the HV trap is limited to maximum around 5mm. The electric field inside the trap is simulated by *Electric Currents* (EC) module.

The HV was set at 10kV. The SPLF module in COMSOL was used to investigate the velocity and pressure of the gas and the PTFL module was used to study the particle trajectory. After simulations, the appropriate dimensions of the trap were found. Figure 5.3(a), (c) and (d) shows the simulation view and the dimensions of the trap. Figure 5.3(b) is the prototype version for the experiment. It was made from Poly methyl methacrylate plates and epoxy resin to form the HV chamber. The bottom and top electrodes were simply made from the printed circuit board.

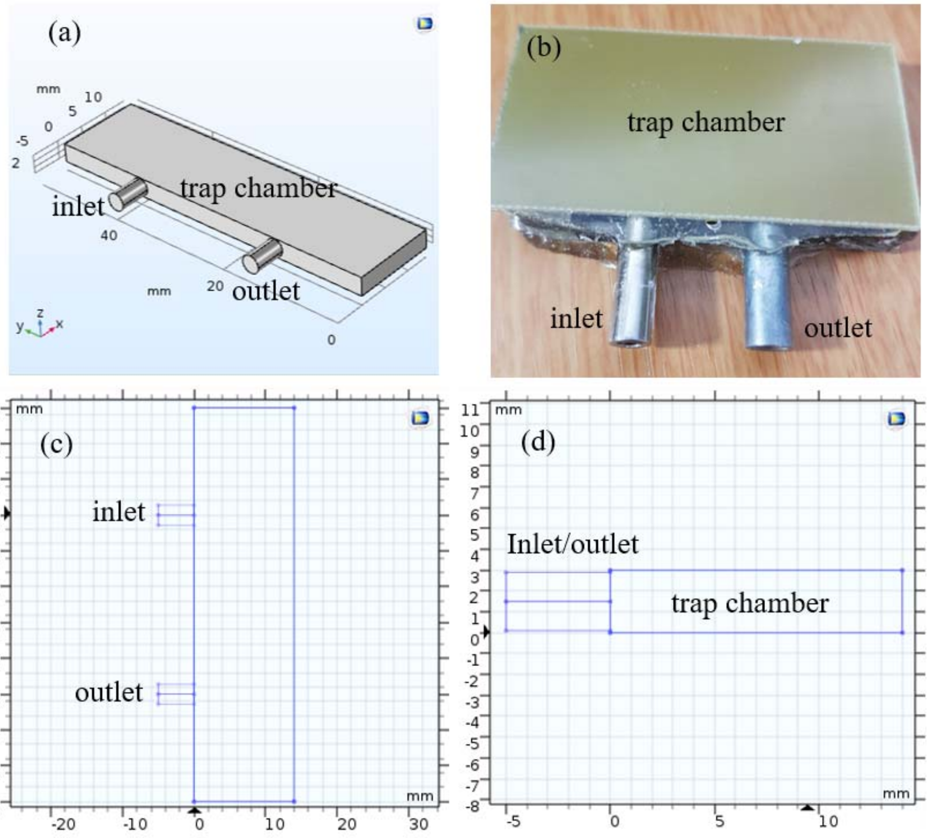

Figure 5.3. HV trap simulation and practice structure. (a): 3D simulation view of the HV trap; (b): HV trap casted by clear epoxy resin; (c): projection of the HV trap on the x-y plane; (d): projection of the HV trap on the x-z plane.

5.3.3. Experiment setup

After the cyclone separator and the HV trap were built, these parts were connected with each other to make a system filter (an air sampler). The outlet of the cyclone separator was linked to the inlet of the HV trap by a 90° brass connector and a soft plastic pipe. In the system, there were two vacuum pumps with different functions. Vacuum pump 1 is a 12V and 2.5L/min air flow pump, which is mainly used to draw the air into the system for sampling. Vacuum pump 2 was a 16V and

40L/min which was mainly used to clean the HV trap chamber. The two vacuum pumps were connected with each other by a brass T-connector. The rest inlet of the T-connector was attached to the outlet of the HV trap by a soft plastic pipe.

The entire setup diagram for the experiment is shown in Figure 5.4(a), and the practical setup is Figure 5.4(b). The inner of box 1 is shown in Figure 5.4(c), where the cyclone separator and the two fans can be seen. The testing system had two boxes, box 1 and box 2 with dimensions of 42cm × 50cm × 25cm (width × length × height) and 28cm × 48cm × 18cm (width × length × height) respectively. In the larger box, there were two fans which could create turbulent air flow to drag powder samples put on the bottom of the box 1. Fan 1 worked at 12V, and it span at 9,996rpm ± 7rpm. Fan 2 worked at 120V, and its spin was 6,397rpm ± 5rpm. The function of box 2 was simply to keep the particulates released from the outlet of the vacuum. A three relay circuits were controlled by an Atmega-328P Arduino board. The relays turned on/off the vacuum pumps and the HV circuit connected to the HV trap.

To perform the experiment, a procedure was set up. The procedure for the experiment is as the followings:

- Phase 1: Turning on Fan 1 and Fan 2 → turbulent air will take the powder sample off from the bottom of box 1 → it will result in powder mist in box 1.
- Phase 2: Turning on HV circuit to supply around 10kV for HV trap, and at the same time, turning on pump 1 to sample the air in box 1 → the cyclone filters out large particulates and passes the rest particulates to the HV trap → the trap catches the large particulates in the coming air → the small particulates will be released into box 2.
- Phase 3: After 1 minute, turning off both of HV circuit and pump 1. Investigate the sample in the HV trap by the Olympic microscope (actually, at this step, another HV trap device, which is installed thermopile detectors, infrared source and silver mirrors, will start to measure infrared intensity for later analysis. This work is to be published in another paper).
- Phase 4: Turning on pump 2 in 5 seconds to clean the HV trap chamber.

After the experiment for a certain sample is finished, box 1 must be cleaned for a new sample test. The next section shows the results from simulations and from the experiments.

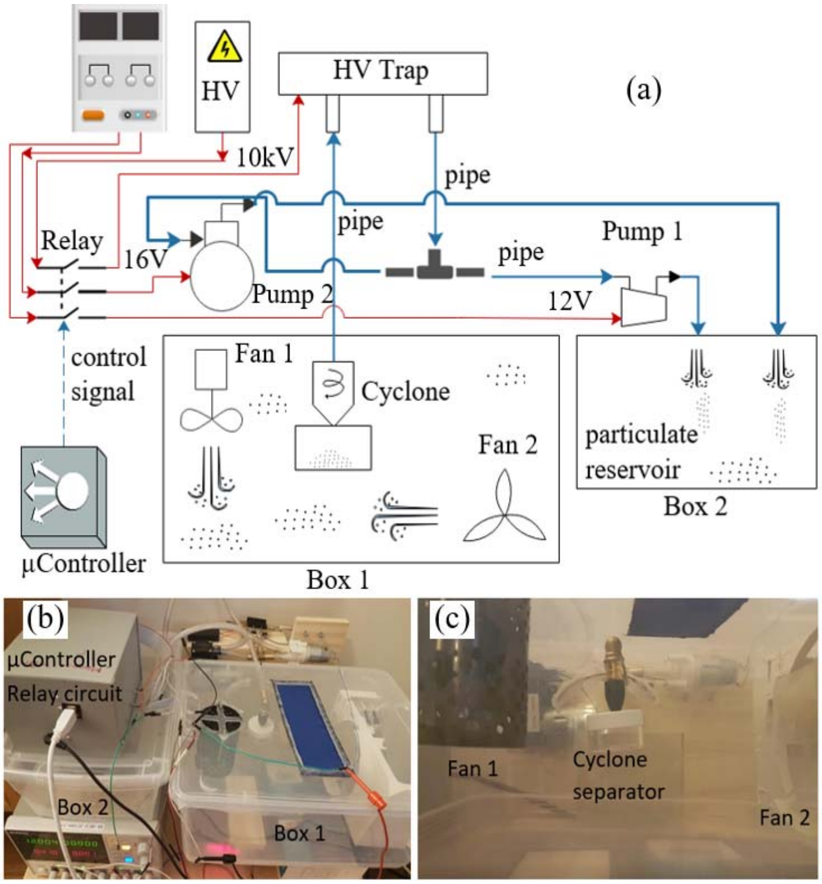

Figure 5.4. Complete experiment setup diagram; (b): hardware experiment setup; (c): internal view of box 1.

5.4. Results and discussion

5.4.1. Simulation

5.4.1.1. Cyclone separator

Running SPLF module provides the velocity and pressure of gas in the cyclone. The necessary parameters for the simulation have been discussed in previous section. Figure 5.5 shows the magnitude of the gas velocity and the gas pressure in the cyclone. Figure 5.5(a) mainly shows the gas velocity magnitude in the cyclone chamber and the outlet pipe, as the velocity changes in these parts. At the top center area of the outlet, the velocity of the gas is largest. The velocity in that area is around 8m/s. Figure 5.5(b) describes the velocity magnitude distribution along the red line which goes from the bottom of the reservoir to the outlet. The X-axis is the arc length from the bottom of the reservoir to the outlet. In Figure 5.5(b), zero point corresponds to the bottom of the reservoir, 50mm point is around the center point of the cyclone chamber, and the highest point with the coordinate of 80mm, is the center point of the outlet. From Figure 5.2(d) the lowest edges of the inlets are at 54mm. At the points from 50mm to 0mm, Figure 5.5(b) shows that the velocity is 0m/s. Consequently, the particulates falling into the space lower than that point will settle down onto the bottom of the dust reservoir by gravity. Again, it can be seen from Figure 5.5(b) that the gas velocity at the outlet center is largest, and the gas velocity decreases quickly to the center point of the cyclone chamber.

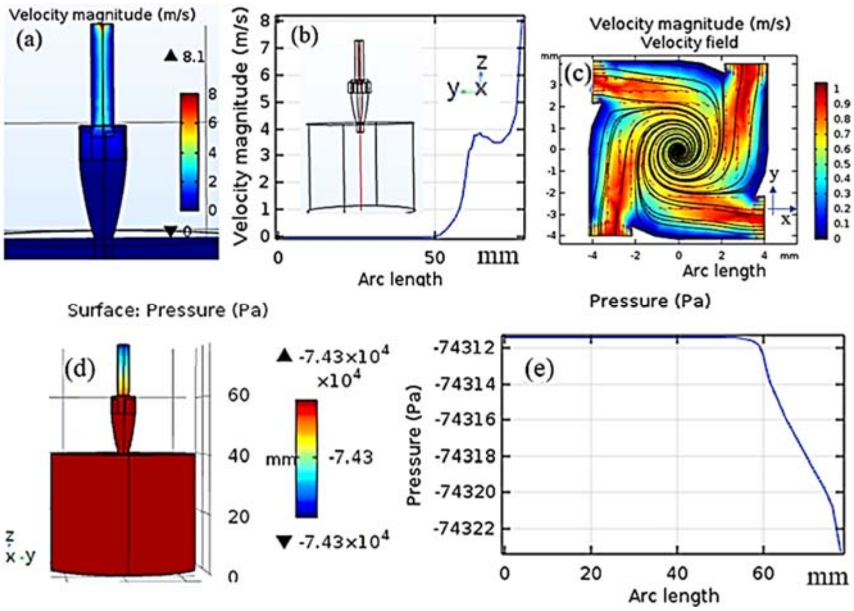

Figure 5.5. Plots of the velocity and pressure of the gas inside the cyclone separator. (a): gas velocity magnitude; (b): gas velocity magnitude distributing from the reservoir bottom to the outlet; (c): gas velocity magnitude and its streamline distributing on x-y surface going through z = 56 mm; (d): pressure in the cyclone; (e): pressure distributing from the bottom to the outlet.

Figure 5.5(c) describes the air velocity magnitude and its streamline on x-y plane which is perpendicular to the quad-inlets and goes through z = 56. From the figure, the gas velocity close to the cyclone wall is very weak. It can be seen the spinning radius of gas reduce when it goes close to the center. Figure 5.5(d) and (e) illustrate the gas pressure in the cyclone separator. From the legend of Figure 5.5(d), it can be seen that the gas pressure is strongest from the cyclone chamber to the reservoir and the pressure is unchanged in this space. Figure 5.5(e) provides more detail of the gas pressure distributed from the reservoir bottom corresponding zero point to the outlet corresponding 80mm point on the x-axis.

In the followings, the simulation of the powder particles and Fusarium spores are presented. The mass density of wheat powder is 657kg/m^3 [C5.25], turmeric is 1,341kg/m^3 [C5.26], and Fusarium spore is 1,000kg/m^3 [C5.27]. In the simulations, the number of particles released into the cyclone through the inlets was 500 particles. In the simulation, the numbers of the particles in the cyclone chamber, the reservoir and the outlet pipe were monitored to study the change and movement of the particles by applying PTFL module. Figure 5.6 depicts the simulation of particle trajectories in the cases: d_p = 20μm, d_p = 40μm, d_p = 75μm, d_p = 140μm and d_p = 200μm when investigating the wheat powder sample was conducted.

It can be seen that no particulate settles down into the reservoir for d_p = 20μm. When d_p = 40 μm, d_p = 140μm and d_p = 75μm, the wheat particulates can be seen both in the outlet and the reservoir. However, the larger the particles, the less they can be seen in the outlet. When d_p is large enough, such as d_p = 200μm, there will no wheat particles presenting in the outlet. These trends are not different from the turmeric and Fusarium cases, except happening at different particle sizes.

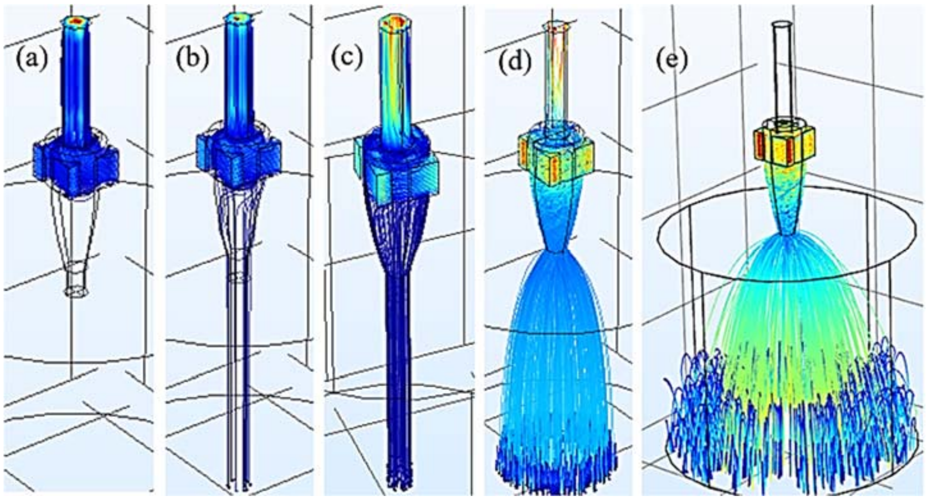

Figure 5.6. Wheat particle trajectories. (a): d_p = 20μm; (b): d_p =40 μm; (c): d_p =75 μm; (d): d_p = 140μm; (e): d_p = 200μm.

From simulations, the wheat particle movements in the parts of the cyclone separator can be studied. Figure 5.7 shows the simulations of the wheat particle movements at different sizes in the cyclone separator. The blue, red and green lines describe the particulate numbers in the cyclone, through the outlet and in the reservoir respectively.

In Figure 5.7(a), (b) and (c), when d_p is smaller than 30μm, the particles would be hardly going to the reservoir. Moreover, when d_p is too small, such as d_p = 1μm, the particle hardly goes into the reservoir, but not all of them can go to the outlet. It is because a part of the in-coming particles will be stuck in the cyclone chamber or bounced back to the inlets from the opposite walls. Figure 5.7(c) shows that when d_p is large enough, most of them will go to the outlet, such as d_p = 3μm. Finally, in Figure 5.7(g), (h) and (i), when particles are large, then the particles mainly go to the reservoir.

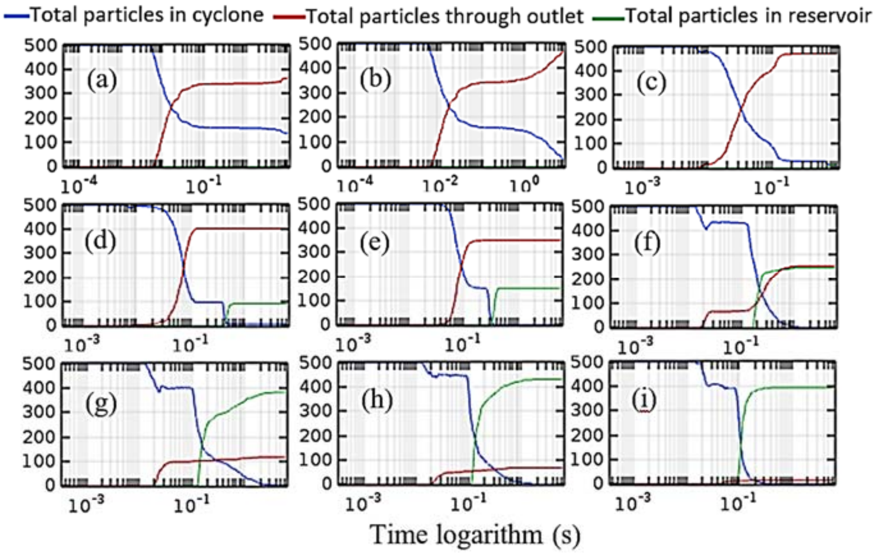

Figure 5.7. Plots of the wheat particulate numbers in the cyclone, through the outlet and in the reservoir at different diameters. (a): d_p = 1μm; (b): d_p = 3μm; (c): d_p = 30μm; (d): d_p = 40μm; (e): dp = 50μm; (f): d_p = 75μm; (g): d_p = 90μm; (h): d_p = 120μm; (i): d_p = 140μm;

For the turmeric and *Fusarium* cases, the changing trends are pretty similar to the wheat case. The difference in the changing trends depends on the particle diameter and the particle mass density.

From monitoring the particle movements in the parts of the cyclone separator above, the correlation functions between the outlet particle number and the particle diameter of the wheat, turmeric and *Fusarium* cases are formed. Figure 5.8 shows the correlation functions in three cases. From Figure 5.8(a) and (b), when investigating the wheat case, $d_{High, 50}$ = 75μm; $d_{High, 50}$ = 52.5μm, when the turmeric case is studied. In *Fusarium* case, $d_{High, 50}$ = 67μm which is shown in Figure 5.8(c).

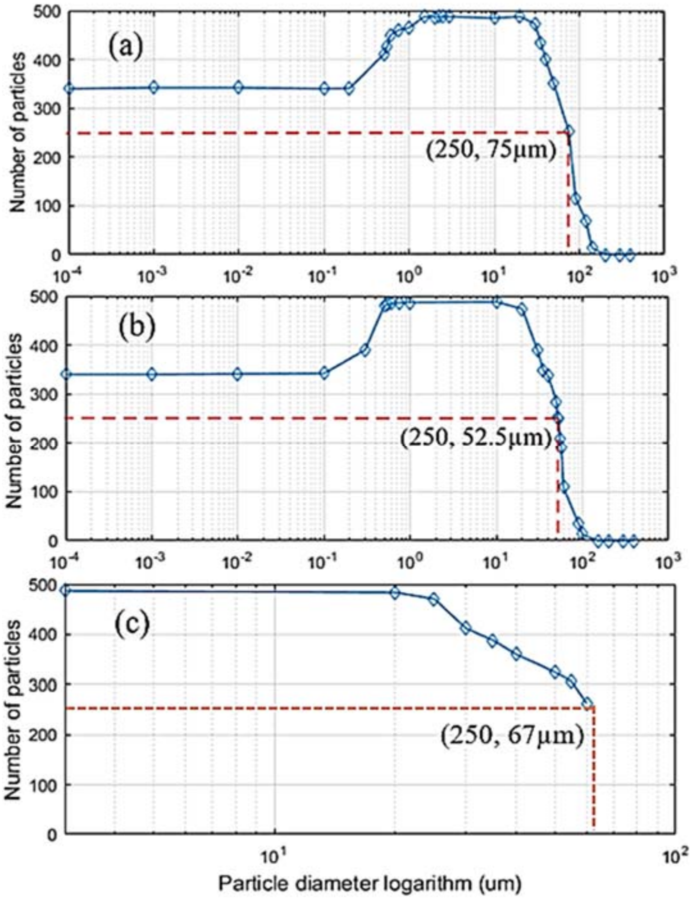

Figure 5.8. Plots of the relation of outlet particle numbers and diameter logarithm. (a): wheat powder case; (b): turmeric powder case; (c): *Fusarium* case.

5.4.1.2. High voltage trap

The necessary physics modules of COMSOL for the HV trap simulation are EC module to simulate the electric field caused by the HV, SPLF module to simulate the gas flow inside the trap, and PTFL. These modules also help to simulate the interaction between the particles and the electric field, the gravity effect and the particle trajectories. Because the cyclone separator and the HV trap are connected to each other, the velocity simulation result, which is around 8m/s, at the outlet of the cyclone will be the velocity at the inlet of the HV trap. Running EC and SPLF physics modules provide the electric field, gas velocity and pressure in the trap. Figure 5.9 shows the electric field, the gas velocity magnitude and the pressure in the HV trap. From Figure 5.9(a), the electric field is almost homogeneous inside the space between the two plates. The magnitude is $0.37*10^7$V/m. In Figure 5.9(b), the red arrows are the velocities of the inner air. It can be seen there are two main spinning zones. One spinning zone is small and the other zone is larger. Although, the inlet gas velocity is set up at 8m/s, the maximum gas velocity inside the trap chamber is just around 4.2m/s. In Figure 5.9(c), although the green lines separate the different pressure layers, they can be grouped into three main pressure zones, in which the two-end zones are almost the same in pressure which can be seen through yellow darkish color. The middle zone has greenish color which means its pressure is weaker than the other two zones. The difference in pressure can explain for the reason why there are two main spinning zones observed in Figure 5.9(b). This difference results in air movement inside the trap.

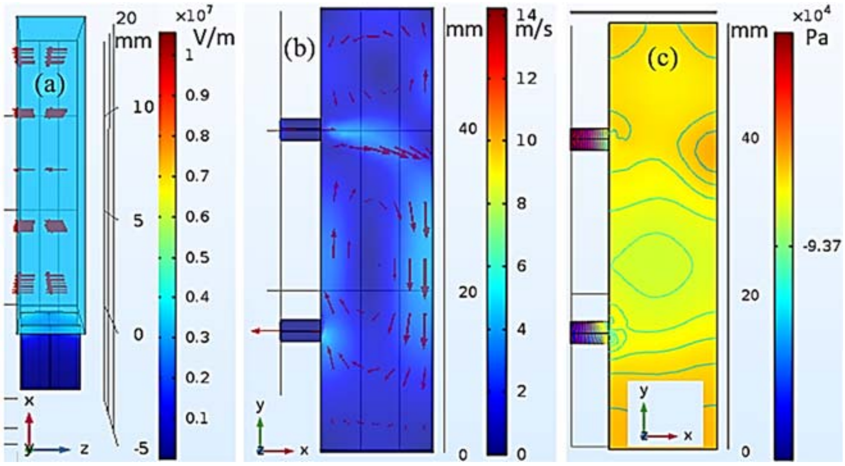

Figure 5.9. Plots of the physics quantities in the HV trap. (a): electric field (V/m); (b): gas velocity (m/s); (c): pressure (Pa).

From equation (5.7), to simulate the interaction between particulates and electric field, it is essential to determine relative dielectric of the medium, ε_m, and relative dielectric of the particulate, ε_p. The investigated medium is the air, so $\varepsilon_m = 1$ [C5.33]. Therefore:

$$F_{DEP} = \pi \frac{d_p^3}{4} \frac{(\varepsilon_p - 1)}{\varepsilon_p + 2} \nabla |E|^2 \tag{5.8}$$

Equation. (5.8) shows that when ε_p increases, $\frac{(\varepsilon_p-1)}{\varepsilon_p+2}$ will also increase, but the slope will gradually decrease. When ε_p increases to a large value, $\frac{(\varepsilon_p-1)}{\varepsilon_p+2}$ will move close to value 1. Therefore, the change of ε_p does not change F_{DEP} as much as d_p, because $F_{DEP} \sim d_p^3$.

From the studies on wheat permittivity in [C5.34, C5.35], the average value of ε_p can be taken at 5 for simulation. Figure 5.10 shows the particle trajectories in the HV trap at four typically different diameters. From the simulation results, in the trap, the particle distributions corresponding different particle sizes are different from each other. The large particles, such as d_p = 100µm, mainly distribute close to the inlet area, and the medium particle, such as d_p = 50µm, distribute from the area close to the inlet to the furthest side of the trap. The small particles, such as d_p = 2µm, will suffer less F_{DEP}, more particles escape through the outlet.

Conducting simulations and monitoring the numbers of the particles of the three sample cases in the inlet, in the HV trap, on the electrode surfaces and through the outlet for the all cases, the relation functions between the particles in these parts can be built. In the simulations, the number of the particles released into the inlet was 500 particles. Figure 5.11(a), (c) and (e) illustrates the relation functions of the particles in the inlet and the particles in the chamber or on the electrodes of the HV trap of wheat, turmeric and *Fusarium* respectively.

To find the transfer functions for the HV trap in the three sample cases, the later equation is used:

$$R_{HVtrap} = \frac{N_{d_p}}{N_{d_{p\_in}}} \tag{5.9}$$

where N_{d_p} is the number of the particles with diameter d_p caught by the device; $N_{d_{p\_in}}$ is the number of the particle with diameter d_p coming into the inlet. In the simulation, $N_{d_{p\_in}}$ = 500 particles. Equation (5.9) is also applied for the cyclone separator simulation to find the transfer function, $R_{cyclone}$. Now, the transfer function of the system which includes the HV trap and the cyclone separator can be found by:

$$R_{system} = R_{cyclone} * R_{HVtrap} \tag{5.10}$$

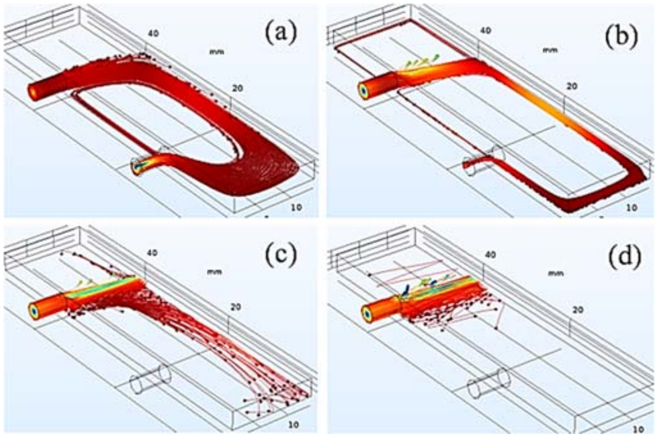

Figure 5.10. Particle trajectories. (a): d_p = 2µm; (b): d_p =19.5 µm; (c): d_p = 50µm; (c): d_p = 100µm;

The transfer function plots for wheat, turmeric and *Fusarium* are respectively shown in Figure 5.11(b), (d) and (f). In these figures, the transfer function plots of the cyclone separator and the HV trap are also depicted.

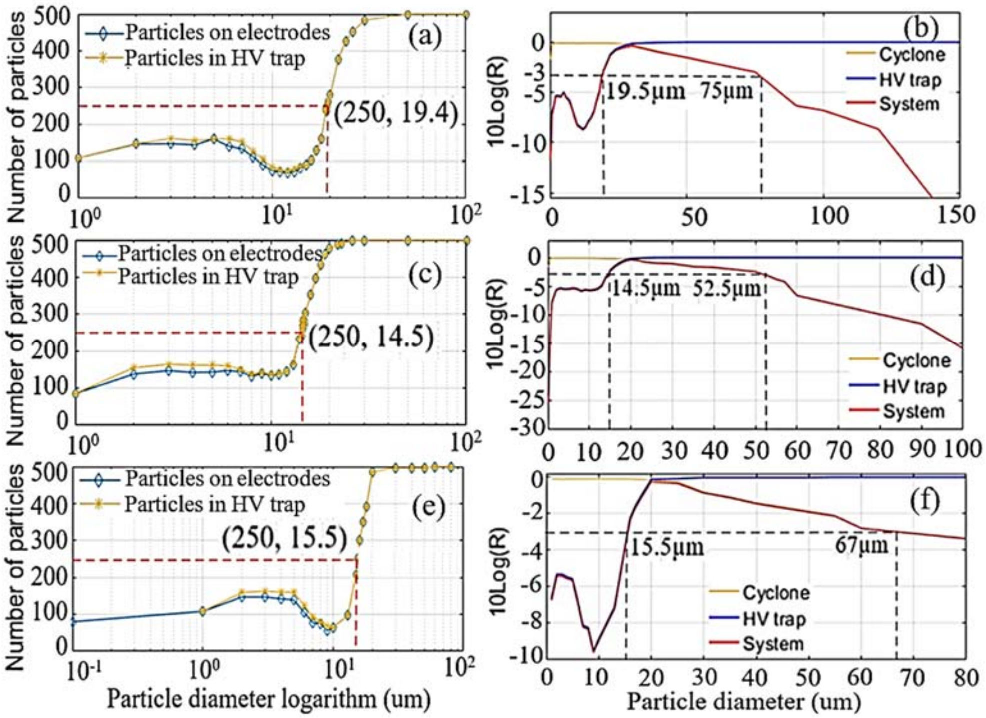

Figure 5.11. Transfer plots of: (a): HV trap and wheat sample; (b): system and wheat sample; (c): HV trap and turmeric sample; (d): system and turmeric sample; (e): HV trap and *Fusarium* sample; (f): system and *Fusarium* sample.

Noticing that, there is not much information about the dielectric coefficients of turmeric and *Fusarium* samples. Because turmeric powder texture is very similar to wheat powder, it can be assumed that the turmeric and wheat dielectrics are the same. Thus, the turmeric relative dielectric value used in the simulation was 5. For *Fusarium*, another assumption was considered. As both of *Fusarium* spore and *Bacillus megaterium* spore have nucleus and lipid in their bodies according to [C5.36- C5.38], their relative dielectric values can be considered similar. Based on the relative average permittivity of *Bacillus megaterium* spore, which is around 120 [C5.39], so the relative dielectric of *Fusarium* spore equals to that value.

5.4.1.3. System response

From the cyclone separator and HV trap simulations, the particle bandpass ranges and the slopes of the two sides of the transfer functions of wheat, turmeric and *Fusarium* are shown in Table 5.1. In this table, the bandpass ranges were calculated by using $D_{Low,\ 50}$ and $D_{High,\ 50}$.

Table 5.1. Particle bandpass and slopes

Sample	Left slope (particle/ μm)	$D_{Low,\ 50}$ (μm)	$D_{High,\ 50}$ (μm)	Right slope (particle/ μm)
Wheat	44.25	19.5	75.0	5.9
Turmeric	58.25	14.5	52.5	9.5
Fusarium	61.2	15.5	67.0	8.8

5.4.2. Experiment

In the experiment, to be able to view the particulates caught by the HV trap, a piece of black-smooth rectangular paper was put underneath one electrode. Consequently, the particulates would lay on the black-smooth paper, instead of on the electrode. The particle size distribution was investigated by the OLYMPUS U-MSSP Japan Microscope [C5.28]. The equation to calculate the frequency distribution [C5.1, C5.40] is:

$$F_i = \frac{d_{p,i} * N_i}{\sum_i^n N} \tag{5.11}$$

where, $d_{p,i}$ is the diameter of particle *i*; N_i is the number of the particle *i*; *n*: number of different sizes of the particles.

In the cyclone separator test, after running the test system as described in Section III-*C*, the particles samples of the turmeric and wheat samples, which were collected from the reservoir, were analyzed. From the analysis, the frequency distributions of the particles sampled from the reservoir are illustrated in Figure 5.12(a). The x-axis is the particle diameter, and the y-axis is the frequency distribution percentage. Figure 5.12(b) is the magnified photo of the turmeric. Analyzing the microscope-magnified photos of the wheat and turmeric samples used in the experiments, the frequency distribution of the turmeric and wheat samples are charted in Figure 5.12(c). Figure 5.12(d) is the magnified photo of the original turmeric sample.

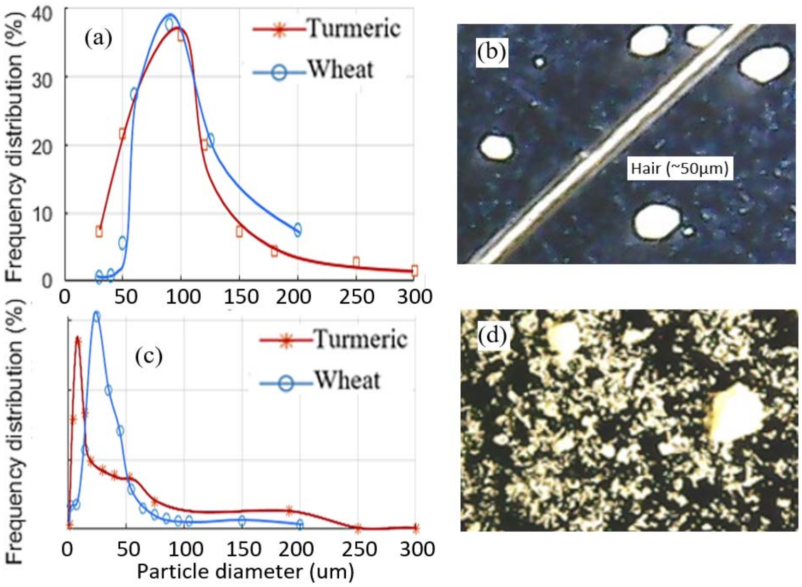

Figure 5.12. Frequency distribution plots and photos of the turmeric and wheat samples in two cases; (a): turmeric and wheat samples from the cyclone reservoir after running test in 1 minute; (b): magnified photo of the turmeric sampled by the cyclone reservoir; (c): original turmeric and wheat samples which would be used for experiments; (d): magnified turmeric photo of the original sample.

From the image analysis, the particle diameters of the peaks of these distributions were found and shown in Table 5.2. It can be seen that the wavelengths of the peaks of the frequency distributions of the two original samples are smaller the wavelengths of the peaks of the two corresponding samples collected from the reservoir.

Table 5.2. The particle diameters of the peaks of frequency distribution of turmeric and wheat

Sample	Original sample	Reservoir sample
Wheat	25±5µm	90±10µm
Turmeric	8.5±1.5µm	100±10µm

For the HV trap test, at first, the trap was tested by letting it work in one minute without the cyclone, then the turmeric and wheat samples were collected in different experiments. These experiments would help to check if the large particles as well as small particles can be caught by the HV trap. Later, the cyclone separator was connected with the HV trap. The cyclone function is filtering away large size particles, and these large size particles are kept in the cyclone reservoir.

After running the experiments for the turmeric and wheat samples in one minute, observing the particle distribution on the black sampling paper can provide a clear view about the effectiveness of the system. From Figure 5.13(a) and (e) and their grayscale images (c) and (g) respectively, it can be seen that without the cyclone separator, both large (>70μm) and small particles were caught on the trap. When the cyclone separator was used, the large particles were filtered effectively which can be seen in Figure 5.13(b) and (f) and their grayscale images (d) and (h). In Figure 5.13(c), (d), (g) and (h), the red dash lines show the high particle distribution areas. The distributions of (c) and (g), or (d) and (h) are very similar to each other.

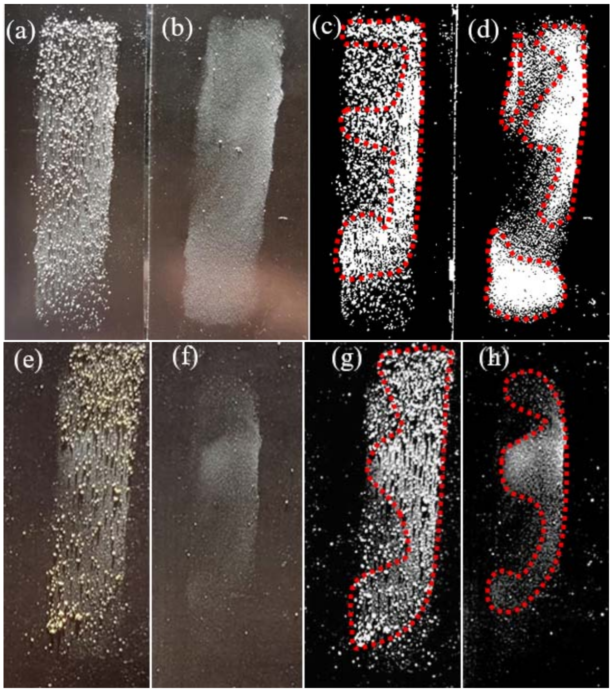

Figure 5.13. Non-magnified photos; (a): wheat sample and without using the cyclone; (b): wheat sample and with using the cyclone; (c) and (d): grayscale photos of (a) and (b) respectively; (e): turmeric sample and without using the cyclone; (f): turmeric sample and with using the cyclone; (g) and (h): grayscale photos of (a) and (b) respectively.

Using the microscope again to investigate these samples can provide the frequency distributions of the particles of the turmeric and wheat samples. To check the simulation results with the practical results, there are two ways can be applied here. Firstly, let's name some essential quantities for the calculation:

- S_{total}: the total sample going to the system;
- $S_{cyclone}$: the cyclone sample going through the cyclone separator and coming into the HV trap;

- S_{HVtrap}: the HV trap sample which is only caught by the HV trap and there is no the cyclone in the test.
- S_{syst}: the system sample which is caught by the system which includes the cooperation of the cyclone and the trap;

From these definitions, one can have:

$$S_{cyclone} = S_{total}*R_{cyclone} \tag{5.13}$$

$$S_{HVtrap} = S_{total}*R_{HVtrap} \tag{5.14}$$

$$\begin{aligned} S_{system} &= S_{total}*R_{system} \\ &= S_{total}*R_{cyclone}*R_{HVtrap} \\ &= S_{HVtrap}*R_{cyclone} \end{aligned} \tag{5.15}$$

As the experiment (*exp*) samples of the two cases of using and not-using the cyclone separator as a pre-filter were collected, there would be, correspondingly, $S_{HVtrap\text{-}exp}$ and $S_{system\text{-}exp}$. From (5.15), if $R_{cyclone}$ from the simulations times with $S_{HVtrap\text{-}exp}$, one can predict the sample caught by the system, which is named as $S^{A}_{system-pred}$. On the other hand, the frequency distributions of the samples introduced in Figure 5.12(c) were calculated from the origin samples, *S*. If *S* can be considered as S_{total}, then $S^{B}_{system,\ pred}$, which is the system particle sample, is possibly estimated from S_{total}. From $S_{HVtrap\text{-}exp}$, $S_{system\text{-}exp}$, $S^{A}_{system-pred}$ and $S^{B}_{system-pred}$, the frequency distributions were estimated and shown in Table 5.3 for the turmeric and wheat samples respectively.

Viewing the correlation between the frequency distribution of the system through experiment and the prediction frequency distribution in Table 5.3 is the key to see which prediction method is good. Table 5.4 shows the correlation coefficients (Corr.) of the two samples.

For the test of *Fusarium*, *Fusarium chlamydospores* (*Chl.*) were sprinkled at the front of the inlets of the cyclone to see if the trap could catch the spores and fairly distribute the test sample on to every area of the electrodes by using the 2.5L/min vacuum pump. Then the 40L/min vacuum pump was tested if it can clean the sample in the trap. After observing *Fusarium* test and the tests of the turmeric and wheat samples above, the experimental observation was recorded and shown in Table 5.5. The table provides information about how well the system works, such as catching, filtering, smoothly distributing and cleaning abilities.

5.4.3. Discussion

In our interest application of *Fusarium* spore detection, eliminating the particles having the sizes out of the *Fusarium* spore size range [10µm - 70 µm] is essential. In the research in [C5.17], PM_{10} and $PM_{2.5}$ contribute much in the air, so filtering these two types of particle group is necessary. By using the quad-inlet cyclone separator and HV trap to build a filter system, the method has proven that it can satisfy the requirement well through the simulations as well as through the experiments.

The simulations assist in understanding about system operation and provide a method to adjust the parameters of the cyclone and HV trap to meet system requirements. The simulations have shown that the bandpass filter for *Fusarium* is [15.5µm, 67µm] which is somewhat close to the expected range. In addition, the bandpass particle ranges of wheat and turmeric are [19.5µm, 75µm] and [14.5µm, 52.5µm], so we can expect the system can filter well the PM_{10} and $PM_{2.5}$. The experiment proves that the sample distribution on the electrode surface is fairly good due to the uniform electric field in the HV trap. This is also important for our purpose of detecting and analyzing *Fusarium* by applying infrared radiation and thermopile detector [C5.15].

Table 5.3. Frequency distribution of the samples

Turmeric sample					
Diameter (µm)	1-5	6-10	11-25	26-60	>60
Distribution of $S_{HVtrap-exp}$ (%)	6.70	47.00	11.30	6.00	29.00
Distribution of $S^{A}_{system-pred}$ (%)	9.48	66.45	15.53	5.59	2.95
Distribution of $S^{B}_{system-pred}$ (%)	19.50	26.00	25.60	23.10	5.80
Distribution of $S_{system-exp}$ (%)	9.50	66.00	16.00	8.40	0.10
Wheat sample					
Diameter (µm)	1-5	6-10	11-25	26-60	>60
Distribution of $S_{HVtrap-expe}$ (%)	30.00	18.00	32.00	18.00	2.00
Distribution of $S^{A}_{system-pred}$ (%)	32.20	19.37	33.33	13.87	1.23
Distribution of $S^{B}_{system-pred}$ (%)	1.31	1.37	17.05	69.03	11.24
Distribution of $S_{system-exp}$ (%)	33.10	19.00	31.80	15.50	0.60

Table 5.4. Correlation coefficients between predicted and experimental distributions of the two samples

Sample	Turmeric		Wheat	
Group	$S_{system\text{-}exp}$ & $S^{A}_{system-pred}$	$S_{system\text{-}exp}$ & $S^{B}_{system-pred}$	$S_{system\text{-}exp}$ & $S^{A}_{system-pred}$	$S_{system\text{-}exp}$ & $S^{B}_{system-pred}$
Corr.	0.997	0.575	0.995	-0.207

Table 5.5. Experimental observation

Procedure	System catch	<10µm filter away	>70µm filter away	Distribution	System clean
F. chl.	Good	NA	NA	Pretty good	Good
Wheat	Good	Good	Good	Good	Good
Turmeric	Pretty good	Good	Good	Pretty good	Good

It is also essential to check simulations by comparison them with experiment. The simulation results have been checked by applying the transfer functions formed from the simulation results. Observing Table 5.3, we can see that the frequency distributions of $S_{system,\ exp}$, which was achieved from the experiment, and $S^{A}_{system-pred}$ predicted from $S_{HVtrap\text{-}exp}$ by multiplying it with the cyclone transfer function are very close to each other except the large particles (>60µm). This can be explained that the small particles in the turmeric and wheat samples dominate large particles (Figure 5.12(c)), so the statistic of the small particles is much better than the large particles.

Although, using the statistical information about the original samples as the input information for the filter system seems to be logical, it is not as we expect. When comparing the frequency distributions of $S_{system\text{-}exp}$ and $S^{B}_{system-pred}$, which was predicted by using the original samples, we can see in Table 5.4 that the correlation coefficients are very poor. Therefore, the statistical data of the original turmeric and wheat sample cannot be used for the prediction. If the entire particle distribution patterns in Figure 5.9 are superposed onto each other, then we can figure out the pattern will look like a flip vertical E letter. Thus, it will be similar with Figure 5.12. Because the mass density of turmeric and *Fusarium* spore are not much different, the experiment of turmeric can be used as reference for *Fusarium* spore case.

Comparing of the separation efficiency coefficients from the research about four different axial inlet cyclones in [C5.18] and helical-roof inlet cyclone [C5.41] with the efficiency of the quad-inlet cyclone, we can see that d_{50} values, which are around 1.7μm to 2μm of the axial inlet cyclones are much smaller than the values in our research. The cyclones (in meter) in these studies are much larger than the cyclone (in millimeter) in this paper. The research in [C5.42] showed the simulation of four different inlet cyclones. One of them is also a quad-inlet cyclone separator. Its dimensions are also much larger than the dimensions of the quad-let cyclone separator of our design. In Khazaee [C5.42], d_{50} of the quad-inlet cyclone is about 5.5μm which is again smaller than d_{50} values in our research. These have proven that the dimension adjusting for the quad-inlet cyclone is effective. To increase the d_{50}, the diameter of the cyclone should be decreased.

As the simulations have been proven by the experiments, simulation results can be used as reference. Based on simulations, the correlation between the particles caught on the electrodes and the particles at the inlets is to be setup.

5.5. Conclusion

A new method to form a bandpass particle filter to sample spores in the air and eliminate undesired particulates has been proposed. In the filter system, a quad-inlet cyclone separator structure was also introduced. The quad-inlet cyclone separator was simply extended and developed from the previous cyclones [C5.18, C5.19] by modifying the number and the direction of the inlets. With four perpendicular inlets located at four directions, the device can sample the air more effectively. The sample dispersal on the electrode surfaces was smooth and not clumped. It is because of the homogeneous electric field in the HV trap. This feature is favourable for sample analysis.

Our proposed device can help to eliminate effectively large and small size particles. The bandpass of the Fusarium spore in the experiment is close to the expectation range. From both simulation and experiment, PM_{10} and $PM_{2.5}$ can be well eliminated. The sample caught in the HV trap can be cleaned easily by using the 40L/min vacuum pump. From the experiment, the cleaning process is simple by turning off the HV and turning on the cleaning vacuum.

From the simulations and experiments, the particle filter bandwidth of the system can be adjusted by changing the cyclone diameter, the diameter of the top exit pipe, and the size of the inlets. Besides, adjusting the applied voltage also can help to move the low-cut-off diameter.

References

[C5.1] Horiba Scientific, *A Guidebook to Particle Size Analysis*, www.horiba.com/fileadmin/uploads/Scientific/Documents/PSA/PSA_Guidebook.pdf. Accessed May 17, 2019.

[C5.2] Anne Renstrom, “Exposure to airborne allergens: a review of sampling methods,” *J. Environ. Monit.*, vol. 4, no. 4, pp. 619–622, Jun. 2002.

[C5.3] K. Toma et al., “Repetitive Immunoassay with a Surface Acoustic Wave Device and a Highly Stable Protein Monolayer for On-Site Monitoring of Airborne Dust Mite Allergens,” *Anal. Chem.*, vol. 87, no. 20, pp. 10470–10474, Oct. 2015.

[C5.4] Z. D. Bolashikov, A. K. Melikov, W. Kierat, Z. Popiołek, and M. Brand, “Exposure of health care workers and occupants to coughed airborne pathogens in a double-bed hospital patient room with overhead mixing ventilation,” H V A C & R Research, vol. 18, no. 4, pp. 602-615, 2012.

[C5.5] R. S. Dungan, “Estimation of Infectious Risks in Residential Populations Exposed to Airborne Pathogens During Center Pivot Irrigation of Dairy Wastewaters,” *Environ. Sci. Technol.*, vol. 48, no. 9, pp. 5033–5042, May 2014.

[C5.6] J. R. Brown et al., “Influenza virus survival in aerosols and estimates of viable virus loss resulting from aerosolization and air-sampling,” *J. Hosp. Infect.*, vol. 91, no. 3, pp. 278–281, Nov. 2015.

[C5.7] A. S. Weissfeld, R. A. Joseph, T. V. Le, E. A. Trevino, M. F. Schaeffer, and P. H. Vance, “Optimal Media for Use in Air Sampling to Detect Cultivable Bacteria and Fungi in the Pharmacy,” *J. Clin. Microbiol.*, vol. 51, no. 10, pp. 3172–3175, Oct. 2013.

[C5.8] J. Marciniuk, A. Grabowska-Joachimiak, and P. Marciniuk, “Differentiation of the pollen size in five representatives of Taraxacum sect. Palustria,” *Biologia (Bratisl.)*, vol. 65, no. 6, pp. 954–957, Dec. 2010.

[C5.9] F. Leslie, B. A. Summerell and S. Bullock, *The Fusarium Laboratory Manual*. Iowa Blacwell, 2006, https://doi.org/10.1371/journal.pone.0037859.

[C5.10] Gary C. Begstrom Melissa D. Keller and Elson J. Sheilds, “The aerobiology of Fusarium graminearum,” *Aerobiologia*, vol. 30, pp. 123–136, Nov. 2013.

[C5.11] B. Feng, B. Chen, W. Zhuo, and W. Zhang, “A new passive sampler for collecting atmospheric tritiated water vapor,” *Atmos. Environ.*, vol. 154, pp. 308–317, Apr. 2017.

[C5.12] S. J. Hayward, T. Gouin, and F. Wania, “Comparison of Four Active and Passive Sampling Techniques for Pesticides in Air,” *Environ. Sci. Technol.*, vol. 44, no. 9, pp. 3410–3416, May 2010.

[C5.13] T. G. Jacek Namiesnik, “Passive Sampling,” *Trends Anal. Chem.*, vol. 21, no. 4, pp. 276–290, 2002.

[C5.14] M. Dvořák, P. Janoš, L. Botella, G. Rotková, and R. Zas, “Spore Dispersal Patterns of Fusarium circinatum on an Infested Monterey Pine Forest in North-Western Spain,” *Forests*, vol. 8, no. 11, p. 432, Nov. 2017.

[C5.15] Son Pham, Anh Dinh, and Khan Wahid, “A Nondispersive Thermopile Device with an Innovative Method to Detect Fusarium Spores,” *IEEE Sens. J.*, vol. 19, issue: 19, pp. 8657-8667, Oct. 2019.

[C5.16] G. Titos, I. Foyo-Moreno, H. Lyamani, X. Querol, A. Alastuey, and L. Alados-Arboledas, “Optical properties and chemical composition of aerosol particles at an urban location: An estimation of the aerosol mass scattering and absorption efficiencies,” J. *Geophys. Res. Atmospheres*, vol. 117, no. D4, p. 12, 2012.

[C5.17] E. Pattey and G. Qiu, “Trends in primary particulate matter emissions from Canadian agriculture,” *J. Air Waste Manag. Assoc.*, vol. 62, no. 7, pp. 737–747, Jul. 2012.

[C5.18] L. Duan, X. Wu, Z. Ji, Z. Xiong, and J. Zhuang, “The flow pattern and entropy generation in an axial inlet cyclone with reflux cone and gaps in the vortex finder,” *Powder Technol.*, vol. 303, pp. 192–202, Dec. 2016.

[C5.19] W. Peng, P. J. A. J. Boot, A. C. Hoffmann, H. W. A. Dries, J. Kater, and A. Ekker, “Flow in the Inlet Region in Tangential Inlet Cyclones,” *Ind. Eng. Chem. Res.*, vol. 40, no. 23, pp. 5649–5655, Nov. 2001.

[C5.20] Daniel A. Vallero, *Fundamentals of air pollution*, 4th Edition, Amsterdam; Boston: Elsevier, 2007.

[C5.21] X. C. Zhilong Zou and Tiebing Lu, “Analysis of dielectric particles charging and motion in the direct current ionized field,” *IEEE Power Energy Syst.*, vol. 2, pp. 88–94, Mar. 2016.

[C5.22] Y.-H. Tai, C.-W. Lee, D.-M. Chang, Y.-S. Lai, D.-W. Huang, and P.-K. Wei, “*Escherichia coli* Fiber Sensors Using Concentrated Dielectrophoretic Force with Optical Defocusing Method,” *ACS Sens.*, vol. 3, no. 6, pp. 1196–1202, Jun. 2018.

[C5.23] G. E. Bowker and H. C. Crenshaw, “Electrostatic forces in wind-pollination—Part 1: Measurement of the electrostatic charge on pollen,” *Atmos. Environ.*, vol. 41, no. 8, pp. 1587–1595, Mar. 2007.

[C5.24] J. S. C. Herbert A. Pohl, “Dielectrophoretic Force,” *J. Theor. Biol.*, vol. 37, no. 1, pp. 1–13, Oct. 1972.

[C5.25] Anval Valves PVT Ltd, “Bulk Density Chart,” www.anval.net/downloads/bulk%20density%20chart.pdf, p. 15.

[C5.26] A. M. M. S Balasubramanian, T. J. Z. K K Singh, and T Anand, “Physical Properties of Turmeric (Curcuma longa L.),” *J. Spices Aromat. Crops*, vol. 21, no. 2, pp. 178–181, Jun. 2012.

[C5.27] S. D. R. Binbin Lin and D. G. S. Aaron J. Prussin, “Seasonal associations and atmospheric transport distances of fungi in the genus Fusarium collected with unmanned aerial vehicles and ground-based sampling devices,” *Atmos. Environ.*, vol. 94, pp. 385–391, May 2014.

[C5.28] Olympus, Instructions - *BX-RLA2 Reflected Light Brightfield/Darkfield illuminator*, http://metallurgicalmicroscopes.com/wp-content/uploads/2013/07/Olympus-BX-RLA2-Reflected-Light-Brightfield-Darkfield-Illuminator-Manual.pdf, 2006.

[C5.29] Climate Science Informing Action, “SaskAdapt - Wind,” *Climate Science Informing Action*. [Online]. Available: http://www.parc.ca/saskadapt/extreme-events/wind.html. [Accessed: 09-Apr-2019].

[C5.30] “Wind Resource Atlas,” *SaskWind.* [Online]. Available: https://www.saskwind.ca/wind-atlas-sk. [Accessed: 09-Apr-2019].

[C5.31] R. S. McGowan, “The quasisteady approximation in speech production.,” *J. Acoust. Soc. Am.*, vol. 94, no. 5, pp. 3011–3013, 1993.

[C5.32] K.-T. H. Yamaguchi, *Engineering Fluid Mechanics*, vol. 85. 38402 Saint Martin d’Hères Cedex, France: Springer, 2008.

[C5.33] “Dielectric Constant | Relative Permittivity | Electronics Notes.” [Online]. Available: https://www.electronics-notes.com/articles/basic_concepts/capacitance/dielectric-constant-relative-permittivity.php. [Accessed: 15-Apr-2019].

[C5.34] R. Torrealba-Meléndez, M. E. Sosa-Morales, J. L. Olvera-Cervantes, and A. Corona-Chávez, “Dielectric properties of cereals at frequencies useful for processes with microwave heating,” *J. Food Sci. Technol.*, vol. 52, no. 12, pp. 8403–8409, Dec. 2015.

[C5.35] S. Sokhansanj and S. O. Nelson, “Dependence of dielectric properties of whole-grain wheat on bulk density,” *J. Agric. Eng. Res.*, vol. 39, no. 3, pp. 173–179, Mar. 1988.

[C5.36] D. R. Lang and D. G. Lundgren, “Lipid Composition of Bacillus cereus During Growth and Sporulation,” *J. of Bacteriology - Am Soc Microbiol*, vol. 101, no. 2, pp. 483-489, 1970.

[C5.37] M. Plomp, A. M. Carroll, P. Setlow, and A. J. Malkin, “Architecture and Assembly of the Bacillus subtilis Spore Coat,” *PLOS ONE*, vol. 9, no. 9, p. e108560, Sep. 2014.

[C5.38] R. Marchant, “Fine Structure and Spore Germination in Fusarium culmorum,” *Ann. Bot.*, vol. 30, no. 3, pp. 441–445, Jul. 1966.

[C5.39] E. L. Carstensen, R. E. Marquis, S. Z. Child’, and G. R. Bender, “Dielectric Properties of Native and Decoated Spores of - Bacillus megaterium,” *J BACTERIOL*, vol. 140, no. 3, pp. 917-928, 1979.

[C5.40] Bruce B. Weiner, “What is a Discrete Particle Size Distribution?” *Brookhaven Instrum.*, pp. 1-4, May 2011.

[C5.41] D. Misiulia, A. G. Andersson, and T. S. Lundström, “Computational Investigation of an Industrial Cyclone Separator with Helical-Roof Inlet,” *Chem. Eng. Technol.*, vol. 38, no. 8, pp. 1425–1434, 2015.

[C5.42] I. Khazaee, “Numerical investigation of the effect of number and shape of inlet of cyclone and particle size on particle separation,” *Heat Mass Transf.*, vol. 53, no. 6, pp. 2009–2016, Jun. 2017.

6. Using Artificial Neural Network for Error Reduction in a Nondispersive Thermopile Device

Published as

S. Pham and A. Dinh, "Using Artificial Neural Network for Error Reduction in a Nondispersive Thermopile Device," in *IEEE Sensors Journal*, February 2002, doi: 10.1109/JSEN.2020.2975201

In the previous chapters, the mechanism of *Fusarium* detection and analysis are described. However, the error reduction process is only briefly mentioned. In this chapter, the description of the thermopile data structure, the approach to process the errror of the thermopile data and the method of collecting information of the operating conditions of the device are provided. The manuscript also provides an innovative and comprehensive view of manipulating the information of operating conditions, background noise, and thermal noise for error reduction. The effectiveness of the applied approach is proven through the experimental results. Adding the 3rd thermopile along with NN technique is the new approach to further improve performance and reliability of the system under the changes of operating conditions.

The main contribution comes from the student (the first author), while the supervisor provides the editing and revising for the manuscript.

Using Artificial Neural Network for Errror Reduction in a Nondispersive Thermopile Device

Son Pham, Anh Dinh

Abstract

The outputs of some devices are sensitive to the noise (thermal noise, background noise, etc.) and the change of operating conditions such as temperature or power supply voltage. As a result, the output data may have errors. Theoretically, if these changes can be monitored, they can be used to support to correct the error. The device using three nondispersive thermopiles to detect Fusarium encounters the same problem. The three outputs come from broadband, λ_1, and λ_2 thermopiles. The broadband thermopile works in 1μm to 20μm range; λ_1 and λ_2 thermopiles work in 6.09μm±0.02μm and 9.49μm±0.22μm respectively. One temperature sensor and two voltage-monitoring modules were installed to monitor the operating conditions of the device. The information from the changes and the background noise of the device are used to train an artificial neural network. The training data are collected under unstable operating conditions. After the training, the trained neural network is used to fix errors in the output data. From the experiments results, the best error ratios of the raw and corrected data, $E_{raw}/E_{corrected}$, are 23.6, 13.8, and 18.5, respectively. The results were achieved by applying the external training and forcing method. Through the promising results, the technique of using support inputs and artificial neural network to correct data can be applied in any device which encounters similar problem. This method can help to improve accuracy and reliability of the sensor systems.

Index Terms— neural network, data correction, nondispersive thermopile device, operating conditions, background noise.

6.1. Introduction

Signal processing is sometimes arduous because of noise which tends to obscure the useful signal. Noise can be sorted into intrinsic noise and extrinsic noise [C6.1]. Intrinsic noises have five main types: shot, thermal, flicker, burst, and avalanche noises [C6.1]–[C6.4]. Flicker and burst noise can be reduced by lowering the level of contamination in semiconductor materials [C6.1], [C6.2], [C6.5]. Thermal noise depends on temperature and resistance. Thermal noise can be decreased by using small resistors at possible places. Extrinsic noise can be from capacitive coupling, conductive coupling, cross talk among conductive paths, or electromagnetic wave interference. Shielding the sensitive parts, increasing the distance between the conductive paths to mitigate the crosstalk, or avoiding earth loop in the circuit are effective approaches to prevent extrinsic noise [C6.1].

To reduce the influence of DC and low-frequency noise of the intrinsic noise, E. Serrano-Finetti et al. proposed ac-coupled amplifiers [C6.7], and R.Wei et al. suggested chopper-stabilized amplifier [C6.7]. In the project of *Fusarium* spore detection [C6.8], many noise-reduction techniques were applied. Furthermore, the AD8629 ICs were deployed in the amplifiers as this IC family use chopper-stabilization technique and have a high common-mode rejection ratio (CMRR) of 140dB [C6.9]. As the output signal-to-noise ratio (SNR) of an amplifier is proportional to CMRR (SNR=CMRR*$\frac{V_{in}}{V_{noise}}$), a high CMRR value will lead to high SNR. Since the signals from the thermopiles were very small (~µV to nV), to make the signals readable, the gains for the signals from λ_1, λ_2, and reference thermopiles were G_{λ_1}=106.85dB, G_{λ_2}=86dB, and $G_{reference}$=52dB respectively [C6.8]. In the research of thermopile analysis [C6.10], the background noise at the input voltage caused by the bias current and the offset voltage is $V_{DCinput\text{-}noise} = I_b*R_d+V_{offset}$. The large amplification gains lead to the large DC or background (BG) noise at the outputs [C6.8]. I_b and R_d are not constant and they may drift with temperature [C6.8], [C6.11]. Therefore, V_{output} is also being affected.

Besides, with the purpose of making the *Fusarium* detection device portable, a 12V battery was used [C6.8] to power the voltage regulators of an infrared (IR) light source and the other electronic parts. The battery output can affect the regulators in the similar way as described in the 24-bit visible spectrometer [C6.12], when the battery output decreases to a certain value. As a result, the IR source which provides an IR spectrum for the thermopiles to analyze samples are not constant.

Consequently, the outputs of the thermopiles are unstable and the outputs contain errors.

To correct these errors, the information of the background noise, environment temperature agitation, and regulator voltages can be used. The information is collected by using a temperature sensor and voltage monitors. If the correlation between the signals, ***Y***, and noises, or unstable conditions, ***X***, is linear, the output correction problem can be feasibly fixed by polynomial regression models based on least squares. In practice, the correlation between ***Y*** and ***X*** can be nonlinear. In this case, data with errors can be corrected by the divide and conquer algorithm which was applied in [C6.12]. In that algorithm, the main domain is divided into subdomains to linearize the studied problem.

Another way to process the output data with error is applying Deep Machine Learning (DML) or Artificial Neural Network (ANN) [C6.13]–[C6.15]. ANN is a versatile method which can be used in pattern recognition [C6.16], motion artifact correction [C6.17], controlling nonlinear system [C6.18], dynamic error correction for a gas sensor [C6.19] to noise reduction in seismic data [C6.20]. In the research of "abnormal odor detection in electronic nose", L. Zhang et al. [C6.21] proposed self-expression model (SEM) and extreme learning machine (ELM) base self-expression (SE^{2}LM). In their work, errors were used to distinguish the targets and the abnormal odors. The only trained data of the targets were used to train SEM and SE^{2}LM, and some abnormal data were used to test the algorithms. In theoretical research of digital signal processing, D. Wang et al. [C6.22] suggested a multi-innovation stochastic gradient algorithm (MISG) to process error system of multi inputs and multi outputs. The algorithm was proven as being useful and effective for filtering and signal processing.

In this study, to train ANN modules and correct the errors of thermopile data, an innovative method was proposed by using:

- Background noises received from processing the thermopile data.
- Multiple support inputs collected from operating-condition monitors.

The operating-condition monitors are a temperature sensor and two voltage-monitors installed into the device. The support inputs, background noises and the trained ANN modules can fix data with errors. The rest of the paper is structured as follows. Section 2 is the background of the data processing technique and ANN theory. Section 3 provides the methodology to collect and process data. Section 4 introduces results and discussion about the results. Finally, section 5 concludes the work.

6.2. Background

Based on the biology neuron, an artificial neuron includes *I* inputs $\{x_1, x_2,\ldots, x_I\}$ standing for dendrites, *I* weights standing for synapses $\{w_1, w_2,\ldots, w_I\}$, a summation and an activation function σ standing for a cell body, and an output, a, presenting an axon [C6.14], [C6.15]. Besides, an artificial neuron can have a threshold or bias b. The output is:

$$a=\sigma(b+\sum_{i=1}^{I} x_i w_i)=\sigma(z) \tag{6.1}$$

where: $z=b+\sum_{i=1}^{I} x_i w_i$. The activation function can be a linear function, sigmoid function, binary step, tanh, hyperbolic tangent, rectified linear unit (ReLU), Leaky ReLU, sigmoid-weighted linear unit (SiLU), softplus functions, etc. [C6.14], [C6.15], [C6.23], [C6.24]. As ANN requires training processes to find weights and biases based on training data and certain training conditions such as Bayesian information criterion (BIC), Akaike information criterion (AIC), quadratic loss, absolute loss, or number of epochs [C6.15], [C6.23], [C6.25]. Since the quadratic loss is feasible, it is usually used in ANNs:

$$L(y,\hat{y})=\|\boldsymbol{O}-\boldsymbol{Y}\|^2 \tag{6.2}$$

in which $\boldsymbol{Y}$ is the estimate from the training, and $\boldsymbol{O}$ is the truth or target [C6.25]. If $\boldsymbol{X}|_k=[x_1|_k, x_2|_k, \ldots, x_i|_i, \ldots, x_I|_k]_{Ix1}$ is the data vector input, and $\boldsymbol{O}|_k=[o_1|_k, o_2|_k, \ldots, o_p|_k, \ldots, o_P|_k]_{Px1}$ is the output target at the k^{th} training dataset. *k* can be also considered as the discrete-time *k* in training. From (6.2), the mean squared error (MSE) or the quadratic cost function is defined as:

$$C(\boldsymbol{O},\boldsymbol{Y})=\frac{1}{2}\|\boldsymbol{O}|_k-\boldsymbol{Y}|_k\|^2=\frac{1}{2K}\sum_{k=1}^{K}\sum_{p=1}^{P}[o_p-y_p]^2 \tag{6.3}$$

As $\boldsymbol{Y}$ is expected to be as close as possible $\boldsymbol{O}$ or MSE is minimum, the training process is actually an optimal problem of weights and biases. For training ANN, there could be three methods such as supervised, unsupervised and reinforcement learnings [C6.15], [C6.23]. Backpropagation algorithm (BPA) or chain rule of derivative to estimate the gradient descent (GD) of the cost function of an ANN [C6.15] is a popular method of supervised learning. The weights and biases of the ANN will be adjusted by following the gradient descent of $C(\boldsymbol{O},\boldsymbol{Y})$. Thus, the BPA requires the activation function must be partially differentiable. The main drawback of applying the equation (6.3) in BPA is it can last long as it requires all the learning samples [C6.26]. Another method is stochastic gradient descent (SGD) [C6.25], [C6.27]. In this algorithm, with *K* samples, there will be *K* times to update the parameters. A training from loading all *K* samples is called one epoch. Let an ANN be defined as multilayers in Figure 6.1. There are L+1 layers in the ANN. $\boldsymbol{X}^{(0)}$ and $\boldsymbol{Y}^{(L)}$ are the input and output vectors of the input layer (0) and the output layer (L) respectively. $\boldsymbol{A}^{(1)}$, …, $\boldsymbol{A}^{(l)}$, …, $\boldsymbol{A}^{(L-2)}$, $\boldsymbol{A}^{(L-1)}$ are the output vectors of the layers (1), …, (l), …, (L-2), (L-1), (L) respectively. $\boldsymbol{W}^{(1)}$, …, $\boldsymbol{W}^{(l)}$, …, $\boldsymbol{W}^{(L-1)}$, $\boldsymbol{W}^{(L)}$ and $\boldsymbol{B}^{(1)}$, …, $\boldsymbol{B}^{(l)}$, …, $\boldsymbol{B}^{(L-1)}$, $\boldsymbol{B}^{(L)}$ are the weight and bias matrices between the layers: {(0)&(1)}, …, {(l-1)&(l)}, …, {(L-2)&(L-1)}, {(L-1)&(L)} respectively. The number of nodes of each layer can be seen in Figure 6.1.

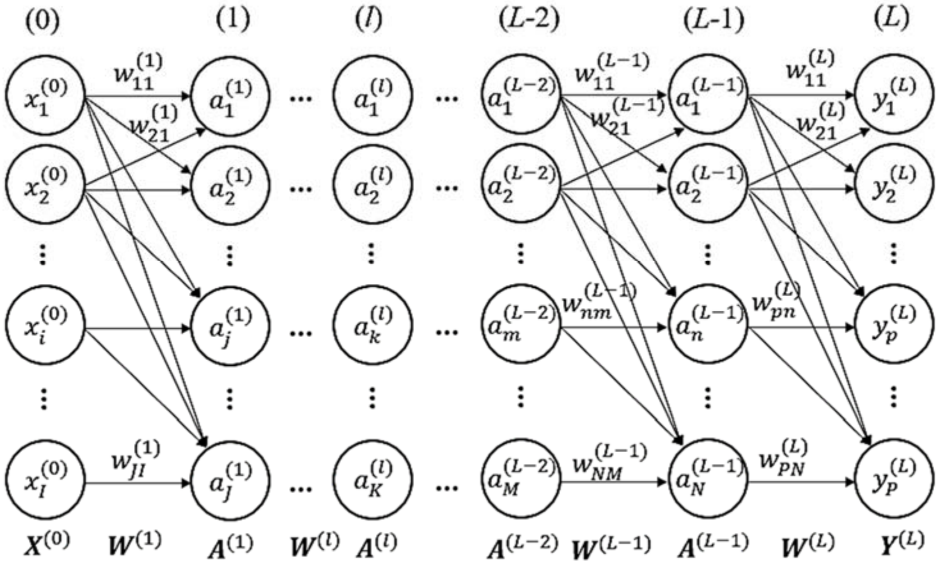

Figure 6.1. Illustration of an FNN with multilayers and multi nodes. The number of the nodes of each layer can be adjusted by a desire.

In training, all the weights and biases are randomly initiated for calculation. From equation (6.1), the output of the k^{th} neuron of the hidden layer l is:

$$a_k^{(l)}=\sigma\left(b_k^{(l)} + \sum_{r=1}^{R} w_{kr}^{(l)} . a_r^{(l-1)}\right)= \sigma\left(z_k^{(l)}\right) \tag{6.4}$$

where $z_k^{(l)}=b_k^{(l)} + \sum_{r=1}^{R} w_{kr}^{(l)} . a_r^{(l-1)}$, $a_r^{(l-1)}$ is the output of the r^{th} neuron of the layer (l-1), and $w_{kr}^{(l)}$ is an element at the r^{th} column and k^{th} row of $\boldsymbol{W}^{(l)}$. The equation (6.4) and (6.5) can be written in matrix forms which are useful for programing:

$$\boldsymbol{A}^{(l)}= \sigma\left(\boldsymbol{B}^{(l)} + \boldsymbol{W}^{(l)}.\boldsymbol{A}^{(l-1)}\right) \tag{6.5}$$

$$\boldsymbol{Y}^{(L)}= \sigma\left(\boldsymbol{B}^{(L)} + \boldsymbol{W}^{(L)}.\boldsymbol{A}^{(L-1)}\right) \tag{6.6}$$

The cost function in SGD at discrete time k is:

$$C(\boldsymbol{O},\boldsymbol{Y}) = \frac{1}{2}\|\boldsymbol{O}|_k - \boldsymbol{Y}|_k\|^2 = \frac{1}{2}\sum_{p=1}^{P}[o_p - y_p^{(L)}]^2 \tag{6.7}$$

The adjustment for $w_{pn}^{(l)}$ and $b_p^{(l)}$ can be found by finding gradient of equation (6.7) [C6.25]. From the observation of the above equations and the calculation rule, the SGD-BPA can be formed for a certain layer (l):

$$\boldsymbol{E}^{(L)} = [\boldsymbol{O} - \boldsymbol{Y}^{(L)}] \odot \boldsymbol{D}^{(L)} \tag{6.8}$$

$$\boldsymbol{E}^{(l)} = (\boldsymbol{W}^{(l+1)})^T . \boldsymbol{E}^{(l+1)} \odot \boldsymbol{D}^{(l)} \tag{6.9}$$

$$\Delta \boldsymbol{W}^{(l)}|_{k+1} = -\eta . [\boldsymbol{E}^{(l)}|_k . (\boldsymbol{A}^{(l-1)}|_k)^T] \tag{6.10}$$

$$\Delta \boldsymbol{B}^{(l)}|_{k+1} = -\eta . \boldsymbol{E}^{(l)}|_k \tag{6.11}$$

The symbol ⊙ is used in the Hadamard product [C6.25]**.** η is the learning rate. If η is so small then the training NN can last long, but if η is large, the training NN cannot converge and fluctuate surrounding the global minima. To be easier in finding the solution, gradient descent with momentum was suggested. The idea is based on the slope or gradient of the calculated weight at time k to update the weight at time k+1 [C6.25], [C6.28]. Nesterov gradient is an upgraded momentum method by using the gradient of the previous gradient multiplying a momentum constant [C6.25], [C6.29], [C6.30].

6.3. Signal processing methodology

6.3.1. Device description

From the existed system of *Fusarium* detection in [C6.8], a DS18B20 temperature sensor [C6.31] and two simple voltage-monitoring (VM) modules were installed into the device to monitor the output of the 5V and 9V regulator circuits. DS18B20 device is a 1-wire digital thermometer and provides "9-bit to 12-bit Celsius temperature measurements" [C6.31]. The VM modules are digitalized by 10-bit analog-to-digital integrated circuit (ADC) modules which belong to an Atmega-328P Arduino board [C6.32]. The spore-trap chamber sketch and the detection system are shown in Figure 6.2. In Figure 6.2(b), the temperature sensor - T, 5V-monitor – V1, and 9V-monitor – V2 were installed to monitor operating conditions. In Figure 6.2(a), the IR MEMS source is a 2.2mm×2.2mm JSIR350-4-AL-C-D3.7-2-A5-I using MEMS technology [C6.33] which can provide an infrared (IR) spectrum of 1 to 20μm. In the experiment, the MEMS source operated at 5.65V and 141.mA. The broadband thermopile is a 2mm×2mm 2M thin film-based single element thermopiles of Dexter Research Inc. [C6.11]. This thermopile responds to the spectrum of 100nm to 100μm. This thermopile was used to monitor the IR light source. From Beer-Lambert law, a group distinction coefficient equation was proposed in [C6.8], in which if two distinct monochromatic light intensities of an IR spectrum are known, the corresponding substance can be identified. From the *Fusarium spore* absorption spectrum described in [C6.8], the two distinct chosen wavelengths are λ_1=6.09μm and λ_2=9.49μm thermopiles. Two thermopiles which work at these two distinct wavelengths were designed by a combination of two 2mm×2mm 2M thermopiles and two optical narrow-band window filters of λ_1=6.09±0.02μm and λ_2=9.49±0.22μm. The IR filter windows are made by Northumbria Optical Coatings Ltd [C6.34].

When the IR light from the MEMS source enters the three thermopiles, it is converted into analog signals which are very small and must be amplified. The amplifier positions are illustrated in Figure 6.2(b). The preamplifiers and the second stage amplifiers are the AD8629 [C6.9]. The final stage amplifier is the OPA320 [C6.34]. These amplified signals are digitalized by a 24-bit LTC2400 ADC [C6.36]. The ATMEL 328-P controls the 74HC4051D [C6.37] multiplexer to read data from the three thermopiles and the three operating-condition monitors. The data are then sent to a computer for signal processing. MATLAB programs are used to receive, save and process data from the device. The vacuum pump in Figure 6.2(b) draws the outer air into the trap chamber. The high voltage module provides electrostatic charges to sample the particles in the air.

6.3.2. Data and signal feature

The *Fusarium* detection device is powered by the GW Instek GPD-4303S power supply which has 0-30V/0/30/05V/05V corresponding 0-3A/0-3A/0-3/0-1A outputs. In the experiments, the GW Instek GPD-4303S supplied voltages to the IR source of the *Fusarium* device by channel 2. The output from a channel of the GW Instek was set at 12.300V, 12.000V, 11.700V, 11.400V, 11.100V, 10.800V, 10.400V, and 10.100V to simulate the unstable power supply, respectively. At each voltage, 500 data were automatically recorded, numbered, and saved in a folder by a data-collected program. Thus, 4,000 data samples were collected in these cases. The data were automatically and consecutively collected in about a week from daytime to nighttime to mimic the normal operating condition. As the IR source cannot be turned ON for a long time, it was alternatively switched ON and OFF in the measurement. The ON time was 1.5s, and the OFF time was 6s. When the IR source was in ON and thermal-balancing periods (Figure 6.3(b)), the data set of a thermopile was called as peak data (PD). The data structure which was sent to the computer is shown in Figure 6.3.

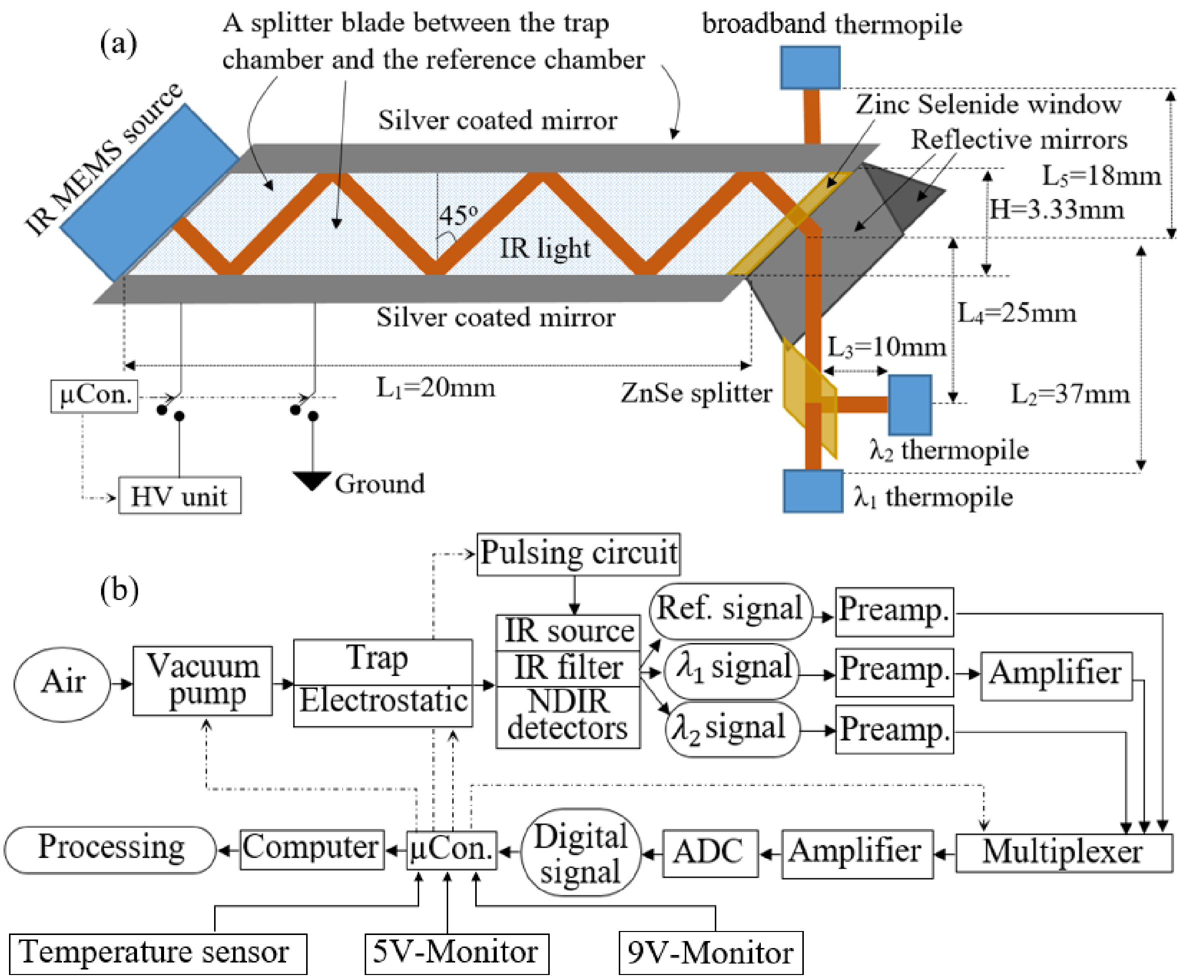

Figure 6.2. (a): the designed trap chamber structure; (b): the detection system diagram. The controlling buses are the dash lines.

The temperature data (T1 and T2) of the air and the output voltage data of the 5V regulator (V1 and V3) and 9V regulator (V2 and V4) were measured two times at the beginning and ending of a data file. The average values of these quantities provide the information of the operating conditions. These data and the data of the three thermopiles are separated by “00”, “11”, “22”, and “33” as shown in Figure 6.3 (a). “ST” and “LR” show the *start* and *end* of the data. The next data are collected after 2 minutes after the last recorded data.

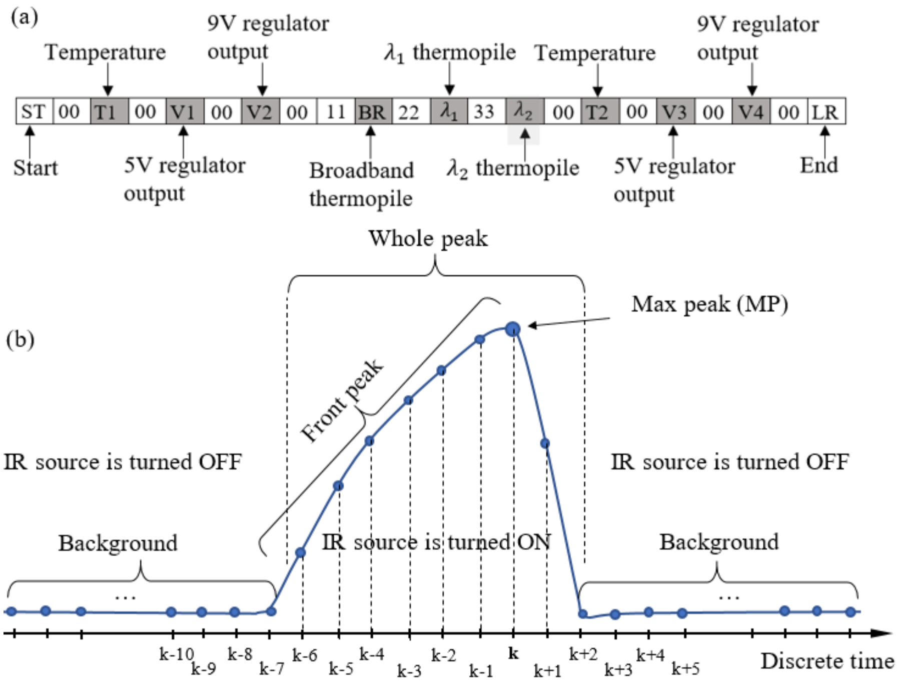

Figure 6. 3. Data structure. (a): a data file structure; (b): an IR pulse structure.

The gains of the amplifiers can be affected by many factors such as environment temperature, unstable power supply [C6.12], background noise, etc.. For short, these effect factors are called as "β". As mentioned above, the temperature and the unstable-power-supply effect are monitored by the temperature sensor and voltage monitors. The mean value of the background of data (Figure 6.3) is named BG. Therefore, β = (BG, T1, T2, V1, V2, V3, V4). At certain β condition, we can have:

$$y = x_E * G(\beta) \tag{6.12}$$

where G is the gain of the amplifier, and x_E is the input of the amplifier. The gains of the amplifiers for the signals from the thermopiles are high, so small changes of β can result in unstable output y. From equation (6.12), if x_E and β are unchanged, y will be also unchanged. Unfortunately, β are not constant, so y will be changed even x_E=constant. To overcome the difficulty, let's set standard-operating conditions, $\beta = \beta_s$, for the system, so: $y_s = x_E * G(\beta_s)$ is the standard output. When $\beta \neq \beta_s$, so $y = x_E * G(\beta) \neq y_s$. Let's define a ratio function R:

$$R = \frac{y_s}{y} \rightarrow R = \frac{G(\beta_s)}{G(\beta)} \tag{6.13}$$

From (6.13), $R \in \beta \,\&\, \beta_s$. In the later measurements, at a certain β condition, then the standard output of any x_E can be found again by applying (6.13):

$$y_s = y * R = x_E * G(\beta) * R \tag{6.14}$$

Therefore, equations (6.13) and (6.14) provide a method to correct the output in case of the operating conditions are not standard. To be able to correct the output at any case, the output at all operating conditions should be measured with x_E kept unchanged. In practice, the output of the device can be investigated under many conditions of β.

With a digital signal processing (DSP) module, if the current output depends on the input at the previous times, the DSP module is a causal module. In case of that the output of a DSP module at a certain time depends on the inputs of the latter times, the DSP module is considered as a non-causal module [C6.38]. In Figure 6.3(b), the BG, front peak (FP), whole peak (WP), and max peak (MP) of one pulse of a thermopile are shown. Let's define k is the time when MP occurs. Any training case which uses the data of later discrete times (k+1, k+2, k+3, …) is a non-causal training (NCT).

6.3.3. Signal processing

In experiments, for a sample case, data of each thermopile were measured in many batches (batch set) to learn the rule of change. In each batch, a BG, FP, WP, and MP of each thermopile along with T, V1, and V2 were calculated from the data structure shown in Figure 6.3. From data structure in Figure 6.3(b), BG is the mean of the background, and MFP is the mean of the front peak; MWP is the mean of the whole peak; MP is the maximum value of a whole peak. In a batch set, **BG** and **MP** are the data vectors of a set of BG and MP respectively. Likewise, **T1**, **T2**, **V1**, **V2**, **V3**, **V4**, **MFP**, and **MWP** are the data vectors of T1, T2, V1, V2, V3, V4, MFP, and MWP.

When BG changed, then WP as well as MP changed in a similar trend. In another word, BG affected most to WP and MP. Thus, for each thermopile case, before the training, it was significant to choose a BG from the measured **BG** to set as a standard BG (SBG). Corresponding SBG, a max peak was chosen by averaging **MP** and named as SMP. With a certain β = (BG, T1, T2, V1, V2, V3, V4), it would provide a MP which is equal SMP. Thus, the selection of SBG and SMP was also the selection of a standard condition, β_s. For a thermopile case, choosing SBG was based on the histogram or probability density of **BG** of 4,000 samples. BG with the greatest-appearance frequency was chosen. Figure 6.4 shows a signal processing procedure of λ_1 thermopile. Figure 6.4 points out that with the chosen SMP, the ratio $\boldsymbol{R} = {}^{\mathrm{SMP}}/_{\mathbf{MP}}$ can be calculated. The vector $\boldsymbol{R}$ will be the reference output for the training ANN. The training vector **BG**, **T1**, **T2**, **V1**, **V2**, **V3**,

V4, **STD(BG)**, **MFP**, and **MWP** can be group as the training inputs β for the ANN. The outcome of the training is a trained ANN.

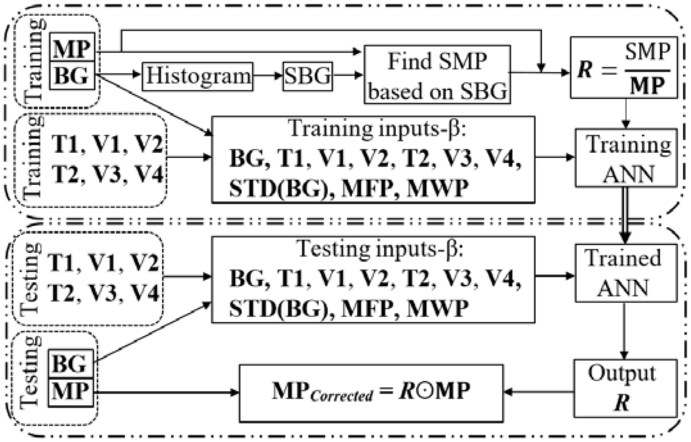

Figure 6.4. Training ANN and testing ANN diagram. **STD(BG)**=Standard deviation of background vector; **MP**, **BG**, **T1**, **T2**, **V1**, **V2**, **V3**, **V4**… are data vectors; SBG and SMP are scalar values.

The testing inputs were used to test the trained ANN. The inputs were loaded by the trained ANN, the output was the ***R*** ratio vector. Applying (6.14) would lead to $\mathbf{MP}_{corrected}$ vector. From the corrected data, the error of the corrected data can be calculated and shown in Figure 6.5. The stop conditions were *loop-index n* ($n<n_o$?) and *absolute error E* ($E<constant\ error$?). If the condition is not satisfied, the program will go back to the training again. The training procedures for three thermopiles are the same.

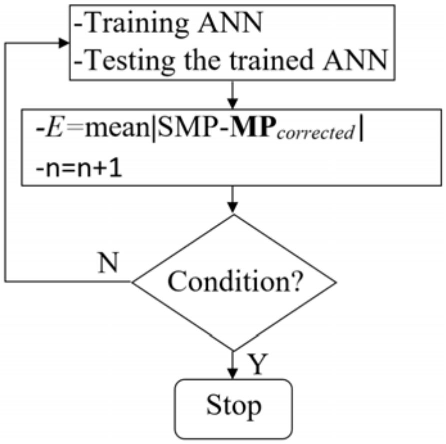

Figure 6.5. Training ANN and testing the trained ANN and stop condition

The inputs are grouped into several different groups to check the work efficiency. The efficiency is mainly based on the error as it is feasible. In the latter groups, the training can be causal or non-causal training.

- Causal training with **BG**.
- Causal training with **BG**, **T1**.
- Causal training with **BG**, **T1**, **V1**, and **V2**.
- Causal training with **BG**, **T1**, **T2**, **V1**, **V2**, and **BG** difference.
- Non-causal training with **BG**, **T1**, **T2**, **V1**, **V2**, **V3**, **V4**, and BG difference.
- Non-causal training with **BG**, $\overline{\mathbf{T}}$, $\overline{\mathbf{V}}\mathbf{1}$, $\overline{\mathbf{V}}\mathbf{2}$, **BG** difference, and mean of the front peak (**MFP**), mean of the whole peak (**MFP**).
- Non-causal training with **BG**, $\overline{\mathbf{T}}$, $\overline{\mathbf{V}}\mathbf{1}$, $\overline{\mathbf{V}}\mathbf{2}$, **BG** difference **ΔBG**, mean of the front peak (**MFP**), mean of the whole peak (**MFP**), and standard deviation (**STD**)….

In practice, a battery is used to power the device. The data were collected to test if the trained ANN can work well, a 12V battery was connected to the *Fusarium* device. The data were loaded by the trained ANN to evaluate the error of the data before and after the correction.

Although ANN does not require normalizing the training data, the training is better in terms of speed and convergence. In the program, the data are normalized in the range of [-1,1] by Min-Max normalization (MMN) [C6.39]. With a data vector $\boldsymbol{X}\{x_1, x_2, \ldots, x_i, \ldots, x_I\}$, the de-normalized vector $\overline{\boldsymbol{X}}\{\bar{x}_1, \bar{x}_2, \ldots, \bar{x}_i, \ldots, \bar{x}_I\}$ is:

$$C=\frac{2}{\max(\boldsymbol{X})-\min(\boldsymbol{X})} \quad \text{and } D=\frac{\max(\boldsymbol{X})+\min(\boldsymbol{X}}{\min(\boldsymbol{X})-\max(\boldsymbol{X})} \tag{6.15}$$

$$\bar{x}_i = x_i{*}C+D \tag{6.16}$$

As a result, after the training, the output data are de-normalized by reversing:

$$x_i = (\bar{x}_i - D)/C \tag{6.17}$$

6.4. Results and discussion

6.4.1. Data analysis

The device which was used in this work was introduced in [C6.8]. In that work, it mainly presented *Fusarium* detection method and the group distinction coefficients of Fusarium (1.144 ±

0.153), pollen (0.136 ± 0.116), starch (0.939 ± 0.073), and turmeric (0.794 ± 0.139). In this current work, the focus was on evaluating the support inputs for processing data by ANN to reduce **BG** or **DC** error. BPA and MSE were used in the ANN. Figure 6.6 shows the data values of the quantities illustrated in Figure 6.3. Figure 6.6(a), (b), and (c) introduce magnitude, structure, and order of the data in a measurement or a data batch. Figure 6.6(d), (e), and (f) are the 3D plots of 4,000 data batches, data points, and **PD**. The correlation between **BG** and **PD** of BR, λ_1, and λ_2 thermopiles can be seen clearly through Table 6.1.

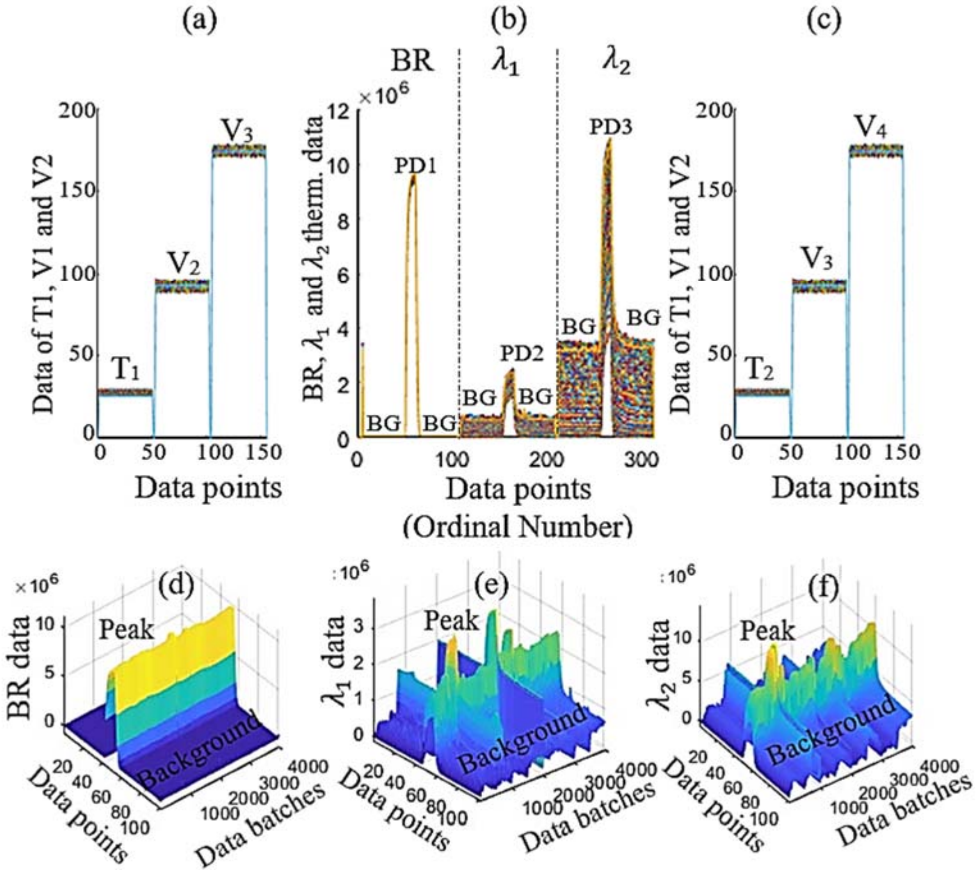

Figure 6.6. Data values from the quantities. (a): start: T1, V1, V2 data; (b): BR, λ_1 and λ_2 data; (c): end: T2, V3, V4 data; (d): 3D plot of BR data; (e): 3D plot of λ_1 data; (f): 3D plot of λ_2 data;

Table 6.1 provides the maxima of **BG** and **MP** variance ranges ($\Delta\mathbf{BG} = |\mathrm{SBG} - \mathbf{BG}|$ and $\Delta\mathbf{MP} = |\mathrm{SMP} - \mathbf{MP}|$), and the correlations (Corr.) between **BG** and **MP**, inverse temperature (T^{-1}) and **MP** of the thermopiles. Table 6.1 also displays the variance ranges of temperature ($\bar{T} = \frac{T1+T2}{2}$), 5V-monitor module ($\bar{V}_1 = \frac{V1+V3}{2}$), and 9V-monitor module ($\bar{V}_2 = \frac{V2+V4}{2}$), the correlation between $\bar{\mathbf{V}}_1$ and $\bar{\mathbf{V}}_2$; $\Delta T = \max(\bar{T}) - \min(\bar{T})$; $\Delta\bar{V}_1$=$\max(\bar{V}_1) - \min(\bar{V}_1)$; $\Delta\bar{V}_2$=$\max(\bar{V}_2) - \min(\bar{V}_2)$;

Table 6.1. Thermopile BR, λ_1, and λ_2 evaluation

Thermopile	**ΔBG**	**ΔMP**	Corr. (**BG**, **MP**)	Corr. ($\boldsymbol{T^{-1}}$, **MP**)	ΔT (°C)	$\Delta\bar{V}_1$ (V)	$\Delta\bar{V}_2$ (V)	Corr. ($\bar{\boldsymbol{V}}_1, \bar{\boldsymbol{V}}_2$)
BR	$1.8*10^4$	$1.0*10^6$	0.3969	0.4624	7.3	0.22	1.26	0.5625
λ_1	$2.0*10^6$	$2.3*10^6$	0.9753	0.0811				
λ_2	$6.4*10^6$	$10.5*10^6$	0.9799	0.1337				

Figure 6.7 presents a better view of the correlation between **BG** and **MP**. The lower curves in each plot are the **BG** plots. The higher curve in each plot is of the **MP**.

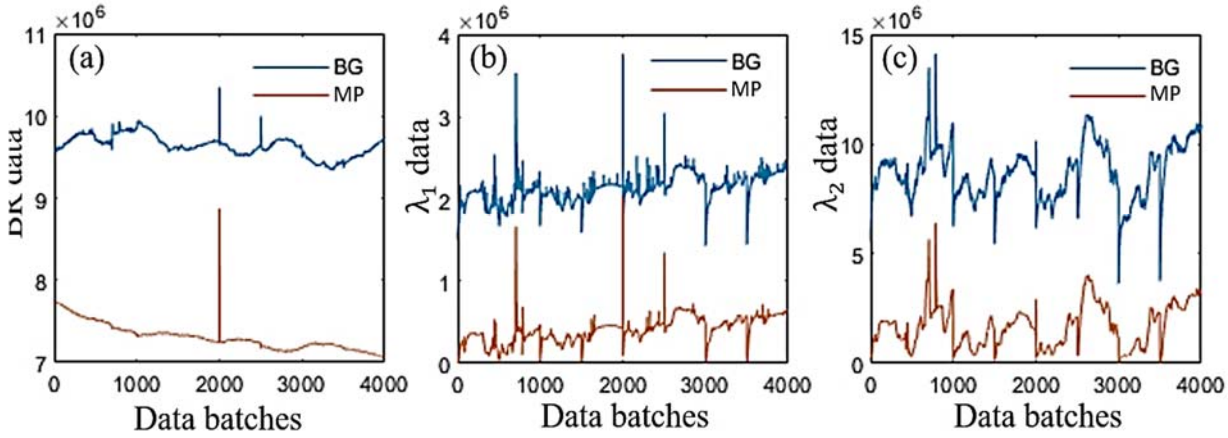

Figure 6.7. Visual evaluation of the correlation between BG and MP through the plots. (a): BR thermopile data plot; (b): λ_1 thermopile data plot; (c): λ_2 thermopile data plot.

To choose SBGs for the thermopiles, the **BG** histograms were investigated and shown in Figure 6.8. Based on the frequency distribution of the **BG**, the SBGs could be selected. The selected SBGs were based on the largest frequency in each histogram of each thermopile.

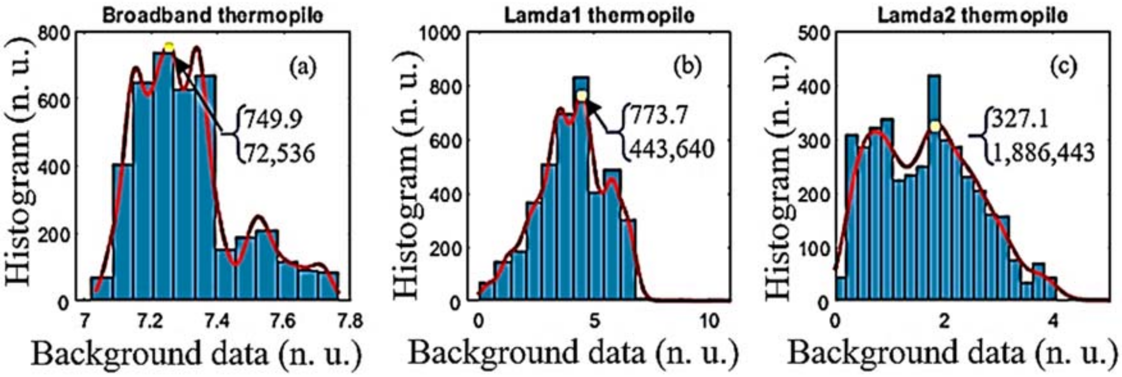

Figure 6.8. Histogram bar charts and fitting plots. (a): broadband thermopile; (b): λ_1 thermopile; (c): λ_2 thermopile.

From the selected SBGs and the MPs of data batches, the SMPs are extracted. Table 6.2 shows the frequency density, the SBGs, and SMPs of the thermopiles.

Table 6.2. BR, λ_1, and λ_2 frequency, SBG and SMP values

Thermopile	Frequency	SBG	SMP	Total samples
BR	749.9	72,536	9568778	4,000
λ_1	773.7	443,640	2,155,801	
λ_2	327.1	1,886,443	9,012,986	

6.4.2. Internal training

Internal training means that the training NN used the training samples to test the solution after each training. The raw max peak data set was symbolized as **MP**$\{MP_1, MP_2, \ldots, MP_i, \ldots, MP_{4000}\}$. The controlling criterion was based on the mean of absolute error of the corrected outputs of max peaks. The corrected max peak data set was symbolized as **MP**$_C\{MP_{c1}, MP_{c2}, \ldots, MP_{ci}, \ldots, MP_{c4000}\}$. The absolute error of the raw data was:

$$E = \sum_{i=1}^{4000} |MP_i - SMP| \tag{6.18}$$

Similarly, the absolute error of the corrected data was:

$$E_c = \sum_{i=1}^{4000} |MP_{ci} - SMP| \tag{6.19}$$

The designed ANN had 3 layers: one input layer, one hidden layer, and one output layer. As discussed in section *C*, part III, the support information pieces for the training NN were recorded.

The number of the nodes of the input layer depends on which training information is chosen. If only BG information is chosen for the training, then there is only one input node. The designed hidden layer had 3 nodes. The output layer had one node which was the ratio *R* in equation (6.13). In each training, the criteria to stop the training were the epoch number N (N=1000) and the gradient descent error which was 10^{-7}. To assure that the solution achieved from the training in each case was good enough, the training was repeated 20 times, and then the best solution was chosen. After the training, with a certain condition β, the trained ANN module provided a ratio $\boldsymbol{R}\{R_1, R_2, \ldots, R_i, \ldots, R_{4000}\}$. From equation (6.14), multiplying MP_i or y_i with R_i will provide the corrected MP_{ci} or y_{ci} which is close to MP or *y* in standard conditions β_s. Applying equations (6.18) and (6.19) results in Table 6.3.

Table 6.3. Errors of BR, λ_1, and λ_2 thermopiles in different cases

Case	E_{BR}	E_{λ_1}	E_{λ_2}
0	**$6.2521*10^{5}$**	**$6.8927*10^{6}$**	**$1.0116*10^{6}$**
1	$7.4780*10^{4}$	$2.3485*10^{4}$	$11.879*10^{4}$
2	$1.2118*10^{4}$	$1.4044*10^{4}$	$7.8280*10^{4}$
3	$1.1951*10^{4}$	$1.4013*10^{4}$	$7.5830*10^{4}$
4	$1.1591*10^{4}$	$1.3985*10^{4}$	$6.8520*10^{4}$
5	$1.1554*10^{4}$	$1.3897*10^{4}$	$6.8330*10^{4}$
6	$0.4113*10^{4}$	$1.0151*10^{4}$	$5.0540*10^{4}$
7	$0.4109*10^{4}$	$1.0112*10^{4}$	$5.0550*10^{4}$
8	$0.3717*10^{4}$	**$1.0034*10^{4}$**	$5.0670*10^{4}$
9	**$0.3698*10^{4}$**	$1.0117*10^{4}$	**$5.0460*10^{4}$**
$E_{raw}/E_{corrected-min}$	**169.0**	**686.9**	**20.0**

Case 0: uncorrected data; Case 1: **BG**; Case 2: **BG** and **T1**; Case 3: **BG**, **T1**, **V1**, and **V2**; Case 4: **BG**, **T1**, **V1**, **V2**, **V3**, and **V4**; Case 5: **BG**, **T1**, **V1**, **V2**, **V3**, **V4**, and **ΔBG**; Case 6: **BG**, $\overline{\mathbf{T}}$, $\overline{\mathbf{V1}}$, $\overline{\mathbf{V2}}$, **ΔBG**, mean front peak (**MFP**); Case 7: **BG**, $\overline{\mathbf{T}}$, $\overline{\mathbf{V1}}$, $\overline{\mathbf{V2}}$, and mean front peak (**MFP**); Case 8: **BG**, $\overline{\mathbf{T}}$, $\overline{\mathbf{V1}}$, $\overline{\mathbf{V2}}$, (**MFP**), and mean whole peak (**MWP**); Case 9: **BG**, $\overline{\mathbf{T}}$, $\overline{\mathbf{V1}}$, $\overline{\mathbf{V2}}$, **MFP**, **MWP**, and standard deviation of **BG** (**STD(BG)**);

Figure 6.9 depicts the **MP** data with error and the corrected **MP** data from case 1 to case 9 which were applied for the data of the three thermopiles Case 0 corresponded to without processing the error of the **MP** data. Case 1 used **BG** input to train the ANN. In the next cases, one or two more support inputs were added for the training ANN module respectively. Case 9 had the most support inputs for the training. If all of the errors are removed from the data, the corrected plot should be a straight line and parallel with the *x*-axis. Briefly looking through all the results, case 9 achieves the best results.

To have a visual view of the training and their errors in these cases, Figure 6.10 illustrates the absolute errors of the three thermopiles in each training. In each training case, 20 sub trainings were conducted to select the best weights and biases, in which, the corresponding absolute error was the smallest. Because the solution from a training time depends on the initial weights and biases, these sub trainings can help to find a global minimum. Thus, the best trained ANN can be found. Through the plots, one can see that some trainings provided errors far from the smallest absolute error. Thus, repeating the training is a good method to achieve good solutions.

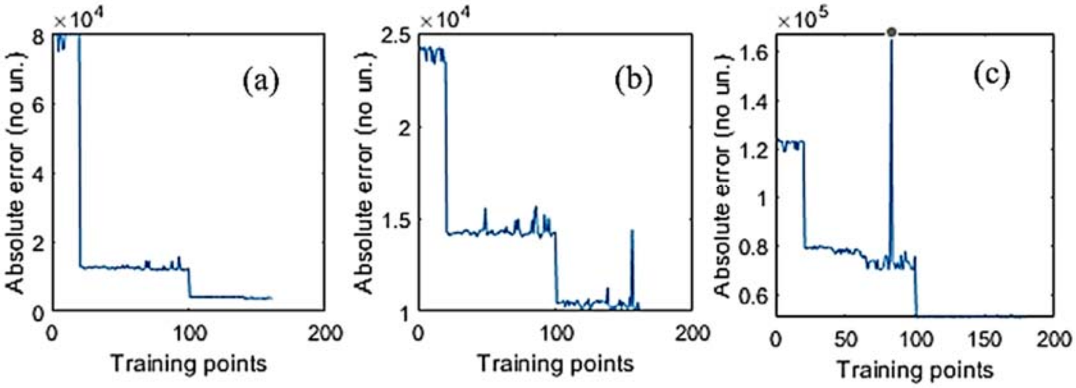

Figure 6.9. The illustrations of the absolute errors in the nine training cases. (a): broadband thermopile; (b): λ_1 thermopile; (c): λ_2 thermopile.

After having the three trained ANN modules for each thermopile, these modules were tested by different data which are different to the training data. The 12V battery introduced in section *C*, part III was used to power the *Fusarium* device. Then, data were collected. The data were processed by the trained ANN modules. The number of batches was 1000, so there were 1000 data samples being used for the test. For each thermopile, the trained ANN module was selected based on the corresponding smallest error shown in Table 6.3. Table 6.4 shows the absolute errors of the uncorrected and corrected data by applying equation (6.18), (6.19), and the trained ANN for the testing data.

Table 6.4. Errors of BR, λ_1, and λ_2 thermopiles in two cases

Case	E_{BR}	E_{λ_1}	E_{λ_2}
raw	$1.0470*10^5$	$1.0547*10^5$	$9.0116*10^5$
corrected	$7.9973*10^4$	$1.2629*10^4$	$5.4954*10^4$
$E_{raw}/E_{corrected}$	1.31	8.35	16.39

The visual view to evaluate the efficiency of the correction is presented in Figure 6.11. In the figure, the plots of the raw **MP** data and corrected **MP** data are introduced. It can be seen that the **MP** correction of broadband thermopile was poor. The corrections of λ_1 and λ_2 thermopiles were good.

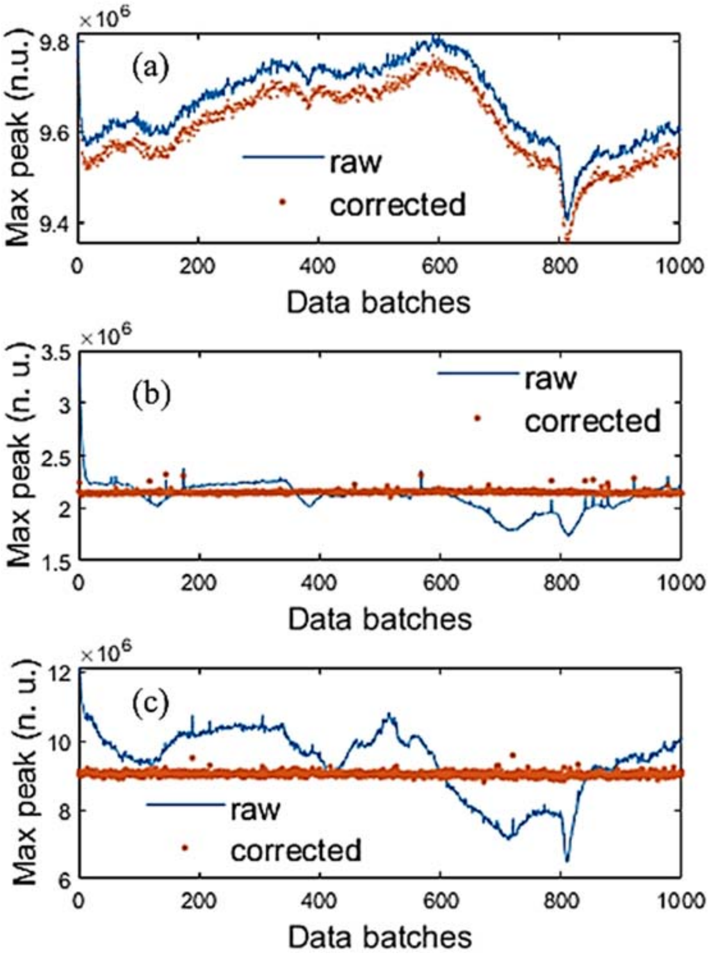

Figure 6.10. The illustrations of the absolute errors of the uncorrected and corrected data. (a): broadband thermopile; (b): λ_1 thermopile; (c): λ_2 thermopile.

6.4.3. External training

External training means the training ANN will use the external data which are different from the training samples to test the solution after each training. The testing is the data collected when the battery powers the device. From equation (6.18), the absolute error of the corrected data can be calculated. Table 6.5 shows the errors in the different cases. The studied cases in Table 6.5 were introduced in part *B* of this section.

Again, to have a visual view of the training, Figure 6.12 shows the plots of the corrected and uncorrected data. There could be seen an improvement when looking at Table 6.4 and 6.5.

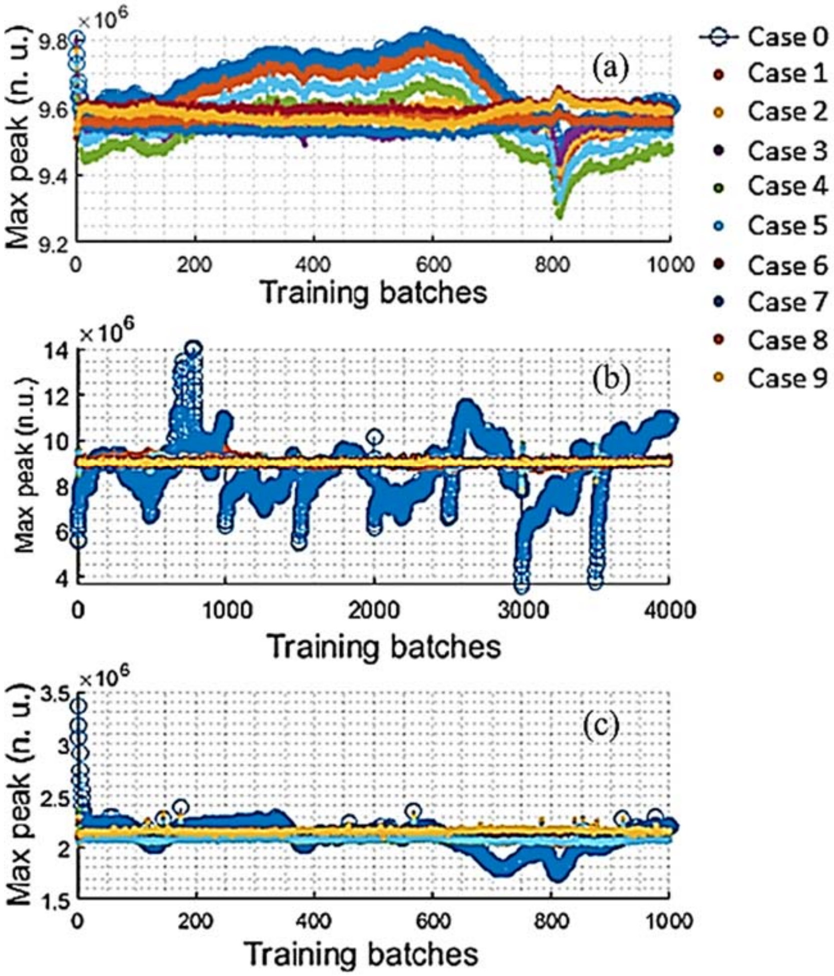

Figure 6.11. Max peak data of the three thermopiles in ten cases. (a): BR thermopiles; (b): λ_1 thermopile; (c): λ_2 thermopile.

However, this improvement is not as expected. Therefore, in the next subsection, we applied the *forcing training*, in which the training ANN was forced to run until reaching the assigned goals or conditions.

6.4.4. Forcing training

Through experiments, case 9 of grouping is chosen based on the errors in Table 6.3 and 5. In this case, the support inputs include **BG**, $\overline{\mathbf{T}}$, $\overline{\mathbf{V1}}$, $\overline{\mathbf{V2}}$, mean-of-front peak (**MFP**), mean-of-whole peak (**MWP**), and **STD**.

Table 6.5. errors of BR, λ_1, and λ_2 thermopiles in different cases

Case	E_{BR}	E_{λ_1}	E_{λ_2}
0	**1.0470*10^5**	**1.0547*10^5**	**9.4137*10^5**
1	0.7812*10^5	6.6324*10^4	2.7054*10^5
2	1.1853*10^5	8.0331*10^4	2.0331*10^5
3	0.9062*10^5	8.1524*10^4	2.7010*10^5
4	0.9950*10^5	8.7102*10^4	2.1898*10^5
5	0.8098*10^5	8.2281*10^4	2.2356*10^5
6	0.6003*10^5	1.1409*10^4	0.5224*10^5
7	1.3062*10^5	0.9472*10^4	0.5339*10^5
8	0.4250*10^5	**0.9249*10^4**	0.5230*10^5
9	**0.3731*10^5**	1.2770*10^4	**0.5106*10^5**
$E_{raw}/E_{corrected-min}$	**2.81**	**11.40**	**18.43**

In the training, the goals were set up for the thermopiles: *absolute error<10,000* or reaching *1000 loops*. Table 6.6 shows the absolute errors, the signal to noise ratios (*SNR*s), the standard deviations of the backgrounds ($\overline{STD}$(**BG**)), and the standard deviation of the corrected **MP** data (*STD*(**MP**)) before and after the corrections. Although, the method was simple, all of the results were improved. $E_{corrected}$ values of the thermopiles were also all improved well, especially the BR and λ_1 thermopiles. According to A. Felinger in [C6.40], the SNR of a stable signal can be estimated by:

$$\text{SNR}=\frac{mean\ of\ signal}{STD\ of\ signal} \tag{6.20}$$

As expected, the **MP** should be stable in the measurements. The definition of equation (6.20) can be applied for both of the uncorrected and corrected **MP**. $\overline{STD}$(**BG**) is the average of standard deviation of **BG**. In Table 6.6, $SNR_{STD(\mathbf{MP}_{uncorrected})}$ and $SNR_{STD(\mathbf{MP}_{corrected})}$ were calculated by equation (6.20). In this table, $SNR_{\overline{STD}(\mathbf{BG})}$ values which were estimated by $\overline{STD}(\mathbf{BG})$ also introduced. These $SNR_{\overline{STD}(\mathbf{BG})}$ values provide the figuration of the limitation of $SNR_{STD(\mathbf{MP}_{corrected})}$ which the trainings ANNs can reach. This can be explained by the fact that the background noises of the thermopiles will keep contributing to the noise of the peak data and **MP** data as well. Therefore, $SNR_{STD(\mathbf{MP}_{corrected})}$ values are rarely larger than $SNR_{\overline{STD}(\mathbf{BG})}$, thereby the training goal and stopping conditions can be set up based on these values.

Table 6.6. Investigation of BR, λ_1, and λ_2 thermopiles in applying the forcing method

Quantities	BR	λ_1	λ_2
E_{raw}	**1.0470*10^5**	**1.0547*10^5**	**9.4137*10^5**
$E_{corrected}$	**4.4435*10^3**	**7.6301*10^3**	**5.0848*10^4**
$E_{raw}/E_{corrected}$	**23.5627**	**13.825**	**18.5135**
$\overline{\mathrm{MP}}_{corrected}$	9.6621*10^6	2.1571*10^6	9.0194*10^6
$STD(\mathbf{MP}_{uncorrected})$	8.6504*10^4	1.4662*10^5	9.8848*10^5
$SNR_{STD(\mathbf{MP}_{uncorrected})}$	41dB	42.6dB	19.2dB
$STD(\mathbf{MP}_{corrected})$	5.4013*10^3	1.5999*10^4	6.889*10^4
$SNR_{STD(\mathbf{MP}_{corrected})}$	65dB	42.6dB	42.3dB
$\overline{STD}(\mathbf{BG})$	53.6069	9.6402*10^3	5.9474*10^4
$SNR_{\overline{STD}(\mathbf{BG})}$	105.1dB	47dB	43.6dB

To see how good the corrections of the **MP** data of the thermopiles, the plots of the uncorrected and corrected **MP** are shown in Figure 6.13. In the figure, the red dots and the blue circles are the plots of the corrected and uncorrected **MP,** respectively.

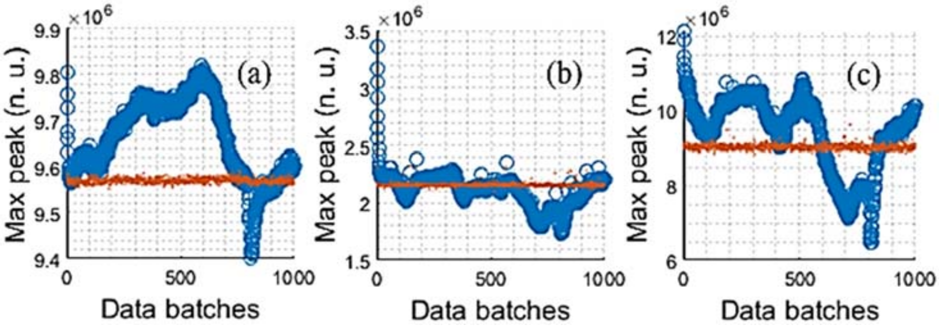

Figure 6.12. Max peak data of the three thermopiles in uncorrected (blue circle) and corrected (red dots) cases. (a): BR thermopiles; (b): λ_1 thermopile; (c): λ_2 thermopile.

The final trained ANN diagram for the thermopiles are presented in Figure 6.14. The weights and biases of each thermopile are different in values but similar in size with the other thermopiles.

The activation function for the hidden layer is a hyperbolic tangent sigmoid function [C6.16]:

$$f(x) = tansig(x) = \frac{2}{1+e^{-2x}} - 1 \tag{6.25}$$

The activation function for the output is identity function:

$$f(x) = x \tag{6.26}$$

An example of the weight and bias matrices of λ_1 ANN module:

$$[\mathbf{W}]_{3x7}$$

$$\begin{bmatrix} 0.7843 & -0.2677 & 0.7130 & -0.0979 & -0.6613 & -0.0637 & 0.2825 \\ -0.6653 & 0.0869 & 0.1575 & -0.0211 & 0.1268 & 1.8016 & 0.0969 \\ 1.1568 & -0.3625 & 0.6878 & -0.0866 & 0.6642 & -1.3996 & 0.2659 \end{bmatrix}$$

$$[\mathbf{B}]_{3x1} \quad \begin{bmatrix} 0.4175 \\ 1.0571 \\ 0.2646 \end{bmatrix} \qquad [\mathbf{W}]_{1x3} \quad \begin{bmatrix} 0.8829 & -1.2047 & -1.0695 \end{bmatrix} \qquad [\mathbf{B}]_{1x1} \quad \begin{bmatrix} 0.2430 \end{bmatrix}$$

The output is the ratio function $\boldsymbol{R}$, so one can write the output function as:

$$\boldsymbol{R}=[tangsig([\mathbf{W}]_{3x7}*[X]_{7x1} + [\mathbf{B}]_{3x1})]^{T}*[\mathbf{W}]^{T}_{1x3} + [\mathbf{B}]_{1x1} \tag{6.27}$$

From equation (6.27) and applying equation (6.19), one can get the corrected MP data as shown in the previous tables and figures.

6.4.5. Discussion

Figure 6.7, Table 6.1, 6.3, 6.5, and 6.6 show that the greater the correlation between **BG** and **MP** is, the better the correction will be. The correlation between $\overline{\mathbf{T}}$ and **MP** of the BR thermopile is larger than the other thermopiles. Thus, the **MP** correction of BR thermopile is better than the other thermopiles correction (Table 6.3 and Table 6.5: comparing case 1 of using **BG** information with case 2 of using **BG** and **T1** information).

As ANN is deep machine learning, the training data and the external data should be large enough to cover as much as possible the operating conditions. Adding more support inputs can help to fix data better. However, the trade-off is the training time as it requires a longer time to find the global minima. It is due to the fact that the more variables there are, the more local minima the error cost function will have. These minima can deter the training ANN from finding the global minima. To reduce the training time, only important inputs are kept, and unimportant inputs or similar inputs are eliminated such as **V1**, **V3**, **V2, V4, T1**, or **T2**.

In case 6, when adding **MFP** or **MWP**, the correction results are developed. It can be explained that during the data collection of an IR pulse, the data points of peaks can also be influenced by noises and deviated from the sloping trend. Therefore, the slope is not as smooth as the illustration in Figure 6.3. **MFP** or **MWP** takes roles of reference information to adjust the **MP**. The standard deviations of the background noises of the BR, λ_1, and λ_2 thermopiles also assist in the correction process. The effect can be seen in Table 6.3 and 6.5.

The external training provides better results in comparison with the internal training. In the internal training, because the training data are reused to test the solutions, it can favorably satisfy the stop condition. However, it cannot satisfy well the external data. On the other hand, the external training using the external data to test the solution at each training, so the method forcing the ANN must find a solution which can satisfy the external data rather than the training data.

From Table 6.6, it is recommended to find the $SNR_{\overline{STD}(\boldsymbol{BG})}$ or at least $\overline{STD}(\mathbf{BG})$ to set up an appropriate training goal and stop condition. If this step is not conducted, the training can fall into two cases of either running too long but cannot achieve the goal, or pseudo-global minima when the goal is badly set up.

A weak point is that at a few points of the corrected **MP** data, the corrected **MP** points are not really good and diverted from the straight line. This can be explained that these **MP** points are affected by burst noise or outliers which cannot be monitored by the installed monitoring modules. In case **BG** is affected by the burst noise, then it will lead to the wrong correction of **MP**.

The choice of SBG is not really strict. However, with careful choice such as using the histograms, it can increase the reliability and confidence of the device. If a chosen SBG is too far from the most frequent BG, then the program will often potentially process large errors. As a result, the corrected data can still contain some errors.

6.5. Conclusion

The NN, background data, and support inputs which are the data vectors from the add-on sensor and the monitoring modules are used to correct data with error in a nondispersive thermopile device. The other statistical quantities such as the standard deviations, the mean-of-front peak, or the mean-of-whole peak also can be used to improve the correction. ${E_{raw}}/{E_{corrected}}$ of broadband, λ_1, and λ_2 thermopiles are improved by 23.5627, 13.825, and 18.513 times, respectively. To achieve these results, the *forcing training* was applied in the training, but the tradeoff, in this case, is time-consuming. The mean-of-front peak or the mean-of-whole peak, and standard deviation of the background of the thermopile signals are also quite useful in the error correction. The research also revealed that the external training provides a better solution than the internal training. As the number of weights and bias are small, these parameters can be embedded into a microcontroller to process signals.

The data with burst noise are difficult to fix. Using preprocessing techniques such as digital filters, Kalman filter, and outlier elimination techniques can help to overcome the problem. The application of using the support inputs and neural network to fix error data can be applied in electronics devices which have unstable outputs and the operating conditions which can be monitored.

References

[C6.1] G. Vasilescu, “Physical Noise Sources,” in *Electronic Noise and Interfering Signals - Principles and Applications*, Printed in Germany: Springer, 2004, pp. 45–67.

[C6.2] Texas Instruments, “Noise Analysis in Operational Amplifier Circuits,” *Texas Instrument*, 2007. [Online]. Available: http://www.ti.com. Accessed: 01-Aug-2019.

[C6.3] L. Dan, W. Xue, W. Guiqin, and Q. Zhihong, “A Methodological Approach for Detecting Burst Noise in the Time Domain,” *Int. J. Electron. Commun. Eng.*, vol. 3, no. 10, p. 5, 2009.

[C6.4] E. B. Moullin and H. D. M. Ellis, “The spontaneous background noise in amplifiers due to thermal agitation and shot effects,” *Inst. Electr. Eng. - Proc. Wirel. Sect. Inst.*, vol. 9, no. 26, pp. 81–106, 1934.

[C6.5] Analog Devices, “Op Amp Noise,” *Texas Instrument*, Accessed: 08-Jan-2019.

[C6.6] E. Serrano-Finetti and R. Pallas-Areny, “Noise Reduction in AC-Coupled Amplifiers,” *IEEE Trans. Instrum. Meas.*, vol. 63, no. 7, pp. 1834–1841, Jul. 2014.

[C6.7] R. Wei, Z. Liu, and R. Zhu, “Low noise chopper-stabilized instrumentation amplifier with a ripple reduction loop,” *Analog Integr. Circuits Signal Process.*, vol. 96, no. 3, pp. 521–529, Sep. 2018.

[C6.8] Son Pham, Anh Dinh, and Khan Wahid, “A Nondispersive Thermopile Device with an Innovative Method to Detect Fusarium Spores,” *IEEE Sensors Journal,* vol. 19, no. 19, pp. 8657-8667, October 2019.

[C6.9] Analog Devices, “Zero-Drift, Single-Supply, Rail-to-Rail Input/Output Operational Amplifier AD8628/AD8629/AD8630,” *Analog Device*, 2014. [Online]. Available: www.analog.com, Accessed: 01-Aug-2019.

[C6.10] S. Pham and A. Dinh, “Analysis on Nondispersive Infrared Device Characteristics Using Thermopile,” *IEEE 32nd Can. Conf. Electr. Comput. Eng., CCECE Edmont. Can.*, p. 4, May 2019.

[C6.11] Dexter, “2M Thin Film Based Thermopile Detector,” *Dexter Research Center*. [Online]. Available: https://www.dexterresearch.com/. Accessed: 01-Aug-2019.

[C6.12] S. Pham and A. Dinh, “Using the Kalman Algorithm to Correct Data Errors of a 24-Bit Visible Spectrometer,” *MDPI, Sensors*, vol. 17, no. 12, p. 2939, Dec. 2017.

[C6.13] Amir Amani and Dariush Mohammadyani, *Artificial Neural Networks: Applications in Nanotechnology.* INTECH Open Access Publisher, 2011.

[C6.14] K. Suzuki, Ed., *Artificial Neural Networks - Architectures and Applications,* INTECH Open Access Publisher, 2013.

[C6.15] K. Suzuki, Ed., *Artificial Neural Networks - Methodological Advances and Biomedical Applications,* INTECH Open Access Publisher, 2011.

[C6.16] X. Zhang, L. Zhao, W. Zhao, and T. Xu, "Novel method of flatness pattern recognition via cloud neural network," *Soft Comput.*, vol. 19, no. 10, pp. 2837–2843, Oct. 2015.

[C6.17] G. Lee, S. Jin, and J. An, "Motion Artifact Correction of Multi-Measured Functional Near-Infrared Spectroscopy Signals Based on Signal Reconstruction Using an Artificial Neural Network," *Sensors (Bassel)*, vol. 18, no. 9, p. 2957, Sep. 2018.

[C6.18] A. Alexandridis, M. Stogiannos, N. Papaioannou, E. Zois, and H. Sarimveis, "An Inverse Neural Controller Based on the Applicability Domain of RBF Network Models," *Sensors (Bassel)*, vol. 18, no. 2, p. 315, Jan. 2018.

[C6.19] J. Roj, "Correction of Dynamic Errors of a Gas Sensor Based on a Parametric Method and a Neural Network Technique," *Sensors (Bassel)*, vol. 16, no. 8, p. 1267, Aug. 2016.

[C6.20] D. Bhowmick, D. K. Gupta, S. Maiti, and U. Shankar, "Deep Autoassociative Neural Networks for Noise Reduction in Seismic data," *Cornell Univ.*, p. 6, May 2018.

[C6.21] L. Zhang and P. Deng, "Abnormal Odor Detection in Electronic Nose via Self-Expression Inspired Extreme Learning Machine," *IEEE Trans. Syst. Man Cybern. Syst.*, vol. 49, no. 10, pp. 1922–1932, Oct. 2019.

[C6.22] D. Wang and F. Ding, "Performance analysis of the auxiliary models based multi-innovation stochastic gradient estimation algorithm for output error systems," *Digit. Signal Process.*, vol. 20, no. 3, pp. 750–762, May 2010.

[C6.23] Y. Zhang, *Machine Learning*, INTECH Open Access Publisher, 2010.

[C6.24] C. Nwankpa, W. Ijomah, A. Gachagan, and S. Marshall, "Activation Functions: Comparison of trends in Practice and Research for Deep Learning," *Cornell Univ.*, p. 20, Nov. 2018.

[C6.25] K. P. Murphy, *Machine learning: a probabilistic perspective*. Cambridge, MA: MIT Press, 2012.

[C6.26] N. Agarwal, Z. Allen-Zhu, B. Bullins, E. Hazan, and T. Ma, “Finding Approximate Local Minima Faster than Gradient Descent,” *Cornell Univ.*, p. 28, Nov. 2016.

[C6.27] X. Li, “Preconditioned Stochastic Gradient Descent,” *IEEE Trans. Neural Netw. Learn. Syst.*, vol. 29, no. 5, pp. 1454–1466, May 2018.

[C6.28] G. Liu, Z. Zhou, H. Zhong, and S. Xie, “Gradient descent with adaptive momentum for active contour models,” *IET Comput. Vis.*, vol. 8, no. 4, pp. 287–298, Aug. 2014.

[C6.29] W. Su, S. Boyd, and E. J. Candes, “A Differential Equation for Modeling Nesterov’s Accelerated Gradient Method: Theory and Insights,” *J. Mach. Learn. Res.*, vol. 17, no. 153, pp. 1–43, 2016.

[C6.30] H. Ninomiya, “A novel quasi-Newton-based optimization for neural network training incorporating Nesterov’s accelerated gradient,” *Nonlinear Theory Its Appl. IEICE*, vol. 8, no. 4, pp. 289–301, 2017.

[C6.31] Maxim Integrated, “DS18B20 - Programmable Resolution 1-Wire Digital Thermometer,” *Maxim Integrated*. [Online]. Available: https://www.maximintegrated.com/. Accessed: 01-Aug-2019.

[C6.32] Microchip, “Atmel 8-Bit Microcontroller with 4/8/16/32kbytes In-System Programmable Flash,” *https://www.microchip.com*. [Online]. Available: https://www.microchip.com. Accessed: 01-Aug-2019.

[C6.33] Micro-Hybrid, “Infrared Radiation Source JSIR350-4-AL-C-D3.7-A5-I,” *Micro-Hybrid*. [Online]. Available: http://www.eoc-inc.com/micro-hybrid/IRSource/JSIR350-4-AL-C-D3.7-A5 l.pdf. Accessed: 01-Aug-2019.

[C6.34] Northumbria Optical, “Narrow Band Pass,” *Northumbria Optical Coatings Ltd*, 2018. [Online]. Available: https://www.noc-ltd.com. Accessed: 01-Aug-2019.

[C6.35] Texas Instruments, “OPAx320x Precision, 20-MHz, 0.9-pA, Low-Noise, RRIO, CMOS Operational Amplifier with Shutdown 1,” *Texas Instrument*, 2016. [Online]. Available: http://www.ti.com. Accessed: 01-Aug-2019.

[C6.36] “24-Bit µPower No Latency ΔΣTM ADC in SO-8,” *Analog Device*. [Online]. Available: https://www.analog.com/media/en/technical-documentation/data-sheets/2400fa.pdf. Accessed: 01-Jun-2019.

[C6.37] Texas Instruments, “74HC4051; 74HCT4051 8-channel analog multiplexer/demultiplexer,” *Texas Instrument*, 2017. [Online]. Available: http://www.ti.com. Accessed: 01-Aug-2019.

[C6.38] S. W. Smith, *The scientist and engineer’s guide to digital signal processing*. San Diego (Calif.): California Technical Pub., 1999.

[C6.39] D. Singh and B. Singh, “Investigating the impact of data normalization on classification performance,” *Elsevier, Appl. Soft Comput.*, 105524, May 2019.

[C6.40] A. Felinger, *Data Analysis and Signal Processing in Chromatography*, vol. 21. Elsevier Science 1998.

7. Adaptive-Cognitive Kalman Filter and Neural Network for an Upgraded Nondispersive Thermopile Device to Detect and Analyze Fusarium Spores

Published as:

Son Pham, Anh Dinh, Adaptive-Cognitive Kalman Filter and Neural Network for an Upgraded Nondispersive Thermopile Device to Detect and Analyze Fusarium Spores, *MDPI Sensors*, 19, 4900, 2019, 21 pages, doi:10.3390/s19224900.

Chapter 4 proposes a non-dispersive device and an innovative method to detect and analyse *Fusarium* spore by applying Beer-Lambert law and group distinction coefficient. Though, the experiments prove that the method works well, there are cases that certain group distinction coefficients are close to each other. As a result, this leads to an incorrect detection from the device. To overcome this problem, the *Fusarium* detection device was upgraded by using a broadband thermopile as the third thermopile along with λ_1 and λ_2 thermopiles to analyse the reflecting IR light from the samples in the HV trap chamber. The third thermopile can be used to confirm whether the sample is *Fusarium* or not. The confirmation is based on the validation area. If the measurement data point is in the validation area, then the sample is *Fusarium*. Thus, the accuracy of the device is improved. To increase the precision, the Kalman algorithm was also applied to process thermal and burst noises, while neural network was employed to eliminate the background noise. The contribution of this work is the proposed signal-data processing not only increases detection confidence but also improves accuracy of the sample quantification.

The main contribution to this manuscript comes from the student (the first author) while the supervisor provides the supervision for the manuscript.

Adaptive-Cognitive Kalman Filter and Neural Network for an Upgraded Nondispersive Thermopile Device to Detect and Analyze *Fusarium* Spores

Son Pham, Anh Dinh

Abstract

Noises such as thermal noise, background noise or burst noise can reduce the reliability and confidence of measurement devices. In this work, a recursive and adaptive Kalman filter is proposed to detect and process burst noise or outliers and thermal noise, which are common electrical and electronic devices. The Kalman filter and neural network are used to preprocess data of three detectors of a nondispersive thermopile device, which is used to detect and quantify *Fusarium* spores. The detectors are broadband (1 µm to 20 µm), λ_1 (6.09 ± 0.06 µm) and λ_2 (9.49 ± 0.44 µm) thermopiles. Additionally, an artificial neural network (NN) is applied to process background noise effects. The adaptive and cognitive Kalman Filter helps to improve the training time of the neural network and the absolute error of the thermopile data. Without applying the Kalman filter for λ_1 thermopile, it took 12 min 09 sec to train the NN and reach the absolute error of 2.7453×10^4 (n. u.). With the Kalman filter, it took 46 sec to train the NN to reach the absolute error of 1.4374×10^4 (n. u.) for λ_1 thermopile. Similarly, to the λ_2 (9.49 ± 0.44 µm) thermopile, the training improved from 9 min 13 sec to 1 min and the absolute error of 2.3999×10^5 (n. u.) to the absolute error of 1.76485×10^5 (n. u.) respectively. The three-thermopile system has proven that it can improve the reliability in detection of *Fusarium* spores by adding the broadband thermopile. The method developed in this work can be employed for devices that encounter similar noise problems.

Index Terms-burst noise; outlier; thermal noise; Kalman; filter; neural network; thermopile; *Fusarium* detection

7.1. Introduction

Fusarium is a hazardous fungus. It can weaken the immunization system of the hosts such as animals and human. It also and cause different diseases such as onychomycosis or keratitis for human [C7.1], or meningoencephalitis in the dog [C7.2]. *Fusarium* also can result in many other diseases on plants such as *Fusarium* wilt on watermelon or bean [C7.3, C7.4], *Fusarium* head blight on wheat [C7.5], *Fusarium* dry on citrus [C7.6] or *Fusarium* root rot [C7.7]. According to *Fusarium* management guide [C7.8], *Fusarium* head blight disease, which is the key factor to cause *Fusarium* damage kernel on wheat, has annually resulted in losses of hundreds of million dollars. Many other previous studies of analyzing and detection *Fusarium* were conducted by applying mass spectroscopy [C7.9], Fourier transform infrared spectroscopy, near-infrared spectroscopy [C7.10, C7.11], polymerase-chain-reaction machine [C7.12], chlorophyll fluorescent imaging [C7.5] or impedance-based gold-electrodes sensor [C7.13]. Though these mentioned approaches are effective, some drawbacks can be seen such as expensive, complex to manipulate and hard to achieve quick detection. Thus, early detecting of *Fusarium* spore help crops to avoid dangerous fungal diseases and losses. *Fusarium* spores can spread out through the water, air and collaborative media of both water and air [C7.14–16]. Based on dispersal mechanisms, it can be sorted in a one-phase mechanism or two-phase mechanism. The one-phase mechanism means that spores can be dispersed by merely air or water. The two-phase mechanism means that the spores can be dispersed by the cooperation of air and water in the form of water drops in wind or bubbles in raining water containing spores [C7.14–C7.19].

From the studies pertaining to *Fusarium*, *Fusarium* spores can be dispersed most through the air phase. From this feature, the *Fusarium* detection method and device proposed in [C7.20] were suggested and designed. In this research, based on the Beer–Lambert law [C7.21], the group-distinction coefficient (GDC) was proposed to distinguish the substances. The group-distinction coefficient was calculated by using signals from two infrared narrow-bandwidth thermopiles. The detection method and the device were proved that worked well. However, the authors encountered some difficulties which are similar GDC values and system noises. In the research in [C7.20], the studied samples were *Fusarium oxysporum* chlamydospores [C7.22], pollen, starch and turmeric, in which, the GDCs of *Fusarium* and starch were very close to each other. The noises are background noise, thermal noise and burst noise [C7.20].

There are many different types of noise such as thermal, background, burst, flicker and avalanche noises [C7.23, C7.24]. These noises mainly occur in electronic or electrical devices and can be processed and treated in different ways to reduce the effects caused by them to the performance of devices. A thermal noise or Johnson noise, which is thermal agitation of electrons within electronic components can be reduced by an analog or digital filter [C7.24–C7.26]. Background (BG) noise or direct current (DC) noise can occur in amplifier circuits as they need bias currents to work, and the currents can be changed by the operating conditions such as temperature [C7.27]. Additionally, BG noise can be caused by input offset voltage along with bias currents of the operational amplifiers [C7.9]. Burst or popcorn noise can happen in semiconductors and is unpredictable [C7.24]. This type of noise can cause outliers in data, as a result, outlier detection and treatment are crucial tasks. In the study on outlier detection [C7.28], Dan L. et al., presented a Haar wavelet transform method to detect burst noise based on the singularity of the noise. In a different work, to detect outliers that were from data in the frequency domain, Deschrijver, D. et al., [C7.29] suggested a modified vector fitting algorithm by solving the least-squares equations of a set of scattering parameter data samples.

This paper proposes a novel method to detect *Fusarium*, to distinguish two substances with similar GDCs, and to introduce techniques to reduce thermal and burst noises or outliers in the data collected from the thermopiles. The method in this paper is upgraded from the previous work. To process both thermal and burst noise, an adaptive and cognitive Kalman filter (ACKF) is proposed. In the filter, a mechanism of outlier detection indicates the outlier positions and the filter will eliminate the outliers. As BG noise affects the impulsive signals or peak data (PD), the PD should be processed to eliminate the effect of the BG noise. The PD with the noise or error are eliminated by an artificial neural network (NN). From [C7.20], the two narrow-bandwidth thermopiles, λ_1 (6.09 ± 0.06 μm) and λ_2 (9.49 ± 0.44 μm), were used. In this research, the third thermopile was added. This add-on thermopile is a broadband (BR) spectrum detector (1 μm to 20 μm), which was upgraded from a reference sensor of monitoring the IR light source [C7.20]. The thermopiles BR, λ_1, and λ_2 can be used to analyze samples. The rest of the paper is structured as follows. Section 2 is the background of the Kalman algorithm and the neural network. Section 3 is about the outlier detection and adaptation mechanism for the Kalman filter. Additionally, it also discusses the NN approach. Section 4 provides the results and discussion. Lastly, section 5 concludes the work.

7.2. Background of the Applied Algorithms

7.2.1. Kalman Algorithm

Kalman algorithm is a versatile tool as it can be applied in many applications such as tracking objects (body parts, missiles, etc.) [C7.30–C7.33], navigation [C7.34], error data correction [C7.35] or finance [C7.36]. Kalman algorithm always has two distinct stages: prediction and measurement. Kalman is an optimal algorithm, as it can continuously improve the system outputs based on a recursive method of calculating the error covariance and prediction. With a linear system in the state-space model, the discrete Kalman can be applied. The discrete-time state evolution equation of a linear system [C7.37] can be defined as:

$$\boldsymbol{X_k} = A\boldsymbol{X_{k-1}} + B\boldsymbol{U_k} + \boldsymbol{W_k}, \tag{7.1}$$

where A is the state transition matrix impacting on $\boldsymbol{X_{k-1}}$, which is the state vector at the discrete-time $\boldsymbol{k-1}$; B is the control-input matrix; $\boldsymbol{U_k}$ and is the control vector and $\boldsymbol{W_k}$ is the process noise vector, which is supposed to be zero-mean Gaussian with the process noise covariance matrix Q, $\boldsymbol{W_k} \sim N(0, Q)$. The prediction Equation (7.1) will go along with an observation equation to describe the correlation between the measured value and the prediction at the discrete-time $\boldsymbol{k}$:

$$\boldsymbol{Z_k} = H\boldsymbol{X_k} + \boldsymbol{V_k}. \tag{7.2}$$

in which, $\boldsymbol{Z_k}$ is the observation vector or measurement vector; H is the observation matrix and $\boldsymbol{V_k}$ is the observation noise vector with the observation covariance matrix R, $\boldsymbol{V_k} \sim N(0, R)$. The A, B, H, Q and R can have the subscript index $\boldsymbol{k}$ if they change with discrete-time, yet they are invariant in most problems. Figure 7.1(a) illustrated the Kalman algorithm. In the diagram, P_k^+ and P_k^- are the updated and predicted state error covariance matrices respectively [C7.37]. $\boldsymbol{X_k^-}$ is called an a priori prediction. The output from the Kalman is the updated $\boldsymbol{X_k^+}$ or an *a posteriori* vector.

There are many systems that their state equation is nonlinear, so Equation (7.1) cannot be applied. The state can depend on a certain function $\boldsymbol{f}$, which is:

$$\boldsymbol{X_k^-} = \boldsymbol{f}(\boldsymbol{X_{k-1}^+}, \boldsymbol{U_k}, \boldsymbol{W_{k-1}}). \tag{7.3}$$

The observation equation of the measurement and prediction vectors can be:

$$\boldsymbol{Z_k} = \boldsymbol{h}(\boldsymbol{X_k^-}, \boldsymbol{V_k}). \tag{7.4}$$

To be able to apply the Kalman filter, a linearization was suggested to approximate the nonlinear problem into a linear problem by first-order Taylor series. At each discrete-time, it is essential to calculate:

$$\boldsymbol{F_{k-1}} = \left.\frac{\partial \boldsymbol{f}}{\partial \boldsymbol{X}}\right|_{(\boldsymbol{X_{k-1}^+}, \boldsymbol{U_k}, \boldsymbol{0}).} \tag{7.5}$$

$$\boldsymbol{h_k} = \left.\frac{\partial \boldsymbol{f}}{\partial \boldsymbol{X}}\right|_{(\boldsymbol{X_k^-}, \boldsymbol{0}).} \tag{7.6}$$

The extended Kalman filter (EKF) algorithm is shown in Figure 7.1(b). Viewing the two algorithms in Figure 7.1(a),(b), the differences are in the prediction equations. The update equations are the same in both algorithms [C7.30, C7.37].

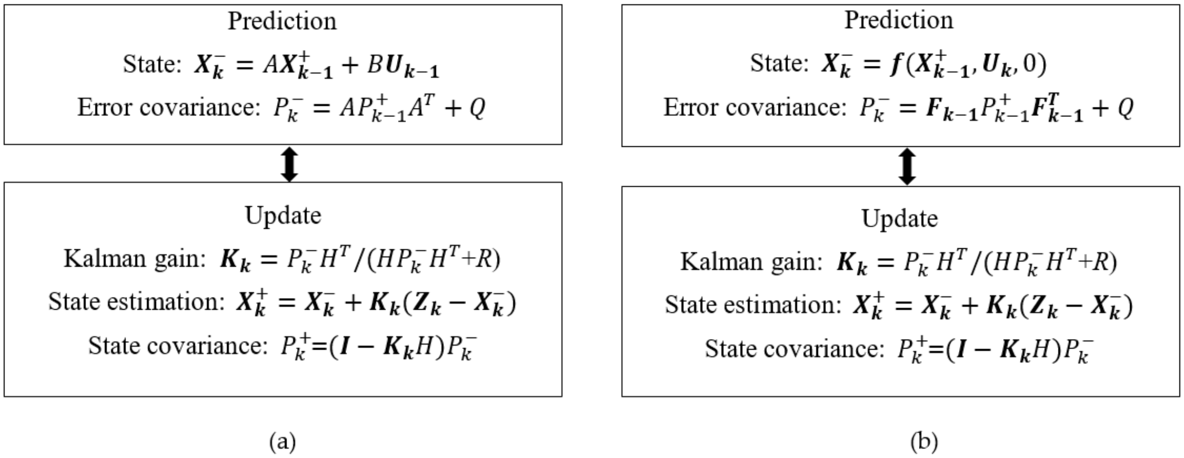

Figure 7.1. Kalman algorithm operation diagram. (**a**): Kalman and (**b**): extended Kalman.

7.2.2. Neural Network

In this work, as the neural network was applied to fix the error data caused by the BG noise, the theory of the neural network was briefly discussed here. An artificial neural network or neural network (NN) copying the work of biological neural systems [C7.38–C7.40] can react with certain inputs to provides outputs. An NN can have many layers, and the number of nodes in each layer is arbitrary. Looking at layer *l* with *K* nodes, one can have the output equation of this layer is:

$$a_j^{(l)}=\sigma\left(b_i^{(l)}+\sum_{r=1}^{R} w_{ij}^{(l)}.a_i^{(l-1)}\right)=\sigma\left(z_j^{(l)}\right), \tag{7.7}$$

where σ is an activation function such as linear function, binary step, hyperbolic tangent, sigmoid function, tanh, rectified linear unit (ReLU), softplus functions or Leaky ReLU [C7.40, C7.41]; $z_j^{(l)} = b_j^{(l)}+\sum_{j=1}^{R} w_{ij}^{(l)}.a_i^{(l-1)}$ is the output of the *j*th neuron of the layer (*l*−1); $\boldsymbol{W}^{(l)} = \{w_{11}^{(l)}, w_{12}^{(l)}, \dots, w_{ij}^{(l)}, \dots, w_{KR}^{(l)}\}$ and $\boldsymbol{B}=\{b_1^{(l)}, b_2^{(l)}, \dots, b_i^{(l)}, \dots, b_K^{(l)}\}$ are weights and biases of the layer *l* respectively.

To have desired outputs from an input vector, the NN must be trained to find the weights and biases of the NN. The training process is actually an optimal problem of finding the global minima of a cost function, which is often based on the mean square error (MSE) [C7.38, C7.42, C7.43]. NN has applications in many areas such as signal processing [C7.44], voice recognition [C7.45], image processing [C7.46] or navigation [C7.47]. The back-propagation algorithm (BPA) is a fundamental algorithm in NN. In this algorithm, it needs a set of training data including input vector ***X*** of *N* elements $\{x_1, x_2, \dots, x_N\}$ and output vector $\boldsymbol{O}$ of *M* elements $\{o_1, o_2, \dots, o_M\}$. The quadratic cost function of the stochastic gradient descent (SGD) is defined as:

$$C(\boldsymbol{O},\boldsymbol{Y})=\frac{1}{2}\|\boldsymbol{O}|_k-\boldsymbol{Y}|_k\|^2=\frac{1}{2}\sum_{m=1}^{M}[o_m-y_m^{(L)}]^2. \tag{7.8}$$

From Equation (7.8), the BPA to update the weight matrix and the bias vector for a hidden layer *l* is:

$$\boldsymbol{E}^{(l)}=(\boldsymbol{W}^{(l+1)})^T.\boldsymbol{E}^{(l+1)}\odot\boldsymbol{D}^{(l)}$$

$$\Delta\boldsymbol{W}^{(l)}|_{k+1}=-\eta.[\boldsymbol{E}^{(l)}|_k.(\boldsymbol{A}^{(l-1)}|_k)^T].$$

$$\Delta\boldsymbol{B}^{(l)}|_{k+1}=-\eta.\boldsymbol{E}^{(l)}|_k$$

In which $\Delta\boldsymbol{W}^{(l)}|_{k+1}$ and $\Delta\boldsymbol{B}^{(l)}|_{k+1}$ are the update matrices for weights and biases of the hidden layer *l* respectively; $\boldsymbol{A}^{(l-1)}$ is the output vector of the layer *l*-1; $[\boldsymbol{D}^{(l)}]_{K\times1}=\sigma'[\boldsymbol{Z}^{(l)}]_{K\times1}$ is the activation derivative matrix with the argument is $\boldsymbol{Z}^{(l)}$ matrix of $z_i^{(l)}$ and $\boldsymbol{E}^{(l)}$ is the error matrix. η is the learning rate. If η is too small, it may take a long time to find the global minima. If η is large, it can never obtain the optimum global minima. To overcome this difficulty, the steepest descent algorithm was proposed by using Taylor approximation to find an appropriate η [C7.39]. In this algorithm:

$$\boldsymbol{E}(\boldsymbol{W} + \eta\mathbf{d}) \approx \boldsymbol{E}(\boldsymbol{W}) + \eta.\boldsymbol{g}^T.\mathbf{d}, \tag{7.9}$$

where, $\boldsymbol{g}$ is the vector gradient of $\boldsymbol{E}(\boldsymbol{W})$, and $\mathbf{d}$ is the descent direction. η should be small enough to make $\boldsymbol{E}(\boldsymbol{W} + \eta\mathbf{d}) - \boldsymbol{E}(\boldsymbol{W}) < 0$. Since η should not be so small, η can be chosen to minimize $\boldsymbol{E}(\boldsymbol{W} + \eta\mathbf{d})$. Thus, $\boldsymbol{E}'_\eta = 0 \rightarrow \boldsymbol{g}^T.\mathbf{d} = 0 \rightarrow \begin{bmatrix}\boldsymbol{g} = 0 \\ \boldsymbol{g} \perp \mathbf{d}\end{bmatrix}$. To increase the convergence speed, Newton algorithm can be used. In this algorithm, the update form of the weights is:

$$\boldsymbol{W}^{(l)}|_{k+1} = \boldsymbol{W}^{(l)}|_k - \eta_k.\boldsymbol{H}^{-1(l)}|_k.\boldsymbol{g}|_k, \tag{7.10}$$

where, $\boldsymbol{H}^{(l)}\big|_k = \nabla^2\boldsymbol{E}\left(\boldsymbol{W}^{(l)}|_k\right)$ is the Hessian matrix. Solving the equation of $\boldsymbol{H}^{(l)}\big|_k.\mathbf{d}|_k = -\boldsymbol{g}|_k$ to find the descent direction $\mathbf{d}|_k$ at discrete time *k*. Equation (7.9) is applied to find η_k [C7.39]. For the least square problems, as the Hessian matrix calculation is difficult sometimes, the Levenberg–Marquardt algorithm (LMA) can be applied to avoid that calculation by the approximation of $\boldsymbol{H} = \boldsymbol{J}^T.\boldsymbol{J}$, in which, $\boldsymbol{J}$ is the Jacobian matrix of first derivative $\nabla\boldsymbol{E}\left(\boldsymbol{W}^{(l)}|_k\right)$ [C7.39]. In our NN, the LMA was applied to find weights and biases.

7.3. Methodology

7.3.1. System

The Fusarium detection device was upgraded from the authors' previous work, which was presented in [C7.20] by removing the reference chamber or the splitting plate to make only one reaction chamber. The trap has two silver-coated mirrors at the top and bottom, one IR source, one ZnSe window, a pair of reflective mirrors to direct IR light to the IR thermopiles, an inlet pipe, an outlet pipe and methyl methacrylate plates to cover the surrounding. The upgraded device structure is shown in Figure 7.2. The reference or broadband (BR) thermopile became the third detector along with the other two thermopiles to analyze the incident IR light. The broadband thermopile has the IR spectrum of 1 µm to 20 µm; λ_1 and λ_2 thermopiles have very narrow bandwidth spectra by using window filters of 6.09 ± 0.06 µm and 9.49 ± 0.44 µm respectively. The window filters were supplied by Northumbria Optical [C7.48] and installed into the 2 mm × 2 mm 2 M thermopiles supplied by Dexter Research Inc. [C7.49]. The typical internal resistance of these thermopiles is about 10 kΩ, and the responsivity R is 18.9 V/W. From [C7.49], the damage threshold P_{thres} is 0.5 W/cm^2, so it is not recommended to expose the 2 M thermopiles to any IR source higher P_{thres}. The IR source is 2.2 mm × 2.2 mm JSIR350-4-AL-C-D3.7-2-A5-I, and its spectrum is around from 1 µm to 20 µm [C7.50]. In the measurement, the biased current and the voltage for the IR source were 141.4 mA and 5.65 V respectively. As the signals from the thermopiles in this research were extremely weak, preamplifiers were necessary. The preamplifiers employed the AD8629 integrated circuit (IC) devices because these ICs have low bias current, low offset voltage, high common-mode rejection ration as well as chopping stabilization circuit [C7.51]. These features will help to lower the output noises. The final amplifier is OPA320 IC [C7.52]. The output of the final amplifier is digitalized by a 24-bit LT2400 analog-to-digital converter (ADC) [C7.53]. The setup voltage for the ADC was 4.096 V, so the resolution was 0.488 µV [C7.20]. In the device, a vacuum pump was attached to the inlet pipe. An output of a 15 kV high voltage (HV) circuit was connected to one of the silver-coated mirrors. In the device, to monitor the operating conditions of the device, a temperature sensor DS18B20 and a 5 V monitor and a 9 V monitor were used to monitor the output of the regulator circuits. When the temperature of the environment and voltages of these regulators change, the changes will be recorded to serve for the data error correction.

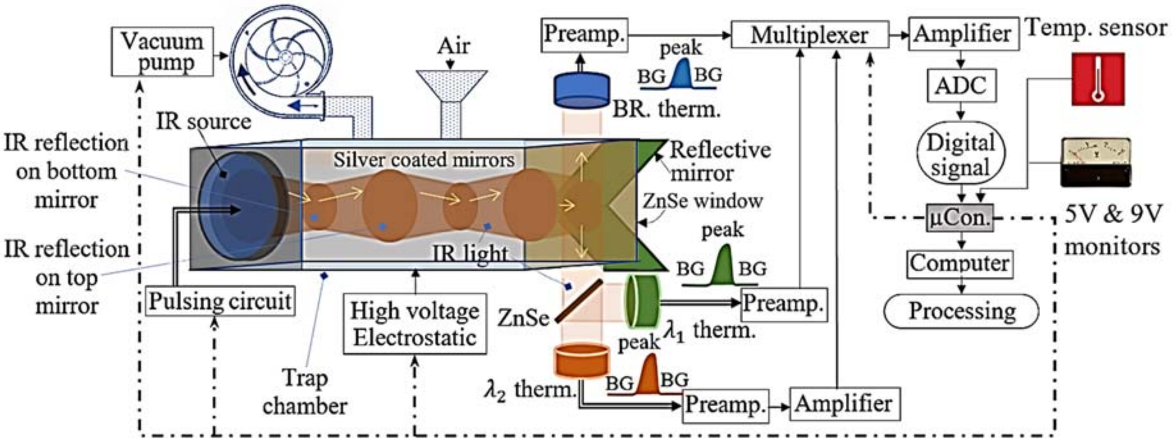

Figure 7.2. High voltage trap chamber and the thermopiles, circuit of the amplifiers and operation diagram.

The microcontroller (µC) used to operate the system is an Atmelt 328p [C7.54]. In Figure 7.2, to start, the µC turns on the vacuum pump to deliver the air into the trap chamber. The particles in the air are caught by the electrostatic charges provided by the HV circuit. After turning off the pump and the HV module, the microcontroller starts to collect data by following the following measurement procedure:

- Phase 1: Measuring environment temperature—T1; then, measuring outputs of the 5 V and 9 V regulators, which are V1 and V2 respectively.
- Phase 2: Measuring background data of BR thermopile in 6 s, when the IR source is still turned OFF; turning ON the IR source in 1.5 s and measuring data from the BR thermopile during this period to have peak data (PD); turning OFF the IR source in 6 s and measuring background data of the BR thermopile again. Thus, the data include background data, peak data PD and background data again.
- Phase 3: Similar to phase 2, λ_1 thermopile data are measured.
- Phase 4: Similar to phase 2, λ_2 thermopile data are measured.
- Phase 5: Repeating phase 1, but renaming temperature as T2, and the outputs of 5 V and 9 V regulators as V3 and V4 respectively.
- Phase 6: Sending all data to the computer in time order for further processing and analyzing.

In the computer, the background data will be averaged to have BG mean value. The data order is T1-V1-V2-BG-PD-BG-T2-V3-V4. After the measurement, one will have one data batch. To have a precise analysis, this procedure can be repeated to have more data batches. The number of the measurement batches is arbitrary. To have a good decision, five batches are sufficient [C7.20].

7.3.2. Analyzing Method

To be able to detect a sample in the device, it is necessary to find a model that depends only on the monochromatic absorbance features of the samples. From Beer–Lambert law, we proposed a group distinction coefficient equation, which can be applied to distinguish a group of samples in the device as follow [C7.20]:

$$\eta = \frac{\varepsilon_{\lambda_1}}{\varepsilon_{\lambda_2}} = \frac{log(\frac{P_{\lambda_1}}{P_{o,\lambda_1}})}{log(\frac{P_{\lambda_2}}{P_{o,\lambda_2}})}. \tag{7.11}$$

In which $P_{o,\lambda}$ is the IR radiant power of a monochromatic light of the IR light source (W/sr); P_{λ} is IR power of the monochromatic light going through a sample (W/sr) and ε_{λ} is monochromatic extinction coefficient (1/obj.). The formula to determine the density of the sample is [C7.20]:

$$D_x = \frac{log\ (\frac{P_{x,\lambda_1}}{P_{xo,\lambda_1}})}{\varepsilon_{\lambda_1} * S} = D \times \frac{\log\ (\frac{P_{x,\lambda_1}}{P_{xo,\lambda_1}})}{\log(\frac{P_{\lambda_1}}{P_{o,\lambda_1}})}, \tag{7.12}$$

where D_x is an unknown density of a sample; D is a known-sample density (obj./cm^2); S is the area of the sample and obj. is the studied object, which is caught on the area S.

Additionally, from experiment results, the Fusarium curve of P_{BR} and D_x can be plotted and in the later measurements, the values of P_{BR} and D_x can be found. Testing whether the data point of (P_{BR}, D_x) is on the curve can consolidate a decision of detection. This additional step helps to eliminate the confusion between two samples having a similar group-distinction coefficient η. Therefore, the third sensor is added to improve the reliability and extend application areas.

Power of incident light coming to a thermopile can be calculated by applying:

$$P_{inc} = \frac{N_{dig} * resolution(\mu V)}{responsivity\left(\frac{V}{W}\right) * Gain}, \tag{7.13}$$

where, N_{dig} is digital output from ADC when reading thermopile data. Actually, when $\frac{P_{x,\lambda_1}}{P_{xo,\lambda_1}}$ ratio is estimated, the resolution, responsivity, and gain will cancel out each other. Therefore, $\frac{P_{x,\lambda_1}}{P_{xo,\lambda_1}} = \frac{N_{dig-x,\lambda_1}}{N_{dig-xo,\lambda_1}}$.

7.3.3. Adaptive and Cognitive Kalman Filter

In our work, the Kalman filter had two functions, which were the noise filter and outlier reducer for the signal data of each thermopile. As mentioned in Section 2.1, Q is the process noise covariance. In our work, the Kalman filter processed signal data of each thermopile, and Q should be called as the process noise error. The process noise, theoretically, depends on the working condition at each discrete-time, but in many problems, this condition is almost unchanged. During the time of turning ON the IR source, the IR radiation changed the working condition, so the process noise errors in the turning ON and turning OFF periods were not the same. The observation error could be determined from the experiments.

Section 3.1 described the measurement procedure. In a turning ON period, the temperature of the IR source promptly increased. Since the IR source used the microelectromechanical system (MEMS), the temperature would soon reach the saturation temperature. As a result, in the early of the turning ON period, the signals on the thermopiles increased quickly but slightly improved in the end of this period. In the turning OFF period, the IR source temperature quickly decreased until reaching the environment temperature, so the data in this period would decline too. In practice, three types of data pulse can be seen as illustrated in Figure 7.3.

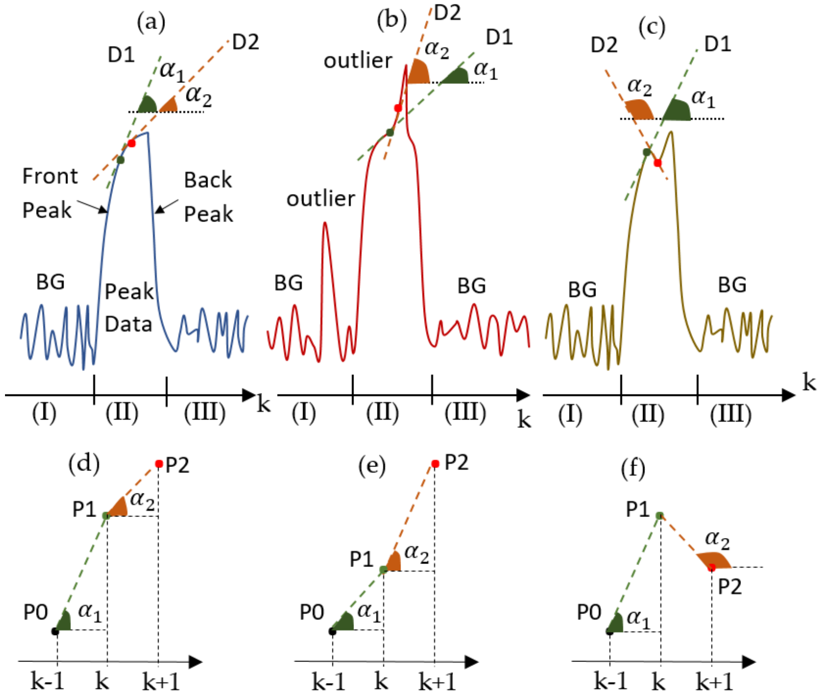

Figure 7.3. Three typical types of pulse data can be seen in the collected data. (**a**) Normal pulse data; (**b**) abnormal pulse data with positive outliers in the background and in the peak; (**c**) abnormal pulse data with a negative outlier in the peak and (**d**–**f**) close view of tangential line angles α_1 and α_2 of cases (**a**), (**b**) and (**c**) respectively.

Figure 7.3(a) illustrates a normal pulse, in which, the front peak (FP) corresponds to turning OFF and the back peak (BP) corresponds to turning OFF and the START of the temperature balance period. In the research, the burst or popcorn noise may occur during the data collection and cause outliers in background and PD. Figure 7.3(b),(c) shows the two typical pulse data with burst noise or outliers. As the front peak data caused by the reaction of the thermopiles with the coming-IR light reflecting from analyzing samples, the data will contain useful information of the samples. Besides, from observation, outliers often appear in FP range. Therefore, we focused on how to process outliers in the FP range. In the FP range (illustrated in Figure 7.3(a)), let us look at two adjacent points, P1 and P2 corresponding to the discrete-time k and k + 1, in a data peak. D1 and D2 are the tangential lines going through P1 and P2 respectively. α_1 and α_2 are the angles of the tangential lines D1 and D2 with the horizontal line. For normal pulses, it can be seen that:

$$\begin{cases} 0 \le \alpha_1, \alpha_2 < 90^o \\ \alpha_2 < \alpha_1 \rightarrow tan(\alpha_2) < tan(\alpha_1) \end{cases} \rightarrow \frac{\text{P2}-\text{P1}}{\Delta t} < \frac{\text{P1}-\text{P0}}{\Delta t} \tag{7.14}$$

where:

$$tan(\alpha_1) = \frac{\text{P1}-\text{P0}}{t_k - t_{k-1}} = \frac{\text{P1}-\text{P0}}{\Delta t};\ tan(\alpha_2) = \frac{\text{P2}-\text{P1}}{t_{k+1} - t_k} = \frac{\text{P2}-\text{P1}}{\Delta t} \tag{7.15}$$

Similarly, the conditions for Figure 7.3(b),(e) are:

$$\begin{cases} 0 \le \alpha_1, \alpha_2 < 90^o \\ \alpha_2 > \alpha_1 \rightarrow tan(\alpha_2) > tan(\alpha_1) \end{cases} \rightarrow \frac{\text{P2}-\text{P1}}{\Delta t} > \frac{\text{P1}-\text{P0}}{\Delta t} \tag{7.16}$$

For Figure 7.3(c),(f), the conditions are:

$$\begin{cases} 0 \le \alpha_1 < 90^o, 90^o < \alpha_2 \le 180^o \\ \alpha_2 > \alpha_1 \rightarrow tan(\alpha_1) > 0\ \&\ tan(\alpha_2) < 0 \end{cases} \rightarrow \frac{\text{P1}-\text{P0}}{\Delta t} > 0 \text{ and } \frac{\text{P2}-\text{P1}}{\Delta t} < 0 \tag{7.17}$$

The conditions in Equations (7.14), (7.16) and (7.17) can be used to determine normal or abnormal pulses in the FP range. P0, P1 and P2 are the digital values of FP range. (P1–P0) and (P2–P1) could be calculated by applying the firs-order discrete derivative of the pulse, and [(P2–P1)–(P1–P0)] is the second-order discrete derivative of the pulse. Let us name $\boldsymbol{f}$ as the function of the peak, so the first and the second-order derivative by discrete-time k are $\dot{\boldsymbol{f}}$ and $\ddot{\boldsymbol{f}}$ respectively. Then (P1–P0) and (P2–P1) become $\dot{\boldsymbol{f}}$(k−1) and $\dot{\boldsymbol{f}}$(k), respectively; [(P2–P1)–(P1–P0)] = $\ddot{\boldsymbol{f}}$(k).

As mentioned above, in the turning ON and OFF periods, the process noise and the other parameters of the Kalman filter should be adjusted. Figure 7.4 shows the adjustment diagram of process noise, and recursive coefficients based on the experiments, the conditions in Equations (7.14), (7.16) and (7.17) for the ACKF.

Let us name Q_o and R_o as the constant process noise and observation noise errors respectively. In the discrete-time zones (I) and (III), the data are BG data. In these discrete-time zones, the process noise error is set at $Q = \beta_1 \times Q_o$ and the observation noise error is $R = R_o$. Attentionally, $R = R_o$ everywhere, and the values $\beta_1, \beta_2, \beta_3, \beta_4$ and β_5, which will be discussed later are cognitively determined by experiments. Figure 7.3(b) shows an example of background range with an outlier that can be fixed by the Kalman filter if β_1 is appropriately chosen. In the discrete-time (II), the FP range is studied. In the FP range, if $\dot{f}(\mathrm{k}) > 0$ condition is true, the condition in Equation (7.16) is considered:

$$\rightarrow \frac{\mathrm{P2}-\mathrm{P1}}{\Delta \mathrm{t}} - \frac{\mathrm{P1}-\mathrm{P0}}{\Delta \mathrm{t}} > 0 \rightarrow (\mathrm{P2} - \mathrm{P1}) - (\mathrm{P1} - \mathrm{P0}) > 0 \rightarrow \ddot{f}(\mathrm{k}) > 0 \tag{7.18}$$

If $\ddot{f}(\mathrm{k}) < 0$, it is normal and $Q = \beta_2 \times Q_o$. If $\ddot{f}(\mathrm{k}) > 0$, it is abnormal and an outlier appears in the FP range. If the outlier is large, it requires a correction for the observation value. In our research, if $\frac{\dot{f}(\mathrm{k}-1)}{\dot{f}(\mathrm{k})} \geq 0.5$, then the outlier is not large → $Q = \beta_3 \times Q_o$. If $\frac{\dot{f}(\mathrm{k}-1)}{\dot{f}(\mathrm{k})} < 0.5$, then the outlier is large. The observation correction is conducted by using the previous normal data points at discrete times k - 1 and k - 2:

$$z^{+}(k) = z(\mathrm{k}-1) + \eta \times (z(\mathrm{k}-1) - z(\mathrm{k}-2)), \tag{7.19}$$

where $z^{+}(k)$ is the observation prediction and η is a percentage constant to take an amount of the difference of $z(k-1)–z(k-2)$. After this prediction, we still put more reliability on the process noise error rather than the observation noise error. In other words, at discrete time k, the observation noise error should be larger than the process noise error ($R > Q$ or $\frac{Q}{R} < 1$; $R = R_o$). It can be seen that:

$$\frac{\mathrm{P1}-\mathrm{P0}}{\mathrm{P2}-\mathrm{P1}} < 1 \rightarrow \frac{Q}{R_o} \sim \frac{\mathrm{P1}-\mathrm{P0}}{\mathrm{P2}-\mathrm{P1}} \rightarrow Q \sim \frac{\mathrm{P1}-\mathrm{P0}}{\mathrm{P2}-\mathrm{P1}} = \frac{\dot{f}(\mathrm{k}-1)}{\dot{f}(\mathrm{k})}.$$

Thus, $Q = \beta_4 \times \frac{\dot{f}(\mathrm{k}-1)}{\dot{f}(\mathrm{k})} \times Q_o$, and Q can adapt to the magnitude of $\frac{\dot{f}(k-1)}{\dot{f}(k)}$. In addition, a recursive mechanism is designed to recall the Kalman filter module itself. The number of recalls, N, depends on whether this ratio is small or large. The smaller $\frac{\dot{f}(\mathrm{k}-1)}{\dot{f}(\mathrm{k})}$ is, the more the Kalman module will recall itself. Basically, even in a normal case, the Kalman filter is called two times, so $N = 2$. If $0.05 < \frac{\dot{f}(\mathrm{k}-1)}{\dot{f}(\mathrm{k})} < 0.1$, $N = 5$. If $0.015 < \frac{\dot{f}(\mathrm{k}-1)}{\dot{f}(\mathrm{k})} \leq 0.05$, $N = 5$. If $\frac{\dot{f}(\mathrm{k}-1)}{\dot{f}(\mathrm{k})} \leq 0.015$, $N = 15$. If $\dot{f}(\mathrm{k}) < 0$, a negative outlier occurs in this range. The observation data point is abnormal, and it will be corrected by applying again Equation (7.19). The process noise error is $Q = \beta_5 \times Q_o$. After being processed, the outlier point becomes a normal data point. If the outlier still exists in the FP range, it will be detected and processed. After being processed by the ACKF, thermopile data are symbolized as $[\mathrm{BG, PD, BG}]_{\mathrm{preprocessed}}$.

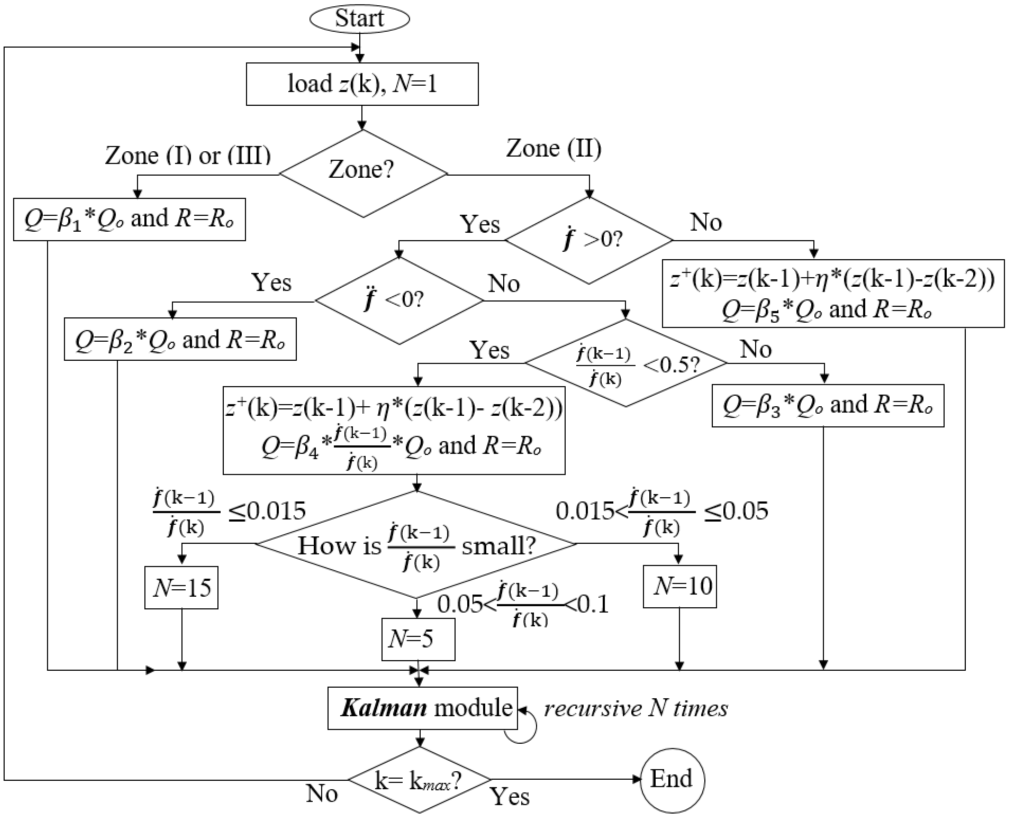

Figure 7.4.The algorithm of the adaptive-cognitive Kalman filter (ACKF). Based on *N*; the Kalman can recall itself *N* times.

7.3.4. Entropy

To evaluate the effectiveness of the filter and outlier-elimination process, the entropies of the raw and preprocessed signals is used:

$$S(y) = \sum_i p(i) * \log_2\left(\frac{1}{p(i)}\right) \quad (7.20)$$

In which y can be x, the raw data, or z, the processed signal data, and $p(i)$ is the probability of $x(i)$ or $z(i)$ to happen [C7.55–C7.57]. Entropy quantity can reveal the uncertainty or the randomness of the investigated signal. To the raw signal containing much noise, the noise can cover the useful information and show a high disorder, so the entropy of the signal is small. If the outlier elimination modules work well, much noise including thermal or burst noise is reduced, then the entropy of the preprocessed signal can be larger than the raw signal.

In the NN training, as the BG noise of each thermopile affects most to the output, it is crucial to choose a standard BG (SBG), and corresponding with each SBG is a standard MP (SMP) based on the measurements of each thermopile. The SBG for each thermopile is chosen based on the appearance frequency of the BG data. The chosen BG should be the highest appearance frequency. We use the absolute-mean error function (AME as a stop criterion and efficiency coefficient). AME equation is:

$$\text{Error} = mean\left(\sum_i \text{abs}\left(\text{SMP} - y(i)\right)\right) \quad (7.21)$$

However, we encountered some cases that the correction values swing around the SMP. To overcome the problem, applying Equation (7.20) of the entropy provides a better operational condition. As discussed above, to a data with much noise or a fluctuation data vector, the entropy will be small. In the training, the program will train NN and drive corrected data to a trend of entropy increase. Therefore, the best entropy will lead to the least swinging correction values.

7.3.5. Error Correction by Neural Network

In Section 3.1, temperature, 5 V and 9 V monitoring voltages and raw data were presented. Section 3.3 introduced the data after being preprocessed. Although the thermal and burst noises can be mitigated by the ACKF filter, the BG noise or error still exists in the data. To reduce this noise, a NN was applied. The NN was trained by a set of collected data from the *Fusarium* detection device. To prepare data for training NN, some estimations should be done first: $\overline{\text{T1}} = \frac{\text{T1+T2}}{2}$, $\overline{\text{V1}} = \frac{\text{V1+V3}}{2}$ and $\overline{\text{V2}} = \frac{\text{V2+V4}}{2}$; BG is the average of background data; STD(BG) is the standard deviation of background data; MP is the maximum of PD; WP is the mean value of the whole PD and FP is the mean value of data points in FP range. To train the NN precisely, many data batches were recorded. Each data batch will have the previously introduced quantities. Gathering data for these quantities from the measured data batches, one will have data vectors, which are presented in bold font: $\overline{\mathbf{T1}}$, $\overline{\mathbf{V1}}$, $\overline{\mathbf{V2}}$, **BG**, **STD**(BG), **MP**, **FP** and **WP**. **MP** vector is used to analyze samples in the trap chamber (Section 3.1), and is the N_{dig} data in Equation (7.13) (Section 3.2).

Theoretically, if the operating conditions and the studied sample are unchanged, **MP** will be stable. However, the operating condition set (**OCS**) of $\overline{\mathbf{T1}}$, $\overline{\mathbf{V1}}$, $\overline{\mathbf{V2}}$, **BG**, **STD**(BG), **FP** and **WP** are hardly stable, so **MP** are changed too. These quantities can affect to the **MP**. In the work, a standard operating condition set (SOCS) from **OCS** was chosen. Corresponding this SOCS is the three standard MP (SMP) values for the three thermopiles. If $\mathrm{r} = \frac{\mathrm{SMP}}{\mathrm{MP}}$ is defined, then r depends on the OCS and SOCS. If N data batches are measured, then **MP** = $\{\mathrm{MP}_1, \mathrm{MP}_2, \ldots, \mathrm{MP}_{\mathrm{i}}, \ldots, \mathrm{MP}_{\mathrm{N}}\}$. From **MP** vector, $\mathbf{r} = \frac{\mathrm{SMP}}{\mathbf{MP}}$ vector can be calculated. From Section 3.1, we know that MP is the digital value of amplified signal from an input signal X. MP can be estimated by: MP = G.X, where, G is the gain of the amplifiers. As an OCS can affect to the gain, so G depends on the OCS. Therefore, SMP = G_S.X, where G_S is the gain at standard condition set. If X is stable, the ratio of MP_{i} is:

$$\mathrm{r}_{\mathrm{i}} = \frac{\mathrm{SMP}}{\mathrm{MP}_{\mathrm{i}}} = \frac{G_S}{G_{\mathrm{i}}}. \tag{7.22}$$

G_{i} depends on the OCS at the measurement ith. The NN would be trained by using **OCS** of $\overline{\mathbf{T1}}$, $\overline{\mathbf{V1}}$, $\overline{\mathbf{V2}}$, **BG**, **STD**(BG), **FP**, **WP** and **r**. The trained NN would be used to determine r_{x} from a new $\mathrm{OCS}_{\mathrm{x}}$ of a new investigation of any new sample. These procedures are depicted in Figure 7.5.

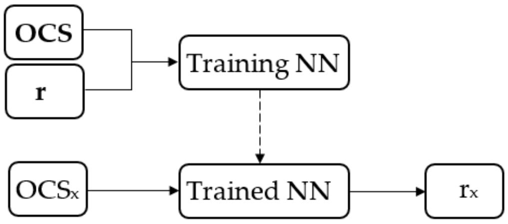

Figure 7.5. Training neural network (NN) and finding the ratio r_{x} diagram.

From r_{x}, MP_{x} of the new sample can be corrected to eliminate the affection of $\mathrm{OCS}_{\mathrm{x}}$ by applying Equation (7.22), so MP_{x} is adjusted to SMP, which is the MP value corresponding the SOCS:

$$MP_{corrected} = SMP = r_x \times MP_x. \tag{7.23}$$

In NN training, the input data and output data to supply into the NN were recorded in two cases of without-sample and *Fusarium* sample and in different operating conditions. In this paper, we mainly focused on the operation of the ACKF and the role of the broadband thermopile in the upgraded nondispersive thermopile device. The collected data would be preprocessed by the ACKF, and then being used to train the NN. To evaluate the effectiveness of the ACKF filter, the NN would be trained by two **OCS**s of raw data and ACKF-preprocessed data. Based on the comparison of the errors, entropies and times of NN training after employing the two **OCS**, the effectiveness can be concluded. The diagram of using the collected data for NN training is shown in Figure 7.6.

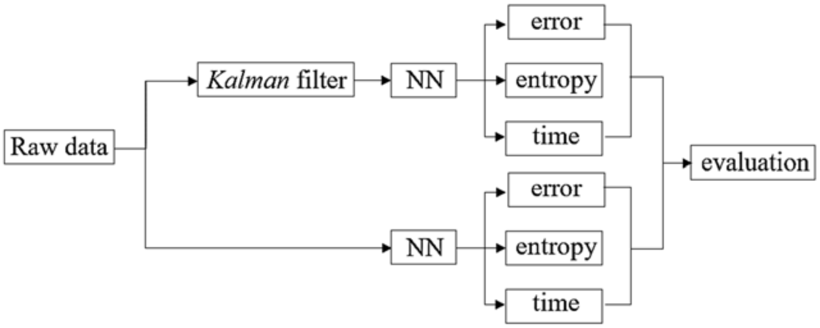

Figure 7.6. Estimation of the effectiveness of the ACKF.

7.3.6. Samples

The samples were used in the experiments are *Fusarium oxysporum* [C7.22] and starch as these two samples have the group distinction coefficients are close to each other. In the previous work, we also used pollen and turmeric to test the device and the analyzing formula, which is the group-distinction coefficient [C7.20]. The *F. oxysporum* was collected from rotten garlic bulbs and nurtured in potato-dextrose-agar Petri dishes by following the instructions in [C7.22]. To be able to collect *Fusarium* samples, it requires at least 4 weeks of fostering. The starch sample was from a local food market. The samples were used to test if the outlier reduction by ACKF and the upgraded *Fusarium* detection device can work effectively.

7.4. Results and Discussion

In [C7.20], four samples were used to test the *Fusarium* detection method and device. In that research, the coefficients of *Fusarium*, pollen, starch and turmeric were 1.144 $\pm$ 0.153, 0.136 $\pm$ 0.116, 0.939 $\pm$ 0.073 and 0.794 $\pm$ 0.139 respectively. It can be seen that *Fusarium* and starch coefficients were very similar to each other. Therefore, if there is a way to process further the samples with similar coefficients, it will be useful. In this work, we focused on mainly the method of using the combination of BR, $\boldsymbol{\lambda_1}$ and $\boldsymbol{\lambda_2}$ thermopiles to distinguish the two samples, *Fusarium* and starch, which have similar group-distinction coefficients.

7.4.1. Reduction of Thermal and Burst Noises

This section presents the operation of the ACKF. Its results and the raw data are shown in Figure 7.7. Figure 7.7(a), (d) shows thermopile signals with noise and outliers. Especially, Figure 7.7(a) has many outliers. Figure 7.7(b), (e) shows the preprocessed signals by applying ACKF to filter out the noise and the outliers. Figure 7.7(c), (f) depicts the entropies of the first-order differentiation of these signals. Each entropy value will stand for an uncertainty level of a signal. As seen, the ACKF work well, a few outliers still can be seen in Figure 7.7(b).

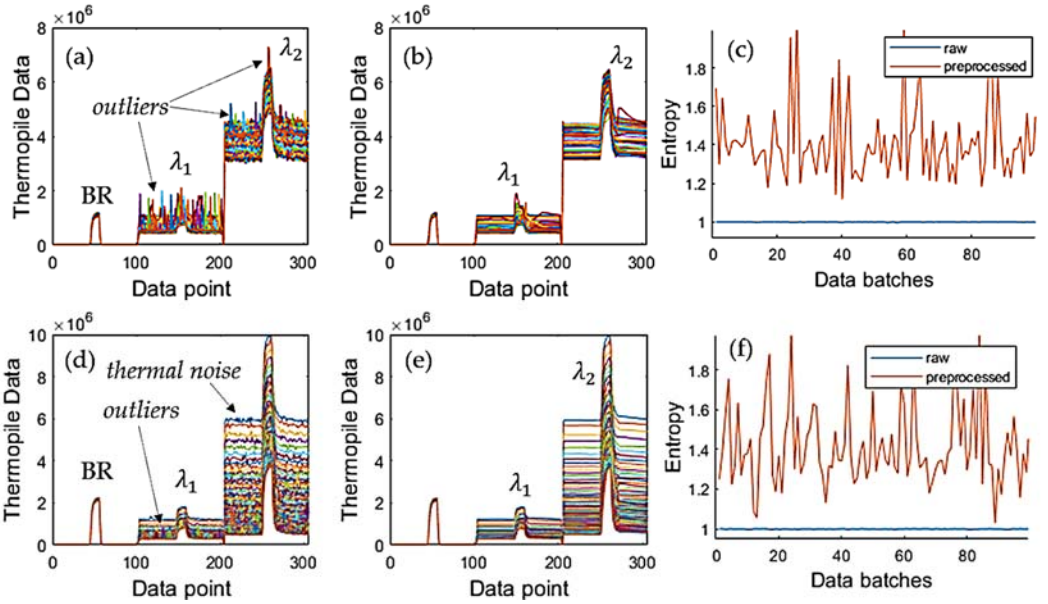

Figure 7.7. One hundred raw signals and their ACKF preprocessed signals when applying the ACKF in two different measurement sets. (**a**,**d**) Raw signal; (**b**,**e**) preprocessed signal and (**c**,**f**) entropies of the first-order differentiate corresponding to each signal.

Figure 7.8 illustrates some cases showing a better view of the effectiveness of the ACKF. The outliers can happen in the background or peak zones as shown in Figure 7.8a,(d)–(f). In these plots, Figure 7.8(f) could not be fixed well as the signal had too much affection from the thermal and burst noises. Figure 7.8(b), (c) did not get much effect from the burst noise and the ACKF function was to smooth the raw signals.

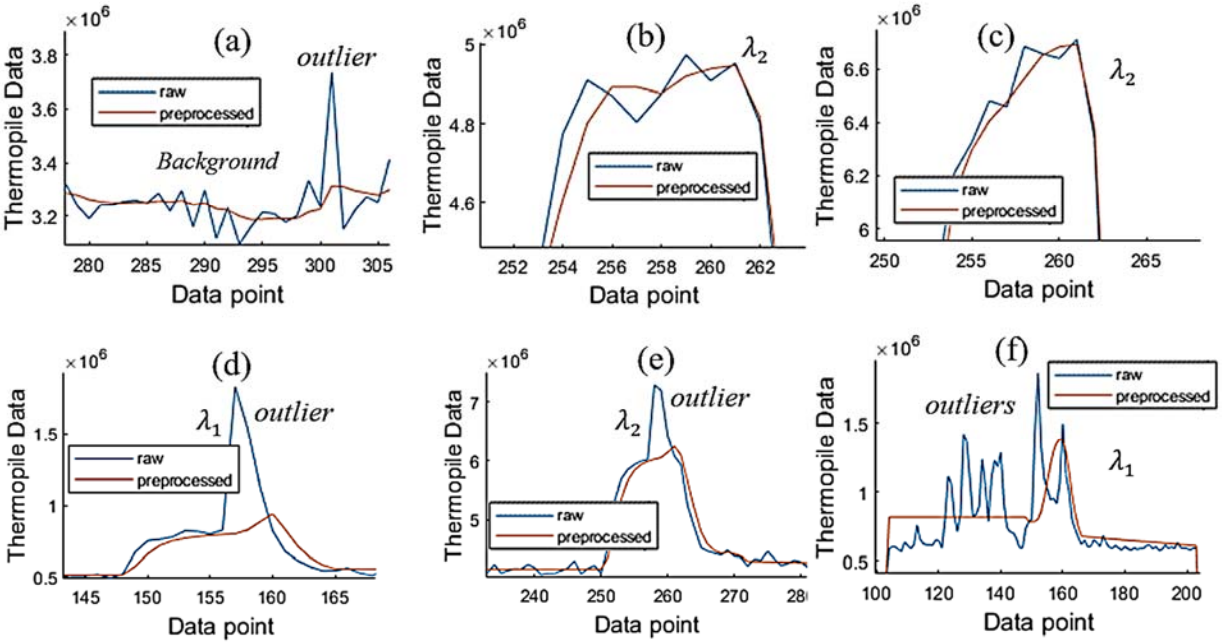

Figure 7.8. Close views of background, λ_1, and λ_2 of the raw and preprocessed signals. (**a**) Background; (**b,c,e**) λ_2 thermopile signals and (**d**, **f**) λ_1 thermopile signals.

Table 7.1 shows the max peak (MP) differences, ΔMP, between the MP of ACKF the preprocessed and raw signals of the three thermopiles. Similarly, it also introduces the entropies of the signals of a typical case of the outlier effect. It can be seen that λ_2 raw signal had an outlier in the peak. Thus, ΔMP of λ_2 was very large, while ΔMPs of BR and λ_2 were very small. The last two columns show the entropies of the signal differentiation of the three thermopiles of the raw and preprocessed signals. Table 7.1 proves that entropies of differentiation of the ACKF preprocessed data were better than the raw data. Thus, the ACKF could process the thermal noise and burst noise well.

Table 7.1. The investigation of the raw and preprocessed signals.

Illustration	**Thermopile**	**ΔMP**	**Entropies of Diff. of Raw Signal**	**Entropies of Diff. of Preprocessed Signal**
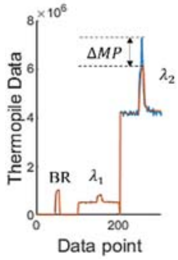	BR	1,162,693	0.9964	1.2808
	λ_1	9471	0.9993	0.9964
	λ_2	1873	0.9964	2.2958

7.4.2. Reduction of Background Noise

For training data of the NN, 5422 data were consecutively and automatically recorded in many days to mimic normal working conditions. To find an appropriate and adequate NN structure for our application, we simply started using a single hidden layer with two nodes, and then the number of nodes was increased. The number of nodes was stopped at eight. The training times and absolute errors from the training were taken note. Then, we increased the number of hidden layers to two layers with m = 2 nodes for the first hidden layers and n = 1 node for the second layers; m was increased until reaching eight nodes for the training. Then, n was increased to two nodes, and again m started at m = 2 nodes. After m = 8 nodes and n = 2 nodes, we stopped there and compared the times and errors in the simulation to find the best NN structure.

The best NN structure had two hidden layers, in which, the first hidden layer had three nodes, while the second had two nodes. To compare the effectiveness of the ACKF, the raw data and the preprocessed data were employed. The data aggregation was of five different samples in which there were no sample, *Fusarium* samples at different densities and starch sample. In each case, the power supply for the IR source and the other circuits were unchanged, so the outputs of the three thermopiles were expected constant. Additionally, the number of batches in each sample-measurement case was arbitrary. However, the working condition was probably unstable and even the power supply could have a certain fluctuation, which could affect the output of the detectors. By using the inputs of the information of the temperature, 5 V and 9 V monitors and the BG to train the NN, we could correct the recorded-unstable outputs of these thermopiles, and return back more stable outputs. Firstly, we checked the efficiency of the ACKF by comparing the training times and the absolute errors of the λ_1 and λ_2 thermopiles. The results are depicted in Table 7.2.

Table 7.2. The training results of raw data vs. preprocessed (prep.) data.

	$\boldsymbol{\lambda_1}$		$\boldsymbol{\lambda_2}$	
	Raw data	**Prep. Data**	**Raw Data**	**Prep. Data**
Time	12 min 09 sec	00 min 46 sec	9 min 13 sec	1 min 00 sec
Error	2.7453×10^4	1.4374×10^4	2.3999×10^5	1.76485×10^5

In the training NN, both error and entropy criteria were applied. As mentioned in the entropy section that the AME may cause the data correction swing even though the AME was optimized through the weights and biases searching. Figure 7.9 shows the plots of the ACKF preprocessed data and corrected data of λ_1 thermopile of using error and entropy as operational criteria.

In the preprocessed MP data of the λ_1 thermopile, Figure 7.8(a) illustrates the results of applying entropy. Figure 7.9(b) is the close view of Figure 7.9(a) of the four different samples. Similarly, Figure 7.9(c), (d) show the results when using the AME criterion. The black lines in the plots are to show the expectation of MP values. The expectation MPs were chosen from view the correlation of the MP data and the SBGs of the three cooperative thermopiles. The close views show data of the other four different samples. It can be seen the entropy operating criterion could work better than the error operating criterion.

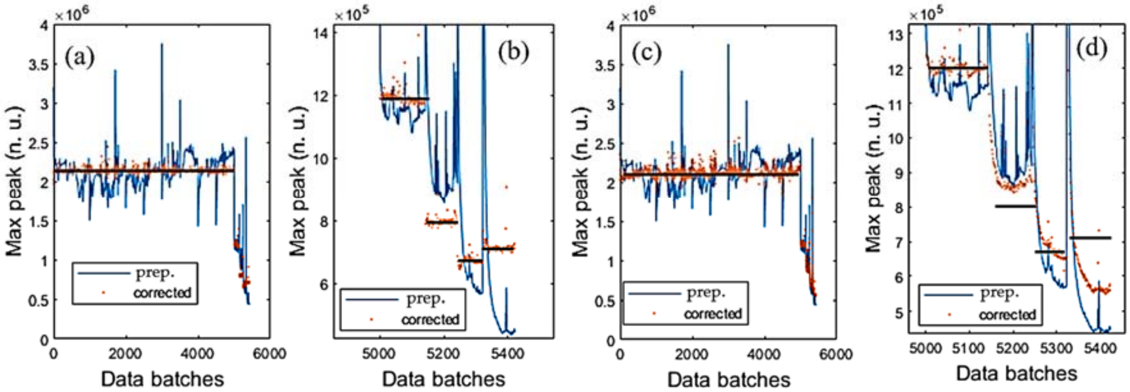

Figure 7.9. The ACKF preprocessed (prep.) and corrected max peak (MP) data of λ_1 thermopile of using entropy and absolute-mean error function (AME) criteria respectively. (**a**) Full view of the data achieved by entropy criterion; (**b**) close view of the data batches from

5001 to 5422 achieved by entropy criterion; (**c**) full view of the data achieved by AME and (**d**) close view of the MP data from the batches of 5001 to 5422 achieved by AME criterion.

Figure 7.10 shows the other views on the operation of these criteria when processing the λ_1 thermopile MP data. Figure 7.10(a), (b) present the relationship between the training time and entropy of differentiation, and error of the corrected data respectively. The two red dots in Figure 7.10(a), (c) are the two optimized entropies, which are close to each other. Figure 7.10(c), (d) are the results that were recorded in one searching batch of 1000 loops.

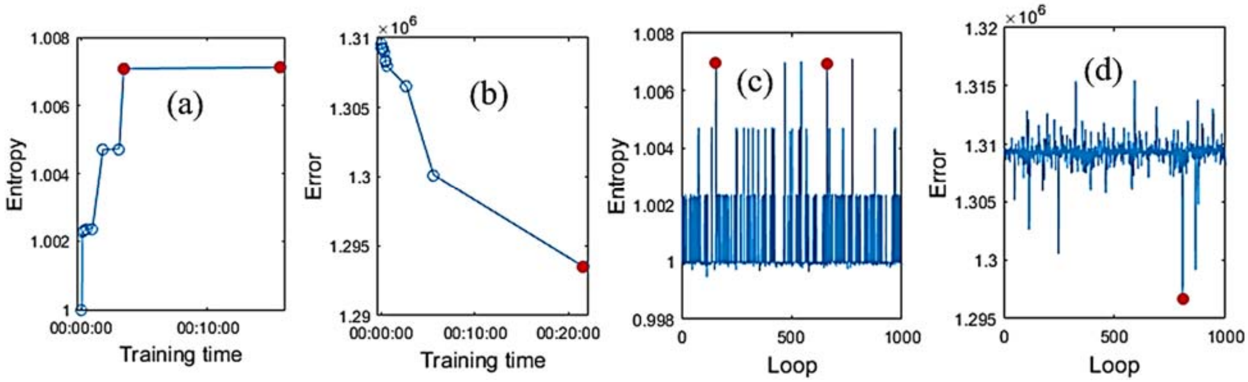

Figure 7.10. The entropies and AMEs were achieved from the training NN, which was trained in 1000 loops for λ_1 thermopile. The red dots show the optimization values. (**a**) Entropies from applying entropy for the differentiated MP data; (**b**) errors from applying the AME criterion; (**c**) recorded entropies after 1000 loops and (**d**) recorded errors after 1000 loops.

Figure 7.11 shows the results of processing BR and λ_2 thermopiles, and the differentiation plots of the data. Figure 7.11(a) is of the BR thermopile and Figure 7.11(b) is of the λ_2 thermopile. A note that the entropy was applied to the differentiation of the preprocessed data and the corrected data. The differentiation plots of the two types of data shown in Figure 7.11 belong to the λ_1 thermopile. Table 7.3 shows the results of applying entropy and AME operating criteria for λ_1 thermopile. In each method, both AME and entropy quantities were recorded for investigation. From Table 7.3, in the entropy operating criterion, when the entropy was optimized, then the error was very close to the optimal error of the error operating criterion. However, in the error operating criterion method, it was not similar to the entropy, in this case, it was less than 1, which is not good. These points of view could be more consolidated by reviewing Figure 7, 9 and 10.

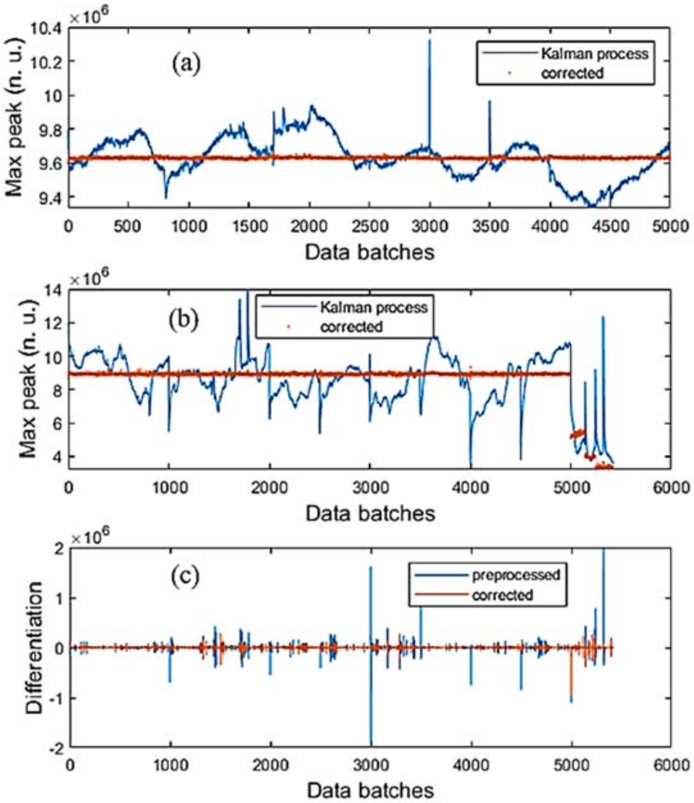

Figure 7.11. The ACKF processed data, the corrected data, and the differentiation of these types of data. (**a**) Broadband (BR) thermopile; (**b**) λ_2 thermopiles and (**c**) differentiation of the preprocessed and corrected data of λ_1 thermopile.

Table 7.3. The operating coefficients of the entropy and error operating criteria.

	Entropy Operating Criterion	**Error Operating Criterion**
Time	15 min 47 sec	21 min 37 sec
Optimal entropy	1.0071	N/A
Optimal Error	N/A	1,293,496.24
Entropy	N/A	0.9999
Error	1.2935×10^6	N/A

7.4.3. Analysis

From experiments, as the group distinction coefficients, η, of the *Fusarium oxysporum* chlamydospore [C7.22], and the starch samples were somewhat similar, in this section, the analysis results of these samples were introduced. Applying the trained NN for these two samples can help to correct or calibrate the data of the three thermopiles. Figure 7.12 shows the ACKF preprocessed data and corrected data of the two samples, which were measured in 50 batches.

From the figure, one can see that the output data of BR were very stable and the correction process calibrates the data. Applying Equation (7.11), the group distinction coefficients of the two samples could be found. Figure 7.13(a) shows η_{starch} and $\eta_{Fusarium}$ plots. It can be seen that η_{starch} and $\eta_{Fusarium}$ were very close to each other. To determine the number of Fusarium in the trap, Equation (12) was employed. Figure 7.13(b) depicts the relation of the number of *Fusarium* and *log*($\frac{P_{\lambda_1}}{P_{0,\lambda_1}}$) in case of applying data of λ_1 thermopile.

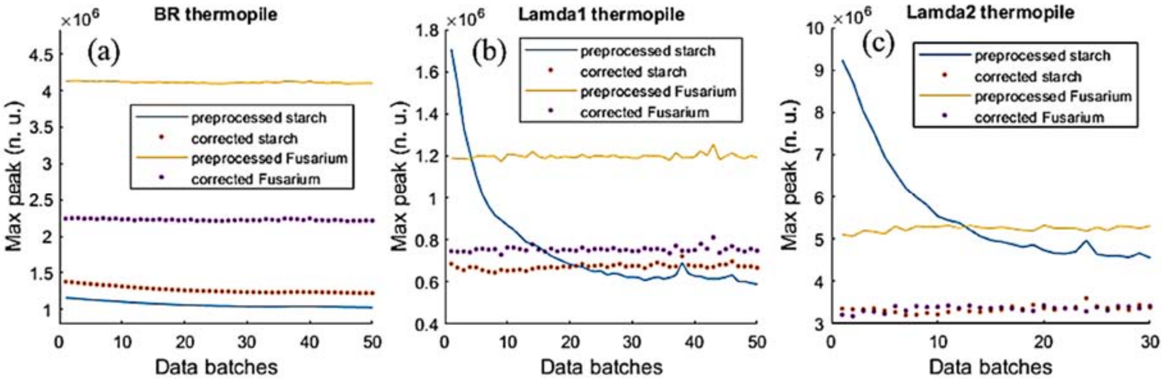

Figure 7.12. The ACKF preprocessed and corrected data of *Fusarium* and starch. (**a**) BR thermopile case; (**b**) λ_1 thermopile case and (**c**) λ_2 thermopile case.

The fitted curve in Figure 7.13(b) was formed by applying data of the *Fusarium* samples, which their known quantities (N):

$$f_{\lambda_1} = \text{fitting}(log(\frac{P_{\lambda_1}}{P_{0,\lambda_1}}), N) \tag{7.24}$$

As the group distinction coefficients of *Fusarium* and starch are close to each other, thus it can cause confusion at certain times. Table 7.4 shows the means of the group distinction coefficients, the absolute errors, and the relative errors of *Fusarium* and starch. From the table, one can see these values were very close to each other.

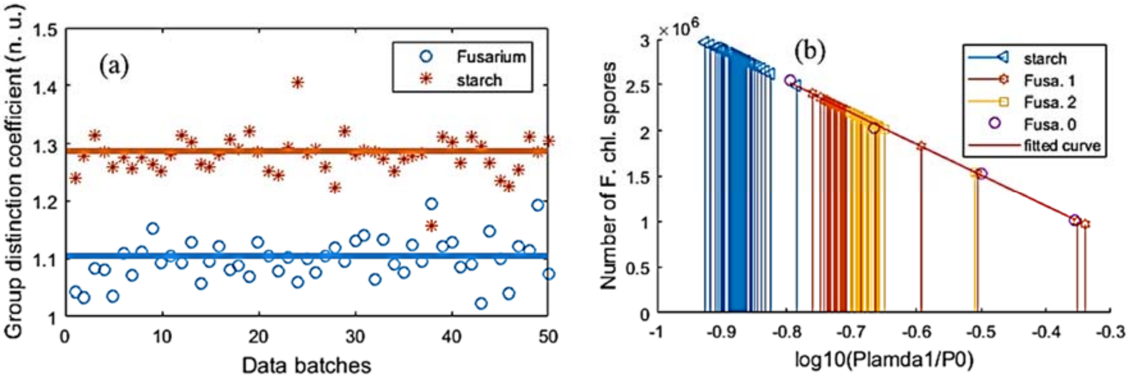

Figure 7.13. Using data of different *Fusarium* samples and starch sample measured by λ_1 thermopile. (**a**) η_{starch} and $\eta_{Fusarium}$ and (**b**) the fitted curve of the known-in-advance *Fusarium* samples, the interpolation and extrapolation of the unknown-different *Fusarium* and starch samples. * Fusa. 0 stands for the known-in-advance *Fusarium* sample. Fusa. 1 and Fusa. 2 are two unknown-quantity samples.

Table 7.4. Group distinction coefficient.

	Fusarium	**Starch**
η	1.125	1.31
$\Delta\eta$	0.110	0.06
ε_η	9.8%	4.6%

To improve the fidelity, the broadband thermopile was used. We investigated the other samples of starch and *Fusarium* that their quantities were unknown in advance. Making an assumption that all the samples were *Fusarium*, we could find the sample quantities N_x by replacing $log(\frac{P_{\lambda_1}}{P_{\lambda_1 0}})$ into f_{λ_1} of Equation (7.24). Figure 7.13(b) illustrates the extrapolated and interpolated values of the new samples. From the data of the BR thermopile and the numbers of known-in-advance F. samples (Fusa. 0), the fitted curve was formed:

$$f_{BR} = \text{fitting}(N, log(\frac{P_{BR}}{P_{0,BR}})) \tag{7.25}$$

Additionally, it is necessary to form the lateral fitted curves for the max and min data points, which can be seen from the error boxes. error1 and error2 are the errors of the numbers of the

Fusarium oxysporum chlamydospore and log10($\frac{P_{BR}}{P_{0,BR}}$) respectively. Thus, the lateral-fitted curves are:

$$f_{BR}max = \text{fitting}(\text{N} + \text{error1}, log(\frac{\text{P}_{\text{BR}}}{\text{P}_{\text{0,BR}}}) + \text{error2}) \tag{7.26}$$

$$f_{BR}min = \text{fitting}(\text{N} - \text{error1}, log(\frac{\text{P}_{\text{BR}}}{\text{P}_{\text{0,BR}}}) - \text{error2}) \tag{7.27}$$

In Equations (7.26) and (7.27), error1 and error2 are the errors of the quantity number of *Fusarium* sample N and *log*($\frac{\text{P}_{\text{BR}}}{\text{P}_{\text{0,BR}}}$) respectively. The lateral curves will create a validation area (VA). In the case of investigating new measurement, if the point of the quantity number N and *log*($\frac{\text{P}_{\text{BR}}}{\text{P}_{\text{0,BR}}}$) is in the VA and η of the sample is in the range of 1.125 ± 0.110, we could conclude that the sample is *Fusarium*. Drawing the points of (N_x, *log*($\frac{\text{P}_{\text{BR,x}}}{\text{P}_{\text{0,BR}}}$)) is presented in Figure 7.14. The figure also provides a visual view of the lateral curve and the VA. In Figure 7.14, the points of starch samples were out of the VA, so along with η of starch, we could go to a conclusion with more confident and reliable. For the other two *Fusarium* samples, we could see that almost all of the measurement points were in the VA, except few points on the left of the figure.

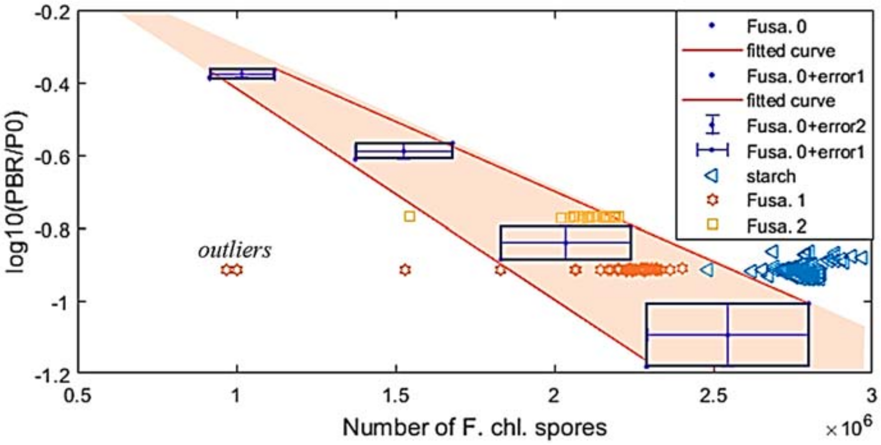

Figure 7.14. f_{BR} = fitting (N, *log*($\frac{\text{P}_{\text{BR}}}{\text{P}_{\text{0,BR}}}$)) and the validation area formed by the lateral curves of Equations (7.26) and (7.27).

7.4.4. Discussion

The ACKF helps to reduce thermal noise and burst noise well. To be able to fix the outliers of BG or peak data, at least some reference data points were not affected by the outliers. From these reference data points, the ACKF could eliminate the outliers. In reality, there are cases that the ACKF cannot fix the error data (Figure 7.8(f)), as the outliers happen too close to each other. Therefore, the reference data points are covered by the burst noise. As a result, the error data cannot adequately be fixed. Besides, from our experiments, we found that the ACKF could also help to reduce the time to search the global minima for the NN. This could be explained as the thermal noise and burst noise occurring in the BG noise were filtered very well by the ACKF (Section 4.1), so the NN could go to the global minima faster. The evidence of this point of view can be seen in Table 7.2.

Entropy is not only a useful tool to evaluate the work of Kalman filter, but also can be applied as an operational criterion to replace the other criteria such as the mean absolute error. The results in Sections 4.1 and 4.2 show the efficiency of the entropy. From Figure 7.8(c),(d), and Table 7.2, although the error was the smallest after 1000 loops, the visual results were not what we expected. The corrected points fluctuated surrounding the expected lines. Entropy was applied to the differentiation of the preprocessed and corrected MP data rather than being applied directly to these data. Loosely speaking, the differentiation step helped to remove the difference in the magnitude of these MP data, as we only focused on the BG noise. The information left was mainly the BG noise, which influenced the MP data (Figure 7.10(c)). Entropy now reveals how much BG noise is removed by comparing the entropies of the differentiation of the preprocessed and corrected MP data.

Figure 7.12 presents the results when the trained NN was used to correct the error data of *Fusarium* and starch in which these samples were measured in many batches. In Figure 7.11(a), one can see that the NN adjusted the MP of both samples. In Figure 7.11(b), (c), the MP data of starch achieved the largest errors as they lasted from around 0.6×10^6 to 1.7×10^6 in the case of λ_1 thermopile, and from around 4.3×10^6 to 9.2×10^6 in the case of λ_2 thermopile.

As the group-distinction coefficient of *Fusarium* and starch were very similar, the addition of another thermopile detector, the BR thermopile, could help to distinguish better these two samples. Figure 7.13 shows that some *Fusarium* points were out of the VA. This could be explained that in the data there were outliers, which the ACKF could not correct them. The figure also introduced a case that the starch point was in the VA. However, in general, one could see that most of the experiment points were in the VA, so the device could distinguish the *Fusarium* sample from other samples. With an adding detector, the ability of the device could be expanded. It could help to detect the group of many more substances.

The group-distinction coefficient of the starch was found in this work was a little bit different from the value in [C7.20], 0.9390 ± 0.0732. This could be explained that the moistures of the starch samples used in this work and in [C7.20] were different. A slight change in moisture of the starch sample might affect its group-distinction coefficient.

7.5. Conclusions

The proposed adaptive-cognitive Kalman filter worked well to reduce the thermal noise and burst noise. The background noise could be mitigated by applying a neural network. The entropy could be applied to replace the mean absolute error as an operational condition. The upgraded device increased the reliability and precision of the current *Fusarium* detection and quantifying by applying the proposed techniques. Additionally, by adding one more thermopile, the group coefficients of substances were more distinct. This assisted the device to distinguish different substances easier with higher accuracy compared to the use of only two thermopiles.

References

[C7.1] M. Nucci and E. Anaissie, “Fusarium Infections in Immunocompromised Patients,” *Clinical Microbiology Reviews*, vol. 20, no. 4, pp. 695–704, Oct. 2007.

[C7.2] J. Evans, D. Levesque, A. de Lahunta, and H. E. Jensen, “Intracranial fusariosis: a novel cause of fungal meningoencephalitis in a dog,” *Vet. Pathol.*, vol. 41, no. 5, pp. 510–514, Sep. 2004.

[C7.3] R. D. Martyn, “Fusarium Wilt of Watermelon: 120 Years of Research,” in *Horticultural Reviews: Volume 42*, J. Janick, Ed. Hoboken, New Jersey: John Wiley & Sons, Inc., 2014, pp. 349–442.

[C7.4] E. D. de Toledo-Souza, P. M. da Silveira, A. C. Café-Filho, and M. Lobo Junior, “Fusarium wilt incidence and common bean yield according to the preceding crop and the soil tillage system,” *Pesq. agropec. bras.*, vol. 47, no. 8, pp. 1031–1037, Aug. 2012.

[C7.5] E. Bauriegel, A. Giebel, and W. B. Herppich, “Rapid Fusarium head blight detection on winter wheat ears using chlorophyll fluorescence imaging,” Journal of Applied Botany and Food Quality, vol. 83, no. 3, pp. 196-203, August 2010.

[C7.6] A. Adesemoye *et al.*, “Current knowledge on Fusarium dry rot of citrus,” Citrograph 29, p. 6, Nov. 2011.

[C7.7] N. A. Foroud, S. Chatterton, L. M. Reid, T. K. Turkington, S. A. Tittlemier, and T. Gräfenhan, “Fusarium Diseases of Canadian Grain Crops: Impact and Disease Management Strategies,” in *Future Challenges in Crop Protection Against Fungal Pathogens*, A. Goyal and C. Manoharachary, Eds. New York, NY: Springer New York, pp. 267–316, 2014.

[C7.8] BASF Canada Inc., “Fusarium Management Guide.” BASF Canada Inc. Available: https://agro.basf.ca. Accessed: 01-Oct.-2019.

[C7.9] C. Marinach-Patrice *et al.*, “Use of mass spectrometry to identify clinical Fusarium isolates,” *Clinical Microbiology and Infection*, vol. 15, no. 7, pp. 634–642, Jul. 2009.

[C7.10] A. Salman, L. Tsror, A. Pomerantz, R. Moreh, S. Mordechai, and M. Huleihel, “FTIR spectroscopy for detection and identification of fungal phytopathogenes,” *Spectroscopy*, vol. 24, no. 3–4, pp. 261–267, 2010.

[C7.11] E. Tamburini, E. Mamolini, M. De Bastiani, and M. Marchetti, “Quantitative Determination of Fusarium proliferatum Concentration in Intact Garlic Cloves Using Near-Infrared Spectroscopy,” *Sensors*, vol. 16, no. 7, p. 1099, Jul. 2016.

[C7.12] J. S. West, G. G. M. Canning, S. A. Perryman, and K. King, “Novel Technologies for the detection of Fusarium head blight disease and airborne inoculum,” *Trop. plant pathol.*, vol. 42, no. 3, pp. 203–209, Jun. 2017.

[C7.13] P. Papireddy Vinayaka *et al.*, “An Impedance-Based Mold Sensor with on-Chip Optical Reference,” *Sensors*, vol. 16, no. 10, p. 1603, Sep. 2016.

[C7.14] C. G. Dobbs, “ON THE PRIMARY DISPERSAL AND ISOLATION OF FUNGAL SPORES,” *New Phytol*, vol. 41, no. 1, pp. 63–69, May 1942.

[C7.15] J. J. Ooka and T. Kommedahl, “Winter and rain dispersal of Fusarium moniliforme in corn fields,” Phytopathology, vol. 67. pp. 1023–1026, 1977.

[C7.16] T. Quesada, J. Hughes, K. Smith, K. Shin, P. James, and J. Smith, “A Low-Cost Spore Trap Allows Collection and Real-Time PCR Quantification of Airborne Fusarium circinatum Spores,” *Forests*, vol. 9, no. 10, p. 586, Sep. 2018.

[C7.17] J. Lacey, “Philip herries gregory (1907–1986),” *Grana*, vol. 25, no. 3, pp. 159–160, Dec. 1986.

[C7.18] P. H. Gregory, E. J. Guthrie, and M. E. Bunce, “Experiments on Splash Dispersal of Fungus Spores,” *Journal of General Microbiology*, vol. 20, no. 2, pp. 328–354, Apr. 1959.

[C7.19] Gary C. Begstrom Melissa D. Keller and Elson J. Sheilds, “The aerobiology of Fusarium graminearum,” *Aerobiologia*, vol. 30, pp. 123–136, Nov. 2013.

[C7.20] Son Pham, Anh Dinh, and Khan Wahid, “A Nondispersive Thermopile Device with an Innovative Method to Detect Fusarium Spores,” IEEE Sensors Journal, vol. 19, issue 19, pp. 8657-8667, Jun. 2019

[C7.21] J. M. Parnis and K. B. Oldham, “Beyond the Beer-Lambert Law: The Dependence of Absorbance on Time in Photochemistry,” *J. of Photochem. & Photobio., A: Chem.*, vol. 267, pp. 6-10, 2103. Available: https://doi.org/10.1016/j.jphotochem.2013.06.006.

[C7.22] J. F. Leslie and B. A. Summerell, *The fusarium laboratory manual*, 1st Edition, Ames, Iowa: Blackwell Pub, 2006.

[C7.23] Texas Instruments, “Noise Analysis in Operational Amplifier Circuits,” *Texas Instrument*, 2007. [Online]. Available: http://www.ti.com/. [Accessed: 01-Aug-2019].

[C7.24] G. Vasilescu, “Physical Noise Sources,” in *Electronic Noise and Interfering Signals - Principles and Applications*, Printed in Germany: Springer, 2004, pp. 45–67.

[C7.25] M. Á. Raposo-Sánchez, J. Sáez-Landete, and F. Cruz-Roldán, “Analog and digital filters with α-splines,” *Digital Signal Processing*, vol. 66, pp. 1–9, Jul. 2017.

[C7.26] L. Luu and A. Dinh, “Using Moving Average Method to Recognize Systole and Diastole on Seismocardiogram without ECG Signal,” in *2018 40th Annual International Conference of the IEEE Engineering in Medicine and Biology Society (EMBC),* Honolulu, USA, pp. 3796–3799, June 2018.

[C7.27] E. B. Moullin and H. D. M. Ellis, “The spontaneous background noise in amplifiers due to thermal agitation and shot effects,” *Institution of Electrical Engineers - Proceedings of the Wireless Section of the Institution*, vol. 9, no. 26, pp. 81–106, 1934.

[C7.28] L. Dan, W. Xue, W. Guiqin, and Q. Zhihong, “A Methodological Approach for Detecting Burst Noise in the Time Domain,” *International Journal of Electronics and Communication Engineering*, vol. 3, no. 10, p. 5, 2009.

[C7.29] D. Deschrijver, L. Knockaert, and T. Dhaene, “Improving robustness of vector fitting to outliers in data,” *IEEE Electronics Letters*, vol. 46, no. 17, pp. 1200–1201, Aug. 2010.

[C7.30] G. M. Siouris, Guanrong Chen, and Jianrong Wang, “Tracking an incoming ballistic missile using an extended interval Kalman filter,” *IEEE Transactions on Aerospace and Electronic Systems*, vol. 33, no. 1, pp. 232–240, Jan. 1997.

[C7.31] Z. Zu-Tao and Z. Jia-Shu, “Sampling strong tracking nonlinear unscented Kalman filter and its application in eye tracking,” *Chinese Phys. B*, vol. 19, no. 10, p. 104601, Oct. 2010.

[C7.32] S. Yin, J. H. Na, J. Y. Choi, and S. Oh, “Hierarchical Kalman-particle filter with adaptation to motion changes for object tracking,” *Computer Vision and Image Understanding*, vol. 115, no. 6, pp. 885–900, Jun. 2011.

[C7.33] H. Zhang, G. Dai, J. Sun, and Y. Zhao, “Unscented Kalman filter and its nonlinear application for tracking a moving target,” *Optik*, vol. 124, no. 20, pp. 4468–4471, Oct. 2013.

[C7.34] A. Motwani, S. K. Sharma, R. Sutton, and P. Culverhouse, “Interval Kalman Filtering in Navigation System Design for an Uninhabited Surface Vehicle,” *The Journal of Navigation*, vol. 66, no. 5, pp. 639–652, Sep. 2013.

[C7.35] S. Pham and A. Dinh, “Using the Kalman Algorithm to Correct Data Errors of a 24-Bit Visible Spectrometer,” *Sensors*, vol. 17, no. 12, p. 2939, Dec. 2017.

[C7.36] D. Lautier, “The Kalman filter in finance: An application to term structure models of commodity prices and a comparison between the simple and the extended filters,” *IDEAS Working Paper Series from RePEc; St. Louis*, 2002.

[C7.37] A. Bensoussan, *Estimation and Control of Dynamical Systems*, vol. 48. Cham: Springer International Publishing, 2018.

[C7.38] Amir Amani and Dariush Mohammadyani, *Artificial Neural Networks: Applications in Nanotechnology.* INTECH Open Access Publisher, 2011.

[C7.39] K. P. Murphy, *Machine learning: a probabilistic perspective*. Cambridge, MA: MIT Press, 2012.

[C7.40] Y. Zhang, *Machine Learning*. INTECH Open Access Publisher, 2010.

[C7.41] C. Nwankpa, W. Ijomah, A. Gachagan, and S. Marshall, “Activation Functions: Comparison of trends in Practice and Research for Deep Learning,” *Cornell University*, p. 20, Nov. 2018.

[C7.42] K. Suzuki, Ed., *Artificial Neural Networks - Architectures and Applications*. InTech, 2013.

[C7.43] K. Suzuki, Ed., *Artificial Neural Networks - Methodological Advances and Biomedical Applications*. InTech, 2011.

[C7.44] S. Amari and A. Cichocki, “Adaptive blind signal processing-neural network approaches,” *Proceedings of the IEEE*, vol. 86, no. 10, pp. 2026–2048, Oct. 1998.

[C7.45] A. Zaatri, N. Azzizi, and F. L. Rahmani, “Voice Recognition Technology Using Neural Networks,” *Journal of New Technology and Materials*, vol. 277, no. 2414, pp. 1–5, Jun. 2015.

[C7.46] C.-C. Huang, C.-F. J. Kuo, C.-T. Chen, C.-C. Liao, T.-T. Tang, and T.-L. Su, “Inspection of appearance defects for polarizing films by image processing and neural networks,” *Textile Research Journal*, vol. 86, no. 15, pp. 1565–1573, Sep. 2016.

[C7.47] J. A. Villacorta-Atienza and V. A. Makarov, “Neural Network Architecture for Cognitive Navigation in Dynamic Environments,” *IEEE Transactions on Neural Networks and Learning Systems*, vol. 24, no. 12, pp. 2075–2087, Dec. 2013.

[C7.48] Northumbria Optical, “Narrow Band Pass,” *Northumbria Optical Coatings Ltd*, 2018. [Online]. Available: https://www.noc-ltd.com. [Accessed: 01-Aug-2019].

[C7.49] “2M Thin Film Based Thermopile Detector,” *Dexter Research Center*. [Online]. Available: https://www.dexterresearch.com/. [Accessed: 01-Aug-2019].

[C7.50] Micro-Hybrid, “Infrared Radiation Source JSIR350-4-AL-C-D3.7-A5-I,” *Micro-Hybrid*. [Online]. Available: http://www.eoc-inc.com/micro-hybrid/IRSource/JSIR350-4-AL-C-D3.7-A5-l.pdf. [Accessed: 01-Aug-2019].

[C7.51] Analog Devices, “Zero-Drift, Single-Supply, Rail-to-Rail Input/Output Operational Amplifier AD8628/AD8629/AD8630,” *Analog Device*, 2014. [Online]. Available: analog.com. [Accessed: 01-Aug-2019].

[C7.52] Texas Instruments, “OPAx320x Precision, 20-MHz, 0.9-pA, Low-Noise, RRIO, CMOS Operational Amplifier with Shutdown 1,” *Texas Instrument*, 2016. [Online]. Available: http://www.ti.com. [Accessed: 01-Aug-2019].

[C7.53] "24-Bit µPower No Latency ΔΣTM ADC in SO-8," *Analog Device*. [Online]. Available: https://www.analog.com/media/en/technical-documentation/data-sheets/2400fa.pdf. [Accessed: 01-Jun-2019].

[C7.54] Microchip, "Atmel 8-Bit Microcontroller with 4/8/16/32kbytes In-System Programmable Flash," *https://www.microchip.com*. [Online]. Available: https://www.microchip.com. [Accessed: 01-Aug-2019].

[C7.55] D. Sh. Sabirov, "Information entropy changes in chemical reactions," *Computational and Theoretical Chemistry*, vol. 1123, pp. 169–179, Jan. 2018.

[C7.56] C. E. Shannon, "A Mathematical Theory of Communication," *SIGMOBILE Mob. Comput. Commun. Rev.*, vol. 5, no. 1, pp. 3–55, Jan. 2001.

[C7.57] S. Aydın, H. M. Saraoğlu, and S. Kara, "Log Energy Entropy-Based EEG Classification with Multilayer Neural Networks in Seizure," *Ann Biomed Eng*, vol. 37, no. 12, pp. 2626–2630, Dec. 2009.

8. Conclusion and Future Work

8.1. Summary and Conclusion

First, the thesis work proposes a method to create a 24-bit VIS spectrometer which can serve for sample analysis. The Beer-Lambert law is used to analyse samples. The problem of unstable output of the light sensor arises since battery is used to power this portable device. The battery energy eventually reduces to a level at which the output of the regulators becomes unstable. This leads to the un-stability of the light intensity which results in the error in the sample spectra analysis. Using a second light sensor to monitor the light source along with the Kalman algorithm reduces errors in the data and increases performance of the spectrometer. The proposed method of applying Kalman algorithm can be applied in any electronic system facing similar problems.

Beer-Lambert law is used again in a non-dispersive thermopile device to detect and analyze *Fusarium* spore in the air. The designed device and detection method overcome the drawbacks from other suggested detection methods in the past. The disadvantages of previous devices are bulky and expensive (FTIR spectroscopy or mass spectrometer), requirement of well-trained operators, and long analysis time. A group distinction coefficient was derived from the Beer-Lambert. Each substance (or sample) should have its own distinct coefficient in the spectrum analysis. To estimate this coefficient, it is required to have two distinct absorbent wavelengths of the target samples. These two wavelengths can be determined from the IR spectra of the samples. For the purpose of *Fusarium* spore detection, the two chosen wavelengths are λ_1=6.088μm and λ_2=9.487μm. Based on these wavelengths, two thermopiles which can respectively react with these wavelengths are used to measure the absorbance level of the *Fusarium* in the detection device.

Since airborne is a common method of spreading of the fungus, the detection device must sample the air which is drawn into and passed through a high voltage trap. The trap creates electrostatic charges on the two silver coated mirrors. The electrostatic charges catch the particles in the air for detection and analysis. The target *Fusarium* spores have specific size therefore it is essential to remove unwanted particles which may cause interference and difficulty in analyzing the data. A new method of combining a quad-inlet cyclone separator and the high voltage trap to make a bandpass particle filter is proposed. The features of the filter are simulated and investigated using the COMSOL Multiphysics software. Appropriate parameters for a filter prototype are determined.

The quad-inlet cyclone is printed by a 3D printer and the high voltage trap is made by resin casting method. The prototype filter is successfully tested in near to practical environment conditions.

In data analysis of the detection device, the challenging is the interference of noises. These noises include thermal noise, burst noise, and background noises. Among the three, background noise affects the most to the detection and analysis as its effect results in the error in the thermopile data. The neural network approach is developed and used to correct the error. To support for the correction, a temperature sensor and two-voltage monitor modules are installed into the device to record the operating conditions. The training data for the neural network are collected in one week in order to record as much as possible the information of real operating conditions. The thermopile data, the information of the operating conditions, and the background noise extracted from the thermopile data are used to train the neural network. The trained neural network is used for error corrections. The results prove the performance of the proposed method in error correction on data affected by noises.

In the detection, there are cases in which the group distinction coefficients of two or more samples can be similar to each other such as *Fusarium* and starch in the experiments. The similarity of the coefficients may lead to incorrect detection. To overcome this problem, a set of three thermopiles (broadband (1μm to 20μm), λ_1, and λ_2 thermopiles) is used in the upgraded device from the previous version of the *Fusarium* detection device. The addition of the broadband thermopile assists in distinguishing the samples having similar group-distinction coefficients. In addition, to increase the precision, an adaptive-cognitive Kalman filter is designed to process thermal and burst noises. The efficiency of method is proven through the experiment results.

In general, the main contribution of the research is providing the group-distinction coefficient formula which is the key to build up the *Fusarium* detection system, a comprehensive approach to build a portable device to detect and analyze biology objects in the air. The approach includes selecting wavelengths, building filter and amplifiers, noise processing, and data analysis. Even the focus of this thesis work is to detect and quantify the *Fusarium* spores in the air to reduce the potential loses caused by *Fusarium*, the methodology can be applied in various areas including agriculture security, food security, or human-living environment.

8.2. Suggestions for Further Studies

Although the introduced method has been proven through building of the prototype and experimental results, more tests should be conducted in the crop fields to observe the other effects of the real environment on the device. Currently, the data collected from the device by the Atmel 328P microcontroller must be sent to a computer for further processing. The Atmel 328P could be replaced by another powerful microprocessor. The microcontroller then can take the role of collecting, processing data, and making detection decision. Noise process is still very complicated. Conducting more research on building better amplifiers or selecting other detectors can increase accuracy and precision of the device. Finding ways to reduce the size of the device can provide more applications for this detection method. For example, if this device is small enough, it can be attached to a drone to cover a larger area and greatly reduce the expense.